Futura

Hydrogen-Electric Helicopter

Final Report

Design
Synthesis Exercise
BSc Aerospace
Engineering
Group 19
July 2, 2019

TUDelft

Faculty of Aerospace Engineering

Futura

Hydrogen-Electric Helicopter

Final Report

Version: 2.0

by

A. Barberia	4537998
K. Dally	4553373
T.M.L. De Ponti	4577612
T. De Smedt	4556003
B. Keltjens	4551311
G. Mancini	4533690
M. Piras	4550552
A. Scoccimarro	4538366
F. Taccaliti	4490231

to obtain the degree of Bachelor of Science
at the Delft University of Technology.

Project duration:	April 23, 2019 – July 4, 2019	
Supervisory team:	Dr. R.M. Groves	TU Delft, supervisor
	Dr. B. V. S. Jyoti	TU Delft, coach
	K. Vidyarthi	TU Delft, coach
	Dr. B. Atli-Veltin	TNO, coach

TU Delft

Executive Overview

During the preliminary phase of this project, the system configuration was determined. Futura, a tilt-rotor powered by fuel cells and batteries, was designed to meet the client requirements the best. This preliminary aircraft serves as a solution to crowded airports and congestion in the aviation sector, while maintaining highly sustainable actions. This report details the development of the market, technical system, production, sustainable actions and future progress of the aircraft. Such analysis serves to understand the capabilities and feasibility of the aircraft.

Although performance is key to a successful product, a market analysis motivates a demand for Futura. To assess the demand, the challenges in mobility must be examined first. Congestion in airports, due to an increase in demand for flying, will lead to a stagnation in growth. Futura aims to relieve the market of this issue by opening up airport slot opportunity for different airlines without having to completely build large new runways. The most important stakeholders in addressing this need are the client, to set the objective of the aircraft, customers, to ensure demand, airports, to manage logistics and the environment. A large focus of this product is to reduce the impact of the life cycle on the environment. Competitors in the market consist of short-haul flights, which are limited in efficiency, taxis, which are limited by price and environment and public transportation, which is limited by comfort and consistency. To maximise the utility of Futura, the market is segmented into smaller parts consisting of business clients, traditional operations, emergency operations, humanitarian work, law enforcement and offshore. With these different markets, the share that Futura will operate in will be limited to 1% in the first year but has the potential to increase to 10% by six years. The major disadvantages which are posed to Futura are the limited range, dependency on small hydrogen suppliers, specific infrastructure, and uncertainty in a new market. However, there are a large amount of benefits that drive the need for this product. These include: diversification of markets, sustainability, comfort, government investment, and a solution to congested airports.

To be able to deliver the benefits mentioned above of Futura, a robust design approach is developed. First, the requirements that drive the design are identified. Requirements on the range, maximum speed, payload, turnaround time, availability and cost of production and operations guide the design process by imposing constraints. The design is focused on the integration of vertical and forward flight capabilities with a battery and fuel cell power plant. A large part of this focuses on reducing the power needed to perform a mission and to mitigate the safety concerns with a novel power plant system, such as a rigorous tank design. The three pillars of the design consist of a Novel Power Plant Design, Optimised Aerodynamic and Propulsion design and Sustainable Integration Design. As aviation produces 5% of global greenhouse gas emissions, a Sustainability Development Strategy was developed to sit at the core of the design process. This strategy is present through production, operation and end-of-life solutions.

The first part of the design is to define clearly the operational space of Futura. The aircraft will operate at both an intra-city and inter-regional level. Many different mission profiles are possible in this design space. However, the design process considers the longest route the most constraining. Hence, the one to design for. A mission profile based on a flight from Amsterdam to Brussels, approximately 300 km is developed. The operational space also includes the need for hydrogen. It is determined that liquid hydrogen is optimal for Futura, with a refuelling time of 26 minutes for 14.30 kg of liquid hydrogen, estimated in the future to be price at about 10.72 €/kg for a total cost of 153.3€ for a full refuel. Combined with battery recharging this would result in a total refuelling cost of 182€. The current cost for a 300 km helicopter mission is at about 227€. To complete a mission, the relevant infrastructure is needed; the

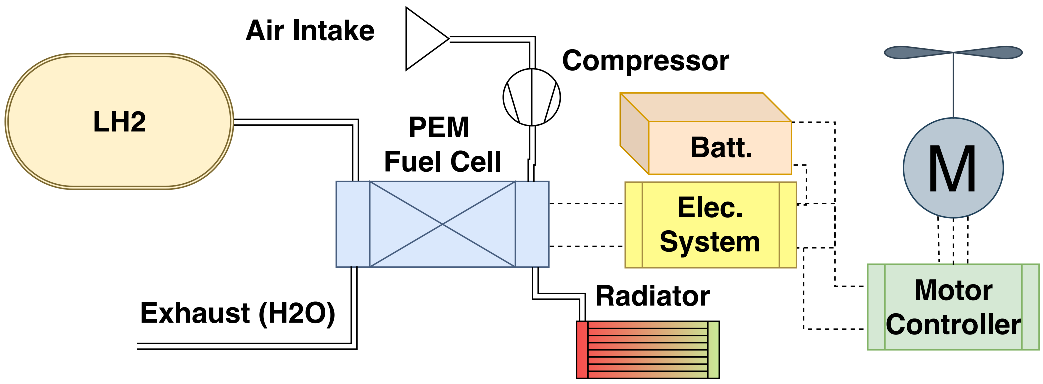

Figure 1: Power plant layout.

main additions are the parking and the take-off and landing sites. The most efficient manner is to place the landing sites near terminals for easy connection between different airports. A turnaround procedure is developed to ensure a 1-hour time frame. The total procedure, including engine shutdown, disembarkment, mechanical checks, refuelling, cleaning, boarding the passengers and starting up the aircraft takes 50 minutes.

To begin the performance analysis of the vehicle subsystems, an aerodynamic analysis is performed. The wing is sized according to constraints on wing loading and power loading. For different flight conditions such as cruise, climb, landing manoeuvring and stall. The design space is constrained by the stall speed and the manoeuvring performance resulting in an optimal wing area of 21.035 m^2. With this different drag and lift coefficients are compared resulting in the NACA 23018 airfoil. An aspect ratio of 5.258 for the wing is determined. As a result of the restrictions of the radiators on the wing only flaps can be used as high lift devices, while simultaneously acting as ailerons; flaperons. Finding the wing flapped area and shift of angle of attack the optimum wing planform design is reached.
An operational envelope is created for the flight of Futura. This takes into account loads in both vertical and horizontal flight by CS-23 and CS-29 requirements. The largest load factor possible on the aircraft is 3.8 while the most negative cannot be 0.4 times the maximum load factor.

To provide a safe and comfortable flight experience, a cabin design is carried out. The cabin is designed by minimising accessories, whilst not sacrificing comfort. The aircraft will boast continuous glass windows, made possible by the lack of the need to pressurise the cabin. The cabin width is 1.48 m and the height is 1.4 m. The aircraft has a main door and an emergency door. With a cabin configuration set, a fuselage design is carried out. The fuselage is designed in the shape of an airfoil to provide lifting capabilities. The airfoil for the fuselage design was selected to conform to the inner cabin design and resulted in the NACA 25121 airfoil.

The final major aerodynamic member of the aircraft are the rotors on the end of both wings. A study of the rotor geometry was carried out to optimise for the lowest power required for the propulsion system over the course of the flight. To do this blade element theory was employed. Each hub has 3 blades with a radius of 4.415 m and a linear twist of $18°$.

With an understanding of the power and energy required from the rotor design, the power plant can be designed. The design of the fuel tank focuses on readily available components to shorten the delivery time of the product. The system consists of three main components: fuel cell, battery and electric motors.
It is essential to control the temperature at which they operate. This is done using radiators, with 50/50 ethylene glycol solution. The total mass of the radiator and cooling liquid, with a pump, is 215.7 kg separated over three radiators in each wing. The main requirements for fuel tank are to maintain the fuel at specific conditions, deliver it to the power plant and allow for easy refuelling. The layout of the tank is

a double tank with a near vacuum between the two layers. Different materials are considered for their material properties and ability to be recycled. The tank is also designed for venting, refuelling and fuel delivery. The final choice for the tank design was an Aluminium 2024 inner and outer shell, evacuated multi-layer insulation with a total mass of 25.8 kg. The total length is 1.12 m. With the radiators and the tanks decided the different components of the power plant system are decided. In the system, batteries supply the peak power requirements, while the fuel cell supplies more energy. The division of the batteries and fuel cell is optimised for ratings, stack design and redundancy measures. The minimum mass is achieved when the fuel stack delivers 343 kW and the batteries deliver the rest with a capacity of 103 kWh. The reliability of the system is analysed to ensure the avoidance of catastrophic events. By using a failure rate model and adjusting the component choices, a failure rate of $3.66 \cdot 10^{-8} h^{-1}$ is found, which allows for safe operation.

With the various locations and masses of the components determined the stability and controllability of the aircraft are designed for. First stability on the ground is considered with landing gear design. The landing gear is sized based on shock absorption and their position. The gears are positioned to avoid tipping and ensure manoeuvrability. This resulted in placing the nose landing gear 3.4 m in front of the centre of gravity and the main landing gear 0.28 m behind. Stability in flight was considered for both vertical and horizontal flight. For vertical control, a swashplate with cyclic and collective is used and in horizontal flight, a T-tail, as well as ailerons, elevators and a rudder, are used. The T-tail is chosen instead of a canard because the canard cannot satisfy stability requirements on this design. The empennage size and wing position are chosen as a function of horizontal stability and controllability and are 13% of the main wing area and 34% of the fuselage length, respectively. For the empennage, both vertical and horizontal, the NACA 0018 airfoil is used. Considering the vertical control, the swashplate is sized to accommodate the different control modes as well as the relevant degrees of freedom by being flapped and feathered. The nacelle hinges are sized for appropriate yaw control, requiring a torque of 43 Nm. For the general control of the aircraft, only one pilot is required to reduce the mass. The pilot's inputs are a stick which controls lateral and longitudinal rotation, yaw pedals, a collective lever, throttle control and a rotating switch to rotate the nacelle. As there is only one pilot, a robust control system is required. This control system resolves the different coupling dynamics in hover as well as determining accurate control modes for easy control by the pilot. The flight control system controls both the navigation and dynamic state of the aircraft.

With the loads on all the wing surfaces known, the surfaces were structurally sized. The sizing considers buckling of the plates and Von Mises stresses in the skin. The load case on vertical hover constrains the main wings. The wing is optimised to not reach yield strength, and have similar maximum bending stress and buckling stress. With this design method a wing weight of 241.8 kg is achieved. A similar procedure is carried out for the empennage wing structure resulting in a total empennage mass of 108 kg. Aluminium 2024 is used for its lower density, price and its excellent recycling capabilities.

With all the separate sub systems sized an iteration of the mass is done resulting in a convergence to 3925 kg. With the complete sizing of the technical design complete models of the exterior and interior are developed to ensure that the complete system fits together.

To understand the connections in the system, a communication flow diagram is developed, showing the connection between the general subsystems. This highlights the flight controls, the power plant, the cabin and the airport. Following this, the connection is elaborated more, with a focus on the hardware required in a hardware and data handling diagram. A series of checks are completed to ensure that the analysis is done correctly. The first one is sensitivity analysis. In these different assumed values are tested to see their effect on the compliance with the requirements. The assumptions on the fuselage weight and propeller weight are made more conservative compared to the rest of the design. It is seen that the same requirements as before are still satisfied. A mass budget is carried out to ensure that the

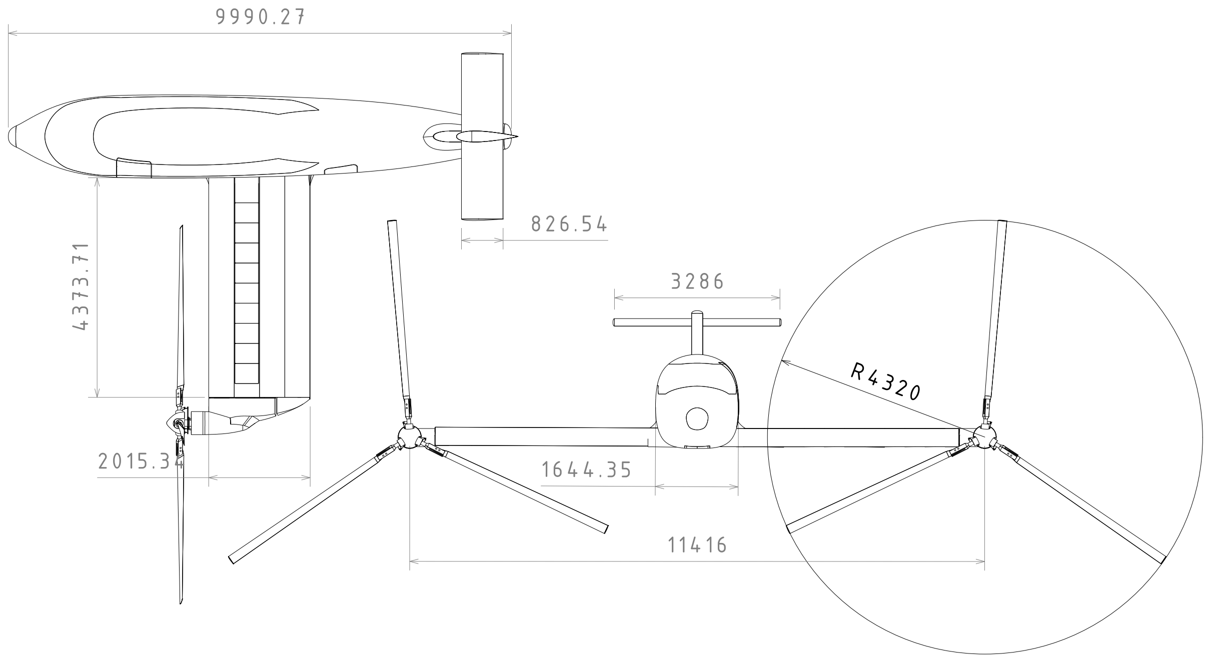

Figure 2: Futura's overall configuration.

mass is consistent over the whole system, and resource budget is thoroughly checked. This also occurs for a power budget over the system.

Finally, a compliance matrix is created. The requirements for the final design are reviewed, and it is clear that all the requirements are met.

To deliver a successful product, manufacturing must also be considered. To manage the use of resources in production, a lean manufacturing philosophy is adopted. Because of this, a part of manufacturing will be done in-house to reduce waste. The main parts and the large structural members are done in-house, such as the fuselage, the wings and the empennage. Sustainability is considered in the manufacturing of all different subsystems. An important manufacturing process is a roll forming for the complex curvature of the fuselage. The main materials used in manufacturing will be Aluminium 7075 and Aluminium 2024. An assembly plan is developed for efficiency to allow for the production of a single product in 28 days.

With the production and operation phases fully described the sustainability of the system is examined to ensure sustainable operation over the entire life cycle. The first aspect addressed is production, as it emits a lot of greenhouse gases. Raw material extraction is reduced by using recycled material. Manufacturing waste is reduced as aforementioned. For fuel production electrolysis, derived from renewable electricity sources, is used. Fuel transportation will generate direct emissions in the order of 50 kg of CO_2 for each tank refill. Noise emissions are addressed as requirements that must be validated through testing as available models do not have sufficient accuracy The aircraft will be disassembled, upon retiring, at an Aircraft Fleet Recycling Association certified plant. The components will either be re-used or re-manufactured, typically engine parts or avionics. A full analysis of the different recycled materials was carried out to assess how much CO_2 and energy are saved: it is found that Futura has a reduction in 97% in CO_2 emissions and 84% in energy consumption over its entire lifetime when compared to conventional helicopters. This can be seen in Table 1.

Table 1: Life cycle assessment of Futura and H145.

		CO2 Emissions [ton]		Energy Consumption [MJ]	
Stage	**Aircraft**	Futura	H145	Futura	H145
Production	Material extraction	39.4	20.3	$6.06 \cdot 10^5$	$2.93 \cdot 10^5$
	Manufacturing	4.24	1.88	$5.55 \cdot 10^4$	$2.5 \cdot 10^4$
Operations	Fuel production, transportation	$4.36 \cdot 10^3$	$5.05 \cdot 10^3$	$2.10 \cdot 10^8$	$5.16 \cdot 10^7$
	Combustion	0	$1.27 \cdot 10^5$	0	$1.3 \cdot 10^9$
End-of-Life	Process	$9.72 \cdot 10^{-1}$	$8.96 \cdot 10^{-2}$	$6.81 \cdot 10^1$	$1.28 \cdot 10^3$
	Potential	-124	-9.87	$-7.14 \cdot 10^3$	$-1.54 \cdot 10^5$
Total		$4.28 \cdot 10^3$	$1.32 \cdot 10^5$	$2.11 \cdot 10^8$	$1.35 \cdot 10^9$
Difference		-96.8%		-84.4%	

With these processes defined the costs and return on investment are detailed. The approximate development cost is 182 M€ for the entire system. To test the aircraft, an approximate cost of 2.62 M€ is found for both flight tests and system tests. For the prototype it was projected that a cost of 5.44 M€ is required, meaning that an external investor such as the government or Clean Sky initiative, parties that interested in sustainability, are required. Comparing with competitors, it is clear that Futura is cheaper, can take higher payload and has a larger cruise speed, apart from the obvious benefits in green energy. With an analysis of the competitors in the market, a selling price of 8 M€ is set. The cost to produce the first aircraft, at 7.93 M€, and full development cost, with a safety factor, of 370 M€ lead to a break-even point in about nine years. This takes account of the reduction in the cost of production with a learning curve and other developments in the market. After 30 years the expected return on investment is 41%.

With a definition of the various aspects of the aircraft in market, performance and production, the risk of the system can be analysed. The reliability is assessed first. Considering the components of the different subsystems total system reliability of 0.9714 is reached, excluding the control system, which must be determined in testing. With these considerations, it is determined that the availability of 90% can be met. For the maintenance, the critical features are identified as the hydraulic and nacelle components. To mitigate the time to maintain the nacelle is made more easily accessible using side panels to access critical features. To ensure safety, CS-29 requirements are kept at the core of the design process. Some emergency safety risks are mitigated, such as, a safety door has been included, more than what safety requirements stipulate, as well as multiple redundancies in the system. A thorough risk analysis was carried out for the different aspects of the system. The largest are the rupture of the fuel tank, hydrogen leaks, battery failure, flight route cancellation, dead man zone in take-off and nacelle rotation failure. For each of these risks, an appropriate mitigation strategy is employed. These strategies move a majority of the risks to remote and unlikely.

Finally, the outlook on the future work of Futura is set out. The main phases to be completed in the first period of development are the Early Configuration and Market Analysis, Product Definition and Detail structural, systems and process design. Among the most important outcomes to be reached in this first phase is the additional government funding needed to go on with the product definition design phase. With a full description of the system, market and processes, Futura is ready to move to the next stage. Futura aims to satisfy a glaring need in the aviation sector while setting a benchmark for the future of sustainable and accessible air transportation.

Contents

List of Symbols

Symbol	Description	Unit
α	Angle of Attack	$^\circ$
α_{0_l}	Zero Lift Angle of Attack of the Airfoil	$^\circ$
α_{0_L}	Zero Lift Angle of Attack of the Wing	$^\circ$
α_{stall}	Stall Angle of Attack	$^\circ$
α_{trim}	Trim Angle of Attack	$^\circ$
μ	Air Viscosity	$\mathrm{kg(sm^2)^{-1}}$
β	Prandtl-Glauert Compressibility Correction Factor	–
$\Delta\alpha_{0_L}$	Variation of the Angle of Attack due to the Presence of the Flap	$^\circ$
$\Delta C_{D_{flap}}$	Increment of the Wing Drag Coefficient due to Flaps	–
ΔY	Airfoil Leading Edge Sharpness Parameter	
η_{FC}	Fuel Cell Efficiency	$\mathrm{W^\circ C^{-1}}$
η_s	Shock Absorption Efficiency	-
η_t	Tire Absorption Efficiency	-
η_B	Battery Efficiency	-
η_{EM}	Electric Motor Efficiency	-
δ_{flap}	Flap Extension Angle	$^\circ$
γ_a	Landing Angle Approach	rad
λ	Non-Dimensional Average Velocity	–
λ_i	Non-Dimensional Induced Velocity	–
λ_∞	Non-Dimensional Upstream Velocity	–
λ	Failure Rate	$\mathrm{h^{-1}}$
$\Delta n_{landing}$	Delta Load Factor at Landing	–
$\lambda_{N_{sim}}$	Failure Rate of N Simultaneously Malfunctioning Rows	$\mathrm{h^{-1}}$
λ_{row}	Failure Rate of a Row of Components	$\mathrm{h^{-1}}$
λ_{stack}	Failure Rate of a Stack of Components	$\mathrm{h^{-1}}$
λ	Thermal Conductivity	$\mathrm{Wm^{-1}K^{-1}}$
η_p	Rotor Efficiency	–
ϕ	Angle Between the Blade Element Velocity and Rotational Plane	rad
ρ_{cell}	Energy Density of a Single Battery Cell	$\mathrm{WhL^{-1}}$
ρ	Air Density at Cruise Altitude	$\mathrm{kgm^{-3}}$
ρ_0	Air Density at Sea Level	$\mathrm{kgm^{-3}}$
Ω	Rotational Speed	$\mathrm{ms^{-1}}$
σ	Rotor Solidity Ratio	–
σ_{SB}	Stefan–Boltzmann Constant	$\mathrm{W/m^2/K}$
θ	Angle Between the Blade Element and the Rotational Plane	rad
θ_l	Tip Back Angle at Landing Touch Down	rad
a	Speed of Sound	$\mathrm{ms^{-1}}$
$d_{airborne}$	Airborne Distance	m
A_{inlet}	Inlet Area	$\mathrm{m^2}$
A	Aspect Ratio	–
A_{rad}	Radiator Area	$\mathrm{m^2}$
S	Wing Surface Area	$\mathrm{m^2}$
b_t	Landing Gear Tire Width	m
C_{d_0}	Zero Lift Drag Coefficient of the Blades	–
C_d	Airfoil Drag Coefficient	–
C_{D_c}	Component Drag Coefficient	–
$C_{D_{climb}}$	Wing Drag Coefficient at Climb	–
$C_{D_{misc}}$	Miscellaneous Drag Coefficient	–
C_D	Wing Drag Coefficient	–
C_{f_e}	Equivalent Skin Friction Coefficient	–
C_l	Airfoil Lift Coefficient	–
W_{ampr}	Aeronautical Manufacturers Planning Report Weight	£
N_{rdte}	Number of Aircraft Built in the RDTE Phases	–
F_{diff}	Relative Program Difficulty	–
N_{st}	Number of Static Test Airframes Built	–
F_{obs}	Observables Characteristics	–
C_L	Wing Lift Coefficient	–
C_{l_α}	Airfoil Lift Curve Slope	–
C_{L_α}	Wing Lift Curve Slope	–

Symbol	Description	Unit
$C_{l_{\alpha=0}}$	Airfoil Lift Coefficient at Zero Angle of Attack	–
$C_{L_{\alpha=0}}$	Wing Lift Coefficient at Zero Angle of Attack	–
$C_{L_{climb}}$	Wing Lift Coefficient at Climb	–
$C_{l_{des}}$	Airfoil Design Lift Coefficient	–
$C_{L_{des}}$	Wing Design Lift Coefficient	–
$C_{l_{max}}$	Airfoil Maximum Lift Coefficient	–
$C_{L_{max}}$	Wing Maximum Lift Coefficient	–
$C_{L_{trim}}$	Wing Trim Lift Coefficient	–
C_m	Moment Coefficient	–
$C_{P_{ind}}$	Rotor Induced Power Coefficient	–
$C_{P_{prof}}$	Rotor Profile Power Coefficient	–
C_T	Thrust Coefficient	–
C_P	Power Coefficient	–
D_0	External Landing Gear Tire Diameter	m
d_{cell}	Diameter of Battery Cell	mm
d	Internal Landing Gear Tire Diameter	m
q	Dynamic Pressure	Pa
$\frac{d\epsilon}{d\alpha}$	Down Wash	–
e	Oswald Efficiency Factor	-
E_{cell}	Energy Capacity of a Single Battery Cell	Wh
e_{myl}	Emissivity of Aluminised Mylar Film	-
E_t	Energy Absorbed by the Main Landing Gear	J
B	Number of Blades in One Rotor	–
F_{tot}	Total Prandlt Loss Function	–
F_{area}	Fuselage Area	m^2
c_f	Flap Chord	m
F_{hub}	Prandlt Hub Loss Function	–
L_F	Fuselage Length	m
W_F	FuselFuelage Mass	kg
F_{tip}	Prandlt Tip Loss Function	–
S_{wet}	Fuselage Wetted Area	m^2
G	Climb Gradient	-
g	Gravity Acceleration	ms^{-2}
h_{cg}	Height of Centre of Gravity from Ground	m
h_B	Height Battery Pack	mm
h_s	Screen Height	m
S_h	Horizontal Tail Surface Area	m^2
HTC	Overall Heat Transfer Coefficient	$\mathrm{W°C}^{-1}$
$I_{FC_{cell}}$	Maximum Current of a Single Cell in a Fuel Cell.	A
$I_{FC_{stack}}$	Maximum Current of the Fuel Cell Stack.	A
L	Lift	N
l_{cell}	Length of Battery Cell	mm
L/D	Lift-to-Drag Ratio	–
l_B	Length Battery Pack	mm
LF	Load Factor	-
l_h	Horizontal Tail Arm	m
q_L	Distributed Lift	Nm^{-1}
l_f	Fuselage Arm	m
l_m	Horizontal Distance from Center of Gravity to Main Landing Gear	m
l_n	Horizontal Distance from Center of Gravity to Nose Landing Gear	m
$\dot{m}$	Mass Flow	kgs^{-1}
$\dot{m}_{air}$	Air Mass Flow	kgs^{-1}
M_{cruise}	Mach Number at Cruise	–
$\frac{t}{c}$	Airfoil Thickness over Chord Ratio	–
$N_{cell_{layers}}$	Number of Battery Cells Layers.	–
$N_{cell_{parallel}}$	Number of Battery Cells in Parallel.	–
$N_{cell_{series}}$	Number of Battery Cells in Series.	–
N_g	Landing Gear Load Factor	-
n_{max}	Maximum Positive Load Factor	-
N_{red}	Number of Redundant Rows in Parallel.	–
N_{row}	Number of Components Rows in Parallel.	–
n_s	Number of Main Gear Strut	-

Symbol	Description	Unit
N_{series}	Number of Components in Series.	–
p_{amb}	Ambient Pressure	bar
P_B	Battery Power	kW
P_{EM}	Electric Motor Power	kW
p_{FC}	Fuel Cell Maximum Fuel Pressure	bar
p_{fill}	Filling Pressure	bar
P_{FC}	Fuel Cell Power	kW
$\frac{W}{P}$	Power Loading	-
P_m	Maximum Static Load per Main Landing Gear strut	N
S_f	Fuselage Surface	m^2
p_{sta}	Refuelling Station Storage Pressure	bar
p_{vent}	Venting Pressure	bar
Q	Heat Load	kW
R	Rotor Radius	m
R	Reliability	–
r	Non-Dimensional Span-wise Location of Rotor Annuli at Each Blade Element	–
r_{hub}	Non-Dimensional Effective Minimum Blade Radius	–
r_{in}	Inner Tank Inner Radius	m
R_e	Reynolds Number	–
$R_{landing}$	Landing Rotational Radius	m
SF	Safety Factor	-
SM	Stability Margin	–
b	Wing Span	m
S_{ref}	Reference Wing Surface Area	m^2
s_s	Maximum Shock Absorber Deflection	m
s_t	Maximum Tire Deflection	m
S_{wf}	Reference Wing Flapped Surface Area	m^2
t	Operative Time in-between Maintenance Operations	h^{-1}
T	Rotor Thrust	N
T_{amb}	Ambient Temperature	°C
T_{cruise}	Temperature at Cruise	K
T_{LH2}	Liquid Hydrogen Temperature	°C
$V_{approach}$	Approach Velocity at Landing	ms^{-1}
v	Induced Velocity at Each of the Rotor Annuli	ms^{-1}
v_{air}	Air Speed	ms^{-1}
$V_{B_{cell}}$	Maximum voltage of a Single Battery Cell.	V
V_{cruise}	Cruise Velocity	ms^{-1}
V_{climb}	Climb Velocity	ms^{-1}
$dotV_{cool}$	Coolant volumetric Flow Rate	$Lmin^{-1}$
$V_{FC_{cell}}$	Maximum Voltage of a Single Cell in a Fuel Cell.	V
$V_{FC_{stack}}$	Maximum Voltage of the Fuel Cell Stack.	V
V_{max}	Maximum Velocity	ms^{-1}
V_∞	Rotor Upstream Velocity	ms^{-1}
$Volume_{cell}$	Volume of Battery Cell	L
$\frac{V_h}{V}$	Velocity Ratio at the Horizontal Tail	–
V_{stall}	Stall Velocity	ms^{-1}
v_{wake}	Rotor Wake Air Speed	ms^{-1}
c	Wing Chord	m
w_B	Width Battery Pack	mm
$\frac{W}{S}$	Wing Loading	Nm^{-2}
L_{wing}	Wing Lift	N
W_l	Landing Weight	kg
w_t	Touchdown Rate at Landing	ms^{-1}
x_{ac}	Wing Aerodynamic Center	m
x_{cg}	Centre of Gravity respect to MAC (%)	m
y	Span-wise Location of Rotor Annuli at Each Blade Element	m
y_{MLG}	Track Width of the Main Landing Gear	m
z_{n}	Height of the Bottom of the Nacelle from the Ground in Vertical Position	m

Acronyms

ATC	Air Traffic Control
ATM	Air Traffic Management
BEMT	Blade Element Momentum Theory
BET	Blade Element Theory
CEF	Cost Escalation Factor
CFD	Computational Fluid Dynamics
CFRP	Carbon Fibre-Reinforced Polymer
CO	Carbon Monoxide
CO_2	Carbon Dioxide
EBD	Electrical Block Diagram
EMS	Emergency Medical Services
EOL	End-Of-Life
GDP	Gross Domestic Product
GH_2	Gaseous Hydrogen
GPU	Ground Power Unit
HLDs	High Lift Devices
LE	Leading Edge
LH_2	Liquid Hydrogen
MAC	Mean Aerodynamic Chord
MLI	Multi-Layer Insulation
MTOW	Maximum Take-Off Weight
NRF	Nederlandse Radiateuren Fabriek BV
OEW	Operative Empty Weight
RDTE	Research, Development, Testing, Evaluation
ROC	Rate of Climb
ROI	Return On Investment
SMT	Simple Momentum Theory
SWOT	Strengths, Weaknesses, Opportunities, Threats
TE	Trailing Edge
VTOL	Vertical Take-Off & Landing

1. Introduction

Aviation today faces the challenge to reinvent itself as society needs a green, fast and reliable mode of transportation. As aviation contributes to 5% of human-made greenhouse gas emissions, governments and the general public exert an increasing pressure on airlines and manufacturers to switch to emission-free aircraft [1]. The automobile industry has already begun its transition to green technologies, thus putting aviation in the spotlight as a significant contributor to climate change. With today's oil consumption rates, world reserves are expected to run out within 50 years, according to BP [2]. To secure a long term market share, manufacturers have to propose innovative designs that rely on renewable energy sources today. Another market trend is the increasing congestion of major airport hubs. It is expected that by 2030, 19 key European airports will reach saturation, thereby severely limiting capacity growth.[1] The need for inter-hub air transportation, without runway occupation, is apparent to ensure aviation keeps growing. It is within this context that Futura, a green Vertical Take-Off and Landing aircraft, was born. It is has been designed as part of the Design Synthesis Exercise, the final project the Aerospace Engineering Bachelor at the Delft University of Technology. For ten weeks of full-time work, the authors of this report have produced the conceptual design of such innovative aircraft.

This report aims at presenting the final conceptual design that successfully fills these market needs. The design process and its results are presented to prove the feasibility of this groundbreaking aircraft. The outcome was the result of several milestones the team achieved over these ten weeks. From the identification of requirements, initial design concepts were generated in a Baseline report. The performance of the most promising designs was analysed to select the most optimum. Trade-off criteria included, amongst others, operations, technology readiness level and sustainability. In this report, the detailed design of this optimum choice is detailed.

First, the market in which Futura operates is analysed in chapter 2. In particular, the market demand is quantified to justify the economic sustainability of the aircraft. Before presenting the design, the approach to obtain the final concept is laid out is chapter 3, including the procedure, followed and the use of resources. Before the actual design of the aircraft, operational characteristics are derived from its defining features: being hydrogen-powered and equipped with Vertical Take-Off and Landing. A detailed plan for operations is presented in chapter 4. The engineering design begins with aerodynamics in chapter 5, as the wing loading and wing design can be performed from the mission profile. From the mission required energy and power, an optimal power plant is designed in chapter 6. This includes individual components' design and their integration. With the main component masses, the stability and control of the aircraft are derived in chapter 7. Required aerodynamic control surfaces are then sized, and the structural design of all aerodynamic surfaces is executed in chapter 8. With all sub-systems sized, their integration is achieved by checking mass and volume constraints as shown in chapter 9. The design of each sub-system is iterated more than a dozen times to meet all requirements to obtain a final conceptual design. From the given mass and material breakdown, a manufacturing plan is presented in chapter 10. With the entire aircraft's life cycle defined, its sustainability is evaluated in chapter 11. Also, with all sub-systems sized, the cost of the aircraft and the return on investment is determined in chapter 12. Chapter 13 discusses the risks associated with developing and operating Futura. It also investigates the reliability, availability, maintainability and safety of the aircraft. Further steps to be taken for the design are presented in chapter 14. Lastly, the report is concluded with an overview of the major design outcomes.

[1] URL `http://europa.eu/rapid/press-release_MEMO-11-857_en.htm` [cited 19 June 2019]

2. Market Analysis

A market analysis is necessary as the success of the project is not based purely on the performance of Futura. Indeed, it is determined by the market in which Futura will operate as well. An essential parameter in this equation is the concept of supply and demand: without the necessary market demand for an innovative transportation mode, the project might not be sustainable.

Therefore, the current mobility challenges and the different stakeholders of the project are assessed in section 2.1 and 2.2, respectively. After that, the existing competitors of Futura are analyzed in section 2.3. Furthermore, market segmentation will be performed in section 2.4 to identify potential markets and to estimate what the future market share of Futura could be. Finally, based on all the gathered information, a SWOT analysis will be carried out to evaluate Futura's market competitiveness.

2.1 Mobility Challenges

In 2017, 1 billion passengers were transported by air in the European Union, with 47% flying intra-EU and 17% flying nationally, resulting in the total growth of 7% compared to 2016 [3]. The total contribution of the air transport sector to the EU's Gross Domestic Product (GDP) was 2.1%, which can be broken down in 300 B€ and 5 million jobs, making it a strategically vital sector.[1] However, at this growth rate, it is predicted that 19 key European airports will be congested by 2030. This issue is already present at the busiest airport in Europe, London Heathrow, and other airports are predicted to follow soon. The result is a capacity crunch: European airport capacity will not be able to keep up with the continuously growing demand for air transport.[2] A study performed by McKinsey & Company concluded that one consequence of this congestion is that the passenger growth will flatten, meaning that major airports will come to a standstill once their maximum capacity has been reached. Also, network connectivity will decrease while ticket prices will increase, making the airport less attractive to customers.[3] For airports to keep growing in the future, these are serious issues.

Therefore, it is of vital importance to find ways to increase airport capacity in the short term. Airport slots, which are the permission to use the airport's terminals and runways, play a crucial role in this challenge[4]: these slots are implemented at airports when the available supply exceeds the demand, and at major airports, such as London Heathrow, runway throughput is usually the constraining factor.[5] The simple solution seems to exist of building new runways and terminals. However, a significant amount of resources needs to be invested to achieve this target. Besides, several major airports are located in the neighbourhood of large cities, which makes expansion a rather tricky process [4]. Therefore, alternative solutions will have to be found to deal with the capacity crunch that major European airports are facing today, and Vertical Take-off & Landing (VTOL) capabilities might play a crucial role in this challenge.

[1] URL `totheEU'sGDP` [cited 19 June 2019]
[2] URL `http://europa.eu/rapid/press-release_MEMO-11-857_en.htm` [cited 19 June 2019]
[3] URL `https://www.mckinsey.com/industries/travel-transport-and-logistics/our-insights/gridlock-on-the-ground-how-airlines-can-respond-to-airport-congestion` [cited 19 June 2019]
[4] URL `https://aci.aero/about-aci/priorities/airport-slots/` [cited 19 June 2019]
[5] URL `https://www.eurocontrol.int/news/what-slot` [cited 19 June 2019]

2.2 Stakeholders

Stakeholders can be defined as the set of people who can affect or are affected by the system [5]. Considering that these stakeholders play a significant role in the development and operation of Futura, it is necessary to assess their influence to complete the project successfully. Therefore, a list of the most important stakeholders of Futura is given as follows: [6]

- **Client:** They line out the project objectives and set the important requirements. Also, they provide the necessary resources for the project and expect a positive return on investment from their investments. Therefore, it is of the utmost importance that these clients are satisfied with the progress and result of the project.
- **Customers:** They buy the Futura from the clients and are therefore vital to the sustainability of the entire project. Without their acquisitions, the project will not be able to continue due to insufficient profits and return on investment.
- **Regulatory Agencies:** They set up the regulations for Futura's type of aircraft, are (partly) involved in the testing and certification of Futura, and enforce their laws and regulations. Besides, they can provide additional funding for Futura, considering that the goal is to create an aircraft fuelled by a renewable fuel type.
- **Environment:** An important objective of the project, is to produce an aircraft with a high degree of sustainability to preserve the environment.
- **Employees:** These are essential in all stages of the project: development, production, operation, and end-of-life. They make sure that all the activities during the different project stages are completed and that Futura can be built and operated. Examples of employees are engineers, marketing and sales, assembly workers, crew.
- **Suppliers:** They deliver the various materials and components required to manufacture and maintain Futura. Therefore, it is essential to communicate clearly with them which materials or components are needed and when.
- **Airports:** They will provide the infrastructure for Futura to land and take off, and will help to complete the turnaround procedure. This includes, for example, runways, terminals, gates, and recharging facilities, etc.
- **Local communities:** The sustainability aspect of Futura also applies to local communities: it must be ensured that Futura will not disturb these communities based on noise and air traffic. Therefore, it is crucial to invest in a positive relationship between Futura and the local communities.
- **Competitors:** They will compete with Futura for market share. Also, they could try to replicate Futura's innovative technology if it has proven to be successful in attracting clients. The risk is then that the profits of the projected decrease due to a reduction in market share and sales.
- **Media:** They can have a considerable impact on Futura's reputation: with positive articles and advertising, Futura's market share could grow as the number of customers is likely to increase. However, if negative articles are written about Futura, potential customers might get scared off. This means that a positive connection with the media is essential to attract customers.
- **EU:** As discussed in section 2.1, the air transport sector is a vital contributor to its GDP. Therefore, it is reasonable to assume that the EU could make some investments in Futura to retain and even increase the sector's contribution to its GDP.

This list shows the most important stakeholders of Futura. However, it is essential to note that there might be more (minor) stakeholders, but these will not be considered in this report.

2.3 Competitor Analysis

A study was performed on the both intra-city and inter-regional level to estimate Futura's market competitiveness [6]. It was concluded that three main transportation competitors currently exist for Futura: flights, taxis, and public transportation such as trains and metros. These will be discussed in subsection 2.3.1, 2.3.2 and 2.3.3 respectively.

2.3.1 Flights

Flights are one of the fastest ways to travel on the inter-regional level. Besides, due to low-cost carriers, current ticket prices are very low, which makes flights an attractive way of transportation. However, when operating on the intra-city level, flights are usually not an option as the distance between airports is too limited. Also, some short-haul flights with current aircraft are starting to get cancelled due to concerns about their sustainability.[6] To get more insight in the predicted market position of Futura, the prices of current competing helicopters and aircraft will be analysed in chapter 12.

2.3.2 Taxis

Taxis are a personal transportation mode that offers a fast connection between two places, and some provide a higher level of comfort. However, they are usually rather expensive and are prone to traffic delays. Furthermore, their emissions are toxic to the environment, which raises questions about the sustainability of the sector. Finally, supply and demand is an issue from time to time, as finding an available taxi might be time-consuming.

2.3.3 Public Transportation

Public transportation is, in general, a very affordable way for passengers to reach their destinations and enables customers to reach almost all places in the city due to its vast network. However, long transit times and unexpected cancellations are only two of the disadvantages of public transportation. These may result in the customer missing a connecting flight if this passenger needs to transfer between two airports in the same city. Besides, the service and comfort provided by the operators are usually not suitable for business customers.

2.4 Market Segmentation

To get a clear overview of the whole market that Futura will operate in, it will be segmented into several smaller markets in which Futura might play a role. These will be analyzed in subsection 2.4.1. After that, a prediction will be made as to what market share Futura could achieve in subsection 2.4.2.

2.4.1 Market Identification

To increase future sales, Futura will not only operate for business customers. Indeed, several other potential markets were identified in which Futura might be used. Therefore, a complete list of potential markets is given below to show the client all the different market opportunities for Futura: [7]

- **Business Operations:** Business customers can use Futura as a means of personal transport, both for themselves as for their clients. They will have the possibility to be transported between air- and heliports with Futura, or even take off and land from their helipad. As Futura will provide a luxurious experience, this is the leading market Futura is targeting.

[6] URL `https://www.thebulletin.be/proposal-cancel-flights-between-brussels-and-amsterdam` [cited 19 June 2019]

- **Traditional Operations:** Of course, Futura can be used for traditional operations provided by airlines as well. This can especially be interesting for airlines who wish to increase their connectivity with major congested airports, as Futura does not necessarily need to use the airport's main runways. In addition, as discussed in section 2.3, some short-haul flights might get cancelled in the future due to concerns about their sustainability.[6] Futura is designed for short-haul flights and has a strong focus on sustainability, creating the opportunity to take over this market.

- **Emergency Medical Services (EMS):** Due to the combination of Futura's VTOL capabilities and high cruise speed, critical passengers can be transported fast to and from airports. Also, its VTOL capabilities can be used to reach congested or remote areas that other transportation modes cannot reach.

- **Humanitarian Work:** Places that have been hit by severe catastrophes like meteorological disasters or war and are difficult to reach for traditional transport vehicles can be provided with immediate support by Futura. These support activities can be to supply food and water, save people from dangerous places, etc.

- **Law Enforcement:** Like for EMS, the high cruise speed and VTOL capabilities allow for fast response to emergencies. Besides, patrolling and high-speed pursuits are possible as well due to the large range of speeds Futura can operate at.

- **Offshore:** Currently, Europe is the only continent in the world in which the number of oil rigs is growing: with 186 rigs in use today, their number more than doubled since last year.[7] As part of these drilling rigs is located offshore, transportation to and from the mainland has to be provided, and helicopters are usually the only feasible option in this case: they transport workers, perform search-and-rescue missions and provide the necessary EMS. Futura can offer the same services as these helicopters, and they can even be used for offshore renewable energy production plants such as wind farms. However, to protect Futura from these marine conditions, corrosion resistant coating will need to be applied where necessary [8].

- **Military:** With the V-22 in use and the V-280 under development, it is clear that the military sees a clear advantage in the use of tiltrotor aircraft for their operations: critical locations can be reached in a fast way, and the tiltrotor can take off and land at virtually every area. Also, Futura will be able to transport both troops and supplies necessary for any mission.

For several of these markets, adjustments have to be made to the design of Futura such as the implementation of medical or police equipment. However, these adjustments will not be considered in this report as the final customer bears responsibility in this matter.

2.4.2 Market Share

Due to the VTOL capabilities of Futura, the achievable market share will be compared with the current helicopter market. In recent years, this market has been dominated by one company: Airbus. With a total market share of 54% in 2018, compared to 21% for runner-up Leonardo, and an annual sales of 163 Futura-like helicopters, it is clear that Airbus is a major competitor of Futura.[8]

As Futura is new in the market and uses innovative technology, it is expected that Futura will only achieve 1% of the market share in its first selling year. As potential customers get to know this advanced technology and start to see its benefits, the market share is predicted to double by the following year to 2%. After a gradual annual increase in sales, it is expected that a market share of 10% can be achieved in its sixth selling year as Futura can be used in a large variety of markets and combines the advantages of both aircraft and helicopter. This would put Futura on a shared fourth place in leading helicopter manufacturing companies, resulting in an annual sales of 30 Futura aircraft.

[7] URL `https://essentrapipeprotection.com/rigs-around-the-world/` [cited 19 June 2019]
[8] URL `https://www.airbus.com/helicopters/key-figures.html` [cited 19 June 2019]

2.5 SWOT

To identify Futura's competitive position, a SWOT analysis was performed: this acronym stands for Strengths, Weaknesses, Opportunities, Threats. It helps to assess Futura's potential and the challenges the project may encounter. A schematic overview can be found in Figure 2.1.

Strengths and Weaknesses are internal factors: these can be changed and are within the control of the company. On the other side, Opportunities and Threats are external factors: these are elements outside the company that influence the project but cannot be controlled. However, the company can use the advantages of Opportunities and try to protect itself against the Threats.[9] Besides, it is evident that Strengths and Opportunities are positive factors while Weaknesses and Threats are negative factors.

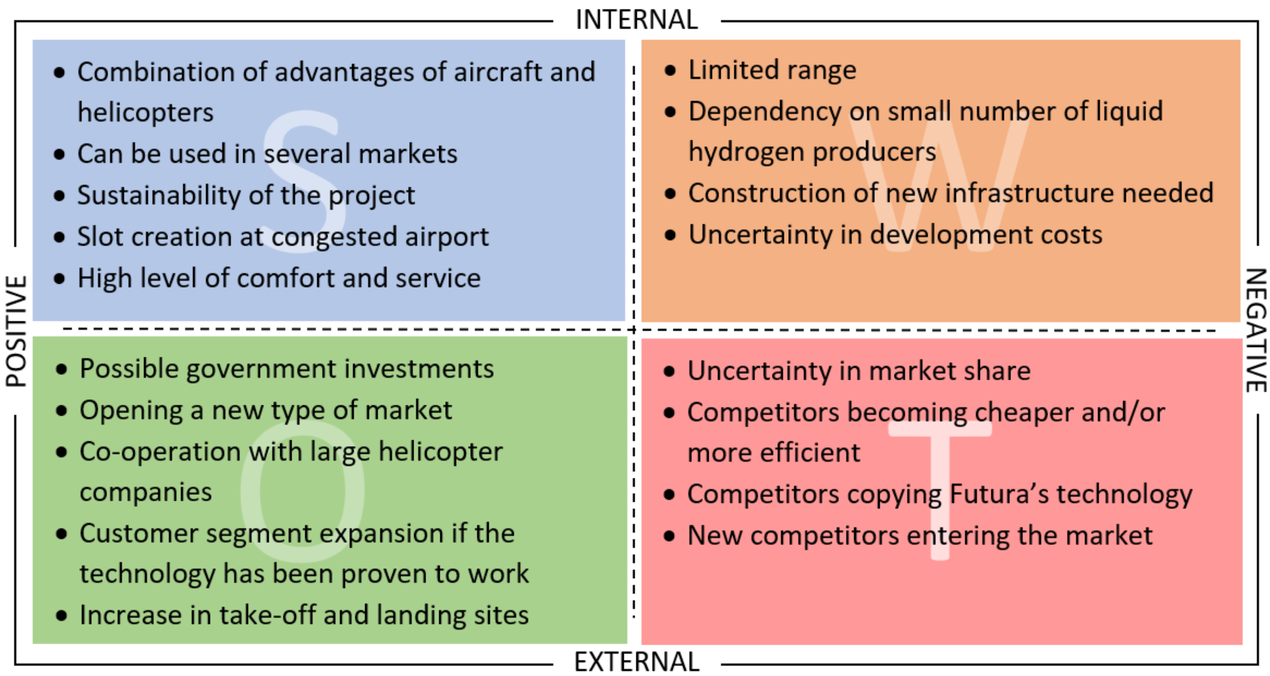

Figure 2.1: SWOT analysis of Futura. SWOT stands for strengths, weaknesses, opportunities, threats.

Conclusion

With the growth of 7% in 2017 and a contribution of 2.1% to the EU's GDP, it is clear that the air transport sector is a strategically vital sector. However, due to several major European airports getting congested, the sustainability of this growth is endangered. Therefore, innovative solutions need to be found to solve this serious problem. Stakeholders of this challenge include the EU, airports, customers, and the environment. Several markets for Futura have discovered: traditional and business operations are possible, but other potential markets such as EMS and offshore services were explored as well. Based on the VTOL capabilities and the fact that Futura can combine the benefits of both aircraft and helicopters, it is expected that a market share of 10% is achievable in the long run, making Futura the fourth biggest competitor in the market. Its main competitors will be flights, taxis, and public transportation. After having gathered all this information, the SWOT analysis showed that the main strengths of Futura are that it provides a solution to airport congestion and that it combines the advantages of aircraft and helicopters. However, its limited range and uncertainty in development costs are weaknesses of the project. A significant opportunity is the possibility to use government investment to provide funds for the project, but uncertainty in the market share can pose a threat to the sustainability of the project.

[9] URL `https://www.liveplan.com/blog/what-is-a-swot-analysis-and-how-to-do-it-right-with-examples/` [cited 19 June 2019]

3. Design Approach

Having outlined the market space Futura will occupy in chapter 2, the design approach can be laid out. First the requirements for the aircraft are detailed in section 3.1. Design choices and the engineering results obtained up to the final design phase are summarised in section 3.2. The engineering objectives have also been outlined in section 3.2. After that, the core of the innovative engineering aspects is presented in section 3.3, establishing what makes Futura stand out from its competitors. The design procedure adopted is presented in section 3.4 that highlights the logical engineering steps taken to iterate the design to converge to a final concept. The use of resources in the design is summarised in section 3.6 to highlight which experts were involved in the design procedure. Eventually the sustainable development strategy which dominates the design is presented in section 3.5.

3.1 Requirements

The requirements that Futura has to meet were established, analysing all the requirements imposed by the customer and producing with derived ones. However, at the same time, the following list includes also some derived requirements based on other driving characteristics that the aircraft shall have. The customer requirements are indicated with **Futura-TECH-VCM** and **Futura-TECH-VCS**, they include respectively all the system mission and capabilities requirements, while the **Futura-CONS-SUS** includes the sustainability requirements and finally **Futura-CONS-RES** includes the resources requirements. Only the customer requirements and the most important requirements coming from them are listed here. Then, in section 9.8, all these requirements will be examined and verified if they are met.

1. **Futura-TECH-VCM-1** The range shall be at least 200 km.
2. **Futura-TECH-VCM-2** The maximum speed shall be 400 $\mathrm{km h^{-1}}$.
3. **Futura-TECH-VCM-3** The cruise speed shall be at least 350 $\mathrm{km h^{-1}}$.
4. **Futura-TECH-VCM-4** Futura shall achieve vertical take-off and landing (VTOL) capabilities.
5. **Futura-TECH-VCM-5** The payload shall be at least 900 kg.
6. **Futura-TECH-VCM-6** The maximum take-off weight (MTOW) shall not exceed 4000 kg.
7. **Futura-TECH-VCM-7** The service ceiling shall be of at least 1500 m.
8. **Futura-TECH-VCM-8** Futura shall have, at maximum, a 1 h turnaround time.
9. **Futura-TECH-VCM-9** Futura shall have 90% availability, by considering the time required for other scheduled and unscheduled maintenance.
10. **Futura-TECH-VCS-3** Futura shall use hydrogen as source of energy.
11. **Futura-CONS-RES-1** The design and manufacturing cost of the first prototype shall not exceed 2 million €.
12. **Futura-CONS-RES-3** The cost of refuelling a full tank shall not exceed 345€.
13. **Futura-CONS-SUS-5** Futura shall not produce any emissions other than water.
14. **Futura-CONS-SUS-12** All parts shall be assigned a sustainable end-of-life (EOL) solution among reuse, re-manufacturing, recycling or downcycling.

3.2 Design Overview

The design development of Futura came about with a market analysis: this was necessary to identify the need for a new aircraft that would quickly connect airport hubs as outlined in chapter 2. This analysis was the fundamental pillar of the design, which greatly influenced all other aspects: from an operational point of view to the design configuration of the cabin. The functions that the aircraft has to perform are summarised in the functional flow and functional break down structures which are shown in Appendix A. These were used as a guide in identifying the main functions of the aircraft and its related systems to be designed. The final conceptual design presented in the rest of this report is the result of a preliminary analysis of several configurations and different power plant systems. A trade-off analysis led the team to focus its design on a tilt-rotor aircraft powered by a combination of a fuel cell and batteries. The design was chosen since it was the one which would have allowed to meet the requirements on MTOW while keeping the aircraft completely sustainable: Futura will produce no emission other than water. In the final phase, the team focused on several aspects of the design.

On the one hand, the aircraft systems are designed to meet the customer requirements on performance summarised in section 3.1. To do so, the team's objective was optimising both the aircraft aerodynamic and the new power plant and propulsion system finding the right combination between the fuel cell and battery usage and optimising the rotor design. Also, it was important to investigate the structural design of the most critical component of the aircraft from a safety point: the fuel tank.

On the other hand, it was crucial to explore the operational characteristics of the aircraft further to take into consideration all the infrastructure needed to operate Futura. Furthermore, it was necessary to identify in more detail the operational limits and the mission profile that Futura would have flown within. Eventually, it was crucial to analyse further the risks associated with the aircraft design and operation while keeping sustainability at the heart of the engineering choices. All of these aspects are covered in this report.

3.3 Innovative Approach

Futura's design wants to push the engineering boundaries to prove that it is possible to obtain a fully sustainable, high performing, and cost-effective aircraft. To make this possible, innovative design choices were taken in several aircraft's systems based on engineering ingenuity and novel technologies. The engineering design is based on three pillars: a Novel Power Plant Design, an Optimised Aerodynamics, and Propulsion Design and Integral Sustainable Design.

Firstly, the power plant system is based on a combination of fuel cell and batteries, which makes the aircraft operations completely green. The power plant system had to be optimized in terms of weight to provide the same performance of modern turboprop engines. The application of such power plant system to a tilt-rotor aircraft was achieved thanks to the integration of the radiators in the wings of the aircraft made possible by progressive wing skin panels as it is further explained in section 6.2.

Secondly, the performances of Futura have increased thanks to the adoption of a lifting body fuselage: this design choice, which has almost no approval in other comparable aircraft, nearly doubled the lift over drag ratio of the aircraft as it can be further explained in section 5.4. Furthermore, the design of the rotor allowed to chose its characteristics to optimise every flight phase to satisfy the needs for vertical take-off and landing procedures and regular flight.

Thirdly, sustainability was placed at the core of the design decisions: this reflected the customer's will which the team addressed from day one of the design cycle. Sustainability influenced all design decisions: from the adoption of bio-materials for the cabin's interiors to selecting where the possible sustainable end of life treatment for the aircraft components.

3.4 Design Procedure

The conceptual design of many systems had to be completed in this final phase. The engineering analysis of different systems was completed making sure that the systems' interdependence were taken into account. In chapter 4 the mission profile of the aircraft is established. The wing and fuselage aerodynamics, the power plant characteristics, the control surfaces, and the airframe structural components are then addressed respectively in chapter 5, chapter 6, chapter 7, and chapter 8. The interrelations between the different aspects of the analysis mentioned above are presented here in a logical order. The different design aspects of Futura are integrated into a tool which allows the optimisation and consequent global iteration of the aircraft design, taking into account all the engineering choices and constraints made by the design departments.

Figure 3.1 shows the logic behind Futura's engineering design from a macroscopic level. Firstly the wing

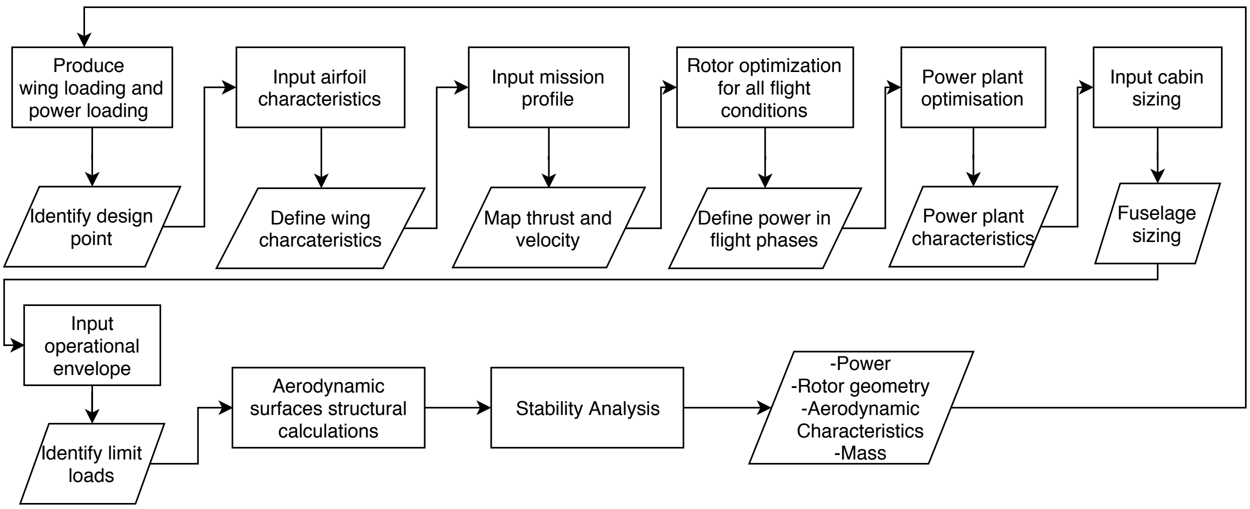

Figure 3.1: Futura's design logic.

loading and power loading diagram have to be produced to identify the design point of the aircraft based on a set of aerodynamic desired characteristics. Then the wing characteristics are further specified and improved based on the airfoil choice. In this manner, the wing design is completed and using the mission profile characteristics, thrust and velocity are obtained for different flight phases. With these parameters, the rotor geometry has been optimised, and the power required at different flight phases was obtained. Hence the power plant's characteristics could be calculated deriving the best combination of fuel cells and batteries to complete the mission. Afterwards the fuselage aerodynamics is designed to improve the lift to drag ratio of the whole aircraft. Eventually, the operational envelope is obtained, and the structural characteristics of the wing and empennage are derived before Futura's ground stability is verified. This is the design logic that the team followed to come up with Futura's final conceptual design. However, going through this design process only once is not enough. A series of iterations were completed to make sure that the design would converge and their specifications are treated in chapter 9. It is important to mention that all the design phases were conducted to meet the set of requirements specified in section 3.1

3.5 Sustainability Development Strategy

The sustainability development strategy is defined as the root of this project. As aviation represents up to 5% of greenhouse gas emissions and continues to grow, it is clear that the industry needs to reinvent itself with climate-friendly air transportation. Futura is a breakthrough emission-free aircraft that proves such revolution is possible. At each stage of Futura's life, adverse environmental and societal impacts are assessed and minimised, both in terms of the direct effects (e.g., flight emissions) and indirect effects (e.g., emissions from fuel production).

This begins with production, encompassing material extraction and manufacturing. Both of these processes have environmental impacts in terms of CO_2 emissions and societal impacts in terms of energy consumption. For the material selection and manufacturing plan, these aspects are evaluated with the Eco-Audit tool of the CES Edupack material-selection software [9]. Sustainable solutions include using bio-based materials or recycled material to reduce raw material extraction.
The operations of Futura are exceptionally environmental friendly compared to current aircraft because of its emission-free propulsion system (besides water vapor). Nonetheless, the indirect impact of fuel production should not be overlooked. Indeed, specific fuel production processes could make Futura less sustainable overall than a kerosene aircraft [10]. A plan for sustainable emission-free fuel production is laid-out for the operations of Futura.
The End-of-Life (EOL) of Futura is carefully planned to minimize waste. Starting at material selection, the sustainability of materials based on their EOL solution is weighted against mechanical properties.

Then, a EOL plan from aircraft retirement until the material reuse is proposed. From the recycling into new products to downcycling into lower-value applications, each material is reprocessed.

With a comprehensive sustainable development strategy, Futura's design team takes responsibility to ensure the sustainability of its aircraft. While the operator leads the fuel source selection and recycling of the aircraft, efforts have been put in making these processes convenient with identified European partner companies and economically viable. It is foreseen that with a possible future kerosene tax and regulations on aircraft recycling, the operator will be incentivised to follow the proposed plan for sustainability [11, 12].

3.6 Use of Resources

The design of such sophisticated aircraft requires various types of resources, ranging from experts to design methods, software, and companies' undisclosed information. A summary of the external resources used in the design is presented below.

A valuable resource the team has benefited from is academia experts. While the team knows aerospace engineering, the advice and consultancy from experts in specific fields allow for a more detailed and realistic design. The team's supervisor, Dr. R. M. Groves, has given valuable feedback and advice on various components of the design. Expertise also came from coaches, in particular, Dr. B.V.S. Jyoti and K.Vidyarthi for their knowledge on cryogenic tank design and helicopter design respectively. Other experts in academia were consulted, namely Ir. Jos Sinke on manufacturing processes, Dr. Fabrizio Oliviero on aerodynamics and stability and control, Dr. Wim Verhagen on aircraft maintenance, and finally Dr. Calvin Rans on composite structure design. Working-professional experts were also contacted to obtain a better understanding of current industry practices. This included engineer Anton van Berkel from Nederlandse Radiateuren Fabriek for radiator performance information and researcher Dr. B. Atli-Velti from TNO for advice on cryogenic tank design. Henrik Steen Pedersen, executive vice-president of GreenHydrogen, was contacted to obtain undisclosed fuel production price quotations. Information on battery charging was sought from Valérie de Vlam, an intern at Tesla Motors.

To design an aircraft with a high Technology Readiness Level, the team has striven to use commercially available components for externally-produced parts. For this purpose, the product datasheets of dozens of companies have been used and cited. This includes, among others, Linde, Praxair, PowerCell, Yasa, and Herose for instance.
For the design of specific components, internationally-validated methods were employed. For the blade design, a code based on a refined version of Froude's Blade Element Momentum Theory was developed [13]. The lifting-body fuselage's aerodynamic properties were evaluated using the DATCOM method, developed by the United States Air Force and the McDonnell Douglas Corporation [14]. For the tank's inner shell structural design, the well-established American Society of Mechanical Engineers' code on pressure vessel design was used [15]. Other design elements included theories from engineering textbooks, TU Delft courses, and research papers.

Lastly, engineering software that allows handling a high level of complexity helped the design process. The design calculations of all components are performed with a Python script, which allows for a high number of iterations. Thousands of design configurations are evaluated by a global script to integrate and produce a weight-optimum design. A material selection software from Granta, CES Edupack, is both used as a material and manufacturing information library, and a sustainability evaluation tool. Javafoil, software based on a 3D panel method, was used to verify aerodynamic performance estimations. To make sure the aircraft can be assembled as one product, a 3D rendering was created using CATIA 3D Experience in order validate the design choices.

4. Hydrogen Powered Mobility

Before diving into the pure engineering design, Futura's operations are treated in detail. Some of the locations in which the aircraft is going to provide intra-city and intra-regional airport transfers are explored, and the associated available flights' routes are investigated in section 4.1. Then the mission profile which characterises Futura's operations is presented in section 4.2. This highlights the most important phases of flights and presents Futura's capabilities to land like an aircraft in emergencies. Furthermore, all the necessary operations related to the refuelling of the aircraft are evaluated in section 4.3: all the hydrogen path from production till delivery is thought and costs and time of refuelling are estimated. Then, section 4.4 discusses the operations required to perform battery recharging, presenting an estimate of its recharging time. Eventually, the operations related to the VTOL capabilities of Futura and the turn around procedures are discussed respectively in section 4.5 and section 4.6.

4.1 Flight Routes

As the Futura will operate at both intra-city and inter-regional level, the specific flight routes for both mission types need to be considered, which will be discussed in subsection 4.1.2 and 4.1.3 respectively. This will be done by looking at existing flight routes and analysing how Futura can adhere to them. However, it will also need to adhere to no-fly zones, which will be explained in subsection 4.1.1.

4.1.1 No-fly Zones

No-fly zones change daily. Reasons for this include the construction of buildings and important events for which safety is an essential aspect. To find the most up-to-date information on no-fly zones, the NOTAM database can be consulted by pilots. It provides a complete list of potential hazards and no-fly zones along the envisioned flight route.[1] Before taking off at the airport, this database thus has to be consulted by the Futura pilot to set up the flight plan.

4.1.2 Intra-city Transport

It is assumed that when operating at intra-city level, the mission profile of Futura can be compared to that of a helicopter. Therefore, helicopter routes were researched for the specific case of London: an illustration of the defined helicopter routes for this major city is given in Figure 4.1.[2] From this figure, it can be deduced that helicopters have to follow strict flight paths, indicated by the thick dotted lines and that multiple no-fly zones have been established. Futura will have to adhere to these rules, which will impact the transport time between intra-city airports.

[1] URL `https://notaminfo.com/international` [cited 18 June 2019]

[2] URL `https://www.caa.co.uk/Data-and-analysis/Airspace-and-environment/Airspace/London-helicopter-operations/` [cited 18 June 2019]

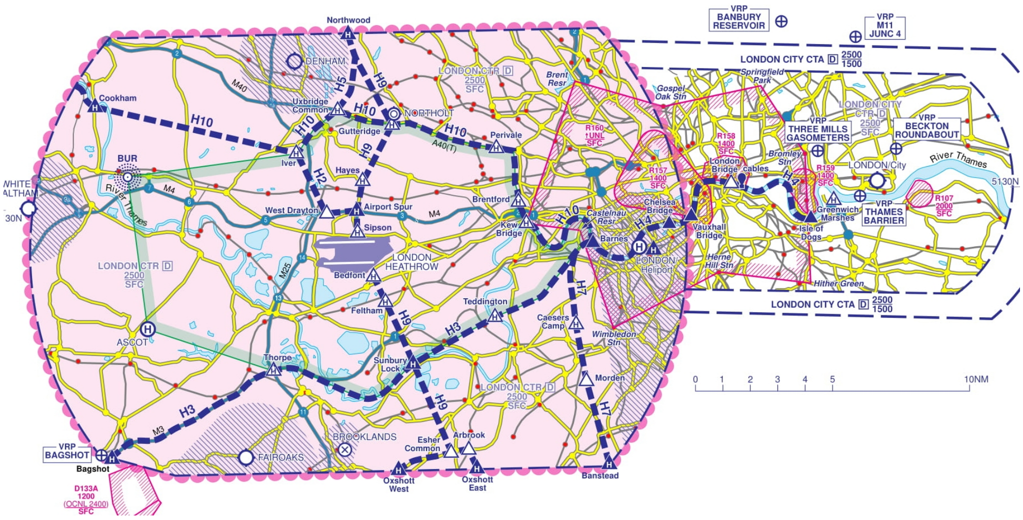

Figure 4.1: Helicopter routes in London, indicated with the thick dotted lines.

4.1.3 Intra-regional Transport

During intra-regional transport, a cruise altitude of 2,000 m and speed of 350 $\mathrm{kmh^{-1}}$ will be achieved. This means that the Futura can be compared to a conventional twin-propeller aircraft and that aircraft routes now have to be considered. These routes are set up and described in detail by Eurocontrol, which manages air traffic in Europe.[3] Again, Futura will have to adhere to these defined flight routes and the no-fly zones indicated by NOTAM.

4.2 Mission Profile

Defining the Futura mission profile is essential to determine the total energy needed to complete the mission and the power required in all the different flight phases. To calculate the duration and distances of each flight phases, first, the entire range was considered. Indeed the requirement **Futura-TECH-VCM-1** from the customer states that the range should be at least 200 km, but a safety factor of 1.5 was applied to this value in order to take into account emergencies, for example, allowing to land in a different and farthest airport and to allow for loitering capabilities yielding to a total range of 300 km. Around this initial value, the mission profile was constructed, and it is shown in Figure 4.2. The mission can be divided into five main flight phases: take-off, climb, cruise, descent, and landing.

Regarding the take-off, a total time of 120 s is assumed, it includes the time where the aircraft engines are turned on, the small taxiing distance that is performing from the gate to the helipad/runway and the hovering phase during take-off before starting the climb.

Then the climb phase takes place; it has a duration of 250 s to arrive at the cruise altitude of 2000 m. The rate of climb that Futura has to achieve was set based on similar aircraft, in term of weight and passengers. This yielded to a value of 8 $\mathrm{ms^{-1}}$. This value is also in line with the capabilities of the Agusta Westland AW609 and also, for this reason, it was chosen [16]. The same was done for the horizontal velocity during the climb, resulting in a value of 60 $\mathrm{ms^{-1}}$, leading to a total horizontal distance of 15 km during this phase. In this mission flight phase, the transition takes place where the rotors and the motors rotate thanks to the mechanism on the nacelle from a vertical position respect the ground, ideal for VTOL performance, to a horizontal position allowing an operation like an aircraft during the cruise.

[3]URL `https://www.eurocontrol.int/articles/eurocontrol-route-network-chart-ern` [cited 18 June 2019]

For the cruise phase, the velocity was assumed to be equal to 350 kmh^{-1}, based on the maximum speed requirement imposed by the customer (**Futura-TECH-VCM-2**). This results in a cruise time of 2777 s for a total distance of 270 km. The altitude at which Futura has to cruise was established based on the minimum altitude allowed in a city environment. The stricter conditions can be identified in the London intra-city operations, indeed there are specific routes that helicopters and aircraft must follow when flying over the city with a minimum cruise altitude of 2,500 ft (726 m) above the highest obstacle in an 8 km radius[4], that in London is The Shard[5] with an altitude of 309.7 m. Based on this, it was decided to perform the cruise at an altitude of 2000 m. This altitude is also lower than the minimum altitude where the pressurisation inside the fuselage is needed (3000 m)[6], this allows to a decrease in the structural weight of the fuselage and allows to use other shapes rather than the conventional circular cross-section, for this reason in Futura an airfoil shape is used. However, at the same, this altitude allows also in a decrease in the power required during the cruise, since for a propeller aircraft it increases increasing the altitude.

Regarding the descent phase, the rate of descent is set to be equal to the rate of climb (8 ms^{-1}), also for the horizontal velocity, again equal to 60 ms^{-1}. Like the climb phase, the descent phase has a duration of 250 s with a total horizontal distance of 15 km. Like the climb, also in this flight phase, the transition takes place, where the engines rotate from a horizontal to vertical position respect to the ground.

Then, the landing phase takes place with again a duration of 120 s that includes hovering and also a small taxiing.

Eventually, one last characteristic of a hypothetical Futura's mission profile is the stall speed. In fact, in an emergency landing situation, the aircraft presents the ability to glide as an aircraft. Hence the landing approach had to be analyzed. The radius of the turn at landing can be found considering the airborne distance, the screen height, and the approach angle.

$$R_{landing} = \frac{\left(d_{airborne} - \frac{h_s}{\tan\gamma_a}\right)}{\sin\gamma_a - 1 + \cos\gamma_a} \tag{4.1}$$

The airborne distance and the screen height were found to be on average 435 and 15.24 m on average based on an investigation of NLR [17]. While the landing angle was taken to be 3° as a typical landing attitude. Then the approach speed could be evaluated using an average landing delta loading factor ($\Delta n_{landing}$) of 0.15 [18].

$$V_{approach} = \sqrt{R_{landing} \cdot \Delta n_{landing} \cdot g} \tag{4.2}$$

Eventually using the relationship $V_{stall} = \frac{V_{approach}}{1.3}$ the stall speed was found to be 50 ms^{-1} [19].

[4]URL `https://www.caa.co.uk/Data-and-analysis/Airspace-and-environment/Airspace/London-helicopter-operations/` [cited 16 May 2019]
[5]URL `https://en.wikipedia.org/wiki/List_of_tallest_buildings_in_Europe/` [cited 18 June 2019]
[6]URL `https://en.wikipedia.org/wiki/Cabin_pressurization/` [cited 18 June 2019]

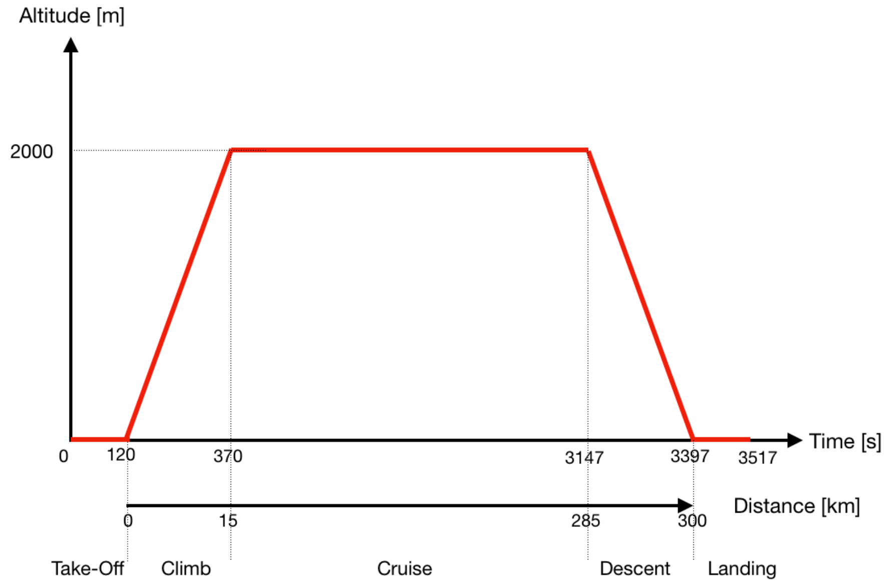

Figure 4.2: Futura mission profile.

4.3 Hydrogen Refuelling

Liquid hydrogen (LH_2) is one of the most promising fuels of the future: it is the cleanest renewable fuel currently available, as it produces zero emissions while running, and has a high energy-to-weight ratio.[7] However, producing LH_2 is a rather difficult process as gaseous hydrogen (GH_2) first has to be produced and then liquefied by cooling to cryogenic temperatures. These two procedures will be discussed in subsection 4.3.1 and 4.3.2 respectively. After that, the differences between on- and off-site production of LH_2 will be analyzed in subsection 4.3.3. Finally, the exact procedures for the refuelling of Futura will be explained in subsection 4.3.4.

4.3.1 Production of GH2

There are three main ways to produce GH_2: with fossil fuels, using biomass, and by electrolysis. A summary of the processes is given in Figure 4.3.

Gas reforming from fossil fuels is the most common and cheapest method to produce GH_2. The process consists of converting alcohols and hydrocarbons into hydrogen by use of chemical processes. As can be seen in Figure 4.3, the primary energy sources are natural gas, oil, and coal. However, when converting these products into hydrogen, emissions such as CO and CO_2 are released during the process, which conflicts with the sustainability requirement of Futura [20]. Therefore, this GH_2 production method will not be used for Futura.

The second production procedure is the chemical conversion of biomass by thermal- or biochemical methods: the former is focused on the gasification of forest or waste wood, while the latter uses microorganisms to ferment and process the biomass. However, a major disadvantage of this process appears to be the inability to deliver the GH_2 in high amounts. Furthermore, just like in the first method, CO_2 is produced throughout the process, which clashes with the sustainability requirement of Futura [20].

The last process is electrolysis, in which water is broken down into oxygen and hydrogen with electricity. The most important advantage of this method is that no emissions are produced during the process,

[7] URL `https://sites.google.com/site/liquidhydrogenvsfossilfuels/the-advantages-and-disadvantages-of-liquid-hydrogen` [cited 18 June 2019]

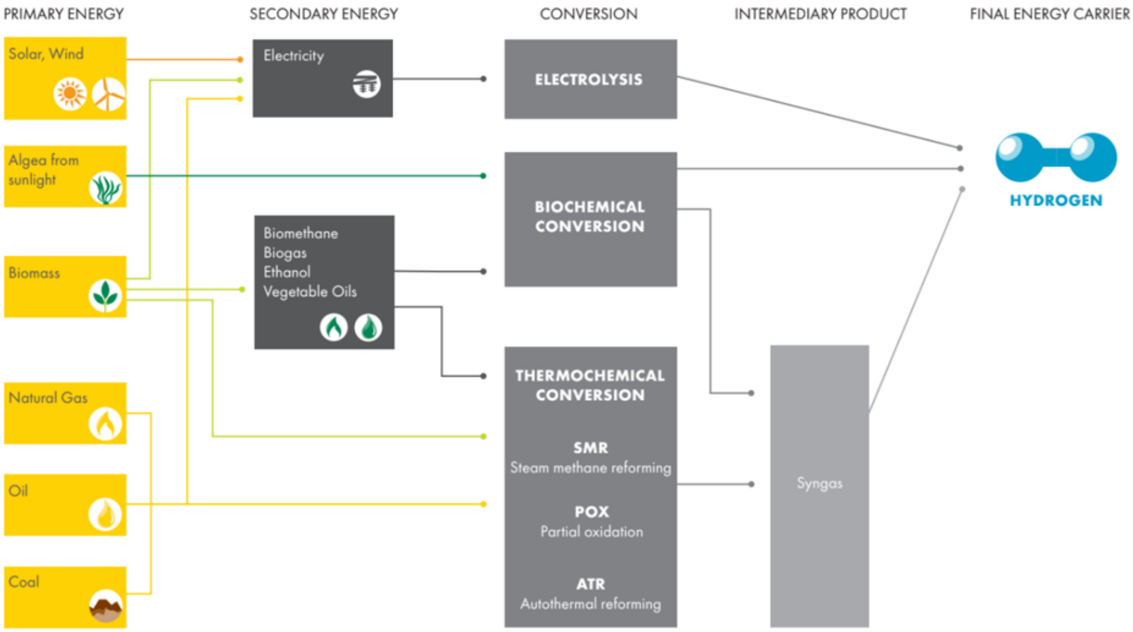

Figure 4.3: Processes for the production of GH_2 [20].

provided that the electricity is generated by sustainable energy sources such as solar and wind energy. The main drawback, however, is that the production cost is higher than other methods: approximately 3.5 €/kg GH_2 (as stated by the company GreenHydrogen in personal emails, June 15 2019) compared to 1.5 €/kg for GH_2 produced from fossil fuels. These values are based on centralised production, meaning that the GH_2 is produced off-site at a specialised company [20].

Taking into account that sustainability is paramount to the client, electrolysis using renewable energy sources will be used to generate the GH_2. The following step is then to liquefy the GH_2.

4.3.2 Liquefaction of GH2 to LH2

As hydrogen appears in gaseous form at ambient temperature, it needs to be cooled down to a temperature of 20 K (or -253 °C) to obtain LH_2. This requires a significant amount of energy, and part of the hydrogen is lost through evaporation, also known as boil-off of LH_2.[8] In order for the Futura to meet its sustainability requirements, the necessary energy for this process again has to be obtained from renewable energy, such as solar or wind energy. The liquefaction of the hydrogen is an extremely crucial process which is necessary to take into account also from a cost point of view. Currently the energy to liquefy hydrogen is estimated to be 11 $\mathrm{kWkg^{-1}}$ [21]. The cost of such energy process is dependent on the energy source used. For this application, an average of the current renewable energy prices is calculated to be 0.19 $ based on Irena 2018 report [22]. Hence, the cost of hydrogen liquefaction can be calculated and consequently the price at which hydrogen liquefaction can be purchased: assuming a producer profit of 50%, the price was found to be 2.795 €/kg. However, it is expected that future research and achieving economies of scale will lower the required energy and accompanied the cost of producing LH_2.

4.3.3 On-site or Off-site

There are two main options to produce LH_2 fuel for airports: on-site or off-site. In the former case, all the production facilities are located on the premises of the airports. The advantages of this option are that the transportation costs from the production center to the fuel pump are low and that the airport can produce LH_2 independently. This means that if an LH_2 producer decides to increase its

[8]URL `https://www.energy.gov/eere/fuelcells/liquid-hydrogen-delivery` [cited 18 June 2019]

price significantly, the airport will not be affected by this price change. Specialised companies like Linde offer the technology to build on-site LH_2 production facilities: these "packages" can already be bought today, and thus no additional resources have to be used to develop the LH_2 production technology.[9] However, the disadvantages of producing LH_2 on-site are that it takes time and resources to build and maintain the production facilities. From personal emails with the company GreenHydrogen, it was found that construction of just one GH_2 production facility costs 2.4 M€ plus an annual servicing fee of 30,000€. The total costs are, of course, increased when liquefaction, storage, and dispensing facilities need to be maintained as well. A serious risk is thus taken when choosing for this option: should LH_2 turn out not to be the fuel of the future, the resources used for the construction of the facilities will have gone to waste. Therefore, it is essential to be sure that there is a sustainable market for LH_2 to fuel the hydrogen-electric rotorcraft before investing in expensive production facilities.

The second option is to obtain the LH_2 from off-site production. This can be achieved by buying LH_2 at specialised producers, such as Linde, and transporting it to the airport.[10] The main advantage of this option is that no LH_2 production facilities have to be built on-site, meaning that the implementation of LH_2 refuelling can be done rather fast and cheap compared to the on-site production option. However, dispensing facilities will still need to be built to be able to refuel the Futura, and LH_2 transportation from the production companies to the airports will come with an extra cost. This transportation can be done by the use of LH_2 tanker trucks or by use of existing hydrogen pipelines.[8,11] As trucks emit CO_2, the most sustainable option for Futura would be to transport the LH_2 using pipelines, but building specialised pipelines for LH_2 is a resource consuming process, meaning that using trucks is the best option for short-term implementation. The risk resulting from buying LH_2 from off-site producers is that these producers have the power to raise the LH_2 prices according to their needs, but this risk can be mitigated by closing long-term LH_2 delivery contracts with a fixed price per kg.

Another option that could be considered is semi-centralised production: producing GH_2 off-site and liquefying it on-site to LH_2. This means that only the liquefying and dispensing facilities have to be built on-site, reducing in part the risk of on-site production. Transportation of GH_2 still has to be ensured, but this can be done with existing hydrogen GH_2 pipeline infrastructure which is a low-cost option when transporting large volumes.[11] However, compared to the off-site production option, the disadvantage for airports of constructing the liquefying facilities is more significant than the benefit of having a bit more independence by liquefying the GH_2 themselves.

Concluding, the best short-term solution is the off-site production option: the implementation of LH_2 refuelling can be performed fast, and no risk is taken by not building resource-consuming production facilities. Also, the costs for infrastructure adaptation are the lowest for this option. If the LH_2 industry keeps growing in the future, it might be beneficial for airports to invest in semi-centralised or even on-site LH_2 production facilities, but at this moment it is difficult to make accurate predictions for the future of LH_2.

4.3.4 LH2 Refuelling of Futura

As discussed before, dispensing facilities will have to be built to refuel Futura. Linde already has the technology for an LH_2 hydrogen refuelling station with a delivery rate of approximately 33.6 $\mathrm{kgh^{-1}}$. This means that it will take $26\mathrm{min}$ to refuel Futura, as each fuelling is around $14.30\mathrm{kg}$. A study from the US Department of Energy predicts that the cost of LH_2 delivery and dispensing, excluding production, will be around $5\$/\mathrm{kg}$ or $4.425€/\mathrm{kg}$ in the near future [23].[12] Combining this cost with the

[9]URL https://www.linde-engineering.com/en/plant_components/hydrogen-fueling-technologies/index.html [cited 18 June 2019]
[10]URL https://www.the-linde-group.com/en/clean_technology/clean_technology_portfolio/hydrogen_energy_h2/h2_one_stop_shop/h2_production/index.html [cited 18 June 2019]
[11]URL https://www.energy.gov/eere/fuelcells/hydrogen-pipelines [cited 18 June 2019]
[12]URL https://www.ofx.com/en-au/forex-news/historical-exchange-rates/yearly-average-rates/ [cited 20 June 2019]

GH_2 production cost of 3.5€/kg and liquefaction cost of 2.795€/kg, a total refuelling cost of 10.72€/kg was found for Futura. Based on this estimate, it will cost 153.3€ to refuel the Futura with 14.30kg of LH_2.

To evaluate Futura's mission cost, it is essential to compare it with the cost of a conventional propeller aircraft or helicopter mission cost. These two were chosen since they are Futura's direct competitors in terms of transport speed and fashion; besides, they also represent the non-sustainable competitors. To compare the aircraft mission cost more easily an average between a similar helicopter and propeller aircraft mission was calculated.

On the one hand, a regression using helicopters with similar payload capacity and cruise speed was performed to find the fuel mass needed for 300 km range. On the other hand, Breguet's equation was used to estimate the fuel consumed by a conventional propeller aircraft. Once the fuel mass was estimated for both cases, the average price of the mission could be found to be 227€.

The refuelling station operates in the same atmospheric conditions as Futura (-40°C to 50°C) and the tank can contain up to 4,000 kg of LH_2. Also, the connection between the fuel nozzle and the fuel tank will be airtight and insulated to ensure that there will be no LH_2 leakage, improving the safety of the entire system. Unfortunately, no exact construction costs were found for Linde's LH_2 fuelling station, but Linde promises low costs and little maintenance effort.[9]

4.4 Battery Recharging

Based on the mission profile in section 4.2, the maximum mission power and energy are 1,147 kW and 1,342 MJ respectively. 392 MJ, or 109 kWh, will be provided by the battery as will be elaborated upon in chapter 6. In order to provide this power and energy, a Ground Power Unit (GPU) will be used to recharge the battery during the turnaround procedure on ground.

Currently, most GPUs are ran on diesel.[13] However, this conflicts to make Futura as sustainable as possible. Therefore, electrical GPUs were looked at, and the Supercharger V3 of Tesla appeared to be the most promising one with a maximum power of 1 MW and an average cost of 0.28 €/kWh in Europe.[14,15] Just as in subsection 4.3.4, this electricity needs to be obtained from renewable energy sources, such as solar or wind energy, to improve the sustainability of Futura. Besides, Tesla would pay for the complete installation and maintenance of the Supercharger station: this means that the only cost for airports for battery recharging is the cost per kWh of 0.28€.[16] Based on a total mission energy of 103 kWh delivered by the batteries, it would cost 28.84€ to completely recharge Futura. Combining this recharging cost with the LH_2 refuelling 182.1€ was found, which is 19.7% cheaper than when a traditional jet-powered airliner would perform the same mission as was calculated in the previous section.

The recharging time of the Futura is found by comparing it to the recharging time of a current Tesla Model S: it takes approximately 1.5 h to completely recharge the Model S's 95 kWh capacity battery at a Supercharger station V2.[17,18] As the Futura has a battery capacity of 103 kWh, or 8.4% more than the Model S, the recharging time of Futura with a Supercharger V2 is estimated to be 98 min. However, taking into account that the new Supercharger V3 can deliver three times more power compared to the Supercharger V2, it is assumed that the recharging time with a V3 is a quarter of the recharging time

[13] URL `http://www.guinault.com/en/aviation/gpu/` [cited 18 June 2019]
[14] URL `https://www.tesla.com/blog/introducing-v3-supercharging` [cited 18 June 2019]
[15] URL `https://www.tesla.com/en_EU/support/supercharging?redirect=no` [cited 18 June 2019]
[16] URL `https://techcrunch.com/2013/07/26/inside-teslas-supercharger-partner-program-the-costs-and-commitments-of-electrifying-road-transport/?guccounter=1&guce_referrer_us=aHR0cHM6Ly9lbi53aWtpcGVkaWEub3JnLw&guce_referrer_cs=DlIrHbXYtMBbawIWdJAcMQ` [cited 18 June 2019]
[17] URL `https://ev-database.org/car/1194/Tesla-Model-S-Long-Range` [cited 18 June 2019]
[18] URL `https://www.tesla.com/en_EU/supercharger?redirect=no` [cited 18 June 2019]

of the V2.[14] Ultimately, this means that the Futura can be completely recharged in 25 min with a Tesla Supercharger V3.

It is important to note that this is a rough estimation as Tesla and other electrical GPU producers are not willing to share specific data of their products, even after contacting them. Also, the linear scaling of recharging time of Futura compared to the Tesla Model S might be prone to errors. Finally, the difference in the chemical composition of the batteries might cause a discrepancy as well. The recommendation for the future is thus to analyse what the exact recharging time is of Futura by performing actual tests.

4.5 VTOL Capabilities

To ensure that Futura's VTOL capabilities can be used to their full potential in existing airports, some adjustments will need to be made to the current infrastructure. The most important process is the implementation of specialised VTOL take-off, parking, and landing sites. Besides, minor changes will need to be made to Air Traffic Management (ATM) and marshalling procedures. These adaptations will be discussed in subsection 4.5.1 and 4.5.2 respectively.

4.5.1 Take-off, Parking and Landing Sites

To avoid the dead man zone when taking off and landing, runways will need to be present at the airports. During take-off and landing, Futura will hover above these runways, similar to a helicopter, and will increase its horizontal velocity while staying at the same altitude. With enough forward speed, the aircraft can then start to climb while staying out of the dead man zone. One option is to use the traditional runways of airports. However, this takes away Futura's advantage of increasing airport slots. A more promising solution is to build new short runways with a length of approximately 80 m. The construction and maintenance costs of these short runways are considered to be negligible compared to traditional runways lengths of more than 3.5 km, along with the time frame needed to build them[19]. In addition, it is assumed that due to the small size of the parking sites and VTOL runways, the need of airport expansion will be very limited. Therefore, a fast implementation of these short runways in the airport's existing infrastructure can be achieved.

As the use of Futura's VTOL capabilities increases airport capacity, new terminals and gates will need to be constructed to provide the necessary services to passengers. However, this process is a resource-consuming process which might be difficult to implement in the short term. Therefore, new VTOL parking sites can be constructed close to the short runways from where the Futura can take off and land. The parking spot for one Futura aircraft will look similar to current parking spots for helicopters: a circle with a diameter of 20 m, which is the length from the tip of one rotor of Futura to the other, with the letter ”F” in the middle to show Futura pilots exactly where they should land. Airport buses will then transport passengers between the existing terminals and the VTOL parking sites, and 5 m will be left in between two parking spots to provide enough space for the bus to pass. In the long term, special VTOL terminals can be built which offer high-standard services and comfort to Futura's passengers. Visual representations of the short- and long-term vision can be seen in Figure 4.4 and Figure 4.5 respectively.

For both the parking sites, i.e., in the short- and long-term vision, several facilities will need to be available: it must be able to board and disembark passengers, recharge, refuel, inspect the vehicle, etc. Boarding and disembarking can be achieved by merely using airstairs from airports: these can be placed against the Futura aircraft and act as standard stairs to enter and exit the aircraft. As decided in section 4.4, a Tesla Supercharger V3 will be used to recharge Futura: the ideal solution would be to implement this charging station in the ground. When the Futura is ready for the turnaround procedure,

[19]URL `https://www.heathrow.com/company/company-news-and-information/company-information/facts-and-figures` [cited 20 June 2019]

the charging cable can then be pulled out of the ground and plugged into the aircraft to start recharging. After recharging is finished, the charging cable will be unplugged from the aircraft and stored back into the storage department underneath the ground. The same process can be followed for the LH_2 refuelling procedure of Futura: by using the LH_2 refuelling stations of Linde and implementing the nozzle cables into the ground, the Futura can be refuelled by pulling the refuelling nozzle out of the ground and plugging it into the aircraft.

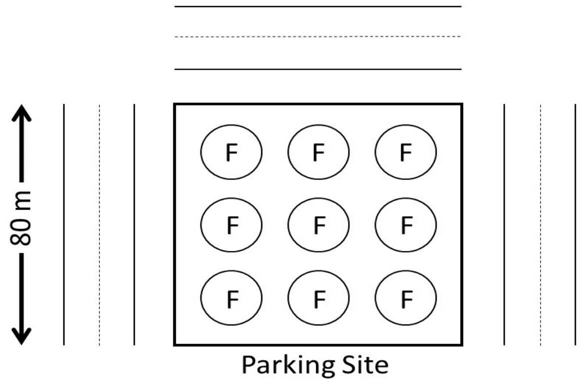

Figure 4.4: Short-term vision of VTOL sites. The circles with F represent the Futura aircraft.

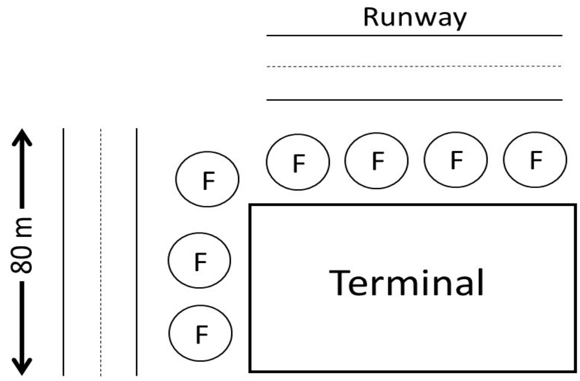

Figure 4.5: Long-term vision of VTOL sites. The circles with F represent the Futura aircraft.

An essential factor to take into account is the position of the VTOL sites compared to surrounding communities: as discussed in chapter 2, it has to be ensured that these do not suffer under the noise created by Futura. However, a study from NASA concluded that the noise from tiltrotor aircraft such as the XV-15 is within the boundaries set out by regulatory agencies: using the scales given by ICAO, the highest noise produced by Futura can be estimated at approximately 91 dB, while a maximum noise of 97 dB is allowed for an aircraft with 4,000 kg MTOW [24, 25]. It must be noted that this is a rough estimation of the noise emissions, and validation was not possible due to a lack of existing rotorcraft data. Therefore, in-depth research and testing must be performed to find the exact noise levels created by Futura and their impact on the surrounding communities.

4.5.2 ATM and Marshalling

The effect of implementing Futura in existing airports for ATM and marshalling will be minor. As the aircraft will operate as a helicopter on the ground, the current marshalling techniques of helicopters can be used to signal Futura visually. These are clearly defined by regulatory agencies like IATA.[20] Hence, there is no need for different marshalling signals.

For ATM there will be an apparent effect: as the airport will increase its aircraft capacity due to the VTOL capabilities of Futura, the ATM will need to be able to assist these additional aircraft in landing and taking off. Also, it is probable that different guiding methods will be used for Futura-like aircraft than for conventional aircraft to not interfere with the main runways of the airport, meaning that new employees will have to be hired or current employees will need specialised training to guide aircraft with VTOL capabilities.

4.6 Turnaround Procedure

The turnaround procedure can be considered to be the largest and most important element of the on-ground operations. In Figure 4.6, this procedure is given for Futura, which may only start after the engines and rotors have entirely been shut down [26]. During this shutdown, chocks will be applied to the tires of Futura to avoid unwanted movement on the ground. After the passengers have been disembarked along with their luggage, the cabin will be thoroughly cleaned, and catering supplies (such

[20]URL `https://www.iata.org/publications/store/Pages/marshalling-signals.aspx` [cite 20 June 2019]

as water and sick bags) filled up by the on-ground personnel.

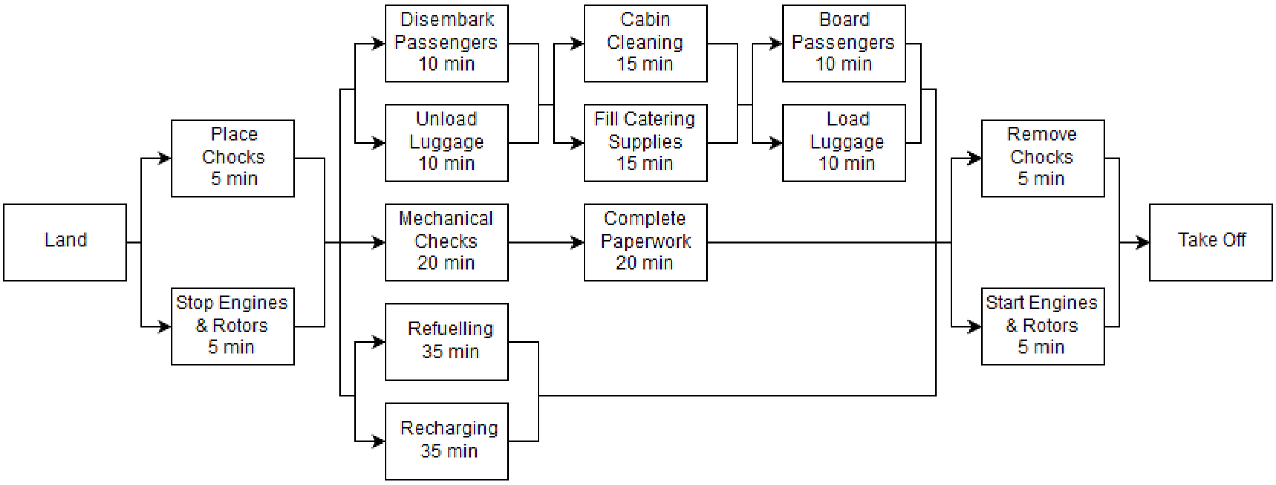

Figure 4.6: Turnaround procedure for Futura.

From Figure 4.6, it can be concluded that the refuelling and recharging blocks take up the most amount of time of the turnaround procedure with 35 min each. To not exceed the turnaround requirement of 1 h, these two procedures will be carried out simultaneously. At the same time, the pilot will carry out visual checks of Futura's mechanical systems and will complete the necessary paperwork after these checks have been completed. Should the pilot notice a malfunctioning component during the mechanical checks, he or she will decide if the aircraft can fly with or without that component: in the former case, the turnaround and take-off procedure will continue as planned, but the aircraft owner shall be notified of the malfunctioning component. During planned maintenance, this component can then be replaced. However, in the latter case, the flight will be cancelled, and the Futura will have to get unscheduled maintenance as will be discussed later in the report.

When all turnaround procedures have been completed, the chocks will be removed, and the engines and rotors will be started up for take-off. Combining all processes, a total turnaround time of 50 min can be achieved which complies with the critical requirement of a maximum turnaround time of 1 h.

Conclusion

As Futura will operate on both intra-city and inter-regional level, it has to adhere to the specific routes and no-fly zones set up by regulatory agencies. The aircraft will be able to complete a maximum range up to 300 km at a cruise altitude of 2000 m. Futura is going to be capable of achieving an 8 ms^{-1} vertical rate of climb and to land like an aircraft in the emergency condition in case full shut down power. Hydrogen refuelling will be achieved by off-site production of LH_2 using the electrolysis process, in which it has to be ensured that the required electricity is generated by sustainable energy sources. Completely refuelling will cost approximately 153.3€ and will take 26 min. Complete battery recharging will be achieved with the Tesla Supercharger V3 for 28.84€, which takes an estimated 25 min to complete. Based on these time frames, the turnaround procedure can be completed in 50 min, which is well within the requirement of 1 h. Due to Futura's VTOL capabilities, take-off, parking, and landing sites will need to be constructed, both for the short- and long-term vision: visual representations can be seen in Figure 4.4 and 4.5. No adjustments will need to be made for marshalling techniques, but ATM will need to hire additional personnel and/or provide the necessary training to guide VTOL vehicles. This chapter establishes all the operational bases needed to present the aerodynamics design and characteristics of the aircraft as outlined in chapter 5.

5. Aerodynamics

The aerodynamics of the aircraft will be presented in this chapter. This is the first step of the aircraft design, because the sizing of the wing, the rotors and fuselage is essential for the design and development of the other components and subsystems. Firstly in section 5.1, the wing is designed, including the wing loading versus power loading diagram, the airfoil selection, the actual wing design including the high-lift devices. Then, once the aerodynamic characteristics are determined, the operational envelope of the aircraft can be defined. After that, Futura's cabin is designed: defining it is essential to give a design space for the design of the fuselage. Then in section 5.4, the lifting-body fuselage will be designed, starting with the airfoil selection and then the actual fuselage design process will be explained. Finally, in section 5.5, the rotor is designed and optimised for the different flight phases to achieve minimum power plant mass.

5.1 Wing

To design and size the full wing, the first step is the construction of the wing loading versus power loading diagram where the wing area can be derived, then the airfoil needs to be selected, and at the end, the wing will be sized. Finally the high-lift devices HLDs are sized and placed on the wing.

5.1.1 Wing Loading vs. Power Loading Diagram

The first step for design the wing for a propeller aircraft is the construction of the wing loading versus power loading diagram. This diagram is based on the sizing for performance process, where the goal is to identify the area in the diagram, where combinations of wing loading and power loading exist that allow meeting the performance requirements.

This graph as is possible to see in Figure 5.1 includes six curves, each of them correspond to the different performance characteristics that Futura needs, the cruise speed, climb rate, climb gradient, manoeuvring performance, stall speed, and landing are displayed. For a normal aircraft usually also the take-off curve is included, but for Futura is not needed since it is a VTOL aircraft and does not perform a normal aircraft take-off.

To plot all these curves, some assumptions are made; in particular, the maximum lift coefficient was assumed based on similar aircraft for weight and passenger capacity. Indeed the lift coefficient (C_L) during the climb, with the $C_{L_{max}}$ in clean configuration and in landing with the flaps deployed was assumed. For the lift coefficient during the climb, a value of 1.25 was assumed, while for the maximum lift coefficient for the clean wing and the flapped wing, respectively a value of 1.5 and 2 was assumed. The value for the clean wing will be then updated after the design of the wing, and the entire process will be iterated until convergence. At the same time also the aspect ratio (A) was assumed, a value of 5.5 is used in the following calculation until the conceptual design of the wing and then the value will be updated and the process iterate again. This value is based on the aspect ratio of similar aircraft, for example, the Bell Boeing V-22 Osprey [27].

The lines in the Figure 5.1 are plotted using the following equations, in particular, the stall speed line is plotted using Equation 5.1, the landing line with Equation 5.2, the cruise speed with Equation 5.5, the climb rate with Equation 5.6, the climb gradient with Equation 5.9 and finally the manoeuvring performance curve with Equation 5.10.

The Futura cruise speed (V_{cruise}) is based on the requirement **Futura-TECH-VCM-3** and it is equal to 97.222 ms^{-1} (350 kmh^{-1}), while the stall speed (V_{stall}) is computed in chapter 4 and it is equal to 50 ms^{-1}. Futura will fly at an altitude of 2000 m so the density (ρ) used in the equations is at this altitude 1.007 kgm^{-3}, while, every time that is indicated as ρ_0 is referring to the density at sea level that is equal to 1.225 kgm^{-3}.[1]

$$\frac{W}{S} = \frac{1}{2} \cdot \rho \cdot {V_{stall}}^2 \cdot C_{L_{max}} \quad [19] \tag{5.1}$$

The MTOW used in the following equation is equal to the 3925 kg from the requirement **Futura-TECH-VCM-6** (multiplied by the gravitational acceleration equal to 9.80665 ms^{-2}) while the fuel weight (W_F) is calculated in chapter 6 and is equal to 18.4 kg.

$$\frac{W}{S} = \frac{C_{L_{max}} \cdot \rho_0 \cdot V_{stall}}{2 \cdot \frac{MTOW - W_F}{MTOW}} \quad [19] \tag{5.2}$$

For the sizing for cruise speed some new parameters are needed, for example the Oswald span efficiency factor (e) that represents the change in drag with lift of a three-dimensional wing and is calculated with Equation 5.3, while the zero lift drag coefficient of the wing (C_{d_0}) is calculated with Equation 5.4 where C_{D_c} for a wing is equal to 0.007, while $C_{D_{misc}}$ is the 15% of C_{D_c} [28].

$$e = \frac{1}{1.05 + 0.007 \cdot \pi \cdot A} \quad [29] \tag{5.3}$$

$$C_{d_0} = C_{D_c} + C_{D_{misc}} \quad [28] \tag{5.4}$$

$$\frac{W}{P} = \eta_p \cdot \left(\frac{\rho}{\rho_0}\right)^{3/4} \cdot \left[\frac{C_{d_0} \cdot \frac{1}{2} \cdot \rho \cdot {V_{cruise}}^3}{\left(\frac{W}{S}\right)} + \left(\frac{W}{S}\right) \cdot \frac{1}{\pi \cdot A \cdot e \cdot \frac{1}{2} \cdot \rho \cdot V_{cruise}} \right]^{-1} \quad [19] \tag{5.5}$$

Then for the sizing for climb rate, calculated with Equation 5.6, the climb performance of Futura are considered, the rate of climb (ROC) is equal to 8 ms^{-1} and is coming from the mission profile, while η_p is the propeller efficiency factor and is assumed to be equal to 0.75 [30].

$$\frac{W}{P} = \frac{\eta_p}{ROC + \frac{\sqrt{\left(\frac{W}{S}\right)} \cdot \sqrt{\frac{2}{\rho_0}}}{1.345 \cdot \frac{(A \cdot e)^{\frac{3}{4}}}{{C_{d_0}}^{\frac{1}{4}}}}} \quad [19] \tag{5.6}$$

For the sizing for climb gradient, the climb gradient is needed that is computed with Equation 5.7 where the climb speed is equal to 60.5 ms^{-1} using the Pythagorean theorem and considering both the ROC and the horizontal velocity during climb again from the mission profile, that is 60 ms^{-1}. Then also the drag coefficient at climb is needed and is assumed using Equation 5.8 where C_L is the climb lift coefficient previously considered and equal to 1.25.

$$G = \frac{ROC}{V_{climb}} \quad [19] \tag{5.7}$$

$$C_D = C_{d_0} + \frac{{C_L}^2}{\pi \cdot A \cdot e} \quad [19] \tag{5.8}$$

$$\frac{W}{P} = \frac{\eta_p}{\sqrt{\left(\frac{W}{S}\right)} \cdot \left(G + \frac{C_{D_{climb}}}{C_{L_{climb}}}\right) \cdot \sqrt{\frac{2}{\rho} \cdot \frac{1}{C_{L_{climb}}}}} \quad [19] \tag{5.9}$$

Finally, the last curve is the sizing for manoeuvring performance and includes the maximum load factor (n_{max}) allowed from regulations that for Futura is 3.5 from CS-29 (large rotorcraft) [31]. Since Futura is a tiltrotor, it can be considered like a helicopter or an aircraft, so in order to find n_{max}, also the regulation

[1] URL `https://www.engineeringtoolbox.com/standard-atmosphere-d_604.html/` [cited 18 June 2019]

CS-23 (normal, utility, aerobatic and commuter airplanes) was checked, but from this the maximum load factor needed is 3.4, consequently it was decided to use the higher of the two.

$$\frac{W}{P} = \frac{2 \cdot A \cdot e \cdot \eta_p \cdot \rho \cdot \pi \cdot V_{cruise} \cdot \left(\frac{W}{S}\right)}{A \cdot e \cdot C_{d_0} \cdot \rho^2 \cdot \pi \cdot {V_{cruise}}^4 + 4 \cdot n_{max} \cdot \left(\frac{W}{S}\right)^2} \quad [19] \tag{5.10}$$

Knowing the equation of all these sizing curves, the wing loading versus power loading diagram was constructed in Figure 5.1, the graph represented is the one after the iterations with the new values of the aspect ratio and the maximum wing lift coefficient in clean configuration.

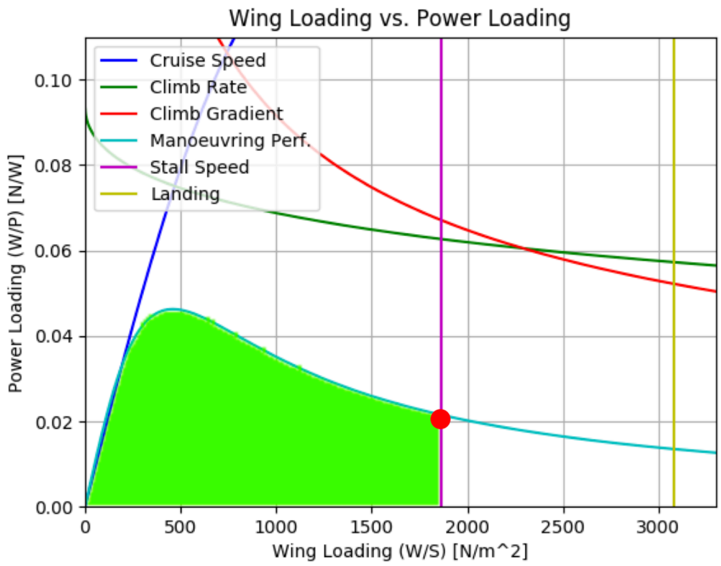

Figure 5.1: Wing loading vs. power loading diagram.

The design point is the point in the green area (area below the curves) that combines the maximum wing loading with the maximum power loading. For clarity, it is represented in the graph with a red dot. Then, knowing the coordinates of this point, it is possible to derive the wing area (S) dividing the maximum take-off weight (MTOW) with the x-coordinate of the design point (the wing loading). In the same manner, for a conventional aircraft, it is possible to calculate also the power at take-off again dividing the MTOW with the power loading resulting from the design point (y-coordinate). However, this was not taken into account since, in the graph, the curve represented the take-off performance was not plotted as said before due to the VTOL take-off procedure of Futura. This results in an optimum wing area of 21.035 m^2 already considering the iterations coming from the new aspect ratio and the maximum wing lift coefficient in clean configuration.

5.1.2 Airfoil Selection

Then, after knowing the optimum wing area for Futura, the airfoil needs to be selected. For it, some parameters are needed, the Reynolds number (R_e), the Mach number at cruise (M_{cruise}), and the dynamic pressure (q).

The Reynolds number (R_e) is calculated with Equation 5.11 and includes the dynamic viscosity (μ) equal to $1.726 \cdot 10^{-5}$ at the cruise altitude of 2000 m and the chord length of the wing (c) that is assumed to be 2 m based on similar aircraft in terms of weight and number of passengers.[2] However, also considering that the wings have to store the radiators, so to increase the height of the airfoil keeping fixed the thickness over chord ratio $\left(\frac{t}{c}\right)$, the chord length should increase. Resulting in a value of $1.134 \cdot 10^7$.

[2] URL `https://www.engineeringtoolbox.com/standard-atmosphere-d_604.html/` [cited 18 June 2019]

$$R_e = \frac{c \cdot V_{cruise} \cdot \rho}{\mu} \quad [32] \tag{5.11}$$

Then the Mach number at cruise was calculated and it is equal to 0.292, it is computed dividing the cruise speed (V_{cruise}) by the speed of sound that includes the cruise temperature at 2000 m equal to 275.15 K adiabatic index (λ) equal to 1.4 for a diatomic gasses and a specific gas constant (R) equal to 287.058 Jkg^{-1}K^{-1}.[3,4,5]

$$a = \sqrt{T_{cruise} \cdot \gamma \cdot R} \quad [32] \tag{5.12}$$

$$M_{cruise} = \frac{V_{cruise}}{a} \quad [32] \tag{5.13}$$

Finally, the last parameter calculated is the dynamic pressure (q) at cruise altitude 2000 m.

$$q = \frac{1}{2} \cdot \rho \cdot V_{cruise}{}^2 \quad [32] \tag{5.14}$$

The first step in the airfoil selection is to define with Equation 5.17 the design lift coefficient of the airfoil ($C_{l_{des}}$), that is the lift coefficient at the most fuel-intensive flight phase of the aircraft mission (the phase at which the aircraft is supposed to fly most of the time). The total lift of the aircraft is set to be equal to the maximum take-off weight (MTOW) (Equation 5.15), then for the wing lift, an extra 10% is considered to compensate for the negative lift contribution generated by the tail to trim the aircraft (Equation 5.16) [32]. The lift produced by the fuselage in the following equations is assumed to be negligible compared to the lift of the wing. Indeed it is just the 5% of the total wing lift.

$$L = MTOW \quad [32] \tag{5.15}$$

$$L_{wing} = 1.1 \cdot L \quad [32] \tag{5.16}$$

$$C_{l_{des}} = \frac{L_{wing}}{q \cdot S} \quad [32] \tag{5.17}$$

After the calculation of the design lift coefficient of the airfoil that is equal to 0.43, the airfoil selection can be made [32]. The following steps are performed to select the optimum airfoil.

1. Assume the thickness over chord ratio $\left(\frac{t}{c}\right)$;
2. Determine the airfoil design lift coefficient $C_{l_{des}}$;
3. For the given $C_{l_{des}}$ look for the airfoil with minimum drag at $C_{l_{des}}$ and the widest possible drag bucket around $C_{l_{des}}$;
4. Select an airfoil with the largest $C_{l_{max}}$ possible. However, avoid airfoils with sharp drop in C_l immediately after stall;
5. Select an airfoil with the lowest C_m possible at $C_{l_{des}}$.

The thickness over chord ratio $\left(\frac{t}{c}\right)$ is assumed to be 0.18, this value was selected to have enough vertical space inside the airfoil to allow the storage of the radiators that are 11.2 cm height without considering all the structural connections, the mechanism that open the wing surface during take-off and the connections between them. Considering the 2 m chord chosen previously, this results in a maximum height for the airfoil of 36 cm. An advantage of a thick airfoil like this is the required lighter structure of the wing due to the increase in the moment of inertia. The only disadvantage is that the form drag increases a bit due to the higher aerodynamic resistance to motion of the airfoil that has a high cross-sectional area.

To select the optimum airfoil, knowing the optimum lift coefficient and the thickness over chord ratio,

[3]URL `https://www.engineeringtoolbox.com/standard-atmosphere-d_604.html/` [cited 18 June 2019]
[4]URL `https://en.wikipedia.org/wiki/Heat_capacity_ratio/` [cited 18 June 2019]
[5]URL `https://en.wikipedia.org/wiki/Gas_constant/` [cited 18 June 2019]

a small trade-off was performed in Table 5.1. The trade-off is between three airfoil, the NACA 23018, the GOE 504 and the UA(2)-180.[6,7,8] Regarding the weight of the trade-off criteria, since they are just three, it was decided to divide on a scale from 3 to 1. The value 3 is given to the maximum lift coefficient $C_{l_{max}}$ criterion since it is a fundamental parameter for the design of the wing. The value 2, to the drag coefficient C_d since the drag is also important for the design of the wing but is also dependent on the lift coefficient and finally 1 to the moment coefficient C_m that is the least important since the pitching moment can easily balance by the horizontal stabiliser (elevator).

Table 5.1: Wing airfoil trade-off ($R_e = 1 \cdot 10^6$, $C_{l_{des}} = 0.431$).

	NACA 23018	GOE 504	UA (2)-180
C_d at $C_{l_{des}}$	0.00891	0.00894	0.01139
$C_{l_{max}}$	1.5196	1.3116	1.4941
C_m at $C_{l_{des}}$	-0.0015	-0.954	-0.0933

From the trade-off it can be seen that the NACA 23018 is performing better on the two most important criterion ($C_{l_{max}}$ and C_d) while for the C_m is a bit worst respect to the others. Overall considering also the weight of the criterion, it is possible to say that it is the best airfoil for the Futura, and for this reason, it was selected. The values of the airfoil considered in the trade-off are derived considering a Reynolds number of $1 \cdot 10^6$; this is not equal to the Reynolds number that the airfoil will be subject during the flight that is $1.134 \cdot 10^7$, but unfortunately, it was not available. However, the lift and moment coefficients are the same increasing the Reynolds number by a power of 10, just the moment coefficient change approximately by 2/3 %, but this was assumed to be negligible.

The NACA 23018 belong to the NACA 5 digits airfoils. This family is appropriated for regional commuters aircraft (M_{cruise}<0.4). They have very high maximum lift coefficient (the highest of all the NACA families), but as a disadvantage, they do not have a docile stall performance. In particular, the NACA 23018, shown in Figure 5.2 has a thickness over chord ratio of 0.18 at the 30% of the chord with a maximum camber of 1.5% at 15% of the chord.

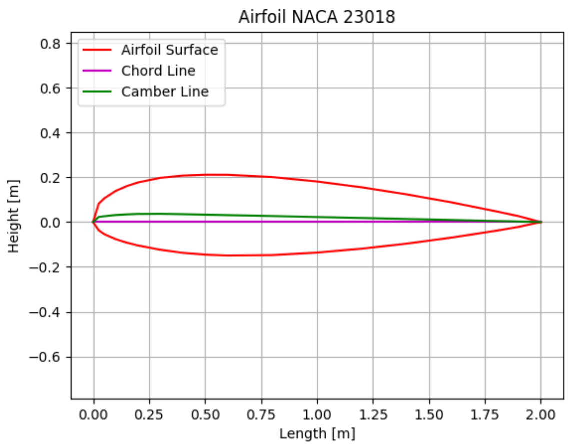

Figure 5.2: Wing airfoil.

In Table 5.2 the aerodynamic characteristics of the NACA 23018 airfoil are presented, the moment coefficient (C_m) is considered at 25% of the chord. These parameters are calculated with Javafoil (a program that use the 3D panel method to compute the aerodynamic characteristics of different shapes).

[6] URL `http://airfoiltools.com/polar/details?polar=xf-naca23018-il-1000000-n5/` [cited 18 June 2019]
[7] URL `http://airfoiltools.com/polar/details?polar=xf-goe504-il-1000000-n5/` [cited 18 June 2019]
[8] URL `http://airfoiltools.com/polar/details?polar=xf-ua2-180-il-1000000-n5/` [cited 18 June 2019]

Table 5.2: NACA 23018 airfoil aerodynamic characteristics ($R_e = 1.134 \cdot 10^7$, $C_{l_{des}} = 0.431$).

$\left(\frac{t}{c}\right)_{max}$	camber$_{max}$	α_{0_l}	$C_{l_{\alpha=0}}$	$C_{l_{max}}$	α_{stall}	C_m at $C_{l_{des}}$	C_d at $C_{l_{des}}$	L/D at $C_{l_{des}}$
0.18	1.5%	$-1.6°$	0.237	1.646	$15.4°$	-0.016	0.01507	28.674

5.1.3 Wing Design

The first step to design a wing is to calculate the required wing lift coefficient with Equation 5.18, considering that the wing loading of the aircraft is changing during the mission due to the fuel consumption and the consequent reduction in weight. The result is a $C_{L_{des}}$ of 0.429, a bit lower than the design lift coefficient of the airfoil. This comparison is also a verification process since the design lift coefficient of the airfoil has to be higher than the wing one.

$$C_{L_{des}} = 1.1 \cdot \frac{1}{q} \cdot \left\{ \frac{1}{2} \cdot \left[\left(\frac{W}{S} \right)_{\text{start mission}} + \left(\frac{W}{S} \right)_{\text{end mission}} \right] \right\} \quad [32] \tag{5.18}$$

At this design condition, the drag can be calculated with Equation 5.8 and results in a value of 0.021.

Then the next step was the evaluation of the wing lift curve slope (C_{L_α}), this was done with the Equation 5.21 from the DACTOM method, that is a collection of statics relations based on designed aircraft, where η is the airfoil efficiency factor equal to 0.95, and β is the Prandtl-Glauert compressibility correction factor calculated with Equation 5.19.

$$\beta = \sqrt{1 - M_{cruise}^2} \quad [28] \tag{5.19}$$

$$C_{L_\alpha} = \frac{2 \cdot \pi \cdot A}{2 + \sqrt{4 + \left(\frac{A \cdot \beta}{\eta} \right)^2}} \quad [28] \tag{5.20}$$

After, knowing this parameter, the wing lift coefficient (C_L) at each angle of attack can be calculated with the DATCOM Equation 5.21, taking into account the zero lift angle of the airfoil (α_{0_L}) that is equal to -1.6.

$$C_L = C_{L_\alpha} \left(\alpha - \alpha_{0_L} \right) \quad [28] \tag{5.21}$$

Then, α_{trim} that is the angle of attack at which the wing has to fly to deliver the design lift coefficient $C_{L_{des}}$ can be derived is calculated with the DATCOM Equation 5.22; it is equal to $2.16°$.

$$\alpha_{trim} = \frac{C_{L_{des}}}{C_{L_\alpha}} + \alpha_{0_L} \quad [28] \tag{5.22}$$

The maximum lift coefficient of a wing ($C_{L_{max}}$) depends on the leading edge (LE) sharpness parameter (ΔY) that is the percentage of the vertical chord between the 0.15% and the 6% of the airfoil chord. The sharper the leading edge, the higher the intensity of the generated leading edge vortices; hence, the higher the $C_{L_{max}}$. Indeed, the shape of the upper part of the airfoil, near the leading edge, is mostly responsible for the formation of these vortexes. It is calculated with the DATCOM Equation 5.23, and is equal to 4.68, in this case, the high value of ΔY, indicates that the airfoil is rounded at the leading edge, so the flow starts to separate at the airfoil trailing edge (TE).

$$\Delta Y = 26 \cdot \left(\frac{t}{c} \right) \quad [33] \tag{5.23}$$

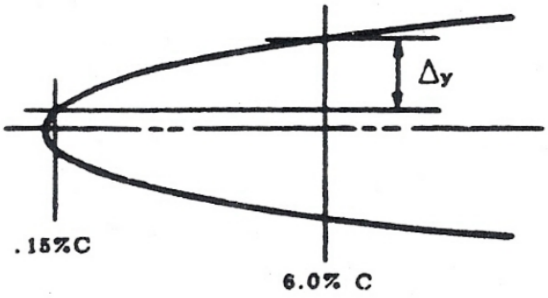

Figure 5.3: Leading edge (LE) sharpness parameter [14].

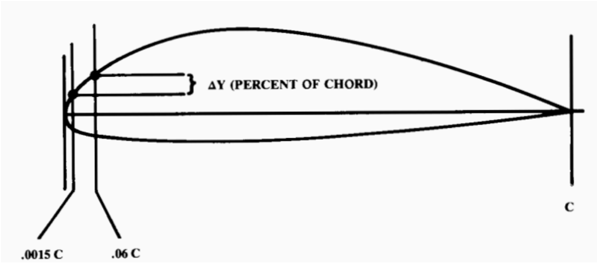

Figure 5.4: Airfoil leading edge sharpness parameter (the airfoil is just an example and does not represent the selected one) [33].

Knowing the leading edge sharpness parameter of the airfoil, it is possible to calculate the maximum lift coefficient of a wing ($C_{L_{max}}$) with the DATCOM Equation 5.24 (for aspect ratio higher than 4) and it is equal to 1.481, where the $\left(\frac{C_{L_{max}}}{C_{l_{max}}}\right)$ value is 0.9 value is taken from the graph Figure 5.5. With this value, it is then possible to perform the iterations. Indeed this maximum lift coefficient value of the wing in clean configuration is used to construct again the wing loading versus power loading diagram instead of the previously assumed value (1.5).

$$C_{L_{max}} = \left(\frac{C_{L_{max}}}{C_{l_{max}}}\right) \cdot C_{l_{max}} \quad [28] \tag{5.24}$$

In the same manner, the wing stall angle (α_{stall}) is calculated with the DATCOM Equation 5.25 (for aspect ratio higher than 4) and results in a value of 13.56°, considering a $\Delta\alpha_{C_{L_{max}}}$ of 2.2 from the Figure 5.6.

$$\alpha_{stall} = \frac{C_{L_{max}}}{C_{L_\alpha}} + \alpha_{0_L} + \Delta\alpha_{C_{L_{max}}} \quad [28] \tag{5.25}$$

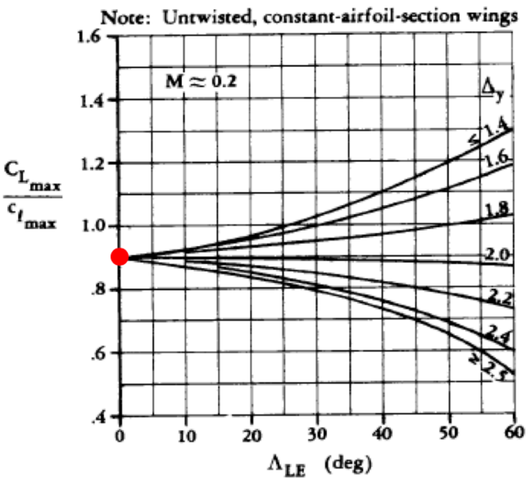

Figure 5.5: Subsonic maximum lift of high-aspect-ratio wings [33].

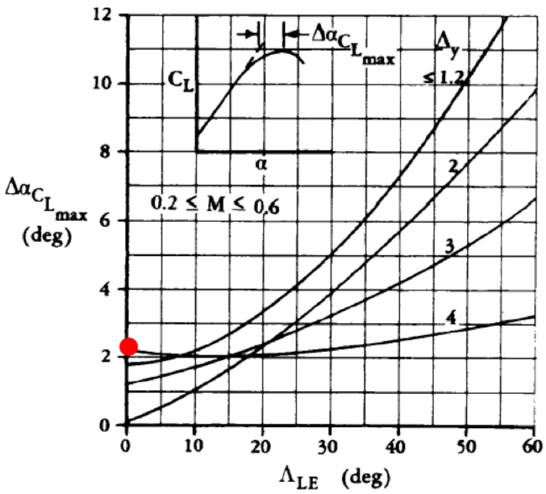

Figure 5.6: Angle-of-attack increment for subsonic maximum lift of high-aspectratio wings [33].

The effect of the transition between an infinite wing and a finite wing is visible in Figure 5.7, the lift curve is rotating around the zero lift angle of attack that remains the same, this affects the maximum lift coefficient that decreases. Knowing this, is then possible to do a verification test, indeed, from the calculation is possible to see that the maximum lift coefficient for the airfoil is higher than the one for the wing. The figure illustrated is just for a visualisation purpose of the effect of finite aspect ratio; it is not related to the airfoil and wing aerodynamic characteristics.

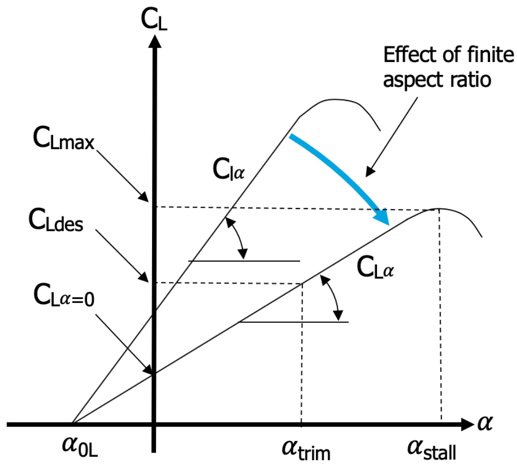

Figure 5.7: Lift curve from airfoil to wing [28].

Finally, the aspect ratio of the wing, is calculated with Equation 5.26, where (b) is the wingspan that is computed with $b=\frac{S}{c}$. With a wingspan of 10.517 m, the aspect ratio of the wing is equal to 5.258. Again, also with this parameter, another set of iterations is possible. Indeed it is used in the generation of the wing loading versus power loading diagram instead of the previously assumed value (5.5). This aspect ratio was not changed, modifying the wing chord, but was kept constant. A quite low aspect ratio has some advantage like the higher roll angular acceleration, the lower parasite drag compared to high wing aspect ratio (however, it has a high induced drag), lower bending stress.

$$A=\frac{b}{c} \quad [32] \tag{5.26}$$

It was decided to use a rectangular wing, without sweep angle, since the Mach number at which Futura will fly is low (0.292) and does not reach the transonic regime. Indeed the main advantage of a swept wing is to delay the wave drag increasing the higher critical Mach number, but in this case, this is not needed. A disadvantage of the swept wing is the big nacelle required to place the rotors; otherwise, the rotor blades will touch the wing due to the sweep angle, this big nacelle increases the weight, and also, for this reason, this design was discarded. Choosing the straight wing leads to an advantage. Indeed the manufacturing process is easier, with lower cost respect to swept wings, but also good stall characteristics of this wing geometry as it is possible to see in Figure 5.8. The stall will start at the wing root and extend to the wing tip, reaching the control surfaces (ailerons and flaps) last, this makes the aircraft controllable also after the stall begins. The wing was placed at the low part of the fuselage (low-wing configuration) not for an aerodynamic reason, since both high-wing and low-wing configuration have similar aerodynamics characteristics. But because is improve the integration with the landing gear without increasing the structural weight and at the same time to allow better visibility above the aircraft from the big window in the fuselage.

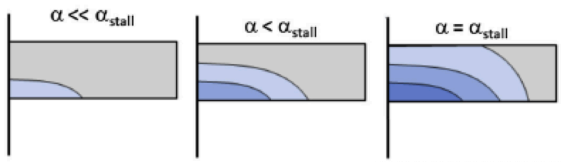

Figure 5.8: Stall progression pattern for a rectangular wing [32].

In Table 5.3, the aerodynamic characteristics of the wing calculated with the DATCOM method and based on the NACA 23018 airfoil are presented. These values are also checked and verified with Javafoil; indeed, the same values result.

Table 5.3: Wing aerodynamic characteristics.

C_{L_α}	α_{0_L}	$C_{L_{\alpha=0}}$	α_{trim}	$C_{L_{trim}}$	C_D at $C_{L_{trim}}$	L/D at $C_{L_{trim}}$	α_{stall}	$C_{L_{max}}$
0.114°	−1.6°	0.182	2.16°	0.429	0.021	20.386	13.57°	1.481

5.1.4 High-lift Devices

The next step is the High-lift devices (HLDs) sizing. To achieve the maximum lift coefficient of 2, to allow a landing as an aircraft during an emergency, it is needed to design some high-lift devices. Unfortunately is not possible to place leading edge high lift devices due to the presence of the radiators and the related air intakes. So it was decided to place the HLDs at the trailing edge (TE) of the wing. Between the vast amount of different trailing edge high-lift devices types, it was decided to put the simple and not extendable plain flap as illustrated in Figure 5.9. It was selected due to the simple and light hinge mechanism that rotates it, that is very reliable, but also due to the capability to also be deflected upward and operate as an aileron, indeed this type of flap that also works like an aileron is called flaperon, this will be better explained in chapter 7. This kind of flap can rotate up to 60° during an emergency landing to reduce the approach speed as much as possible, the stall speed at this $C_{L_{max}}$ will be 39 $\mathrm{ms^{-1}}$. The figure illustrated in Figure 5.9 is just for a visualisation purpose of the flap type; it does not represent the designed airfoil.

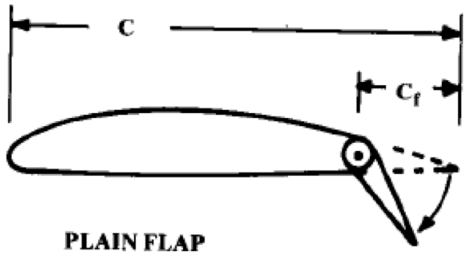

Figure 5.9: Plain flap [34].

Then, the following steps are performed to design the optimum HLDs [34].

1. Evaluating the target $\Delta C_{L_{max}}$;
2. Proposing appropriate types and combinations of High-lift Devices;
3. Estimating the available wing area to place HLDs;
4. Assuming certain chord fractions $\left(\frac{c_f}{c}\right)$ for the HLDs;
5. Calculate the reference wing flapped area $\left(\frac{S_{wf}}{S_{ref}}\right)$;
6. Calculate the shift of the angle of attack ($\Delta\alpha_{0_L}$) due to HLDs.

The target $\Delta C_{L_{max}}$ is calculated subtracting from the maximum lift coefficient with full flap deployed that is equal to 2 the maximum lift coefficient of the clean wing (1.481) and the maximum lift coefficient of the fuselage at the wing stall angle (0.087) that is designed as a lifting-body with the shape of an airfoil, it will explain more in-depth in section 5.4. This results in a value for $\Delta C_{L_{max}}$ of 0.431.

The best flap chord (c_f) for simple plain flaps is about 25% of the wing chord [34], so $\left(\frac{c_f}{c}\right)$ will be 0.25.

Then the reference wing flapped area (S_{wf}), that is the available area in the wing to place the flap (the red part of the wing in Figure 5.10) can be calculated with Equation 5.27, where $\Delta C_{l_{max}}$ is a constant value equal to 0.9 for a fully deployed plain flap [34], and S_{ref} the available reference area that in this case is the total wing area. Again, the figure illustrated in Figure 5.10 is just for a visualisation purpose of the reference wing flapped area; it does not represent the designed wing.

$$\frac{S_{wf}}{S_{ref}} = \frac{\Delta C_{L_{max}}}{0.9 \cdot \Delta C_{l_{max}}} \quad [34] \tag{5.27}$$

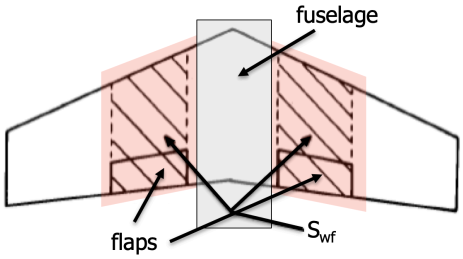

Figure 5.10: Trailing edge (TE) reference wing flapped area [34].

Then, knowing the flap chord and the available area on each side of the wing, it is possible to find the span-wise length that results in a total length of 2.8 m for each wing side, leading to a flap area of 1.4 m^2 again for each side of the wing.

Then, the variation of the angle of attack due to the presence of the leading edge HLDs, is derived with Equation 5.28 using a $\Delta\alpha_{0_l}$ of $-15°$ [34], and results to a value of $-7.99°$, so at a given C_L, the angle of attack will be $-7.99°$ lower.

$$\Delta\alpha_{0_L} = \Delta\alpha_{0_l} \cdot \frac{S_{wf}}{S_{ref}} \quad [34] \tag{5.28}$$

The effect of the not extendable trailing edge high-lift devices on the wing is visible in Figure 5.11. This kind of HLDs will increase the maximum lift coefficient of the wing without changing the lift curve slope (because the wing surface is not increased), but at the same time decreasing the stall angle, promoting the leading edge stall (the lift curve is shifted backward). The figure illustrated is just for a visualisation purpose of the effect of the flap on the lift curve; it is not related to the wing and flap aerodynamic characteristics.

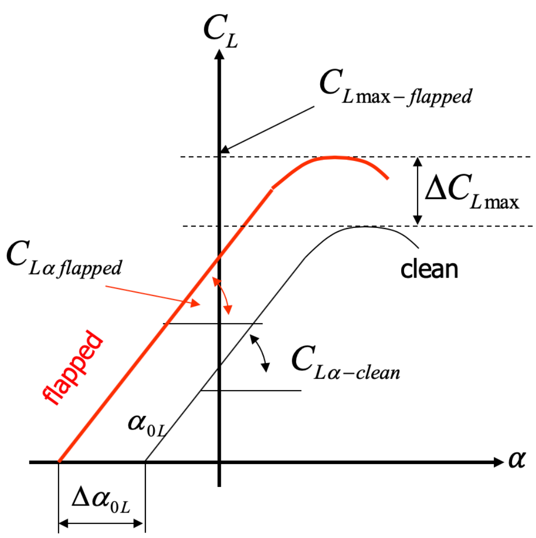

Figure 5.11: Lift curve with plain flap [34].

The increment of the wing drag coefficient ($\Delta C_{D_{flap}}$) due to the presence of the flap can be calculated with Equation 5.29, where F_{flap} is a constant equal to 0.0144 for plain flap and δ_{flap} is the flap deflection in degrees (the equation can be used for a flap deflection higher than $10°$).

$$\Delta C_{D_{flap}} = F_{flap} \cdot \left(\frac{c_f}{c}\right) \cdot \left(\frac{S_{wf}}{S_{ref}}\right) \cdot (\delta_{flap} - 10) \quad [28] \tag{5.29}$$

As it is possible to see in Figure 5.8, for a rectangular wing the stall will begin at the wing root and then extend to the wing tip, for this reason, the flap (flaperon) will be placed at the end of the wing, so the aircraft remain controllable after a hypothetical stall. These values calculated with the DATCOM method previously explained, are also checked and verified with Javafoil; indeed, the same values result.

Table 5.4: Flapped wing aerodynamic characteristics ($\delta_{flap} = 60°$).

C_{L_α}	α_{0_L}	α_{stall}	$C_{L_{max}}$	C_D at $C_{L_{max}}$	L/D at $C_{L_{max}}$
0.114°	−9.59°	5.57°	2	0.119	16.8

The final wing and flap dimensions are illustrated in Figure 5.12.

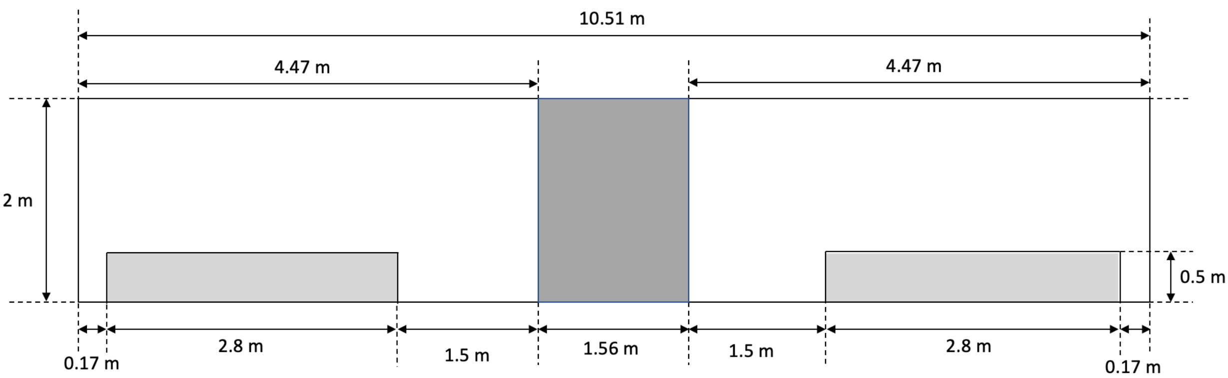

Figure 5.12: Wing and flaperon dimensions.

5.1.5 Verification and Validation

The calculations done with the Python code are compared with an excel file; in this way, all the functions in the code are tested. At the same time, all the airfoil parameters taken from Javafoil are checked with XFoil (another 3D panel method software), and the calculated aerodynamic properties for the 3D wing with the DATCOM method are checked with Javafoil. Furthermore, it was also checked that the lift coefficient of the airfoil was always higher respect to the wing lift coefficient at the same angle of attack as can be seen in Figure 5.7.

5.2 Operational Envelope

Defining the operational envelope of the aircraft is essential to identify the conditions in which it is going to be able to operate. To ensure Futura's success, the loads the aircraft will have to sustain in vertical and horizontal flight have to be calculated respecting regulation as well. Futura overlaps both helicopters and aircraft operations. For this reason, two types of load limitations are considered: those deriving from CS-29 regulation for Category B rotorcraft, and those deriving from CS-23 aircraft regulation [35, 36].
To determine the maximum load the aircraft has to bear, the load factor ($LF = \frac{L}{W}$) as a function of speed was produced for the aircraft operation. Once this value was obtained, it was compared to the maximum load established by CS-29 regulation and the highest of the two is the one used for the design.

Hence, for what concerns the helicopter operation, CS-29 regulation establishes a positive limit load factor of 3.5 and a negative limit load factor of -1 the rotorcraft has to sustain during any phases of flight

[35].

For what concerns the determination of the limit load boundaries in aircraft mode, the intersection of the manoeuvre and gust loading diagram has to be computed as established by CS-23 regulation [36]. The two diagrams were computed for different altitudes with the aircraft at MTOW, and the most restricting condition was found to be for a flight at the sea-level condition. According to CS-23 regulation, the aircraft shall be able to withstand a positive load factor greater than $2.1+\frac{2400}{W+10000}$ (W being the aircraft weight in pounds), but a limit load (n_{max}) not higher than 3.8. As a consequence, the upper limit for the manoeuvre loading diagram is 3.4 as it can be seen in Figure 5.13. The negative limit load factor, according to CS-23 regulation, is -1. Point S is the point at which the aircraft is stalling in clean configuration. In other words, the lift is equal to the weight with a maximum lift coefficient in clean configuration $C_{L_{max}} = 1.481$. Point SF shows a landing load of 1.15 with full flaps deployed with a relative maximum lift coefficient of $C_{L_{max}} = 2$. Point A speed is calculated using $V_A = \sqrt{\frac{2n_{max}mg}{C_{L_{\max}}S}}$ with maximum lift coefficient in clean configuration and maximum load being 3.4. Point D is the last point of interest in the manoeuvre loading diagram since it is the point at which a dive speed is achieved. By regulation the dive speed is $V_D = 1.25 \cdot V_C$, but the aircraft is never going to attain this flight velocity (437 ms^{-1}) [37].
For what concerns the gust loading diagram, the red lines show the load factors the aircraft can encounter due to a gust speed, at different flight horizontal velocities. For the CS-23 aircraft three different flight speed are considered: cruise, dive and flight speed during bad weather. The endpoints of the dotted lines (G_B,G_A, G_D) which bound the gust are found using Equation 5.30.

$$n_g = 1 + \frac{1}{2} \cdot \frac{\rho_0 \cdot C_{L_\alpha}}{MTOW \cdot \frac{g}{S}} \cdot U \cdot V \cdot K_g \cdot \mu_g \quad \text{[37]} \tag{5.30}$$

U is the vertical speed that can be encountered respectively with V_C, V_D and V_B for the above mentioned conditions respectively. The values of the vertical speeds for the different conditions are respectively $U_C = 16$ms^{-1}, $U_D = 8$ms^{-1} $U_B = 20$ms^{-1}. The remaining factors of the equations are K_g and μ_g which are found with the following two equations in SI units: [37]

$$K_g = \frac{0.88 \cdot \mu_g}{5.3 + \mu_g} \tag{5.31}$$

$$\mu_g = \frac{2 \cdot \frac{W}{S}}{\rho \cdot c \cdot C_{L_\alpha} \cdot g} \tag{5.32}$$

Where $\frac{W}{S}$ is the wing loading of the aircraft. While the cruise speed and the dive speed are already known, the speed during bad weather can be found with the equation below.

$$V_B = V_{stall} \sqrt{1 + \frac{K_g \cdot \mu_g \cdot U_B \cdot V_{cruise} \cdot C_{L_\alpha}}{498 \cdot \frac{W}{S}}} \quad \text{[37]} \tag{5.33}$$

Where in this case K_g and μ_g are in imperial units.

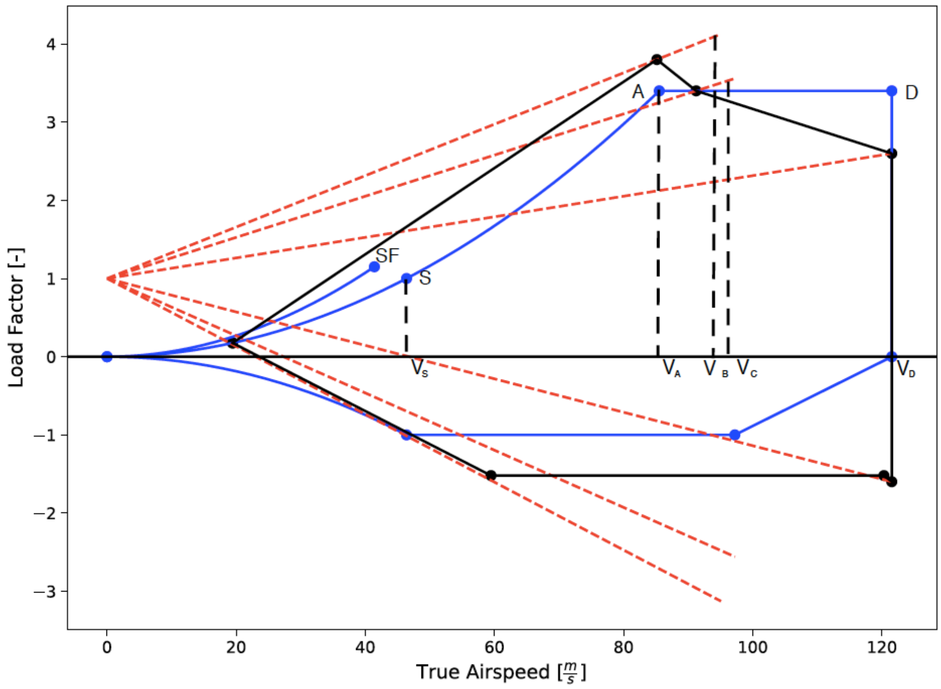

Figure 5.13: Combined loading diagram sea level conditions.

By combining the manoeuvre and gust loading diagram, the operational envelope can be obtained as the black line. The upper n_{max} is 3.8 as specified by CS-23 requirement as well as its negative counterpart, which cannot be 0.4 times the positive limit [36]. These two conditions limit the natural extension of combined loading diagram given by the intersection between the gust and manoeuvre loading. Eventually, it can be noticed that the load factor established by CS-23 regulation is stricter than that one of CS-29 regulation for vertical take-off and landing operations.

5.3 Cabin Design

The design of the cabin is an important factor to attract new business customers to become Futura's clients. The cabin will be minimal in terms of accessories to minimize the weight, without sacrificing the comfort of the passengers.

5.3.1 Cabin Characteristics

The first characteristic that set it aside its competitors is the continuous glass window that replaces the typical aircraft windows. The material for such window was chosen to be Alumino Silicate - 1720, which presents strong resistance against crack propagation and debris impact [9]. This material selection has been made possible by the fact that the fuselage is not going to be pressurised. One main door and one emergency door is going to be present in the cabin
The cabin will have a standard seat configuration for six business passengers with business seats. Every passenger's seat is equipped with one table and one small compartment in which beverages and snacks can be taken during the flight. In the back of the aircraft within the cabin area, a small cargo area is going to host the hand luggage of the passengers. The material for the cabin's interior was chosen to be Ecopaxx (PA410): this novel material can replace the conventional plastic that is widely used in fuselage interiors, increasing the sustainability of the aircraft.[9] Eventually, the division between the cockpit and the passenger cabin is going to be created by a simple curtain place in front of the two exit doors. The cockpit is going to be particularly designed to be centred around one pilot.

[9]URL `https://www.dsm.com/markets/engineering-plastics/en/products/ecopaxx.html` [cited 18 June 2019]

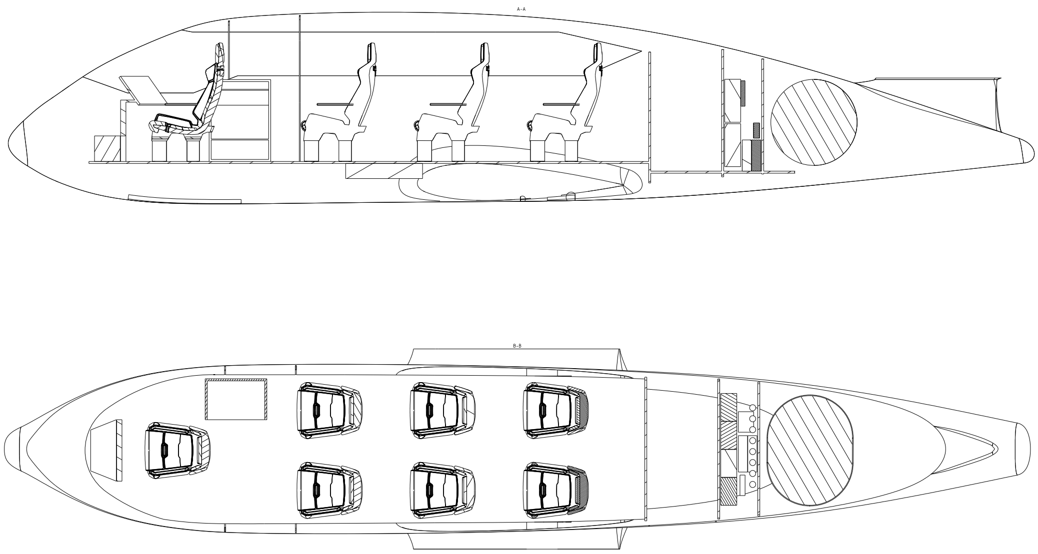

Figure 5.14: Cabin interior illustration.

Figure 5.14 shows an illustration of the cabin from the top and side view. As it can be seen the shape of the fuselage is non conventional. The advantages of adopting such shape are treated in section 5.4.

5.3.2 Cabin's Component Masses

The cabin doesn not only contain everything visible to the passengers, but it also includes important flight instruments. The masses of the flight instruments and the cabin furnishing have been estimated using Roskam III estimation [38]. The avionics mass was calculated using Roskam relationship.

Table 5.5: Cabin's component masses.

System	**Mass** [kg]
Radar Antenna	3.6
Air Conditioning	69.5
Avionics	72.0
Flight Control	80.6
Furnishing	225.0

The antenna mass was assumed to be 5% of the total mass of avionics. The mass of the flight control was estimated using Roskam relationship too. Futura is going to be controlled by one single pilot. Then the air conditioning mass based on Roskam relationship was decreased by 65% since no pressurisation in the cabin occurs. Eventually the mass of the business seat was estimate using a typical value given by Roskam and applying a correction factor of 1.5 in order to account for extra comfort during flight. Lastly, the mass of the small compartment with beverages and snacks was estimated to be 5 kg per passenger.

5.3.3 Cabin's Dimension: Verification and Validation

The internal cabin's dimensions were initially set to be the same as the comparable aircraft Mitsubishi MU-2 which presents a similar MTOW. Hence the width of the cabin was set to be 1.48 m while the cabin height 1.4 m. These values are the most conservative ones, and they are going to vary once the fuselage lifting body is designed. To verify the ergonomics and dimensions of the cabin, a CATIA V6 model was produced; with this program, a virtual reality experience was completed to check whether or not the aircraft's space was liveable.

5.4 Fuselage

To design and size the fuselage, the first step is the sizing; the dimensions are derived from the cabin sizing previously done. Then the airfoil can be selected, and finally, the aerodynamic characteristics of the fuselage can be computed.

5.4.1 Airfoil Selection

The first step in the fuselage design is dimensioning. From the operation team, the cabin sizing was given, and around these values, the entire fuselage was constructed. The cabin internally needs to be 5.45 m long, 1.48 m wide and the height has to be 1.4 m. It the cabin was divided into the pilot cockpit and the passenger cabin. Indeed the pilot cockpit was designed to be 1.2 m long and corresponds to the nose cone while the rest 4.25 m is for the passenger. Then the tail cone was sized to have a total fineness ratio $\left(\frac{d}{L_F}\right)$ of around 0.15, value in the range of typical subsonic jet aircraft and ideal to have a low pressure drag [39]; at the same time it allows to have enough space to place all the needed components like the fuel cell and the tank. The internal dimensions of the fuselage are visible in Figure 5.15. Regarding the external dimensions, it was assumed to consider a structural thickness of 0.04 m all along the fuselage; this value is quite small because a pressurised structure is not needed.

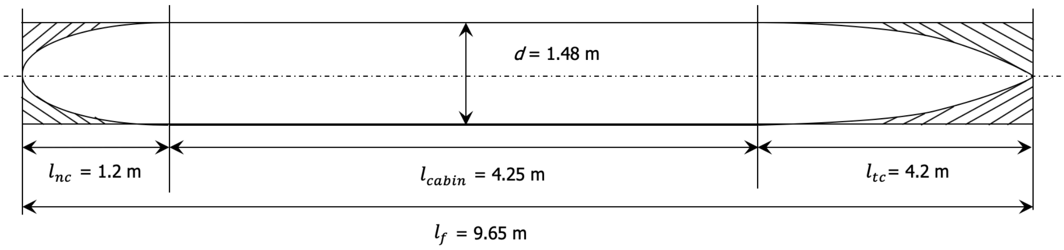

Figure 5.15: Fuselage internal dimensions [39].

As stated in the previous section, the fuselage was designed to be a lifting-body, with a shape like an airfoil. This because pressurisation is not needed due to low altitudes, and so a circular cross-section (that is the most suitable concerning the capability to carry the tension loading and the bending loading due to the different pressure with the outside) is not required. For this reason, a shape with better aerodynamic characteristics was designed, to reduce the drag and produce some lift.

Then the three-dimensional fuselage shape was constructed. First it was assumed to be like a rectangular wing with a chord of 9.73 m and span of 1.56 m (external fuselage dimensions), but then to design the nose cone and the tail cone and to make the body more slender but at the same time also more captivating, the parts illustrated with the oblique line in Figure 5.15 were discarded. Then, knowing the final dimensions, the fuselage aspect ratio is found with the formula for not rectangular wing $A = \frac{b^2}{F_{area}}$, where F_{area} is the fuselage area and results in a value of 0.213.

Then the Reynolds number (R_e) needs to be updated since it is different from the one of the wing due to the different chord length, resulting in $5.519 \cdot 10^7$, again using Equation 5.11.

The airfoil selection for the fuselage was not performed like the one for the wing with a trade-off, because for this, a particular shape is required to allow enough internal space for the passenger cabin and the storage of all the needed components. However, at the same time, an airfoil similar to the wing one is required to have similar aerodynamic characteristics. Indeed since no already used airfoil was ideal for this specific task, it was decided to create an airfoil based on the interested parameters, and this results in an airfoil that belongs to the NACA 5 digits airfoils, and that can be called NACA 25121 as shown in Figure 5.16. This airfoil has an optimum lift coefficient equal to the wing airfoil (0.431), a thickness over chord ratio ($\frac{t}{c}$) of 21% at 30% of the chord and a maximum reflex camber of 2% at 25% of the chord (camber line that curves back up near the trailing edge (TE)). This particular shape enables to have a height of 1.4 mm at the end of the passenger cabin.

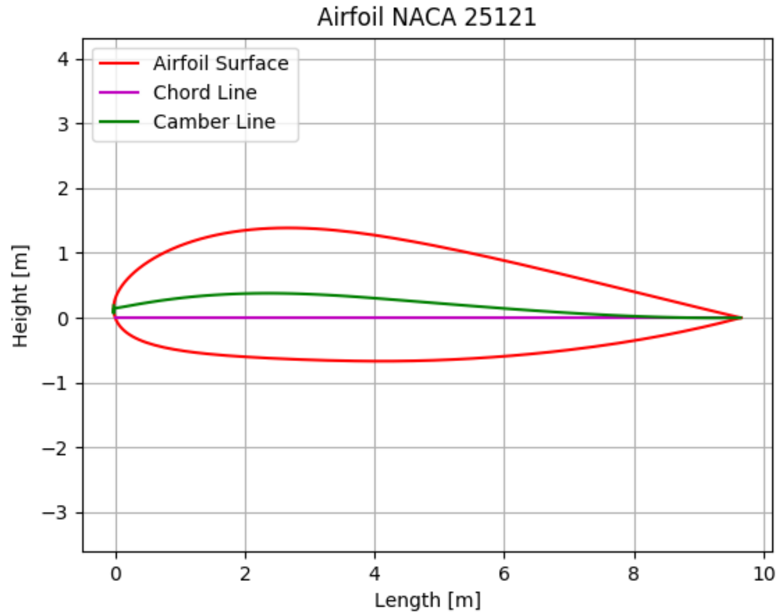

Figure 5.16: Fuselage airfoil.

In Table 5.6 the aerodynamic characteristics of the NACA 25121 airfoil are presented, the moment coefficient (C_m) is considered at 25% of the chord. These parameters are calculated with Javafoil.

Table 5.6: NACA 25121 airfoil aerodynamic characteristics ($R_e = 5.519 \cdot 10^7$, $C_{l_{des}} = 0.431$).

$\left(\frac{t}{c}\right)_{max}$	camber$_{max}$	α_{0_l}	$C_{l_{\alpha=0}}$	$C_{l_{max}}$	α_{stall}	C_m at $C_{l_{des}}$	C_d at $C_{l_{des}}$	L/D at $C_{l_{des}}$
21	2%	$-1.5°$	0.211	1.917	18.1°	0.003	0.0131	33.224

5.4.2 Fuselage Design

To design the fuselage, the first step is to evaluate the wing lift curve slope (C_{L_α}) with the DATCOM equation Equation 5.21 again taking into account the Prandtl-Glauert compressibility correction factor calculated with Equation 5.19. Then, the wing lift coefficient (C_L) at each angle of attack can be calculated with the DATCOM Equation 5.21, taking into account the zero lift angle of the airfoil (α_{0_L}) that is equal to -1.5.

To calculate the drag coefficient of the fuselage (C_D) at each angle of attack with Equation 5.8, some parameters are needed, like the Oswald efficiency factor (e) calculated again with Equation 5.3 and the zero lift drag coefficient of the fuselage (C_{d_0}) with Equation 5.34, where $\left(\frac{S_{wet}}{S_{ref}}\right)$ is the wetted area over the reference area (area of the wing), that for a twin engine light aircraft is equal to 5 from Figure 5.17 and C_{f_e} that is equivalent skin friction coefficient, for this kind of aircraft is 0.0045. The $\left(C_{f_e} \cdot \frac{S_{wet}}{S_{ref}}\right)$ part in the equation is the total zero lift coefficient of the aircraft, the factor 0.9 is a reduction factor to take out the excrescence and leakage for a propeller aircraft (miscellaneous drag) and the zero lift coefficient of the wing previously calculated was subtracted as well [28].

$$C_{d_0 fuselage} = 0.9 \cdot \left(C_{f_e} \cdot \frac{S_{wet}}{S_{ref}} \right) - C_{d_0 wing} \quad [28] \tag{5.34}$$

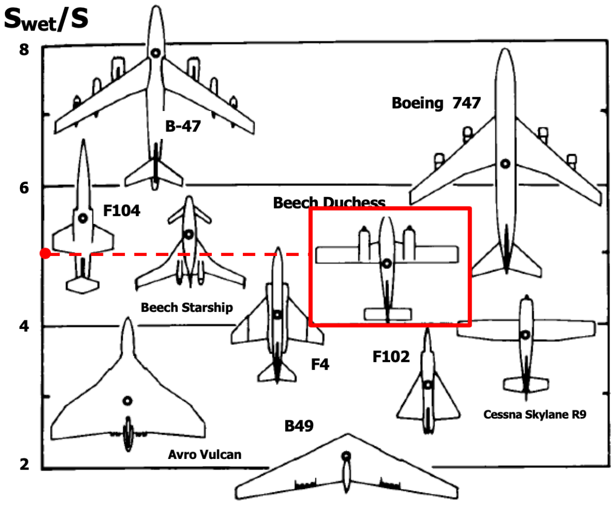

Figure 5.17: Wetted area ratios [33].

After all these calculation, the results are presented in Table 5.7, where the aerodynamic characteristics of the fuselage calculated with the DATCOM method and based on the NACA 25121 airfoil are listed. It is possible to notice that the lift over drag ratio for the designed fuselage at the trim condition is higher than 1. This means that the fuselage will produce more lift than the drag, this value for a conventional fuselage with a circular cross-section is lower than 1. This result confirms that the design of the fuselage was successful; indeed it helps to decrease the drag and increase the lift, increasing the lift over drag of more than 230% respect to conventional circular cross-section fuselage. However, it is also needed to say that the lift coefficient created by the fuselage is very small compared to the clean wing one at trim conditions (5% respect to the wing). This value is due to the low aspect ratio of the fuselage, the value of the lift coefficient calculated with the DATCOM method previously explained was also checked and verified with Javafoil, indeed, the same value results.

Table 5.7: Fuselage aerodynamic characteristics.

C_{L_α}	α_{0_L}	$C_{L_{\alpha=0}}$	α_{trim}	$C_{L_{trim}}$	C_D at $C_{L_{trim}}$	L/D at $C_{L_{trim}}$
0.00577°	−1.5°	0.00866	2.16°	0.0211	0.0174	1.215

Estimating this novel fuselage mass is extremely challenging as it is strongly dependent on its structural design. However, the external dimensions of Futura's fuselage on average are comparable to similar aircraft, even considering its lifting characteristics. For this reason, the mass of the fuselage has been estimated using similar twin propeller aircraft in the same weight category [40]. A fuselage mass of 278 kg was obtained statistically based on the maximum take-off weight of Futura and applying a reduction of 15% for the use of new technology [40]. This value is likely to change in future design iterations, especially since the fuselage structural design has not yet been completed. This does not mean that the fuselage mass might only increase because of its innovative shape, but also decrease since the statistical estimate is based on pressurised aircraft whose structural mass is particularly big. Hence this factor has been taken into account in section 9.5. Eventually the material chosen for the fuselage frame has been selected to be Aluminium 7075 T73 as it is widely used in aero-structural applications [41]. The fuselage skin panels, however, are preliminary selected to be made in Aluminium 2024 T6 which has a lower specific mass [9, 41]. The fuselage floor, finally, is made of aluminium -polyethylene composite panels in order to limit its mass [9].

5.4.3 Verification and Validation

Verification of the calculations was done by comparing the results from the Python code with an excel file, where each function in the code is tested. At the same time, all the fuselage airfoil parameters taken from Javafoil are checked with XFoil (another 3D panel method software), and the calculated aerodynamic properties for the 3D fuselage with the DATCOM method are checked with Javafoil. Furthermore, it was also checked that the lift coefficient of the airfoil was higher respect to the fuselage lift coefficient at the same angle of attack as can be seen in Figure 5.7.

5.5 Rotor Design

Following with the aerodynamics design, the study of the rotor is of uttermost importance to analyse the power and energy required to perform the different phases of the flight. An optimised rotor geometry can contribute to a weight save of almost 100 kg compared to a non optimised one, as will be presented in this section. A Blade Element Momentum Theory (BEMT) code was developed to compare different blade designs and provide accurate estimates of power and energy following the method by J.G. Leishman [42].

5.5.1 Blade Element Momentum Theory

The blade element momentum theory combines the Blade Element Theory (BET) and the Simple Momentum Theory (SMT). This provides a model that is based on solid physical principles, relatively free of empirical relations. Another advantage of applying this method is that it serves as a tool to design the blades of the rotor, and provide more accurate estimates of power and thrust for different blade designs compared to SMT. Using conservation of mass, momentum and energy to different annuli of the rotor disk, the BEMT allows to calculate the aerodynamic loads over the blade, accounting for hub and tip losses.

Starting with principles of momentum theory, the thrust produced by a rotor annuli can be computed as the product of the mass flow through the annuli and the induced velocity at that same location, as shown in Equation 5.35. Each rotor annuli is located at a certain y distance from the center of the rotor [43, 44].

$$dT = v \cdot d\dot{m} = 2\pi\rho(V_\infty + v)y\,dy \tag{5.35}$$

As on many mathematical and physical derivations, non-dimensional equations will be used to generalise the problem and gain insight regarding the influence of different parameters on the final outcome. Therefore, from now on, all the derivation will be followed with dimensionless quantities, until the final values of thrust and power are computed at the end. The thrust coefficient, which now gains importance, can be written as specified in Equation 5.36.

$$dC_T = \frac{dT}{\rho(\pi R^2)(\Omega R)^2} \tag{5.36}$$

Following helicopter conventions, the speeds can be non-dimensionalised by the tip speed, as written in Equation 5.37 and Equation 5.38. On a similar manner, the span-wise location of the different blade elements can be described by Equation 5.39.

$$\lambda = \frac{v}{\Omega R} \tag{5.37}$$

$$\lambda_\infty = \frac{V_\infty}{\Omega R} \tag{5.38}$$

$$r = \frac{y}{R} \tag{5.39}$$

Now, the thrust coefficient can be expressed in a more elegant form in Equation 5.40, with the relation of the average induced velocity shown in Equation 5.41.

$$dC_T = \frac{2\rho(V_\infty + v)v(2\pi y\,dy)}{\rho\pi R^2(\Omega R)^2} = 4\lambda\lambda_i r\,dr \tag{5.40}$$

$$\lambda = \lambda_i + \lambda_\infty \tag{5.41}$$

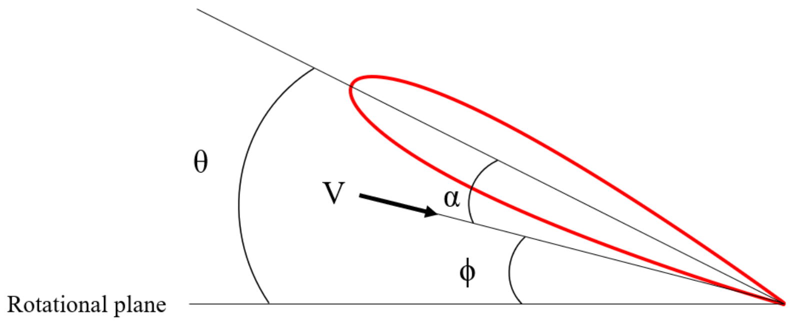

Figure 5.18: Representation of the rotor angle of attack (α), and incoming flow angle (ϕ) and blade geometric angle (θ) with the rotational plane at a given blade element.

An interesting advantage of BEMT is that it can account for blade loss effects due to the vorticity generated at the tip and at the root of the blade. Using Glauert's corrections in Equation 5.42 and Equation 5.43, these losses can be computed.

$$F_{tip} = \frac{2}{\pi}\cos^{-1}\left(\exp\left(-\frac{B}{2}\frac{1-r}{\sin\phi}\right)\right) \qquad (5.42)$$

$$F_{hub} = \frac{2}{\pi}\cos^{-1}\left(\exp\left(-\frac{B}{2}\frac{r-r_{hub}}{r_{hub}\sin\phi}\right)\right) \qquad (5.43)$$

The total loss due to the vorticity effects can then be found in as the product of both of these loss factors $F_{tip} \cdot F_{hub}$. In this equations, the hub and tip loss are calculated as a function of the angle ϕ, which is the angle of the incoming flow each blade element experiences, and the rotational plane. A graphical representation of this angle, together with the angle of attack of each blade element (α) and the geometric angle of each blade with the rotational plane (θ) can be seen in Figure 5.18. This angle ϕ is therefore a function of the induced velocity λ at the blade element. A more accurate value of C_T can now be found according to Equation 5.44 using SMT [45]. This equation can be compared to that obtained by pure blade element theory, where the thrust obtained by a blade element is shown in Equation 5.45.

$$dC_T = 4F_{tot}\lambda\lambda_i r dr \qquad (5.44)$$

$$dC_T = \frac{1}{2}\sigma C_l r^2 dr = \frac{\sigma C_{l_\alpha}}{2}\left(\theta r^2 - \lambda r\right)dr \qquad (5.45)$$

The relation shown in Equation 5.46 can be derived between the loss factor F_{tot} and the induced velocity λ, combining the two equations above. As it was derived above, the loss factor F_{tot} is a function of the induced velocity λ, which is itself a function of the loss factor. Equation 5.46 can be solved numerically with a fix point iteration for an initial estimate of F_{tot} at each of the blade elements.

$$\frac{\sigma C_{l_\alpha}}{2}\left(\theta r^2 - \lambda r\right) = 4F_{tot}\lambda(\lambda - \lambda_\infty)r \qquad (5.46)$$

Once convergence is achieved, the induced velocity distribution can be found at each of the blade elements. An accurate prediction of the aerodynamic loads can be obtained, providing the desired value of C_T. Similarly, with λ one can predict the power required to drive the rotor. This power has two components, one derived from the induced power required to keep the aircraft in the air found in Equation 5.47, and another required to spin the rotor and overcome the drag of the rotating blades specified in Equation 5.48. Once more, first the non-dimensional coefficients are computed, and these values are then dimensionalised.

$$C_{P_{ind}} = \int_{r=0}^{r=1} \lambda_i dC_T \qquad (5.47)$$

$$C_{P_{prof}} = \int_0^1 \frac{1}{2}\sigma C_d r^3 dr \qquad (5.48)$$

In such equations, the induced power can easily be calculated by numerical integration of the induced velocity by the thrust coefficient at each of the rotor annuli. The calculation of the profile power, on the other hand, is more cumbersome. A first estimate of this value can be provided by using the zero lift profile drag of the airfoil of choice. More accurate results are achieved when the drag coefficient is computed at each blade element angle of attack. As will be shown later, a correction method needs to be present. Due to the different operational regimes of the rotor (from hover to almost 100 ms^{-1} at cruise), a wide range of angles of attack is experienced at different locations of the rotor. A high angle of attack correction needs to be implemented to ensure realistic values of the profile drag. The Viterna method was employed to extrapolate airfoil lift and drag coefficients beyond usual wind tunnel experiment data [46]. A set of existing data as initial values is required to estimate the aerodynamic performance of the given profile at any angle of attack. This method is applied to the NACA 0012, which is the airfoil used all along the blade. This airfoil is chosen as it is a typical selection for the blades of rotorcraft [47]. Equation 5.49 and Equation 5.50 can be employed to compute the C_l and C_d of the airfoil, respectively, from α_{stall} to 90°.

$$C_l = A_1 \sin 2\alpha + A_2 \frac{\cos^2\alpha}{\sin\alpha} \quad (5.49)$$

$$C_d = B_1 \sin^2\alpha + B_2 \cos\alpha \quad (5.50)$$

The values of A_1, A_2, B_1 and B_2 are based on the initial data available for the airfoil. These relations can be found in Equation 5.52, Equation 5.53, Equation 5.54 and Equation 5.55, with the relation shown in Equation 5.51. At this stage of the design, the aspect ratio (A) of the rotor has to be estimated to compute the extrapolated C_l and C_d. The initial estimate for this value is of little importance, as it has very little impact on the results. An initial estimate of 10 was therefore selected [46].

$$C_{d_{max}} \simeq 1.11 + 0.018A \quad (5.51)$$

$$A_1 = \frac{C_{d_{max}}}{2} \quad (5.52)$$

$$B_1 = C_{d_{max}} \quad (5.53)$$

$$A_2 = \frac{(C_{L_{stall}} - C_{d_{max}} \sin\alpha_{stall} \cos\alpha_{stall}) \sin\alpha_{stall}}{\cos^2\alpha_{stall}} \quad (5.54)$$

$$B_2 = \frac{C_{d_{\text{stall}}} - C_{d_{max}} \sin^2\alpha_{stall}}{\cos\alpha_{stall}} \quad (5.55)$$

To obtain the extrapolated values for $\alpha > 90°$ and $\alpha < \alpha_{min}$, the calculated data can simply be reflected. The results obtained for the NACA 0012 before and after applying the Viterna method can be found in Figure 5.19 and Figure 5.20.

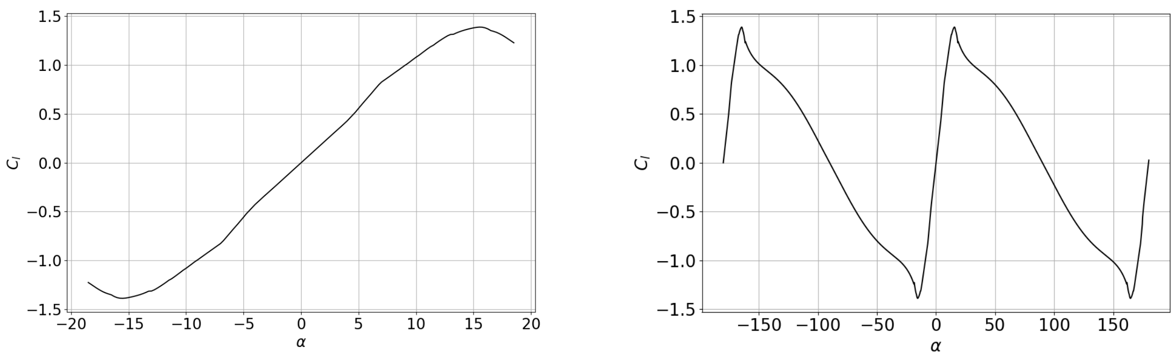

Figure 5.19: NACA 0012 lift coefficient data using XFoil (left) and Viterna extrapolation method (right).

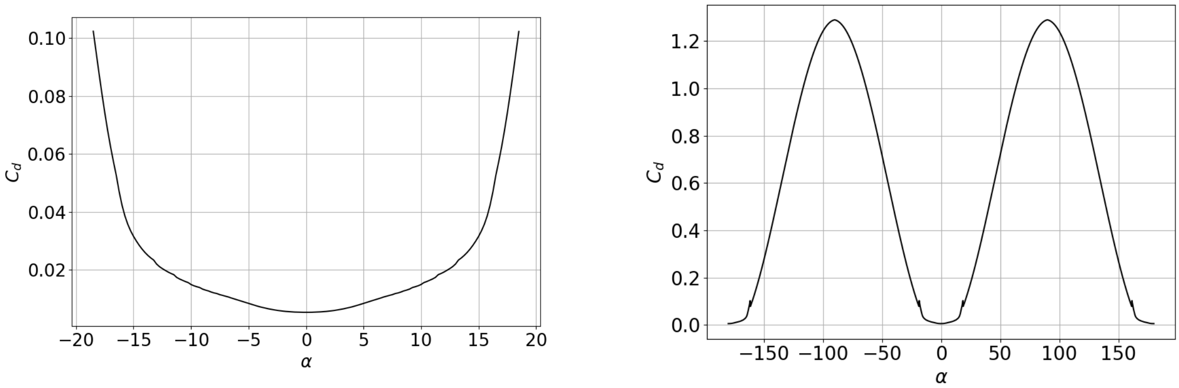

Figure 5.20: NACA 0012 drag coefficient data using XFoil (left) and Viterna extrapolation method (right).

The values obtained can be compared with experimental data to assess the validity of the model. In Figure 5.21 the values of C_l are compared between the Viterna method and wind tunnel experiments performed by NASA [48].

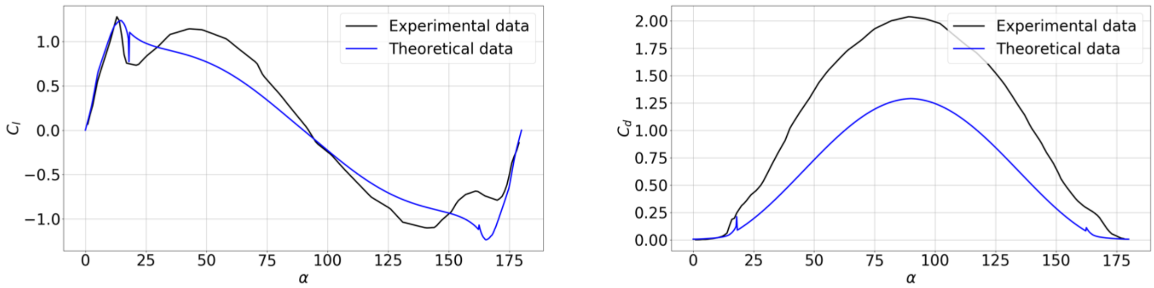

Figure 5.21: Comparison of NACA 0012 lift (left) and drag (right) coefficient data using Viterna method (blue) and experimental data (black), at Reynolds number $5 \cdot 10^5$.

As it can be noticed in Figure 5.21,the Viterna extrapolation method provides a very good estimate of the C_l for the range of α. The C_d, on the other hand, seems to be underestimated when compared to the values obtained from wind tunnel tests. It must be noted the experiments carried out to get the values represented in Figure 5.21 proved discrepancies between different airfoils. Symmetric airfoils with different thickness to chord ratio were tested, and the discrepancies in the data obtained seemed greater than what could be expected for such changes in the thickness to chord ratio [48]. Since the Viterna method is widely accepted and used for experimental data extrapolation, the values obtained from such method will be used for the purpose of this design. Wind tunnel tests will have to be performed to validate the results presented in this section. On a similar note, the Montgomerie method to extrapolate airfoil data proved to show very similar values as those of Viterna, justifying the use of the data obtained from the latter method [46].

Once the C_d is calculated for a wide range of α, the $C_{P_{prof}}$ can be computed in a more accurate manner than with standard XFoil data. Finally, the values of power and thrust can be obtained dimensionalising C_P and C_T, respectively. As will be analysed in more detail in the next section, different blade geometries prove to have an important effect on the performance of the rotor. Different blade parameters will be analysed in order to obtain an optimised design.

5.5.2 Blade Design Optimisation

Radius, twist, tip Mach number, solidity, number of blades or airfoil selection are just a few of the many variables a designer has to determine with the objective of optimising performance. However, the influence that each of these factors has on the behaviour of the rotor varies considerably. While some parameters may be almost trivial, such as the exact blade cutout location at the root, other parameters prove to be of great significance to the power required to drive the rotor, such as the twist distribution along the blade. In this subsection first the parameters kept fixed throughout the design are described. Then, the parameters optimised are explained and analysed in detail. Finally, the results of the optimisation are presented.

For the design of Futura, two main relevant outcomes of the rotor design determine the weight of the power plant system: power and energy. Since the aircraft is equipped with a hydrogen powered system, peak powers shall be kept as low as possible as a general guideline to maintain a relatively low mass of the power plant system. These two concerns drive the design of the blade, and the optimum one is found based on the lowest associated power plant mass.

The selection of the rotor radius is possibly the most determining factor on the aerodynamic performance of a helicopter. Bigger rotor radius prove to decrease the overall power for tilt rotor, which, as specified above, is one of the main objectives of this blade design. One main constraint on the rotor size is the interaction with the fuselage. The tip of the rotor shall be at a distance which prevents collision between the two parts, as well as low disturbance on the cabin. A distance of 0.6 m was evaluated adequate, since it allows for low power with low interaction with the fuselage, yielding a rotor radius value of 4.32 m. The next value to choose is the rotor inner cutout. A choice between 0.1 and 0.25 of the rotor radius is a typical value, but of little relevance to the performance of the rotor. A value of 0.2 was taken. The size of the rotor is directly linked to the tip speed and the rotational speed. Bigger rotors mean slower rotational speeds for the same tip speed. Increasing the speed of the blades generates more thrust in the rotor. A limit is reached when drag divergence appears at the tip of the rotor, the point with the highest speed. For the airfoil chosen, the NACA 0012, drag divergence effects appear at a Mach number of 0.8. This means the tip of the blade should not reach this speed, or an excessive amount of drag will be encountered, as well as compressibility losses [47]. This value was taken with a margin, and a maximum tip speed of Mach number 0.75 was selected for the rotor.

The last values to be determined are the number of blades, and the taper. The number of blades is a parameter that has little influence on the performance of the rotor. A more interesting variable is the rotor solidity, which is optimised for minimum weight of the propulsion system. 3 blades were selected for the rotor as it provided a fair compromise between weight and induced tip losses [49]. Finally, the taper of the blades had to be selected. Even if an optimum combination of twist and taper could have benefits of the performance of the helicopter, the twist of the blades alone proves to have a higher influence over the behaviour of the rotor than the taper alone [47]. Similarly, adding twist and taper complicates further the manufacturability of the blades. Therefore, despite a possible improvement in the performance of the blades, non-tapered wing were selected.

The optimisation of the rotor blades entails selecting blade twist and rotor solidity to achieve minimum power plant weight. The twist along the blade is directly related to the lift generated by the rotor, as well as the profile power, as it controls the angle of attack of each blade element. Different types of twist were considered, ranging from ideal to linear twist. Very little difference in the power required was found for the ideal twist compared to the linear twist. Only linear twist was therefore considered due to the simpler manufacturability of the blade. The rotor solidity, on the other hand, is related to the thrust and drag-producing surface. As it will be shown, different values for the twist distribution along the blade and rotor solidities will yield very different power required at the specified thrusts. It should be noted that these parameters will not be optimised for one condition only, as many helicopters are, but rather for a range of operating conditions. These operating conditions come from the peculiar mission profile Futura needs to satisfy. Different combinations of rotor twists and solidities were compared and evaluated. As an example, Figure 5.22 shows the power required throughout the mission for three different profiles. In blue, the power required for a low solidity (0.02) low twist (-1° difference between the tip and

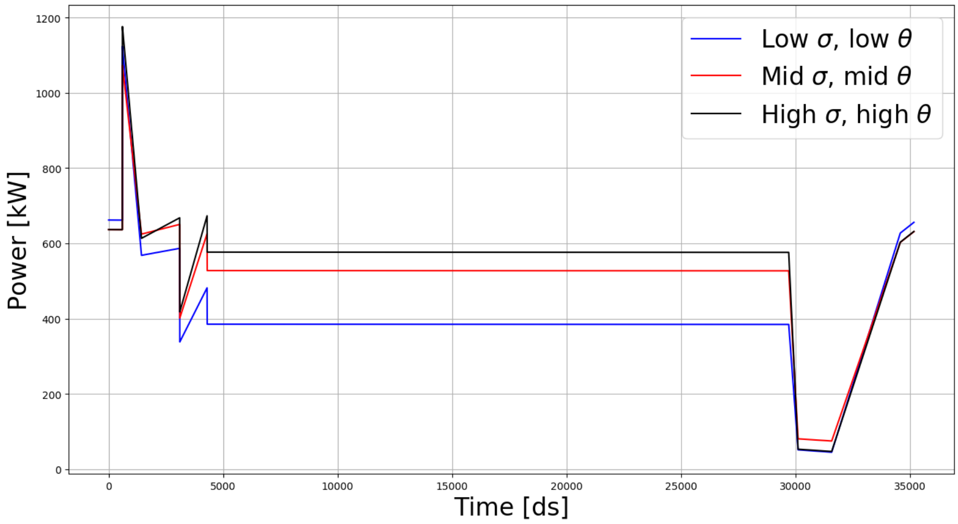

Figure 5.22: Power required for three different rotor designs throughout the mission.

the root) is plotted throughout the mission time. Similarly, in red, the figure shows the power required for a mid solidity (0.05) mid twist (-15° difference). Finally, in black, the power required for a high solidity (0.09) high twist (-30° difference) is shown.

Some interesting conclusions can be derived from Figure 5.22. Firstly, it can be noted that the maximum power required at hover is for the low solidity, low twist rotor. This rotor, however, performs considerably better at cruise, with almost 200 kW less than the worst performing one. The maximum power required is achieved by the high solidity high twist rotor, at a value of 1175.95 kW. The mid solidity mid twist rotor shows and interesting behaviour. It requires the smallest peak power, but at cruise almost 550 kW are required to drive it. From Figure 5.22, it can be concluded that the lowest weight of the power plant mass, derived from low peak powers and mission energy, will be a combination of low to mid solidity, and low to mid twist. If different values of solidity and twist are tested, a more continuous link between the curves in Figure 5.22 is found.

As will be explained later in chapter 6, the weight of the power plant system cannot be computed directly based on the maximum power and energy required to fulfil the given mission. Rather, the lowest system mass is found by means of a complex algorithm that considers battery and fuel cell integration, that contemplates the different powers throughout the mission. This algorithm is explained in more detail in chapter 6, but will be used now to determine the optimum blade choice. The mass of the power plant can now be plotted against different blade designs, as shown in Figure 5.23. In this figure, multiple rotor solidities and blade twists are compared. The different blade designs are grouped in the following manner: the first blade (index 0) has a solidity of 0.01, and a twist of -5°. Every consecutive blade increases the twist by a 6° difference between the tip and the root. Every five blades, a new solidity is simulated, starting the value of twist at 6° again. This way, five consecutive blades in the graph belong to a certain solidity, from 0.01 to 0.04. It can be noticed that almost all of these groups of blades have a parabolic shape, where for a given solidity, the associated weight of the power plant mass is first high for low twist, then goes down as twist increases, but then increases again after a minimum is reached. On a similar manner, the solidity shows a similar trend. First, the power plant mass is high with a solidity of 0.01. Then, it experiences a drop at a value of σ equal to 0.02, to then increase the weight of the associated power plant system again for higher values of solidity. The solidity value of 0.02 is then tested for further optimisation of the twist, as can be seen in Figure 5.24. A more fine search for the best performing blade is performed for different root twists, keeping the tip at 0° twist, and having a linear twist distribution.

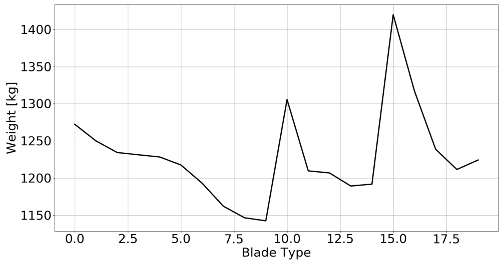

Figure 5.23: Power plant weight for different blades.

Figure 5.24: Power plant weight for different twist angles, with σ= 0.02.

The minimum power plant mass is obtained at a rotor solidity of 0.02, and root twist of 18.3°, with a value of 1132.4 kg. As mentioned before, this optimised blade allows for a minimum weight decrease of 100kg compared to other sub-optimal solidities, as shown in Figure 5.23.
It is worth mentioning that this is a relatively low value of solidity compared to normal helicopters. However, this can be explained by the fact that higher rotor solidities allow for big stall margins at the blade, something conventional helicopters must account for manoeuvrability. On a tilt rotor, on the other hand, during almost all the flight the propeller only experiences axial flow and flow parallel to the rotor does not occur.

Eventually the mass of the propeller hub and shaft are estimated using empirical relationship [47]. The mass of the blades have been estimated to be 110.6 kg applying a mass reduction factor of 15% for use of composites. The materials chosen for the propeller, in fact, have been selected using the CES Software [9]. Epoxy glass fiber honey comb is going to be used for the core, while Polymide carbon fiber woven prepreg has been selected for the blades cover. For what concerns the hub and shaft, their mass has been estimated to be 205.9 kg applying a mass reduction factor of 15 % for the use of new technology [47]. The materials chosen for these components, in fact, were chosen to be Titanium Ti-6Al-4V; this material was chosen since it represents the new frontier in terms of material for what concerns propeller hubs and shaft [9].[10] Coatings applied to the above mentioned components should be applied in order to take allow their use close to marine environments.

Conclusion

The approach behind the wing sizing was to first select the best airfoil for the mission (given some fixed parameters) that is the NACA23018 and then, around it design the entire wing that has an area of 21 m^2 (including high-lift devices). The same was done for the fuselage; in this case, the airfoil selected was the NACA25121. The fuselage design and sizing, even if innovative, was performed in function of the cabin's requirements and comfort. The operational envelope of Futura has a positive load factor of 3.8. The rotor design was optimised to achieve a power plant system mass of 1132.4 kg. This value was obtained with a rotor solidity of 0.02, and a linear twist with a twist 18.3° at the root, and 0° at the tip.

[10]URL `https://patents.google.com/patent/US6139659` [cited 18 June 2019]

6. Power Plant

The power plant goal is to deliver the necessary power and energy for the correct functioning of Futura. The innovative hybrid nature implicates challenges that have been overcome by choosing readily available and reliable components. This chapter aims to analyse the structure of the power plant system, highlight the technology used and perform a reliability test on both the component and system level.
To enhance the short term delivery of the product, the team focused on finding readily available components to be implemented in the system. However, for some components, this was not possible due to the particular nature and rating required. More precisely, components like the radiators, fuel tank and battery pack have been designed or sized in-house to meet performance requirements.

6.1 System Overview

The system consists of three main components: fuel cell, battery and electric motors. The fuel cell and the battery provide the necessary power for the system to work while the electric motors convert the electric energy in mechanical energy to spin the rotors and allow the aircraft to fly. The energy consumed by the fuel cell is stored under liquid hydrogen (LH_2) form while for the batteries it is stored internally as chemical energy. To connect the power units to the electric motor, a power electronics system is used as seen in Figure 6.12. This subsystem is needed to match voltage levels of different components as well as turn DC power to 3-phase AC power for the motors. The fuel cell also needs a compressor that provides oxygen from the outside air for the chemical reaction with hydrogen to produce electrical power. Finally, radiators are used to reject the waste heat produced by the system to the outside air. A conceptual layout can be seen in Figure 6.1.

6.2 Radiators

One of the crucial aspects of the power plant is the need for cooling. On the contrary of traditional aero-engines that can withstand the operating temperature of several hundred degrees, fuel cell electric propulsion systems have operating temperatures around 90°C. This temperature is determined by the operational limits of the polymer membrane in the fuel cell, of the electric motors and the batteries [50–52]. To remove the heat that is produced by the operation of these components, a cooling fluid absorbs the heat flowing through the component and then rejects it to the outside air flowing through radiators. In the next sections, the sizing of the radiators needed to reject the heat produced by the systems will be presented.

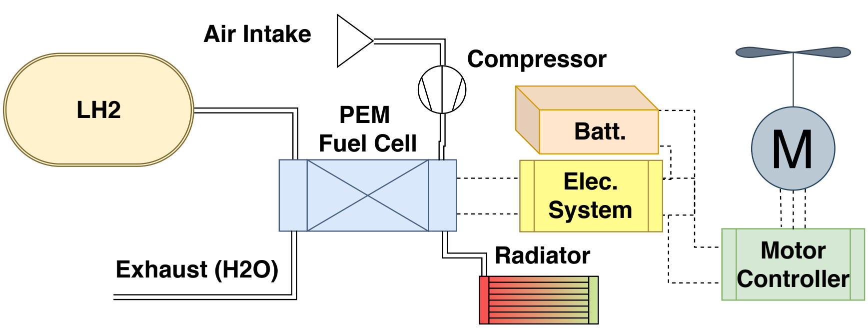

Figure 6.1: Power plant layout.

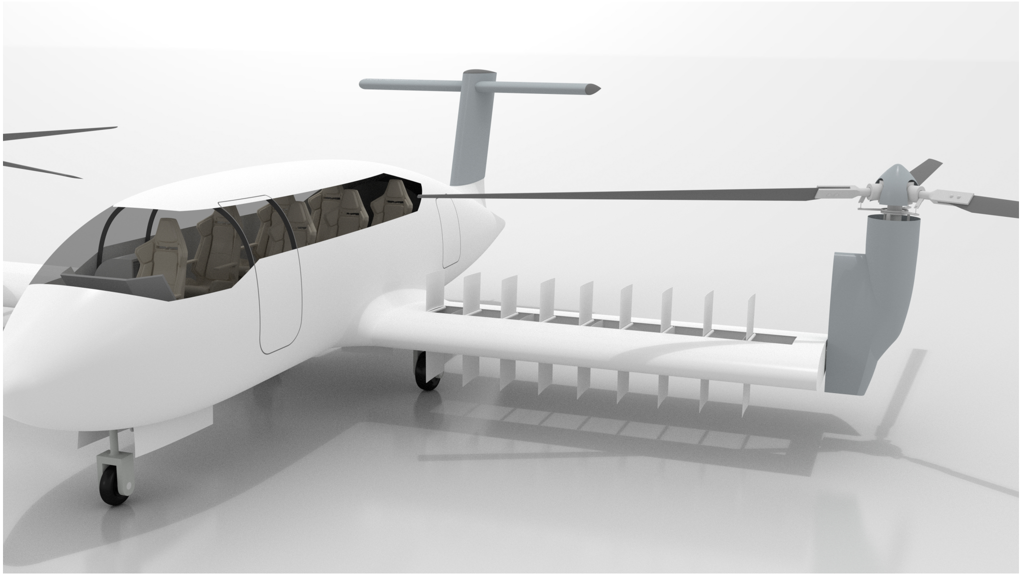

Figure 6.2: Radiator operation at take-off.

6.2.1 Design Parameters and Layout

As radiators need a high mass-flow of air to pass through them to absorb the heat from the coolant, it was decided to place the radiators in the wing to make use of the energetic rotor wake flow. In hover, the wing upper and lower skin within the central section opens up as shown in Figure 6.2. This allows for the rotor wake to flow through the radiators which are placed horizontally in the wing. In cruise, a ram-air inlet in the bottom of the wing allows for the rotor wake to be again redirected through the radiators to cool the system.

The design boundaries of the radiator assembly can be summarised in the following:

- The radiator shall be thin enough to allow air flow between the radiator itself and the wing skin
- The aircraft shall operate at peak power without overheating
- The aircraft shall operate at the boundaries of the operational atmospheric temperature regime without overheating nor freezing

From these requirements, it follows that the outside air temperature considered for the sizing is 50°C while the operating temperature has to remain below 90°C even at peak power. Initially, ethylene glycol was considered as a coolant in a 50/50 solution with water as it is a conventional coolant in industry and remains liquid form up to -37°C which is right at the boundary of the operating atmospheric temperature. As ethylene glycol is toxic the team decided to use a propylene glycol 50/50 solution that has a freezing point of -34°C but the same thermal properties of ethylene glycol 50/50 (specific heat = 3.559 $\mathrm{kJkg^{-1}{}^{\circ}C^{-1}}$).[1,2] Finally, from BEMT, the wake calculated to be 15 $\mathrm{ms^{-1}}$.

6.2.2 Radiator Sizing Calculations

To size the radiator the overall heat transfer coefficient (HTC) needs to be found. This coefficient expressed in $\mathrm{W{}^{\circ}C^{-1}}$ represents how much heat can be rejected by a radiator given a certain temperature difference between the coolant and flow of air. It is dependent on flow speed of both the coolant as well as the air. Contacting the company Nederlandse Radiateuren Fabriek (NRF) a radiator that fitted the needs of Futura has been selected. The radiator has an overall heat transfer coefficient, at an air flow of v_{air}=15

[1]URL `https://pubchem.ncbi.nlm.nih.gov/compound/1_2-Ethanediol#section=Reported-Fatal-Dose&fullscreen=true` [cited 23 June 2019]
[2]URL `https://www.engineeringtoolbox.com/propylene-glycol-d_363.html` [cited 23 June 2019]

ms^{-1} and a coolant flow of 37.5 $Lmin^{-1}$, of 1875 $W°C^{-1}$ (Anton van Berkel, Application Engineer NRF, personal communication, June 17). The remaining specifications of the radiator can be found in Table 6.1.

Table 6.1: NRF radiator characteristics.

HTC	l	w	t	m	v_{air}	$dotV_{cool}$
1875 $W°C^{-1}$	1.45 m	0.375 m	0.112 m	26.15 kg	15 ms^{-1}	37.5 $Lmin^{-1}$

The heat load at take-off can be calculated with Equation 6.1. From the heat load, the number of radiators can be calculated using Equation 6.2 rounding up to the nearest integer.

$$Q = P_{FC} \cdot \frac{1-\eta_{FC}}{\eta_{FC}} + P_{EM} \cdot \frac{1-\eta_{EM}}{\eta_{EM}} + P_B \cdot \frac{1-\eta_B}{\eta_B} \quad (6.1)$$

$$N_{rad} = \frac{Q}{HTC \cdot (T_{cool} - T_{air})} \quad (6.2)$$

When cruise conditions are considered, one can calculate the required mass-flow through the radiators in terms of the ratio of heat loads, as shown in equation Equation 6.3. Finally, the required inlet area can be derived from mass conservation (Equation 6.4) using the mass-flow found previously and the rotor wake speed at a cruise from BEMT.

$$\dot{m}_{air} = \frac{Q_{cruise}}{Q_{hover}} \cdot (v_{air} \cdot A_{rad} \cdot \rho_{air}) \quad (6.3)$$

$$A_{inlet} = \frac{\dot{m}_{air}}{v_{wake} \cdot \rho_{air}} \quad (6.4)$$

6.2.3 Results

From the BEMT and the fuel cell-battery integration optimisation algorithm, the power values as seen in Table 6.2 have been calculated with the resulting heat loads.

Table 6.2: Heat loads at different phases.

	FC	Battery	E. Motor	Total Peak	F.C.	Battery	E. Motor	Total Cruise
P [kW]	343	764.6	1107	-	240.1	87.5	327.6	-
Q [kW]	371.58	31.85	46.13	449.56	260.11	3.65	13.65	277.32

This results in need of 6 radiators at hover (3 per half wing) with a total radiator weight of 156.9 kg. To this value the amount of coolant has to be added that, given an internal volume of the radiator assembly of 0.0438 m^3 and a coolant density of 1000 kgm^{-3}, was calculated to be 43.8 kg.[3] Finally, a pump is needed to provide a total volumetric flow of 225 $Lmin^{-1}$. The Miksan Motors EP 250 Pump has been selected weighing 15 kg [53]. The final radiator assembly weight is thus 215.7 kg.
In cruise condition, the heat load reaches 277.32 kW which means that a mass-flow of 6.16 kgs^{-1} (Equation 6.3) is required to cool the system. From mass conservation (Equation 6.4) the inlet area needed can be calculated and was found to be 0.073 m^2 for cruise conditions (v_{wake}=100 ms^{-1}, ρ=0.85 kg at 2000 m and 37°C).

6.3 Fuel Tank Sizing

The fuel tank is a significant component of the aircraft as it should contain the fuel for the mission, deliver it to the power plant and allow for easy refuelling. It is also a critical component as it uses liquid hydrogen, entailing cryogenic working temperatures and high flammability hazards. These negative aspects come with a higher volumetric specific energy than gaseous hydrogen, which would take up too much space in the fuselage.

[3] URL `https://www.engineeringtoolbox.com/propylene-glycol-d_363.html` [cited 23 June 2019]

6.3.1 Design Parameters and Layout

Operational Constraints

To allow for a short range round-trip from an operational base running on the same fuel tank, the maximum time without refuelling is set as the time of two short flights ($2 \cdot 30\text{min}$) plus the turn-around time (60min), giving $\tau_{\text{max}} = 120\text{min}$.

From the operations of the aircraft, the working conditions can be determined. Negative temperatures, most likely encountered at cruise, are beneficial for thermal control of the tank. All the same, the highest operational temperature is used as critical case, being $T_{amb} = 50°\text{C}$.

The tank operational lifetime is set equal to that of the aircraft, i.e., 30 years with up to 11 flights per day or $1.2 \cdot 10^5$ cycles. This is because the replacement of the tank throughout the operations of Futurawould require the removal of structural members, a process deemed unsatisfactory for easy maintenance.

Properties of LH2

To minimise volume, saturated liquid hydrogen (LH_2) is used. Due to heat input from the environment, evaporation will occur, and the pressure will rise. To avoid overpressurisation for structural reasons, gaseous hydrogen (GH_2) will be vented. That being said, some GH_2 should always remain in the tank to allow for instantaneous pressure relief. GH_2 will also be supplied to the fuel cell. However, the strict requirement on time without refuelling does not allow for enough heat flux input to create the required GH_2 flow rate. LH_2 will thus be heated up by the fuel cell coolant through a liquid-two phase heat exchanger to be the primary fuel source for the fuel cell. This component will be sized at a later stage of the design, as regarded as not critical for the initial conceptual design.
A recommended liquid/gas fraction from literature is $97\%/3\%$ at maximum pressure [54]. The operating maximum pressure should be the pressure above which gas is vented, p_{vent}, and remain as low as possible to decrease the structural mass and tank volume [54]. It is set just above the fuel cell's maximum fuel pressure ($p_{FC} = 2.3\text{bar}$) at $p_{vent} = 2.5\text{bar}$ to ensure that there is a flow between the two. The lowest pressure in the tank, on the one hand, should correspond to the filling pressure p_{fill} therefore allowing for a pressure rise (to p_{vent}) due to an external heat input [55]. On the other hand, it should be higher than the ambient pressure at sea level ($p_{\text{SL}} = 1.0\text{bar}$) to prevent air from getting in the tank and avoid creating an explosive mixture, therefore set at $p_{fill} = 1.2\text{bar}$.

Allowances

Some allowances should be added both to the fuel weight and tank volume. According to Dr. B. Atli-Veltin, expert on cryogenic storage systems from TNO, the tank filling should remain between $f_{\text{min}} = 15\%$ and $f_{\text{max}} = 85\%$ to prevent air from entering the tank and avoid overpressurisation (personal communication, May 29, 2019). On top of this, $c_1 = 5\%$ of the fuel mass is allowed to be vented. A compromise for this value was found between a lower insulation mass (high venting ratio) and a higher tank volume and higher operational costs (low venting ratio). With this value, the refuelling costs remained lower than that of a kerosene aircraft (section 4.3). Additional allowances are taken into account, namely $c_2 = 0.9\%$ and $c_3 = 0.6\%$ of the volume to account for tank contraction due to cooling and space needed for equipment inside the tank, respectively [55].

Shape and Location

For safety concerns developed below, the tank is placed at the very back of the fuselage. Because of the airfoil shape of the fuselage, the height at the back was too low for a spherical tank. To minimise structural weight, the shape was chosen to be as close to a spherical tank as possible with hemispherical ends, yielding a shape factor of $\lambda = 0.6$, defined as the cylinder length to hemisphere radius.

Layout and Materials

For cryogenic hydrogen storage in warm environments, the most weight-efficient layout was found to be a double tank between which near-vacuum environment is created [56, 57]. Because of the near-zero pressure in between, the inner shell bears the internal pressure of the hydrogen while the outer one only resists the external atmospheric pressure. The near-vacuum space is occupied by a Multi-Layer Insulation that ensures low radiation and conduction heat transfers. A different layout with only one inner shell and spray-on foam was found with preliminary calculations to provide a lighter design but could not bear the high heat flux exposure ($50°\mathrm{C}$ environment for $120\mathrm{min}$).

Common materials used in such pressure vessels are metals including stainless steel and aluminium. It was found in the design process that the higher density of steel outweighs its advantages in terms of fatigue, thus yielding a lower structural weight when using aluminium. This was also confirmed in literature, which proposes to use aluminium 2024 in particular for its low density and cost (compared to other alloys) [58]. Using a worse-case scenario, the fatigue limit with a stress ratio of -1 at $1.2 \cdot 10^5$ cycles is found to be $\sigma_{\mathrm{al2024}} = 176\mathrm{MPa}$ [9]. Other properties include a Young's Modulus of $E_{\mathrm{al2024}} = 72.0\mathrm{GPa}$, a Poisson ratio of $\mu_{\mathrm{al2024}} = 0.337$, a density of $\rho_{\mathrm{al2024}} = 2855\mathrm{kgm}^{-3}$ [9]. While some of these properties improve when exposed to cryogenic temperatures, a worse-case scenario with room temperature was used [59]. Innovative materials such as epoxy-based Carbon-Fibre-Reinforced-Polymer CFRP have shown potential weight savings, despite a more difficult End-of-Life (EOL) process. Due to the uniform load distribution, a quasi-isotropic lay-up is preferred. With a fatigue performance in the aforementioned conditions 72% higher ($\sigma_{CFRP} = 478\mathrm{MPa}$ under compression-compression cycles [60]) and a density 46% lower than Al-2024 ($\rho_{CFRP} = 1540\mathrm{kgm}^{-3}$), it performs extremely well in tensile conditions (i.e. for the inner shell). On the other hand, its Young Modulus is 39% lower than Al-2024 ($E_{CFRP} = 44.2\mathrm{GPa}$) and its Poisson ratio of $\mu_{\mathrm{CFRP}} = 0.27$ make it worse-performing under compression (i.e. for the outer shell) [9]. Due to the high permeability of CFRP, an aluminium liner is applied in contact with LH_2, with a typical thickness being $t_{\mathrm{liner}} = 0.635\mathrm{mm}$ [61, 62].
A comparison between three designs is carried out to investigate whether the weight savings are considerable enough to favour a material with a less sustainable EOL solution. *Design 1* has both shells made of CFRP, *Design 2*'s inner shell is made of CFRP while the outer one is made of Al-2024, and *Design 3*'s two shells are made of Al-2024. A conservative safety factor of $SF = 2$, according to a NASA report on cryogenic hydrogen storage, is used [63]. Because the fatigue behaviour of composites is less well-known, the safety factor for CFRP is increased to $SF = 3$ based on experience from a composite material expert (Dr. C. Rans, personal communication, June 12, 2019).

Compartment

LH_2 molecules are tiny, and there exists a risk that they pass through tiny cracks of the material (permeability) or leaks at connections [64]. While this fluid quantity is expected to be extremely low, a mitigation measure is found by isolating the tank. It is located in an air-tight compartment at the back of the fuselage. This ensures that if hydrogen is released outside the tank, it does not reach the cabin.

If the hydrogen volume content exceeds $v_{\%\mathrm{LH}_2} = 4\%$, combustion with air can occur with an extremely small input energy [65]. To avoid this, the hydrogen volume content is monitored at all times by an optical fibre sensor that can detect concentration levels below the lower flammability limit [66]. Because of the absence of electricity in the sensor, sparks risks are eliminated. When a critical level is reached, set at $v_{\%\mathrm{LH}_2} = 1\%$, air in the compartment is evacuated and renewed by way of two electrically-powered openings placed at the top and bottom of the compartment. From the lifting body fuselage shape, air at the bottom naturally flows through the compartment and reduce $v_{\%\mathrm{LH}_2}$ to exit at the top due to the pressure difference. The small actuators are located in insulated boxes to reduce spark risks. When operating the aircraft without airspeed (i.e. take-off, landing, ground operations), the margin in the critical hydrogen volume content provides enough time for an emergency landing and evacuation of the aircraft. This is because this type of hydrogen release is a prolonged process. An representation of this system is shown in Figure 6.5.

Due to the tank proximity to the warm-body of the fuel cell, heat transfer warming up the tank and evaporating hydrogen may occur. To reduce this, a Multi-Layer Insulation panel between the two compartments is placed. Because an ambient temperature of $T_{amb} = 50°\mathrm{C}$ is used for the tank thermal design, the heat transfer from the fuel cell can be neglected.

Verification

Hand calculations checked the algorithm for tank design for single input values of mission fuel. Stability was tested by changing slightly the input value. When the mission fuel was increased 5%, the structural mass of the tank increased only by 3.6%.

6.3.2 Inner Shell Structure

For the inner shell, the fuel volume is determined by applying the allowances on top of the required mission fuel volume ($m_{\text{fuel}} = 13.59\mathrm{kg}$, as determined in the next section). The lowest density is encountered at the maximum pressure p_{vent} and found from interpolation with for the corresponding liquid-gas mixture at $\rho_{\text{LH}_2,\text{min}} = 46.35\mathrm{kgm}^{-3}$. This gives a required tank volume V_{rq} as seen in Equation 6.5.

$$V_{\text{rq}} = \frac{m_{\text{fuel}}}{\rho_{\text{LH}_2,\text{min}}(1-c_1)(1-c_2-c_3)(f_{\text{max}}-f_{\text{min}})} \tag{6.5}$$

From this volume and the shape factor, the tank's radius r_{in} is easily found. The required inner shell thickness can be determined both the the cylinder (t_{cyl}) and the hemispherical ends (t_{hem}) in Equation 6.6 and Equation 6.7 respectively, according to the American Society of Mechanical Engineers (ASME) Boiler & Pressure Vessel Code Section 8, Division 1 [15]. It is an internationally-recognised industry standard on pressure vessel structural design.

$$t_{\text{cyl}} = \frac{p_{vent} \cdot SF \cdot r_{in}}{w \cdot \sigma - 0.6 \cdot p_{vent} \cdot SF} \tag{6.6}$$

$$t_{\text{hem}} = \frac{p_{vent} \cdot SF \cdot r_{in}}{2 \cdot w \cdot \sigma - 0.2 \cdot p_{vent} \cdot SF} \tag{6.7}$$

The welding efficiency for Al-2024 w is conservatively assumed to be 0.8 according to the ASME code, while for CFRP w is equal to one due to the absence of joints (filament winding is used) [15]. No corrosion allowance has been added as the tank is located in an isolated compartment, thus not in direct contact with a marine environment. For both materials, the corresponding fatigue limit σ is used, and for CFRP, a non-structural Al-2024 liner is added before the inner shell.

6.3.3 Sub-Components

Before the thermal design is performed, the sub-components that will create heat conduction from the inner shell to the outer shell have to be sized. This includes pipes to transfer fuel and supports to transfer the inner shell weight to the outer shell.
Piping should allow for venting, tank refuelling and fuel delivery. As venting and fuel delivery are done with the gaseous and the liquid part respectively, two pipes are required at least. For the absence of moving parts and the structural reinforcement around them, the pipes are not expected to fail, therefore allowing for a non-redundant design. To minimise the high heat transfer by conduction of the metal pipes and the weight of the insulation, only two pipes are used. Their inner diameter is dependent on the equipment they are connected to, discussed below.

Venting

Venting, required to avoid overpressurisation, is performed by a safety valve located at the top of the tank that is self-activated when p_{vent} is reached. Because it is a critical safety mechanism and it contains moving part (a spring), a redundant safety valve is added on a Y-shaped junction. Herose's type 06001 safety valve suitable for cryogenic applications is selected, with orifice size $d_{\text{vent}} = 10\text{mm}$ and discharge coefficient $c_d = 0.5$ [67]. The inner diameter of the pipe corresponds to the orifice size to maximise the exit mass flow rate, calculated in Equation 6.8. The required power to evaporate liquid hydrogen and match this flow rate is calculated in Equation 6.9 with h_{fg} being the hydrogen latent heat of vaporisation.[4]

$$\dot{m}_{\text{vent}} = c_d \cdot \rho_{\text{GH}_2} \cdot \pi \cdot \frac{d_{\text{vent}}^2}{4} \cdot \sqrt{\frac{2(p_{vent} - p_{amb})}{\rho_{\text{GH}_2}}} \quad [68] \tag{6.8}$$

$$\dot{Q}_{\text{vent,max}} = \dot{m}_{\text{vent}} \cdot h_{\text{fg}} = 26.6\text{kW} \tag{6.9}$$

This means the valve cannot cope with heat flux inputs higher than 26.6kW, corresponding to the power of a large electrical heater.[5] As the tank will be placed in an insulated compartment, such high heat flux inputs are not expected to occur within the operations of Futura.

Refuelling and Fuel Delivery

For refuelling and fuel delivery, a 2-way normally-closed solenoid valve is fitted at the bottom of the tank to carry LH_2. As it contains electrical components, it is placed in a containment box to reduce the risk of sparks. The selected valve is Valcor's all-welded high-reliability cryogenic V44700 valve [69]. A redundant valve is placed in parallel in case one fails to open, for the aforementioned safety reasons. Downstream of these two valves, two other identical valves are placed at the refuelling port and the connection with the fuel cell, respectively. This creates more redundancy, this case if one valve fails to close. This valve type has a large orifice of $d_{\text{fuel}} = 10\text{mm}$ which allows for the refuelling and delivery flow rate shown in Equation 6.10 and Equation 6.11, assuming a discharge coefficient identical to that of the safety valve.

$$\dot{m}_{\text{refuel}}(p_{sta}, p_{vent}) = 1.04 \cdot 10^{-1}\text{kgs}^{-1} \tag{6.10}$$

$$\dot{m}_{\text{FC}} = (p_{vent}, p_{FC}) = 8.05 \cdot 10^{-2}\text{kgs}^{-1} \tag{6.11}$$

Where the flow rates are calculated according to Equation 6.8, using the mentioned variables in their order of appearance in the formula. The refuelling station storage pressure and the fuel cell maximum fuel pressure are equal to $p_{sta} = 3\text{bar}$ and $p_{FC} = 2.2\text{bar}$ respectively [70, 71]. This satisfies the maximum station delivery of $2.78 \cdot 10^{-2}\text{kgs}^{-1}$ and the required maximum fuel cell fuel consumption of $\frac{P_{\text{max}}}{\text{SE} \cdot \eta_{FC}} = 5.40 \cdot 10^{-3}\text{kgs}^{-1}$ [70].

The refuelling port is designed to be compatible with the recharging station of Futura manufactured by Linde [70]. A quick air-tight coupling system produced by Walther Praezision in cooperation with Linde exists for GH_2 [72]. For safety purposes, an inline safety break-away from Staubli is added to the refuelling connection, in case the refuelling nozzle is accidentally disconnected, and the port does not close automatically [73]. These parts will be modified in cooperation with the producer to work with LH_2 and cryogenic temperatures in particular. It will comply with the international standard ISO $13984:1999$ on liquid hydrogen refuelling, to ensure compatibility with different stations [74].

Pipe Structure and Reinforcement

The inner diameter of both pipes, identical, has been determined from the venting and the fuel flow requirements. Their material is chosen to be austenitic stainless steel 304, commonly used for cryogenic piping applications due to its thermal conductivity being lower than aluminium ($\lambda_{\text{steel}} = 8.43\text{Wm}^{-1}\text{K}^{-1}$) [57, 75]. The thickness calculated according to Equation 6.6 yields an un-manufacturable pipe ($t_{\text{pipe}} = 1.36 \cdot 10^{-2}\text{mm}$), therefore a more conservative thickness of $t_{\text{pipe}} = 1\text{mm}$ is used. To minimise heat

[4]URL `/www.engineeringtoolbox.com/fluids-evaporation-latent-heat-d_147.html` [cited 15 June 2019]
[5]URL `masterwatt.nl/product/calida-high-power-30-kw` [cited 15 June 2019]

conduction, the pipes are extended by a quarter of the tank circumference so that they exit at the half height of the tank. The added material will be located within the insulation material of the tank, between the inner and outer shells. Due to their small size, the compression effect on the insulation material is neglected.

The pipe's holes create stress concentration both in the inner and outer shells. To compensate this, the removed material is relocated within an effective boundary of the hole, as prescribed in the ASME Code [15]. A schematic representation is shown in Figure 6.3.

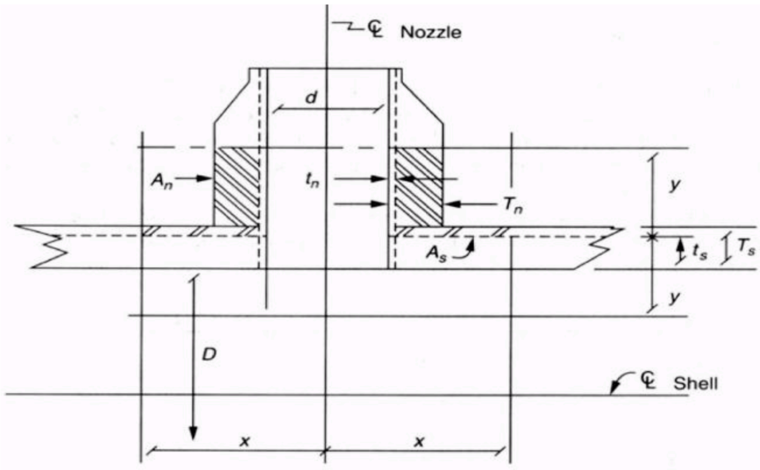

Figure 6.3: Structural reinforcement around hole in pressure vessel [76].

The shell reinforcement thickness T_s is constrained to $T_s = t_s + 2\text{mm}$ with t_s being the original shell thickness. This is to limit the compression of the insulation material, which becomes ineffective when heavily compressed. The nozzle reinforcement thickness T_n is found by solving Equation 6.12, Equation 6.13 and Equation 6.14, with variables are defined in Figure 6.3. This is done both for the inner and outer shells, of which the latter's design is explained further below.

$$A_s = max\left\{\ d(T_s - t_s) - 2\cdot T_n(T_s - t_s),\quad 2(T_s + t_n) - 2\cdot t_n(T_s - t_s)\ \right\}[15] \tag{6.12}$$

$$A_n = min\left\{\ 2\cdot\frac{5}{2}\cdot T_s(T_n - t_n),\quad 2\cdot\frac{5}{2}\cdot T_n(T_n - t_n)\ \right\}[15] \tag{6.13}$$

$$A_s + A_n \geqslant t_s \cdot d[15] \tag{6.14}$$

The nozzle reinforcement thicknesses T_n is found to range between 1.20mm and 1.65mm for depending on the inner shell material. The effective reinforcement boundaries x and y as defined in the ASME code are found to range from 1.00mm to 4.13mm. For the outer shell, the reinforcements are located on the inside to ensure a smooth external surface, while reinforcements of the inner shell are located on its outside. It is checked that the nozzle reinforcement boundaries fit within the insulation space, described further below.

Despite the reinforcement, the piping connection is foreseen to be the tank's structural weakest part due to the shape irregularity. Since the outlets are located at the back of the tank (as seen from the nose), a catastrophic tank failure would lead to a hydrogen release directed to the back. This ensures a higher level of safety, as it would not be directed towards the cabin.

Supports

The weight of the inner shell and the fuel cannot be supported by the insulation material to avoid reducing its insulation properties. Therefore, lightweight G-10 (fiberglass epoxy laminate) supports are used as suggested in literature [77]. This material is chosen for its low thermal conductivity ($\lambda_{\text{G10}} =$

$0.288\mathrm{Wm^{-1}K^{-1}}$) and low density ($\rho_{G10} = 1800\mathrm{kgm^{-3}}$) [78]. To constrain the motion of the shells relative to each other in all directions, 8 flat cylindrical supports are added, with diameter $d_{G10} = 40\mathrm{mm}$ and thickness $t_{G10} = 15\mathrm{mm}$ taken from a similar cryogenic tank design [79]. Despite the different weights, due to the high number of supports this structural member is deemed overdesigned. At a later stage of the design, their dimensions would be further refined.

6.3.4 Thermal Design

The thermal design drives the general design of the tank due to the cryogenic working temperature. As suggested in literature, an evacuated Multi-Layer Insulation (MLI) is used to minimise weight and space, against having vacuum alone or foam. This is also the most sustainable option, as the layer can be separated and its metal recycled, while foams are hardly recyclable. One MLI layer is composed of a fibreglass paper to reduce heat transfer through conduction and an aluminized mylar polymer film which diminishes radiation heat transfer. Because it is evacuated, a near-vacuum environment at $p_{ins} = 1.33 \cdot 10^{-10}\mathrm{MPa}$ is reached which brings convection heat transfers to a negligible level [57]. An uncompressed layer density of $N = 20$ layer $\mathrm{cm^{-1}}$ (i.e. $t_{layer} = 5.00 \cdot 10^{-2}\mathrm{cm}$) for weight efficient a MLI with average density $\rho_{MLI} = 140\mathrm{kgm^{-3}}$ is used [57]. The emissivity of the aluminised mylar polymer film at the critical temperature is estimated to be $e_{myl}(T_{amb}) = 3.10 \cdot 10^{-2}$ [80]. The solid conductance of the fibreglass paper is $h_s = 8.5110^{-2}\mathrm{Wm^{-2}K^{-1}}$ [57]. The compression effects from small difference in thickness between the hemispherical ends and the cylindrical section are neglected. This is because the thermal properties of MLI remain largely unaffected by such small variations [57].

The allowed incoming heat transfer rate $\dot{Q}_{allow}$ to the tank can be found from operational constraints as shown in Equation 6.15. Unlike $\dot{Q}_{vent,max}$, $\dot{Q}_{allow}$ is the heat flow allowed for normal operations which only leads to the evaporation and the waste of $c_1 = 5\%$ of the fuel. Temperature boundaries are set as worse-case scenario, namely $T_{amb} = 50.0°\mathrm{C}$ and $T_{LH2} = -250°\mathrm{C}$. $\dot{Q}_{allow}$ should equal the heat flow transferred through conduction and radiation are in function of the number of layers n, which is solved iteratively.

$$\dot{Q}_{allow} = \dot{Q}_{cond}(n) + \dot{Q}_{rad}(n) = c_1 \cdot \frac{m_{fuel} \cdot h_{fg}}{\tau_{max}}\mathrm{W} \tag{6.15}$$

Conduction Heat Transfer

Conduction through the MLI is calculated in Equation 6.16.

$$\dot{Q}_{MLI,cond} = (T_{amb} - T_{LH2})\frac{A_{m,sphe} + A_{m,cyl}}{n \cdot t_{layer}} \cdot \frac{1}{N}(h_s + \frac{\sigma_{SB} \cdot e_{myl} \cdot {T_{amb}}^3}{2 - e_{myl}}(\frac{T_{LH2}}{T_{amb}})^2(1 + \frac{T_{LH2}}{T_{amb}})) \quad [81] \tag{6.16}$$

$A_{m,sphe}$ and $A_{m,cyl}$ are the conduction shape factors of the respective parts calculated according to Barron and Nellis [81]. The conduction through sub-components, pipes and supports, is shown in Equation 6.17.

$$\dot{Q}_{sub\text{-}c.,cond} = (T_{amb} - T_{LH2})(\lambda_{steel}\frac{A_{pipe}}{\frac{\pi}{2} r_{cyl}} + \lambda_{G10}\frac{A_{support}}{n \cdot t_{layer}}) \quad [56] \tag{6.17}$$

A and λ represent the cross-sectional area and the thermal conductivity of both components, respectively.

Radiation Heat Transfer

The radiation heat transfer through the MLI is calculated according to Equation 6.18.

$$\dot{Q}_{\text{MLI,rad}} = (T_{amb}{}^4 - T_{LH2}{}^4) \cdot \sigma_{SB} \cdot S_{\text{in}} \cdot F \cdot \frac{1}{\frac{2 \cdot n}{e_{myl}} - n - 1 + \frac{1}{e_{\text{in}}} + \frac{1}{e_{\text{out}}}} \quad [81] \tag{6.18}$$

e_{in} and e_{out} are the emissivities of the inner and outer shell material respectively ($e_{\text{al2024}} = 0.70$ if unpolished and $e_{\text{CFRP}} = 0.88$) [82, 83]. S_{in} is the inner shell surface area and F the view factor, equal to 1 as the layers are approximately constant in size.[6]

The number of layers n is found iteratively by solving Equation 6.15, Equation 6.16, Equation 6.17 and Equation 6.18 simultaneously. The thickness of the insulation is defined as $t_{\text{ins}} = n \cdot t_{\text{layer}}$.

6.3.5 Outer Shell Structure

The outer shell bears atmospheric pressure from the outside while the inner vacuum exerts no force on it. The highest atmospheric pressure occurs on the ground, conservatively assuming $p_{amb} = 1.2\text{bar}$. Note that this pressure coincidentally equal p_{fill}, while this will never be the case in real life given that $p_{\text{SL}} = 1.0\text{bar}$. The required shell thickness can be found from the critical buckling pressure p_{amb} iteratively with the Windenburg and Trilling Equation in Equation 6.19, and from Timosenko and Gere in Equation 6.20.

$$p_{amb} \cdot SF = \frac{2.42 \cdot E\left(\frac{t_{\text{cyl}}}{d}\right)^{\frac{5}{2}}}{(1-\mu^2)^{\frac{3}{4}} \left(\frac{L_{\text{cyl}}}{d} - 0.45 \left(\frac{t_{\text{cyl}}}{d} \right)^{\frac{1}{2}} \right)} \quad [84] \tag{6.19}$$

$$p_{amb} \cdot SF = \frac{2 \cdot E\left(\frac{t_{\text{hem}}}{d}\right)^2}{(3(1-\mu))^{\frac{1}{2}}} \quad [85] \tag{6.20}$$

In the equation, d is the outside diameter and L_{cyl} the cylinder length. It is assumed that the cylinder is simply supported at both ends by the G-10 supports.

6.3.6 Configuration Choice

A weight comparison between the three designs configurations is shown in Table 6.3. A useful mission fuel of 13.6kg is used (14.3kg when adding vented fuel, and 18.7kg when counting for the unused fuel f_{min}), from the value shown in the next section.

Table 6.3: Weight comparison of three tank designs. The green column is the selected design.

Component	Design 1	Design 2	Design 3
Inner shell	CFRP + Al-2024 liner	CFRP + Al-2024 liner	Al-2024
Insulation	MLI	MLI	MLI
Outer shell	CFRP	Al-2024	Al-2024
Total Structural Mass [kg]	23.4	19.4	25.8

Table 6.4: Weight breakdown for the selected design.

Component	Mass [kg]
Inner shell	7.54
Insulation	4.33
Outer shell	13.8
Supports, internal pipes	0.11

Although the lightest design corresponds to the hybrid CFRP-Al-2024 *Design 2*, the 25% weight saving compared to *Design 3* is not deemed sufficient against its disadvantage regarding its less sustainable EOL solution. As it will be seen in chapter 9, the MTOW allows for this small weight increase. The weight break down for the selected design is shown in Table 6.4. With the conceptual design, the thermal expansion/contraction was calculated to be less than 10^{-4}m.

[6] URL `https://www.dspe.nl/knowledge-base/thermomechanics/chapter-1---basics/1-2-heat-transfer/radiation/` [cited 21 June 2019]

Layout

The different shell thicknesses are shown in Figure 6.4 and the layout with sub-components in Figure 6.5. The outer diameter of the tank is equal to $d = 867\,\mathrm{mm}$ and its total length is $L = 1.12\,\mathrm{m}$.

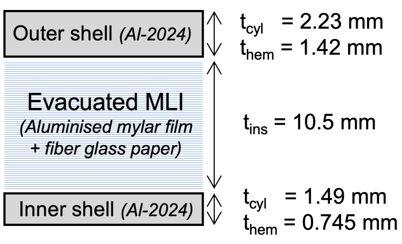

Figure 6.4: Tank structure.

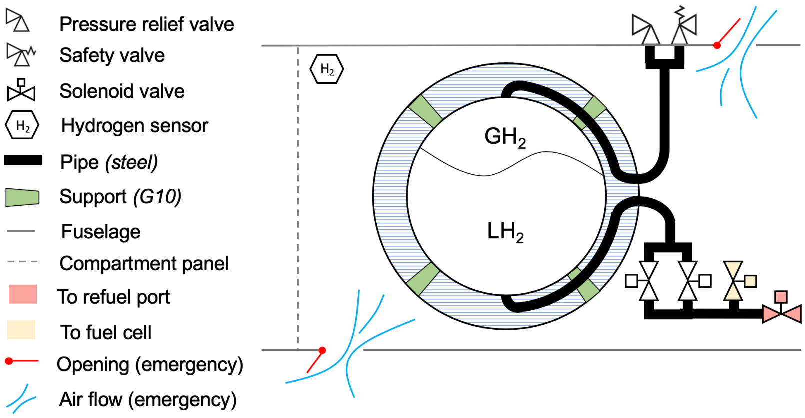

Figure 6.5: Tank sub-components layout.

6.3.7 Validation

Firstly, validation of the design was performed by comparing the tank structural mass to fuel mass ratio of another liquid hydrogen tank for aircraft applications, where a ratio $\frac{m_{\text{tank}}}{m_{\text{fuel}}} = 1.56$ was found by Ball Aerospace [86]. Futura's ratio, equal to $\frac{m_{\text{tank}}}{m_{\text{fuel,mission}}} = 1.92$, is 23% higher most likely due to the non-spherical shape and the more constraining thermal requirements. The thickness of the walls, ranging from $0.724\,\mathrm{mm}$ to $2.16\,\mathrm{mm}$, are found to be similar to other cryogenic tank designs found in literature and are all manufacturable [57, 58, 87]. These comparisons validate that this tank structural design corresponds to industry standards.

6.4 Components Choice

Given the design of the radiators and fuel tank, it is possible to construct the rest of the power plant system. In this section, which components and how they have been chosen is explained. This is the outcome of a double optimisation process on component choice and its integration with batteries.

6.4.1 Optimisation Goals

One of the main challenges of equipping Futura with hydrogen fuel cells was to meet the peak power demand. Fuel cell systems that run on hydrogen have the great advantage to be energy dense. This occurs because hydrogen stores about 142 $\mathrm{MJkg^{-1}}$, more than 3 times as much as jet fuel.[7] On the other hand, for the same power requirement, a fuel cell system weights more than more conventional counterparts as jet engines. This occurs due to the relatively slow rates of reduction and oxidation that can be achieved when compared to more conventional energy conversion methods based on ignition or explosion. Table 6.5 shows a comparison of the average specific energy and power of fuel cell systems, and $LiFePO_4$ batteries [52, 71, 88] and highlights how fuel cells systems having a relatively low specific power compared to batteries but a much higher specific energy.

[7]URL `https://www.engineeringtoolbox.com/fossil-fuels-energy-content-d_1298.html` [cited 23 June 2019]

Table 6.5: Comparison between fuel cell system and battery in specific energy and specific power.

System	Specific Energy [$\mathrm{kWhkg^{-1}}$]	Specific Power [$\mathrm{kWkg^{-1}}$]
Fuel Cell System - H_2 Fuel + Tank	10.270	1.79
Battery	0.448	4.48

The opportunity of improving the power plant weight through the implementation of batteries generates the need for a trade-off between the optimal battery pack and fuel cell stack size to be implemented.
Another problem that arises in the determination of the power plant mass is that the available components on the market might not fit perfectly the specified requirements. Often this leads to components stacks that even if were picked for a specific requirement are over-designed for it and are carrying extra mass not utilised. Through an optimisation process, it is possible to minimise the degree of over-design by choosing the most suitable components for the given requirements.
Finally, reliability shall be addressed in the design and redundancy measures shall be implemented where needed, as explained in section 6.5. The choice of components is strictly related to the redundancy measures to be undertaken. It is indeed true that for the same failure rate the number of redundant elements needed is the same and smaller components will add less weight compared to larger counterparts.

In a nutshell, an optimisation algorithm has to be developed to address weight minimisation in 4 aspects:

- Fuel cell rating and battery pack size
- Power and Energy sizing for batteries
- Component stack over-design
- Redundancy measures

The algorithm used and its main functions are explained in subsection 6.4.2.

6.4.2 Optimisation Algorithm

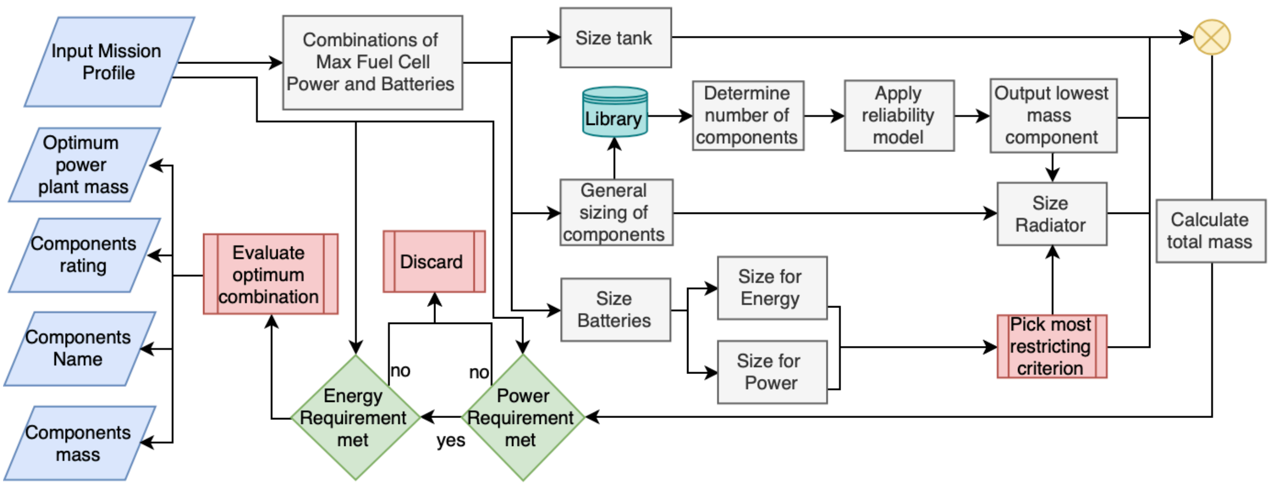

Figure 6.6: Battery integration algorithm.

Figure 6.6 shows the flow of operations from input mission profile to the output of the minimum power plant mass and its architecture.

Fuel Cell Rating and Battery Pack Size

Figure 6.6 shows that from the mission profile it possible to create a set of complementary fuel cell ratings and battery packs sizes to be further analysed. This set encompasses all the possible combinations of the two energy source solutions that span from the maximum power being met through only a fuel cell to only through batteries. The algorithm proceeds to analyse singularly each of these combinations to find which in the end will deliver the lowest weight. This part of the program addresses the first minimisation goal of the trade-off between fuel cell rating and battery pack size.

Power and Energy Sizing for Batteries

The algorithm then proceeds to size the battery pack according to the most restricting requirement between power and energy. It is indeed possible, given power and energy required from a battery pack to estimate the mass through both specific power and specific energy. It is found that when the batteries are used in power intensive phases, the power requirement is more restricting. On the other hand, as soon as the batteries are also implemented in cruise phases, the energy sizing becomes more demanding. This occurs because cruise lasts for several minutes, and to deliver a constant power, a big amount of energy has to be supplied. This part of the code addresses the second optimisation goal and evaluates whether the power or energy requirement is more restricting for batteries.

Component Stack Over-Design and Redundancy Measures

The next process in the algorithm is the sizing of the components stacks of the power plant and is carried through every combination of fuel cell power and battery pack size previously analysed. A library of components was developed from a thorough market search. This contains plenty of examples of fuel cells, electric motors, motor controllers, converters and compressors. The algorithm determines for each system how many of the components stored in the library are needed to be implemented in the corresponding stack. Subsequently, it implements the reliability model and adds any redundant components needed. This allows determining which kind of component stack delivers the best weight for every considered power combination.

Algorithm end and Output

Once the electric motors, fuel cells and batteries have been sized, it is possible to apply the methods described in section 6.2 and section 6.3 to estimate the radiator and tank masses for every combination of power source considered. Finally, all the masses are summed so to find the overall power plant weight. Each combination of the battery pack and fuel cell stack is then checked across both energy and power requirements from the mission profile, and if a combination does not meet these, it is discarded. The final function performed by the program is to evaluate between the combinations that satisfied the requirements which one delivers the lowest mass. The output of the algorithm is then the optimum power plant mass, and the architecture of the components stack with a focus on the name, mass and rating of each of these.

6.4.3 Algorithm Results

In this subsection, the results of the optimisation algorithm are summarised, and the chosen components are described. A particular focus of this section is put on the mass and power output of the components. The disposition and the stack architecture of these are better treated in section 6.6. The algorithm evaluates that the minimum power plant mass of

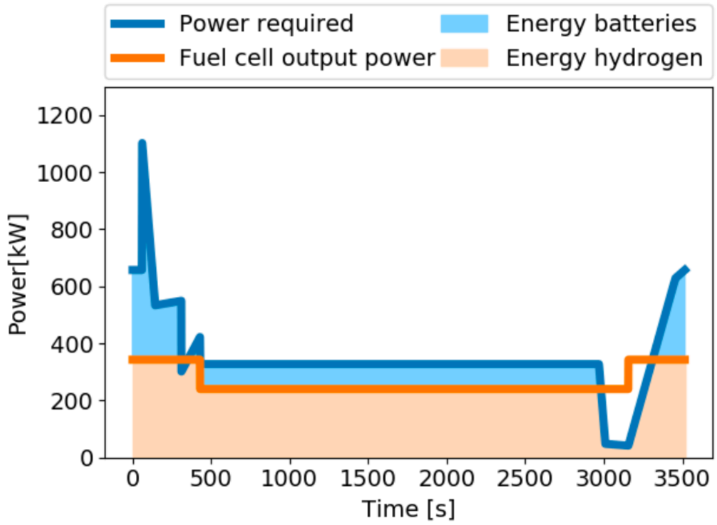

Figure 6.7: Comparison of energy shares throughout the mission profile.

Figure 6.7 shows the activity of the fuel cell throughout the mission and how much energy is delivered by the batteries and how much by the hydrogen. The optimisation algorithm finds that the minimum power plant weight of 1132.4 kg is achieved when the fuel cell stack delivers 343 kW. The rest of the peak power demand is met through the battery pack that has a capacity of 103 kWh. The fuel cell stack runs at maximum power output in take-off and landing but during cruise steps down at 70% of P_{max} to increase lifetime and decrease wear.

As expected, the optimum mass is achieved when batteries are used to meet the peak power in take-off and landing while in cruise, most of the energy is delivered by the fuel cell system. In Figure 6.7 the shaded areas correspond to the integral of power over time that equals energy. It is noticeable how the orange area, the energy delivered by the hydrogen is more dominant than the blue area, the energy provided by the battery pack.

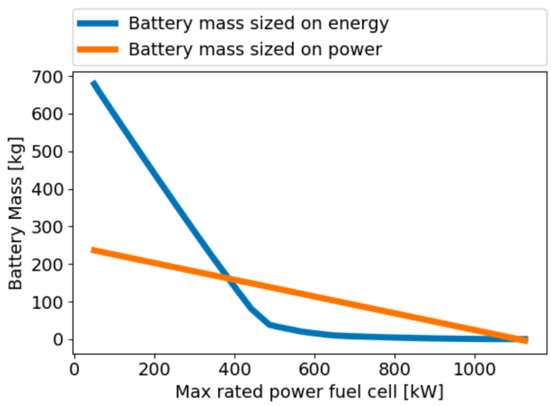

Figure 6.8: Battery mass sizing from energy and power requirement.

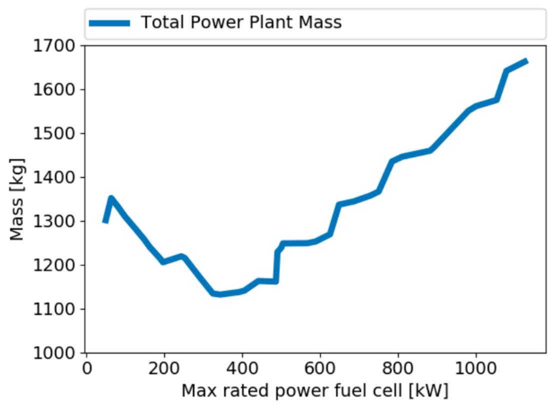

Figure 6.9: Power plant mass for the different combinations of fuel cell stack and battery pack sizes analysed.

Figure 6.8 presents the trade-off between energy and power sizing of the batteries for the different combinations analysed by the algorithm. Going from right to left the fuel cell stack is downsized, and more and more power is met through batteries. The mass derived from the power requirement increases linearly with the battery power output. On the other hand, the mass derived from the specific energy first is flat and then spikes up to around the combination with a fuel cell of 470 kW. This occurs because when the batteries supply only a small percentage of the peak power, the area under the narrow peaks of the mission profile is small leading to a low amount of energy to be stored into the batteries. However, when fuel cell stacks delivering less than 470 kW are considered, batteries will also have to be implemented in cruise. This happens because the fuel cells running at 70% of their max power cannot meet the cruise power of 327.6 kW anymore. It follows that the energy to be stored in the batteries increases rapidly, and so does the weight.

Figure 6.9 plots the power plant mass of the combinations that satisfied the power and energy requirement. The minimum weight is achieved for a fuel cell stack outputting 343 kW. By considering Figure 6.8 again, it can be concluded at this fuel cell stack rating the energy sizing for batteries is more requiring. This also means that for the considered mass, the battery pack can deliver more power than required. The battery pack is indeed able to deliver a maximum reliable power of 1051 kW. It follows that, together with the fuel cell stack, the total reliable power output is 1394 kW.

Table 6.6: Algorithm components output.

Components	**Number**	**Rating**	**Mass [kg]**
Fuel Cell	8	343 kW	168
Battery Pack	1	103 kWh	228
DCDC ormal	3	600 kW	9.6
DCDC Bus	2	40 kW	32
Compressors	8	0.33 g/s	6.3
Radiators	6	na	201
Motor Contr.	14	1200 kW	49
Electric Motors	8	1200 kW	128
Gear Box	2	9600 Nm	266
Tank	1	na	25.8
Hydrogen	na	na	18.7
Total	na		1132.4

Table 6.6 summarises the specification of the the optimal power plant evaluated by the algorithm.

Fuel Cell

The fuel cell stack counts 8 Power Cell S3 167 fuel cells . The fuel cell uses PEM (polymer electrolyte membrane) technology so to be reliable and dynamic, able to deliver max power within seconds [89]. Furthermore, this family of fuel cells have been designed to be used in mobile applications and are able to start and shut multiple times during their lifetime.

Battery Pack

The battery uses $LiFePO_4$ cells that have the advantage to high capacity, high safety, intrinsic stability, acceptable operating voltage (3.4 V vs. Li+/Li), environmental compatibility and low cost [52]. The specific energy and specific power amounts to 0.448 $\mathrm{kWh\,kg^{-1}}$ and 4.48 $\mathrm{kW\,kg^{-1}}$ at the discharge rate of 10 C.

DC/DC Converter

Three Fraunhofer IISB DC/DC converters are used to step down the voltage for the correct operation of compressors and radiators (one is used in the combiner box later explained). These converters are bidirectional and designed to decrease weight by using SiC-Mosfets, ceramic capacitors and custom made low-weight ferrite inductors [90].

DC/DC converter master bus

The electric system of a standard aircraft runs on 28 V lines. Such low voltage step down cannot be achieved by the Fraunhofer IISB DC/DC converter and so the GE aviation 20kw is implemented [91]. This component uses as well SiC MOSFETs and is specifically designed to be plugged in the electrical system of an aircraft and deliver reliable performances.

Compressor

The compressors chosen to feed the fuel cell stack are the Celereton-14-1000 [88]. These are electrically driven diagonal turbo compressors and 8 of them are needed to operate the fuel cell stack.

Motor Controllers

The motor controllers are used to convert DC input into a 3 phase current that is used to tune the electric motors power output. The motor controllers used are the 100 kW SiC-Inverter from Fraunhofer. These motors controllers are again designed to be lightweight so to be used in mobility applications [92]. Each nacelle contains 7 motor controllers

Electric Motor

The electric motor used are the Magnax AXF225 [93]. These motors have a very high specific power of 12.5 $\mathrm{kWkg^{-1}}$. These are axial flux motors and result to be more compact and so lighter than traditional radial flux counter parts. Furthermore, the Magnax AXF225 differently from other permanent magnet motors have a yokeless stator, for the shortest possible flux paths and low iron losses. In order to deliver the maximum mission power and meet reliability constraints, 8 motors are equally spread in the two nacelles are used.

Gearbox

The gearbox is used in order to match the motor shaft rpm to the rotor rpm. From the mission and rotor characteristics it is possible to determine the torque to be delivered by the gearbox.

$$T = \frac{P \cdot 60}{rpm \cdot 2 \cdot \pi} \tag{6.21}$$

where:

P = Power delivered by the propeller
rpm = Rotation per minute at the rotor

The highest torque required from the gear box is achieved at take-off when each rotor delivers about 548 kW at an rpm of 552 [93]. Following Equation 6.21 the required output torque is then 9480 Nm. On the motor side of the gearbox, the input torque is 840 Nm and, assuming an average efficiency of 95%, the required power is 577 kW [93, 94]. Following the same logic as in Equation 6.21 but reversing the operation, the input shaft rotational speed is 6912 rpm. It follows that the required gearbox must have a max output torque of 9533 Nm, the maximum input speed of 6230 rpm and the gear ratio of 12. Due to the demanding specifications, it was not possible to find on the market open to the public a gearbox satisfying all the requirements at once. On the other hand, it was possible to create a set of gearboxes that could meet either the torque or the input speed requirement [94, 95].[8] Through interpolation, it was possible to estimate that a gearbox tailored on Futura will weigh around 133 kg.

[8] URL:`https://www.liebherr.com/en/sgp/products/components/gearboxes-rope-winches/planetary-plug-in-gearbox/details/peg300.html`[Accessed 22/06/19]

6.5 Power Reliability

This section is set to present how the failure rate of components is modelled and how the power plant system was modified to meet regulations. Such a failure rate model does not only apply to the power plant system but can also model any high-level system divided into sub-components as an aircraft and its subsystems.

In the aerospace sector, due to the catastrophic consequences of failures and the complicated maintenance procedures, reliability is crucial, and a commonly accepted failure rate for components amounts to 10^{-8}. From statistics failure rates for aircraft has an order of magnitude of 10^{-6} [96].[9] Assuming that in a sample aircraft there are averagely 10^1 subsystems that further encompass 10^1 component stacks, it can be explained the 10^{-8} figure.[10] It follows that if a system presents higher failure rates, redundancy is needed to deliver safe operability of such.

6.5.1 Failure rate model

The reliability of a system is crucial in the determination of operational safety of such. This value is computed through the analysis of the failure rate of the single components constituting a system. In general terms, the reliability of a component is calculated, as shown in Equation 6.22.

$$R = e^{-\lambda \cdot t} \tag{6.22}$$

where:

R = Reliability
λ = Failure rate of component
t = Operative time in-between maintenance operations

Equation 6.22 shows that reliability can be modelled with a negative exponential curve for a given failure rate and time interval. Mathematically, it follows that an increase in λ or t leads to lower R. This logically occurs because more frequent failures or longer operational times endanger the safe operation of a given component. Another popular method is using Weibull distributions, these allow for a more flexible modelling and the possibility to achieve a "bathtub" shaped distribution, typical of components with high infant and end of life mortality. On the other hand, such probability distribution requires an extra input parameter over-complicating the calculation process already depending on many variables. Negative exponential probability is then confirmed to keep clarity and straightforwardness at the centre of the focus of the section.

A given component can fail in different modes. The failure rate of every single mode can be modelled through statistics or testing. Since the component can fail due to any of the modes, the resultant component failure rate is equal to the summation of these. Equation 6.23 shows how the failure rate of a component that can fail in k ways is calculated.

$$\lambda = \lambda_1 + \lambda_2 + \lambda_3 + ... + \lambda_k \tag{6.23}$$

Taking a step back from the precise regulations in the aerospace sector, a thorough analysis of the relationship between component and its stack has to be performed to fully understand how the failure rate behaves.

[9] URL `https://www.aviationpros.com/home/article/10388070/measuring-reliability-and-availability` [cited 21 June 2019]

[10] As explained in subsection 6.5.1 when elements are connected in series, as in the case of subsystems in an aircraft, the failure rate propagates through addition. It follows that the addition of 10 or more elements in order of magnitude of 10^N will have a magnitude of 10^{N+1}.

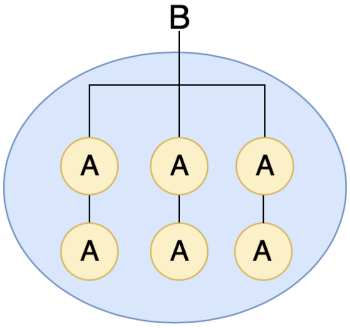

Figure 6.10: Stack B of components A, connected both in series and parallel.

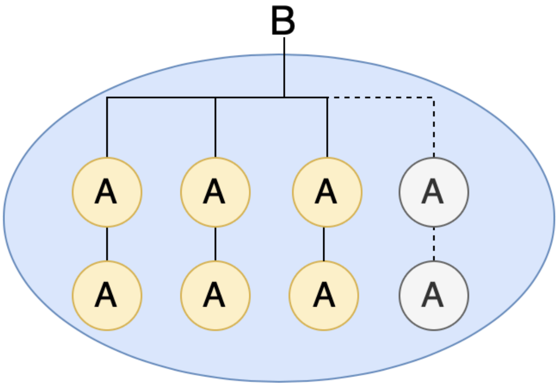

Figure 6.11: Stack B with an extra row of components A in parallel.

Figure 6.10 shows a stack, called B, of a given component A. These components are connected both in parallel and in series. This structure resembles many electrical systems as a collection of Solar Cells (A) in a PV array (B) or battery cells (A) in battery packs (B). From basic electrical engineering theory, unless a proper secondary path has been designed, the failure of a component will bring all of the others connected in series to malfunction as well. This occurs due to the incapacity of the current to overcome and flow around the malfunctioning component. On the other hand, the failure of a row of components does not affect the correct functioning of the others attached in parallel. The singular consequence of such an event to occur is the reduction in the output current of the components stack. It is then explained why redundancy is created in parallel rather than in series. The mathematical consequences of these considerations are shown in Equation 6.24 and Equation 6.25.

$$\lambda_{row} = \lambda \cdot N_{series} \tag{6.24}$$

where:

λ_{row} = Failure rate of a row of components
N_{series} = Number of components in series

$$\lambda_{N_{sim}} = {\lambda_{row}}^{N_{sim}} \tag{6.25}$$

where:

$\lambda_{N_{sim}}$ = Failure rate of N simultaneously malfunctioning rows
N_{sim} = Number simultaneously malfunctioning row

In a nutshell, failure rate propagates through addition in series and multiplication in parallel. Established the basics of failure rate, it is possible to investigate its relationship at the stack level. More precisely, Figure 6.10 shows the scenario in which B meets its set requirements through the correct functioning of all of its subcomponents A. This means that in the case of failure of one or more components, regardless of their disposition, also B will fail to meet its requirements. It follows that:

$$\lambda_B = \lambda_{row} \cdot N_{row} = \lambda_A \cdot N_{series} \cdot N_{row} = \lambda_A \cdot N_A \tag{6.26}$$

where:

λ_B = Failure rate of the components stack B
λ_A = Failure rate of the component A
N_{row} = Number of components rows in parallel
N_A = Number of components A

If λ_B does not meet the set industry requirement of 10^{-8} redundancy is needed. Figure 6.11 shows the scenario in which and extra row of components is added to B in order to increase reliability. In this case, a maximum of one row of components can fail without affecting the functioning of B. It follows that the failure rate of B is the failure rate of 2 simultaneously malfunctioning rows times the amount of combinations of rows that can fail. In mathematical terms:

$$\lambda_B = \lambda_{row}{}^{1+1} \cdot \binom{(N_{row}+1)}{1+1} \tag{6.27}$$

where:

N_{red} = Number of redundant rows in parallel
$\binom{n}{k}$ = Number of combinations of k in n : $\frac{n!}{k!(n-k)!}$

Now if Equation 6.27 is generalised for a given amount N_{red} of redundant components rows, the failure rate of a structured stack is give by:

$$\lambda_{stack} = \lambda_{row}{}^{N_{red}+1} \cdot \binom{(N_{row}+N_{red})}{N_{red}+1} \tag{6.28}$$

Equation 6.28 can be validated by realising that it encompasses also the original case described by Equation 6.26. In such case, the stack was designed to just meet the requirements and so no redundant rows of components are implemented, leading to N_{red} being 0. If such insight is substituted in Equation 6.28 it can be immediately seen that $\binom{N_{row}}{1}$ is equal to N_{row} itself leading back to Equation 6.27. The powerfulness of such model lies in the relationships it draws between the number of components, their disposition, their failure rate and the overall stack failure rate. This means that for a goal failure rate and set of requirements, it is possible to determine how many redundant components shall be implemented.

6.5.2 Design Modifications

The power plant design is presented in section 6.6, where the components stack size and inter-connections are analysed. In this subsection, the underlying reason for the implementation of redundant components is explained supported by calculations following the model presented in subsection 6.5.1. This subsection assumes that components specifically developed for the aerospace industry have been designed to comply with the regulations. Meaning that components as the onboard computer, combiner box, system meters, charge/load controller, quadrature encoders, wing/nacelle swivels and gearboxes are assumed to have a failure rate of $0.5 \cdot 10^{-8}$. The most critical components stacks considered for the calculation of the reliability of the power are the fuel cells, batteries, DC/DC converters, motor controllers and electric motors.

PEM fuel cell failure rate, as explained by a performance evaluation from NASA, amounts to $1 \cdot 10^{-6}$ [97]. Even though fuel cells are both connected in parallel and series, for reliability purpose, these are considered to be connected only in parallel. Such a conclusion is reached through the implementation of secondary "emergency" electrical lines that connect each fuel cell to the charge/load controller. It follows that in case one fuel cell fails, the rest is still able to function properly.
Lithium-Ion battery failure rate is estimated to be $1 \cdot 10^{-7}$ according to models build upon the Boeing 787 Dreamliner battery pack. The battery pack counts 64 rows of 64 cells each.

Radial compressors show a failure rate of $1.65 \cdot 10^{-5}$, the highest value recorded through the power plant system probably linked to the high operational stress in this component. Five compressors are needed to operate the fuel cell stack, and all of them are connected in parallel.
As for the DC/DC converter of the bus, the data sheet reports a mean time between failure of over 50000 hours. This leads to a failure rate of $2 \cdot 10^{-5}$. For the rest of DC/DC converters, the failure rate is estimated to be $2.79 \cdot 10^{-6}$ with mosfet failure dominating above diode, and Capacitor Polypropylene metalised film malfunctions. It is estimated that one converter can handle both the radiator and compressor stacks. Motor controller also mounts a mosfet and are similar in architecture to DC/DC converters differing just in the AC current output. It can be concluded that a similar failure rate to the DC/DC converter can then be assumed also for the motor controller. To operate the motors four controllers connected in parallel

are needed per rotor.

Brush-less DC Electric motors resulted to have a lower failure rate compared to the brushed counterpart logically due to the absence of the failure mode linked to the brushes. The main failure modes registered in ascending order by a study from the University of Johannesburg are related to stator housing, windings, armature and finally above all bearing. More recent studies show that the failure rate of bearings has been improved in the recent year, so to lead to a final total failure rate of $1.15 \cdot 10^{-5}$. To perform the mission, three motors are needed per rotor. In case of failure of one motor, the shaft is assumed to be able to rotate.

Table 6.7: Redundancy design modifications.

Component	N_{series}	N_{row}	$\lambda\,[h^{-1}]$	$\lambda_{initial}\,[h^{-1}]$	N_{red}	$\lambda_{row}\,[h^{-1}]$	$\lambda_{stack}\,[h^{-1}]$
Certified components	7	1	5.00E-09	3.50E-08	0	3.50E-08	3.50E-08
Fuel Cell	1	7	1.00E-06	7.00E-06	1	1.00E-06	2.800E-11
Battery	64	64	1.00E-07	4.10E-04	2	6.40E-06	1.20E-11
DC/DC Bus	1	1	2.00E-05	2.00E-05	1	2.00E-05	4.00E-10
DC/DC	1	1	2.79E-06	2.79E-06	1	2.79E-06	7.78E-12
Motor Controller (L)	1	6	2.79E-06	1.67E-05	1	2.79E-06	1.63E-10
Motor Controller (R)	1	6	2.79E-06	1.67E-05	1	2.79E-06	1.63E-10
E-Motor	1	3	1.15E-05	3.45E-05	1	1.15E-05	7.92E-10
Compressor	1	5	1.65E-05	8.25E-05	2	1.65E-05	1.57E-13

Table 6.7 presents how the design of the power plant has been tuned to deliver the required failure rate. Firstly, $\lambda_{initial}$ is used to determine whether the component stack needs redundant rows to meet the requirement. This is calculated as explained in Equation 6.26. It can be noticed immediately that all the components stacks, except for the ones specifically designed for the aerospace sector, have a failure rate of above 10^{-8}. By applying Equation 6.28, it was possible to evaluate the minimum number of redundant components rows to be integrated to meet the goal failure rate. This finally explains the architecture presented in section 6.6. In conclusion, by adding all the single stacks failure rates, it was found that the power plant system has a failure rate of $3.66 \cdot 10^{-8}\ \mathrm{h}^{-1}$.
It can be concluded that through the implementation of extra components row, the power plant system meets the set target of failure rate, and it is safe to be operated.

6.6 Power Plant EBD

This section presents the architecture of the system. A detailed electrical block diagram, EBD has been developed to display all the components implemented and how they connect. The circuits have been designed not only to connect different components but also to deliver the right voltage and current for the safe and correct operation of the entire system.

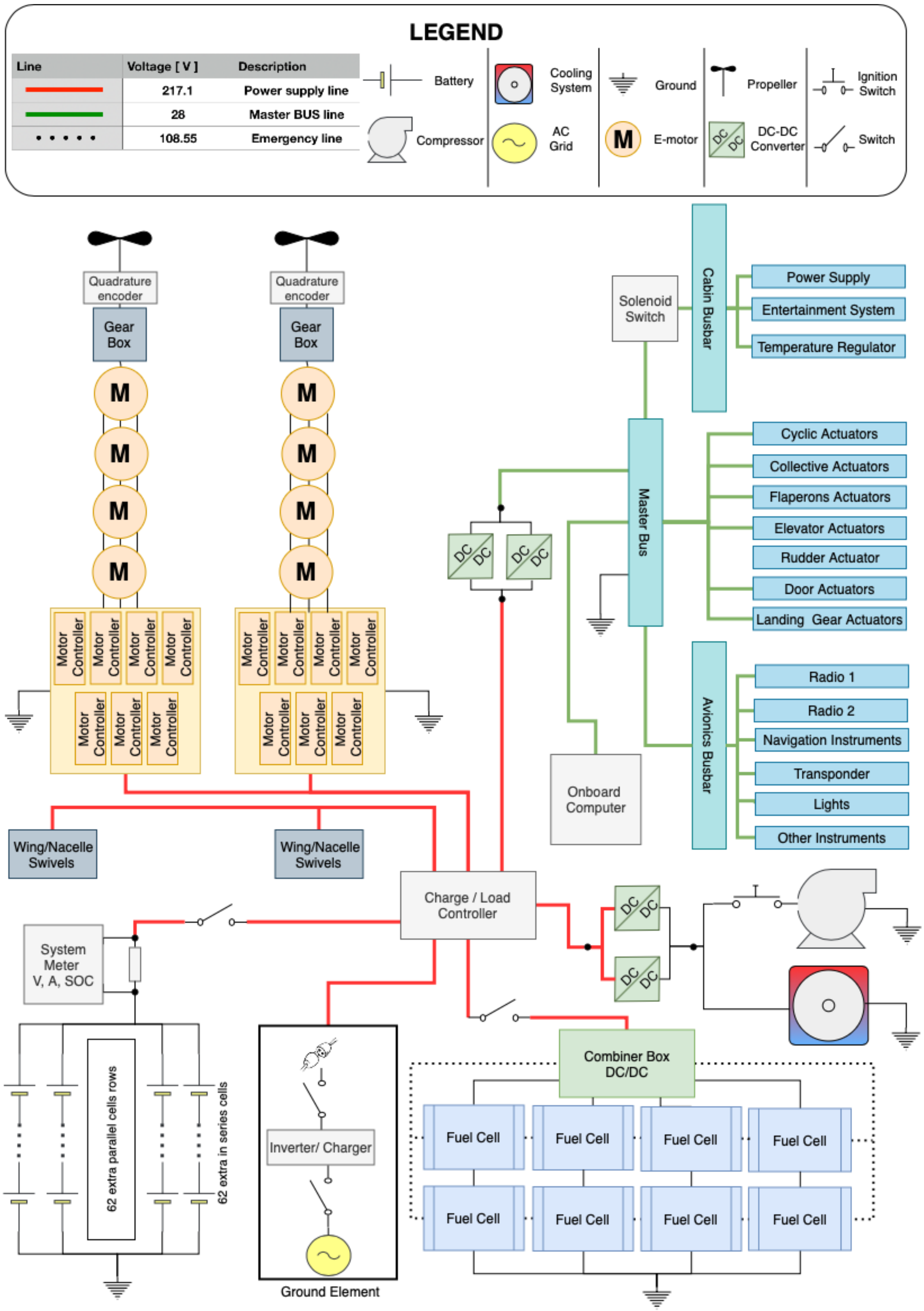

Figure 6.12: Electrical block diagram with a focus on the power plant.

Figure 6.12 presents the architecture of the power plant system. The circuits have been designed to deliver the right voltage and current for the safe and correct operation of the entire system.

Fuel Cell Stack

Starting from the fuel cell stack, there are eight fuel cells, 2 in series and 4 in parallel. The output lines from the fuel cell rows are collected in a combiner box. The function of the combiner box is to pass the output of every row through a fuse and then collect them on a single conductor. The fuses allow for the control of the line and avoid unexpected fluctuations in the rating. The combiner box is also equipped with monitoring sensors, remote rapid shutdown devices and a DC/DC converter. Every fuel cell is

equipped with a secondary emergency line in case the current has to be diverted to avoid a malfunctioning component. In that case, the monitoring tool activates the emergency protocol and the current outputted from the emergency line is tuned to meet the voltages of the other rows. In such a way the combiner box can deliver reliable power at a constant voltage.
The combiner box and its fuses have then to be sized for the most restricting voltage and current requirement. This is reached when a fuel cell fails, and the rest are running at maximum to compensate. The maximum power is reached when each cell of the fuel cells runs at 0.65 V and 450 A [89]. The power cell S3 167 mounts 167 cells leading to the max voltage rating of:

$$V_{FC_{stack}} = V_{FC_{cell}} \cdot 167 \cdot N_{series} = 0.65 \cdot 167 \cdot 2 = 217.1\text{V} \tag{6.29}$$

Where:

$V_{FC_{stack}}$ = Maximum voltage of the fuel cell stack.
$V_{FC_{cell}}$ = Maximum voltage of a singe cell.

The maximum output current of the fuel cell stack can also be calculated as:

$$I_{FC_{stack}} = I_{FC_{cell}} \cdot N_{row} = 450 \cdot 4 = 1800\text{A} \tag{6.30}$$

Where:

$I_{FC_{stack}}$ = Maximum current of the fuel cell stack.
$I_{FC_{cell}}$ = Maximum current of a singe cell.

Battery Pack

The second energy source of the power plant is the battery pack implementing LiFePO_4 cells. This cell chemistry has been around since 1997 and is used in stationary energy storage such as renewable energy and smart grids, as well as on-board energy storage such as HEVs, EVs and PEVs [52]. One of the main challenges of this type of battery is low ionic mobility that can lead to a loss in energy capacity. However, through a graphen flakes based coating on the cathodes, it is possible to tackle the sluggish kinetics of Li-ion transport and achieve specific energy of 0.448 kWhkg^{-1} at 10 C rate of discharge and so 4.48 kWkg^{-1} specific power. Each battery cell has a maximum output voltage of 3.4 V at 10 C discharge rate [52].

The batteries, in the worst case scenario, shall be able to meet the maximum voltage produced by the fuel cell stack so as not to jeopardise the stability of the electrical system. In other scenarios, the output voltage is controlled by the charge/load controller that will be treated in more detailed later on. It follows that the number of battery cells needed in series is:

$$N_{cell_{series}} = \frac{V_{FC_{stack}}}{V_{B_{cell}}} = \frac{217.5}{3.4} \approx 64 \tag{6.31}$$

Where:

$N_{cell_{series}}$ = Number of battery cells in series.
$V_{B_{cell}}$ = maximum voltage of a single battery cell.

In order to enhance the quick launch on the market of the battery pack, industry standards cell packaging has been considered. This would allow for the use of readily available machinery for the packaging while just changing the inside chemistry of the cathode. The industry standards, set by the samsung 21700-48G also used in the Tesla model 3, is a cylindrical cell with diameter d_{cell} of 21 mm and length l_{cell} of 70.5.[11,12] The volume of such battery cell can be calculated to be:

$$Volume_{cell} = \left(\frac{d_{cell}}{2}\right)^2 \cdot \pi \cdot l_{cell} = \left(\frac{21}{2}\right)^2 \cdot \pi \cdot 70.5 = 24418.4\text{mm}^3 = 2.44E-2\text{liter} \tag{6.32}$$

[11] URL `https://www.amicell.co.il/batteries/rechargeable-batteries/li-ion-batteries/` [cited 23 June 2019]
[12] URL `https://www.teslarati.com/inside-tesla-model-3-2170-lithium-ion-battery/` [cited 23 June 2019]

$LiFePO_4$ cells are reported to have an energy density ρ_{cell} of 1000 $\mathrm{WhL^{-1}}$ [52]. It is then possible to calculate how much energy is stored in the standard sized battery cell:

$$E_{cell} = \rho_{cell} \cdot Volume_{cell} = 1000 \cdot 2.44E-2 = 24.418\mathrm{Wh} \tag{6.33}$$

Where:

E_{cell} = Energy capacity of a battery cell
ρ_{cell} = Energy density of $LiFePO_4$ cells
$Volume_{cell}$ = Volume of a battery cell

As explained in subsection 6.4.3, the most constraining sizing requirement for batteries is energy. It follows that, by knowing how much energy has to be stored in the batteries, $N_{cell_{series}}$, E_{cell} and N_{red} it is possible to calculate the number of cell rows in parallel:

$$N_{cell_{parallel}} = \frac{energystorage}{E_{cell} \cdot N_{cell_{series}}} + N_{red} = \frac{100E3}{24.418 \cdot 64} + 2 \approx 66 \tag{6.34}$$

Summarising the deductions carried through, the battery pack will have 66 rows with 64 cells each amounting to approximately 103 kWh. Now it is possible to estimates the size of the battery pack so to be integrated into the overall design. The battery cells need to not be in contact with each other so not to short circuit rows. This can be done by separating the cells with a non-conductive material as a glue or cardboard [13]. The temperature status of the batteries is controlled by a thermistor that indirectly communicates to the cooling system through the onboard computer. The batteries are indeed liquid cooled in the same manner that the fuel cells and the electric motors are. As for minimum temperature control, the battery pack is inserted under the cabin and makes use of its heating system for low-temperature control. To further contain fluctuation in the volume of the battery pack, the cells are wrapped in heat shrink tape and then placed in a lightweight plastic casing. In conclusion, it is estimated that there should be around two mm of space to be left in between the cells to allow for the measures mentioned above to be implemented it follows that:

$$w_B = \frac{N_{cell_{parallel}}}{N_{cell_{layers}}} \cdot d_{cell} + s \cdot \left(\frac{N_{cell_{parallel}}}{N_{cell_{layers}}} + 1 \right) = \frac{66}{2} \cdot 21 + 2 \cdot \left(\frac{66}{2} + 1 \right) = 748.5\mathrm{mm} \tag{6.35}$$

$$l_B = \frac{N_{cell_{series}}}{N_{cell_{layers}}} \cdot d_{cell} + s \cdot \left(\frac{N_{cell_{series}}}{N_{cell_{layers}}} + 1 \right) = \frac{64}{2} \cdot 21 + 2 \cdot \left(\frac{64}{2} + 1 \right) = 738.0\mathrm{mm} \tag{6.36}$$

$$h_B = l_{cell} \cdot N_{cell_{layers}} + \left(N_{cell_{layers}} + 1 \right) = 70.5 \cdot 2 + 3 \cdot 2 = 147\mathrm{mm} \tag{6.37}$$

Where:

w_B = Width of the battery pack.
l_B = Length of the battery pack.
h_B = Height of the battery pack.
$N_{cell_{layers}}$ = Number of layers of cells in the battery pack.

Charge/load Controller and Appendices

Both the battery pack and the fuel cell stack are connected to the charge/ load controller. Safety switches on both connecting lines have been implemented to avoid uncontrolled voltage and current input in the component. One of the main functions of the charge/ load controller is to communicate with the onboard computer and manage the input from both the fuel cell stack and batteries. Furthermore, it tracks the state of charge of the battery pack through voltmeter and ammeter ratings and assures the safe charge and discharge of it. It follows that one side of the recharging line is directly connected to the charge/load

[13]URL `https://www.powerstream.com/BPD.htm` [cited 23 June 2019]

controller while the other is connected to the ground facilities. Here, AC current from the grid is transformed by an inverter/charger in DC current to be fed in the power plant system.
The charge/load controller distributes the produced power to all the relevant systems in the circuit. One specific line is dedicated to compressors and radiators, and voltage compatibility is assured through the implementation of two Fraunhofer DC/DC converters. The ignition switch is placed along the power line of the compressors. When the system is started, the compressors start feeding air to the fuel cells that in seconds already start to produce nominal power.

Nacelle Units

A big portion of the power output from the charge/load controller is directed towards the two nacelles where the propulsion systems are contained. The titanium wing/nacelle swivels assure the rotation of the nacelles. Inside the nacelles motor controllers, electric motors, gearboxes and quadrature encoders are stored.

Firstly, power input is fed into the motor controllers that convert DC current to a 3 phase output tuned to operate the motors. About 600 kW are needed at each nacelle to perform the mission. This power is tuned by seven motor controllers of which one is redundant.
Secondly, the motor train counting four units in each nacelle operates the main shaft. At the end of the shafts, the gearboxes are connected. These are single speed gearboxes that are directly connected to the propellers. Just after the gearboxes, one quadrature encoder per propeller is connected. The quadrature encoder measures the rotational speed of the rotor and, by communicating with the onboard computer and the motor controllers, ensures that the desired rpm is delivered constantly with minimal fluctuations.

Master Bus

The last output of the charge/load controller is towards the master bus. The electric line from the master bus is rated at 28 V. The higher voltage compared to a standard 14 V systems allows for weight saving in the cabling of the cabin as for the same powerless current is needed. Directly connected to the master bus are the aircraft actuators for control, landing and door release. As for the avionics, a dedicated bus bar is connected to the master bus for power delivery. The main avionics connected are the Navigation Instruments (GPS, NAV, etc..), transponder, lights, radio and reserve radio.
The final component attached to the master bus is the cabin bus bar. This delivers power to all the electronics used in the cabin. A solenoid switch is placed just before the bus bar to assure the safety of the system. If the current exceeds the safe limit, the solenoid inductor creates a magnetic field strong enough to operate the safety switch. Once the safety hazard has been tackled, the switch can be reset to its original position through remote control.

Conclusion

The hydrogen powered fuel cell based power plant that powers Futura has been designed to deliver 1394 kW. This was achieved with a total weight of 1132.4 kg. Futura stores energy in chemical form in liquid hydrogen and batteries. The liquid hydrogen needed at refuelling for the mission weighs 14.3 kg and is stored in a tank that was designed to keep cryogenics temperature. The tank uses a combination of materials to provide both structural integrity and insulation and weighs 25.8 kg. Eight fuel cells convert the chemical power stored in hydrogen to electrical power and together with the batteries they are connected to the electric motors through a power electronics system. The eight electric motors provide power and torque to the rotors using a gear box. The system is cooled using radiators that are able to reject a total of 550 kW of heat in critical atmospheric conditions and peak power. Finally, through smart selection of component redundancy a total reliability of 3.66E-8 h^{-1} was reached.

7. Stability and Control

With a layout of the main components of the aircraft, the stability and controllability of the aircraft are assessed. For on-ground stability landing gears are analysed in section 7.1, in section 7.2 the control methods for both vertical and horizontal flight are determined, and in section 7.3 the empennage and wing position are sized for horizontal stability and controllability. Then, in section 7.4 the design of the control surfaces and actuators is done, including the horizontal and vertical empennages as well as the vertical control actuators. An analysis of the control system follows this in section 7.5, an analysis of the mass in section 7.6 and finally validation in section 7.7.

7.1 Landing Gear

Sizing Futura's landing gear is an essential for the aircraft's ground and landing operations. As mentioned in section 4.2, in the emergency condition, the aircraft is capable of gliding as an aircraft to land on a runway. This means that the landing gear has to be able to sustain not only the loads deriving from vertical take-off and landing procedures but also the limiting aircraft like landing case. Hence, the landing in the emergency condition is going to be the limiting case to size the landing gear.

7.1.1 Tires and Shock Absorption Capabilities

Firstly, it is necessary to identify the maximum touchdown rate the aircraft can encounter during landing. This vertical speed is an indicator of the vertical load the gear has to be able to sustain during landing. For CS-23 aircraft category it was be found to be w_t=3.05 ms^{-1} using Roskam IV statistical relationships [98]. During landing, it is assumed that the main landing gear has to absorb all the energy during the touchdown. Hence the maximum energy the landing gear will ever encounter is dependent on the maximum vertical speed according to Equation 7.1 [98].

$$E_t = \frac{1}{2} W_l {w_t}^2 \tag{7.1}$$

Where the landing mass W_l is 88% of the MTOW [99]. A value of 18581 J was obtained. Hence the landing gear shall be designed to absorb at least this energy. The energy that the landing gear is going to be capable of absorbing is established by Equation 7.2 [98].

$$E_t = n_s P_m N_g (\eta_t s_t + \eta_s s_s) \tag{7.2}$$

As a consequence, the parameters in Equation 7.2 have to be determined. The tire energy absorption efficiency has typically a value of η_t=0.47 [98]. Oleo-pneumatic shock absorbers were chosen for the landing gear: their energy absorption efficiency is on average η_s=0.8 [98]. The required stroke length s_s can be computed using Equation 7.3.

$$s_s = \frac{\left[\frac{\frac{1}{2} W_l {w_t}^2}{n_s P_m N_g} - \eta_t s_t\right]}{\eta_s} \tag{7.3}$$

A landing load factor of 3, which is typically of CS-23 aircraft [98], is used and a static load on the main landing gear (P_m) is 92% of the maximum take off weight. With this values, a stroke length of 15.3 cm was found. Eventually the tire design had to be completed. The tire choice was function of the load classification number that was found to be 20 from a statistical regression from 8 aircraft data as provided by Roskam in Layout of Landing Gear and Systems [98]. The load classification number, in fact, establishes the tire pressure given aircraft mass and landing surface. The tire inflation pressure, could be found to be equal to 610 kPa. Hence, given a combination of maximum inflation pressure for the tires and the static load they have to be able to sustain, the tires could be chosen for the nose and main landing gear. It is important to specify that the main landing gear has two struts and two wheels with the loading force acting through the strut axis. The landing gear tires characteristics are summarised in Table 7.1.

Table 7.1: Main and nose landing gear tires characteristics.

Main		Nose	
D_0 [m]	0.43	D_0 [m]	0.35
d [m]	0.22	d [m]	0.15
b_t [m]	0.17	b_t [m]	0.11

Hence, the main landing gear tire defection was found to be s_t=0.017 m using the tire's corresponding loaded radius [98]. Hence the maximum energy the main landing gear is able to absorb could be found to be 19509 J using Equation 7.2. This value is greater than the maximum energy the landing gear will statistically encounter based on w_t.

7.1.2 Position and Dimension

The position of the landing gear on the aircraft had then to be specified in order to provide stability and ensure manoeuvrability on ground. In other words, the normal force on the nose landing gear had to be at least 8% of the total weight of the aircraft. Finding the right spot was an iterative process, since changing l_n and l_m shown in Figure 7.1 would vary the position of the centre of gravity consequently changing the weight distribution over the nose and main landing gear.

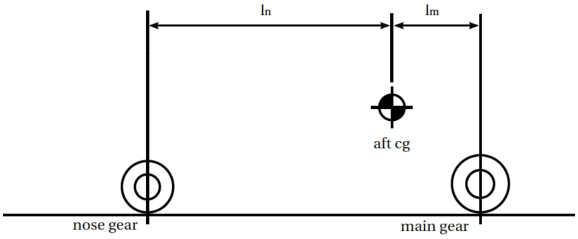

Figure 7.1: Illustration of the landing gear disposition.

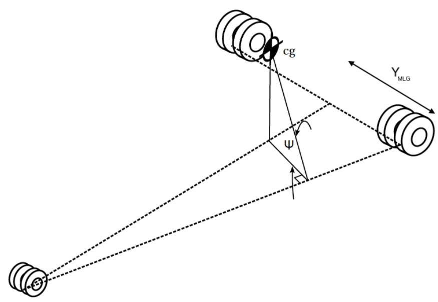

Figure 7.2:
Sideways turnover requirement dimensions.

On top of this condition, landing stability had to be achieved meaning that $l_m \geq= (h_{cg} + s_s + s_t) \cdot \tan\theta_l$ [100]. The landing tip back angle θ_l was approximated to 8.65 ^{o} since this was the angle at which $V_{approach}$ can be attained in clean configuration chapter 5. This case was considered as the limiting one in case of full power shut down and inability to operate the flaps. The maximum deflection of the tire and shock absorber s_s and s_t were determined in subsection 7.1.2. Additionally sideways turnover had to be prevented during turns according to Equation 7.4. This meant setting a relationship between the landing gear track, shown in Figure 7.2, and l_n and l_n.

$$y_{MLG} > \frac{l_\mathrm{n} + l_\mathrm{m}}{\sqrt{\frac{l_\mathrm{n}^2 \tan^2\psi}{h_{cg}{}^2} - 1}} \tag{7.4}$$

Where ψ is the turn over angle which is set to be 55° [98]. Eventually, it was necessary to check for ground engine clearance. In Futura's case, this is particularly relevant at emergency landing when the propellers are tilted upwards, and the nacelle casing is in the vertical position. $y_{\mathrm{MLG}} > y_\mathrm{e} - \frac{z_\mathrm{n}}{\tan\varphi}$ had to be satisfied where z_n is the height from ground of the bottom of the nacelle when in vertical position and

φ has to be at least $5°$. The distance from the centerline to the nacelle is 5.185 m. The value of z_n was 0.523 m.

As mentioned above, the landing gear design process was iterative. As the mass components varied the centre of gravity would change position impacting the various design constraints mentioned above. A summary of the landing gear parameters is presented in Table 7.2. The nose and main landing gear respective masses have been estimated to be 50.5 kg and 122.6 kg using Roskam relationships [40]. The landing gear struts are going to be made of the steel alloy AISI 4340 since this material is preferred for high loaded structures [9, 41]. Additionally, the landing gear wheel is made of Magnesium Elektron ZW3F since this is the typical material used for such applications [9].

Table 7.2: Summary of the landing gear geometry parameters.

y_{MLG} [m]	1	l_n	3.4 [m]
h_{cg} [m]	1.3	l_m	0.28 [m]

7.1.3 Verification and Validation

The verification and validation procedure of the landing gear design parameters has been completed by checking that all the obtained dimension would respect the criteria established in subsection 7.1.2. Also creating the CATIA model of the landing gear allowed to have a much better visual understanding of its integration with other aircraft's systems. For example, it was possible to check the lateral position of the landing gear in the wing. Additionally, it was possible to verify that there would be enough space to store the main landing gear in the fuselage. The movement of the landing was also ensured by developing its kinematic concept. An visual of the landing gear can be observed in Figure 7.3.

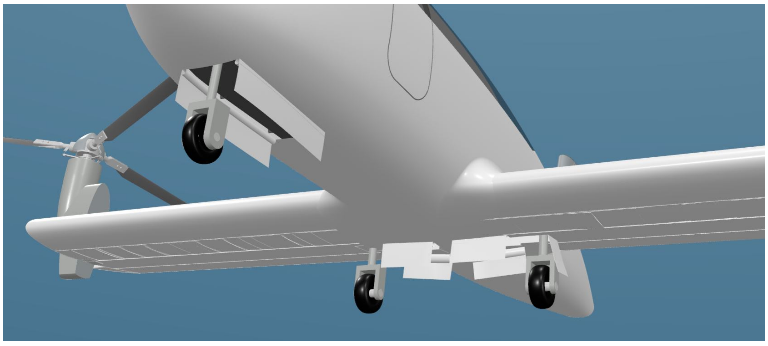

Figure 7.3: Landing gear illustration.

7.2 Control Methods

With two different modes of flight, the most appropriate control methods must be selected to ensure stability and control during flight. For vertical stability and control, the aircraft uses the tilt rotors with collective and cyclic, while for the forward flight the aircraft uses flaperons, elevators and a rudder.

7.2.1 Vertical Stability and Control Configuration

The vertical stability of the aircraft can be achieved in several ways. A starting point is the most analogous to a helicopter, with collective and cyclic. Collective changes the pitch of all the blades on a rotor so that they change in the lift; this increases or decreases the total thrust of the rotor. Cyclic is divided into lateral and longitudinal cyclic pitch and is used to reorient the thrust from the rotor. This mechanism is quite complicated with many moving parts, therefore likely making required maintenance more regular. However, the mechanism is quick in changing the direction of the thrust vector, making the aircraft more quickly controllable. A second solution to provide vertical stability and control is with a fan in the nose of the aircraft and only collective on the rotors of the aircraft. A large benefit of this would be to allow flexible placement of the centre of gravity of the aircraft. However, this would also come with increases in power required and mass, and restrictions on the integration of avionics and nose landing gear placement. Finally, it would also be possible to use only use the collective and the nacelle rotation mechanism. A big drawback is that rotation mechanism with a tremendous torque must be present to provide sufficient high acceleration for longitudinal movement, which adds more mass than the cyclic.

Considering these three different options, the most viable option is the use of collective and cyclic. Although the nacelle rotation, as a primary control method is discarded, the unique aspects of a tilt-rotor can still be used to the advantage of the design. Specifically, for longitudinal pitch, the nacelle can be rotated slightly. For example, for rearward movement, the nacelle can be rotated backwards. The largest drawback is that the c.g. placement is rigorous. The c.g. must lie very near to the rotor so that changes in the angle of thrust can sufficiently change the moments acting on the aircraft.

7.2.2 Horizontal Stability and Control Configuration

The choice of a suitable configuration has driven the design of the empennage. Three options were therefore considered, namely the T-tail, the V-tail, and the canard. To define which configuration to size the empennage for, a brief trade-off was performed. Table 7.3 summarises the main advantages and disadvantages of each of the three options.

Table 7.3: Empennage configurations comparison.

Configuration	Advantages	Disadvantages
V-tail	Lower Structural Weight	Decreased Control Effectiveness
Canard	Positive Lift	Possible Unrecoverable Stall
T-tail	Lower Interference Drag, Improved Fin Efficiency	Deep Stall Considerations, Structurally Heavy

Among them, the V-tail configuration was the first one to be discarded. Indeed, although structural weight savings can be achieved by having two control surfaces instead of the elevator and rudder for standard pitch and yaw control, the disadvantages related to this configuration out weight this benefit. The main drawback of this configuration is related to the fact that the control surfaces would be subjected to the turbulent flow generated by the rotors, consequently additionally affecting the control effectiveness.

When looking at the canard configuration, the following considerations have instead been made: the canard is located in front of the main wing, and it is, therefore, able to provide positive lift helping the wing to support the weight of the aircraft. As a consequence, a lower wing surface area is required. On the other hand, a centre of gravity shift behind the aerodynamic centre of the main wing would result in a dangerous pitch up moment, which is hard to recover from.

Finally, the main advantages of the T-tail configuration can be summarised in lower interference drag and improved fin efficiency. The lower interference drag is because only the lower part of the horizontal stabiliser is connected to the vertical fin, while the enhanced fin efficiency results from the horizontal stabiliser itself preventing the flow of air to flow from the pressure side to the suction side of the fin. A smaller vertical fin surface area would, therefore, result as a consequence of these benefits [101]. A significant disadvantage of this configuration concerns the so-called deep stall, meaning that once the aircraft enters a stall at high angles of attack, such stall is challenging to recover, due to the turbulent flow generated by the stalling main wing [101]. Besides, T-tail configurations are structurally heavier than standard configurations to support the extra moment created by the horizontal stabiliser being located at the top of the vertical fin.

In conclusion, while the canard and T-tail are preferred over the Vtail, it is hard to choose between the remaining two options only based on high-level considerations. A stability and controllability analysis is therefore performed in section 7.3 to assess which configuration is the most feasible for the design.

7.3 Empennage Sizing

The sizing of the empennage follows from satisfying the stability and controllability requirements. The stability and controllability curves delimit the design space where both of them are satisfied in the scissor plot. Combining such a plot with the centre of gravity range for various wing position allows for defining an optimum value for the horizontal stabiliser surface area. While fundamental considerations about the scissor plot are presented in subsection 7.3.1, the payload diagram from which the centre of gravity ranges can be defined is discussed in subsection 7.3.2. The outcomes resulting from the combination of the two are instead presented in subsection 7.3.3. Finally, the approach followed for the sizing of the vertical fin surface area is explained in subsection 7.3.4.

7.3.1 Scissor Plot Diagram: Lifting-Body Fuselage Contribution

Given that a lifting body fuselage is implemented in the design, the performed analysis also takes into account the additional lift that the fuselage itself produces in addition to the one of the main wing and the tail. The main lifting forces affecting stability and controllability for a T-tail aircraft are sketched in Figure 7.4. A comparable sketch and the following reasoning can similarly be done for a canard configuration.

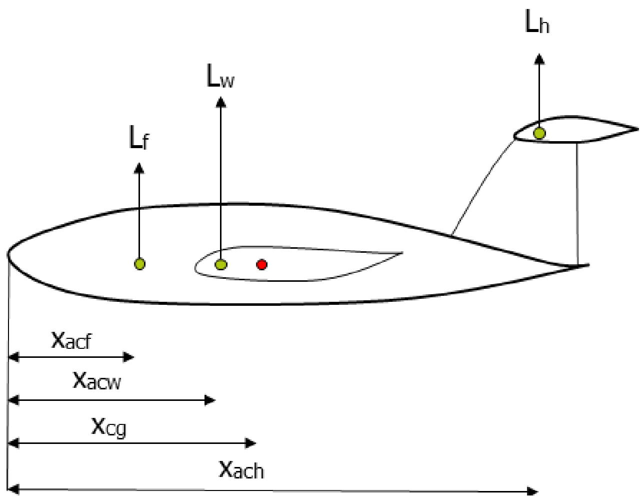

Figure 7.4: Sketch of the lifting forces acting on the aircraft.

It has been assessed that for a T-tail configuration the lift generated by the fuselage negatively affects the stability and the controllability of the aircraft. This conclusion can be drawn on the basis of Equation 7.5 and Equation 7.6 which have been derived to assess the influence of the fuselage on the empennage design space:

$$\frac{S_h}{S} = \frac{\overline{x_{cg}}}{\frac{C_{l_\alpha h}}{C_{l_\alpha w}}(1-\frac{d\epsilon}{d\alpha})(\frac{V_h}{V})^2\frac{l_h}{c}} - \frac{\overline{x_{ac}} - SM - \frac{Cl_{\alpha f}}{C_{l_\alpha w}}\frac{S_f}{S}\frac{l_f}{c}}{\frac{C_{l_\alpha h}}{C_{l_\alpha w}}(1-\frac{d\epsilon}{d\alpha})(\frac{V_h}{V})^2\frac{l_h}{c}} \tag{7.5}$$

$$\frac{S_h}{S} = \frac{\overline{x_{cg}}}{\frac{C_l h}{C_{lw}}(\frac{V_h}{V})^2\frac{l_h}{c}} + \frac{\frac{C_{mac_w}}{C_{lw}} - \overline{x_{ac}} + \frac{C_{mac_f}}{C_{lw}} + \frac{C_l f S_f \cdot l_f}{C_{lw} S \cdot c}}{\frac{C_l h}{C_{lw}}(\frac{V_h}{V})^2\frac{l_h}{c}} \tag{7.6}$$

where the down-wash $\frac{d\epsilon}{d\alpha}$ and the velocity ratio $\frac{V_h}{V}$ take a value of 0 and 1 respectively due to the T-tail configuration. When looking at Equation 7.5, the contribution of the fuselage is represented by the term $\frac{Cl_{\alpha f}}{Cl_{\alpha w}}\frac{S_f}{S_w}\frac{lf}{c}$. Since such term is positive, the stability curve shifts upwards in comparison with the one of a standard configuration, moving the aerodynamic centre of the wing towards the leading edge of the mean aerodynamic chord. Consequently, the design space available for the sizing of the tail results to be reduced. The effect of the term $\frac{CM_{acf}}{Cl_w} + \frac{Cl_f S_f l_f}{Cl_w S_w c}$ has also an analogous effect by shifting the controllability curve upwards.

7.3.2 Payload Diagram

To correctly size the horizontal stabiliser, it is necessary to know the location of the empty weight centre of gravity and how the centre of gravity itself moves when the payload and the fuel are loaded on the aircraft. The location of the different main components of the OEW and the related weights are reported in Table 7.4. Furthermore, the loading diagram of the aircraft corresponding to the final OEW location of 0.465 of the MAC is reported in Figure 7.5.

Table 7.4: Longitudinal position of the subsystem components from the aircraft nose.

Fuselage [m]	4.87	Wing [m]	3.48
Fixed Equipment [m]	3.28	Radiators [m]	4.32
Nose Landing [m]	0.86	Nacelle [m]	4.32
Main Landing [m]	4.54	Propellers [m]	3.32
Cargo [m]	6.81	Horizontal Stabiliser [m]	9.24
Fuel Cell [m]	7.78	Vertical Stabiliser [m]	9.24
Battery [m]	2.92		

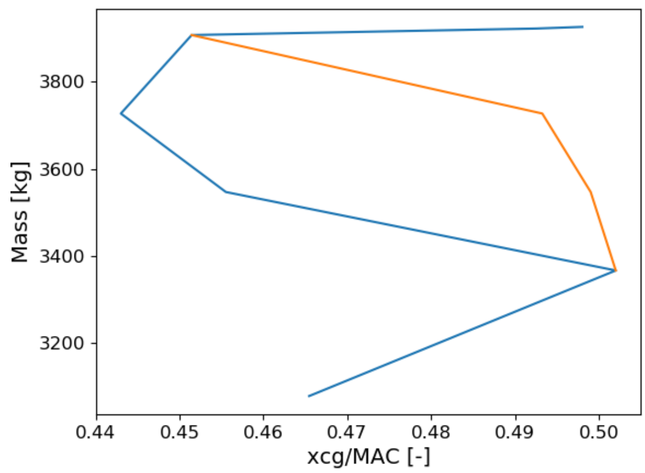

Figure 7.5: Loading diagram.

When looking at Figure 7.5, the first line drawn at the bottom of the diagram represents the loading of the cargo in the cargo compartment. Secondly, the passengers are loaded, from the front to the back and vice versa, as shown by the blue and the orange line respectively. The zero fuel weight sums up to a value of 3907 kg. Finally, the weight of the fuel is added, therefore reaching a MTOW of 3925 kg as shown by the top blue line. As can be seen from the diagram, the maximum centre of gravity shift ranges from 44% to 50% of the MAC.

7.3.3 Combining the Scissor Plot and the Centre of Gravity Range Diagram

Figure 7.6 and Figure 7.7 show the results of the combination of the scissor plot and the centre of gravity range diagram for the T-tail configuration and the canard respectively. It can be noticed in Figure 7.6 that a negative surface area is obtained for the canard. As a consequence, a T-tail configuration is chosen. Although there is an optimum at a different points, the centre of gravity range is constrained to have a most aft position of 0.5 of the MAC behind the wing corresponding to the location of the rotor in the vertical position. The centre of gravity is constrained to this point to be able to make a proper use of the swashplate in vertical control. The centre of gravity must lay in front of the rotor line for the aircraft to automatically tip forward, rather than back. Furthermore, a tail over the main wing surface area ratio of 0.13 is chosen instead of 0.06, the optimum value shown in the plot. This choice is because a surface area ratio of 0.6 seems unfeasible when compared to the ones of the reference aircraft listed in subsection 7.4.1; also, a bigger $c.g.$ range is achievable when the surface area is increased. An horizontal tail surface of 2.69 m^2 is therefore obtained. For this tail surface area, a corresponding wing position is also determined. The leading edge of the wing is positioned at 34% of the fuselage length to achieve stability.

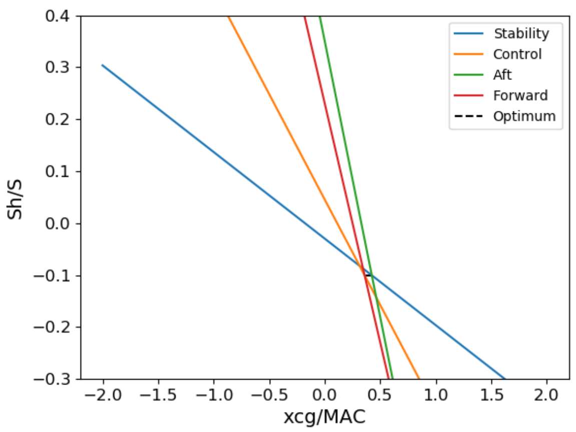

Figure 7.6: Scissor plot canard configuration.

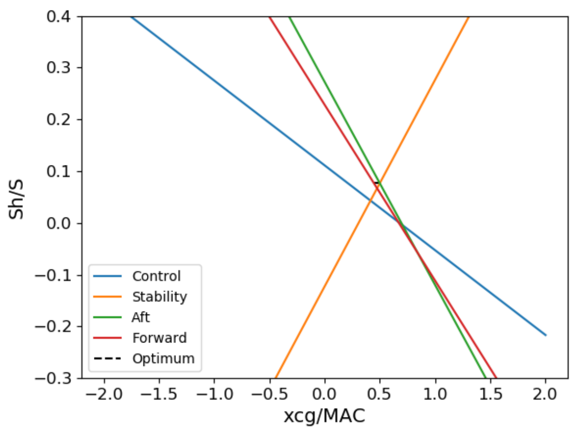

Figure 7.7: Scissor plot T-tail configuration.

7.3.4 Vertical Fin Sizing

The sizing of the vertical tail is usually done considering the situation in which one engine is inoperative. The required tail surface area has to be able to generate enough lift to counteract the moment created by the operative engine about the centre of gravity and to keep the side slip angle at 0°. The most critical condition the tail shall be sized for is at speeds close to the stall speed, when the lift generated by the fin is the lowest. The thrust required to overcome the drag in this condition is 2187.77 N, therefore resulting in a moment of 11299.8 Nm.

A lift coefficient value of 0.764 has been retrieved from Javafoil based on the selected NACA0018 airfoil (see subsection 7.4.1), to which a maximum rudder deflection of 8° has been applied to counteract such moment. Furthermore, a rudder over vertical tail cord ratio of 0.415 has been derived knowing the rudder over vertical fin surface area from reference aircraft as reported [30]. A tail surface area of 1.68 m^2 has therefore been calculated.

7.4 Control Surface Sizing

After defining the vertical and horizontal tail surface area, as explained in section 7.3, the related planform geometry can be defined, and the empennage and main wing control surfaces can be sized. This is done in subsection 7.4.1, subsection 7.4.2 and subsection 7.4.3 respectively. In subsection 7.4.4 the swashplate and nacelle swivels are analysed.

7.4.1 Empennage Planform Geometry

The main parameters characterising the geometry of the horizontal and vertical surfaces are shown in Table 7.5 with their related numerical value. Each of these values has been defined based on reference twin-engine propeller aircraft as reported in [30]. Such values are also shown in Table 7.5. Among the different aircraft categories for which relevant data are provided in [30] the twin-engine propeller aircraft are the most comparable ones to the configuration chosen for Futura, and they have therefore been taken as a category of reference. In particular, the Cessna 402B, the Cessna 414A, the Piper PA-31P, the Duke B60, and the Piaggio P166-DL3 present a gross weight and cruise performance comparable to the ones required for Futura [30].

Table 7.5: Planform geometry values.

	Horizontal Stabiliser		**Vertical Tail**	
Parameter	**Reference**	**Assigned Value**	**Reference**	**Assigned Value**
Aspect Ratio	3.7-7.7	4	0.18-1.8	1.2
Sweep Angle	0-17	0	18-45	18
Taper Ratio	0.48-1	1	0.33-0.74	
Airfoil	NACA009-NACA0018	NACA0018	NACA009-NACA0018	NACA0018
Dihedral	0-12	0	90	90

A brief explanation is here below provided for the main values chosen:

- **Aspect Ratio**: given that for subsonic aircraft the horizontal stabiliser aspect ratio ranges between 3 and 5 a value of 4 has been selected, resulting in a cord of 0.82 m and a span of 3.26 m. For the vertical fin, a value of 1.2 is instead considered appropriate for a T-tail configuration according to what reported in [102]. Knowing the vertical fin surface area, a cord of 1.18 m and a span of 1.42 m is therefore derived.

- **Sweep Angle**: no sweep angle is applied to the horizontal stabiliser. The main advantage of sweep is indeed to reduce the drag divergence Mach Number. However, at low speeds, drag divergence is not an issue, and consequently, there is no need to sweep the horizontal tail. For the vertical tail, a minimum sweep is given by the reference values reported in Table 7.5. A swept fin would increase the vertical tail arm, which is not necessary for the current configuration. Furthermore, also indicates a value of around 20° for aircraft flying at low Mach numbers [102].

- **Taper Ratio**: although the range proposed in Table 7.5 goes only up to 0.74 for the vertical fin, because of the additional structural weight imposed by the horizontal stabiliser on the fin itself, a taper ratio of value 1 seems more suitable for a T-tail configuration, as also reported in [102]. The same taper value applies to the horizontal tail.

- **Airfoil Selection**: typically symmetrical airfoil are used for the empennage since both, positive and negative lift have to be provided by the horizontal tail and the vertical fin. A thickness over chord ratio of 0.18 has been furthermore chosen due to its high stall angle of attack, therefore guaranteeing pitch control even after the stall of the main wing.

7.4.2 Empennage Control Surfaces Sizing

The sizing of the empennage control surfaces of the horizontal stabiliser and the vertical tail is done following two different approaches. The elevator dimensions are obtained from the mentioned reference aircraft, from which the elevator surface area is estimated to be 27.5% of the overall tail surface [30]. Consequently, given the defined tailplane geometry, an elevator cord of 0.22 m is obtained. The dimensions of the rudder follow instead from the sizing of the vertical fin as described in subsection 7.3.4: being the rudder cord 41.5% of the vertical fin cord, a rudder area of 0.69 m^2 is consequently derived. Table 7.6 summarises the discussed results.

Table 7.6: Elevator and rudder dimensions.

	Elevator	Rudder
Surface Area $[m^2]$	0.73	0.69
Cord $[m]$	0.22	0.49
Span $[m]$	3.26	1.42

7.4.3 Aileron Sizing

The sizing of the aileron has been done together with the sizing of the flap, resulting therefore in a flaperon device which combines the functions of both of the systems. The choice of implementing flaperons comes from the need of satisfying a rolling requirement of 0.8 rad in 1.3 s, which is related to the Class I weight category the aircraft belongs to. Following the stepwise approach as explained in [34] and based on the defined wing geometry, a control surface with a chord of 0.5 m and a span of 2.86 m has been designed. The controlled surface so defined allows for a roll rate of 1.029 rads^{-1} with a deflection angle of 15 $\deg$ therefore satisfying the required roll rate. It has been assessed the fact that since the flap already spans over 2.86 m out of the wing half span, sizing the aileron separately on the basis on the remaining available space, would have resulted into a roll rate of 0.38 rads^{-1}. Combining the aileron and the flap into a flaperon was, therefore, the only feasible solution for the roll rate required to be satisfied.

7.4.4 Vertical Control Sizing

To size, the vertical control, a description of both the collective and nacelle hinges are required. Collective is sized according to constraints of different subsystem parts whereas the nacelle is sized according to required torque required for rotation and the maximum and minimum angular setting.

Swashplate

The swash plate is comprised of collective and cyclic. The collective angle must range between$0°$ and $17°$ to supply the full range of the blade performance. For this to be possible, the connections of the blades must be feathered so they can rotate. The collective raises the non-rotating part of the swashplate up and down changing the respective pitch of the blades equally. Cyclic tilts the non-rotating part of the swash plate laterally and longitudinally. This changes the location of the thrust over the centre of the c.g. to create moments that rotate the aircraft appropriately. To actuate the swashplate, three hydraulic actuators are needed to control the height and orientation, in 4 dimensions. For cyclic to be possible flapping capabilities must also be available to prevent over-stressing the blade with constantly changing lift in each rotation. This can be accomplished using an articulated rotor head [103].

Nacelle Hinge

The nacelle range of the aircraft range between completely horizontal, level with the wing at $0°$, and $5°$ beyond vertical, at $95°$. The movement past $90°$ allows for the aircraft to move rearwards.

Rotation of the nacelle requires a torque on the nacelle about the y-axis of the aircraft, out of the wing. The x-axis is fixed to the rotor shaft, and the z-axis is defined in a right-hand coordinate system. The torque needs to accelerate the nacelle about its vertical position. Pilots prefer a control response motion that is not too sluggish yet not too oversensitive. Different pilot preferences are given for response rotation in a given time by experiment and can be seen in Table 7.7 [47].

Table 7.7: Pilot Rotational Preference Response [47].

Axis	Time [s]	Minimum Response [rad]
Longitudinal	1	0.046
Lateral	0.5	0.028
Yaw	1	0.112

Assuming a constant acceleration on the nacelle hinge, the required nacelle rotational acceleration can be found for yaw preferences. For yaw, about the z-axis of the body, the nacelles are assumed to rotate in opposite directions, from the purely stationary vertical position, resulting in a nacelle acceleration of 0.443 rads^{-2}. The moment of inertia of the aircraft was calculated by assuming rotation about two solid cylinders, the fuselage, and the wing. The pitch rate is not constraining as the swashplate can achieve it. From this acceleration, the required torque to rotate can be found using Equation 7.7.

$$I_{yy}\frac{d\omega_y}{dt}+\omega_x\omega_z(I_{xx}-I_{zz})=T_y \tag{7.7}$$

Although there is a rotational velocity on the x-axis, for the rotor along the shaft, there is none along the z-axis, resulting in only the moment of inertia term to calculate the required torque. The nacelle is defined as a cylinder for the moment of inertia calculation. To rotate the 240 kg nacelle at the desired rate, a torque of approximately 43 Nm is required. The method to actuate is a hydraulic force swivel connection. This is chosen in favour of a servo because a large, instantaneous torque is needed in a small space. The mechanism is proven in this application by a similar use by Eaton in the V-22 Osprey [104]. For the equivalent equation to Equation 7.7 in the z-direction, there is a torque exerted due to the rotation in both the y-direction (nacelle rotation) and x-direction (rotor rotation). Considering the rotation of the rotors at 60 rads^{-1} the torque exerted on the wing is 4000 Nm which is significantly less than the bending loading of the wing about the x-axis.

7.5 Aircraft Control Methods

With the stability and controllability of the aircraft established the control system to coordinate the required operation is needed. There are several important aspects to the control system which are discussed, namely: the pilot inputs, the dynamic control system, and the navigational control system.

7.5.1 Pilot Inputs

The inputs of such an aircraft are complicated as the controls must be mixed and described for different phases of flight. For helicopters, pilots make use of a lever for collective, with a rotating handle for throttle, and a column for lateral and longitudinal pitch. For general aviation, a throttle lever is used along with either a column or stick. For weight considerations, especially when considering redundancy, fly-by-wire is used for this application. Fly-by-wire is also used because it poses many benefits for simpler integration of automatic control methods. Different solutions exist for creating a safe and intuitive pilot input system, such as separate controls, controller mixing, and control modes. Because there is only one pilot, it is better only to have one set of controls that can be held simultaneously and that require minimal input.

This results in two placements for the hands of the pilot. The first is a collective lever on the left side of the pilot. Pulling the lever forwards or backward changes the collective of the two rotors simultaneously. The hand grip of the lever rotates to control the throttle of the engines, and the top of the lever has a rotating switch to control the rotation of the nacelles simultaneously. The control system manages the differential control of the collective and nacelle rotation. On the right hand is the stick input that can be moved forward, backward and from side to side to control the pitch and roll of the aircraft. The top of the stick has a simple joystick to move backwards and forwards to control the trim on the elevator. Finally,

the pilot has two pedals that can be used to control the yaw of the aircraft. The controls must have a feedback force for the pilot to understand the current state of controlling the aircraft.
The main philosophy is that the pilot controls the change in state required and the flight control system converts that to different inputs based on the state of the flight. This will be discussed in section 7.5.2.

7.5.2 Flight Control System

The flight control system comprises both the dynamic flight controller and the guidance control, both of which are discussed in this section

Dynamic Control

There are two vital aspects to the control such that an aircraft can transition between different modes of flight. The first is the control modes, and the second is the coupling of the control mechanisms.
The control modes are dependent on the flight conditions during which the pilot does control inputs. A simple way for the control system to understand the state of the aircraft is to base the control mode on the nacelle rotation. As the nacelles rotate forward the control inputs from the pilot on the stick and the pedals translate to different outputs through the control computer. The stick will continuously cause changes for the elevator and the flaperons as they can be used at low airspeeds as well. As the nacelle rotates forward, the cyclic control output from the computer phases out as the control mode of the cyclic becomes more coupled with other motions. The cyclic control must not phase out before $45°$ because the constant forward velocity to be sustained by wings has not necessarily been achieved yet. The value for this transition must be developed further with testing. However, a preliminary value of $45°$ can be taken.

During the phasing of the two different control systems many automatic processes must take place; such as, the control of the flaperons for maximum lift during the transition, control of the motor torque for collective changes, and coupled controls in hover which will be discussed next [103].

The main cross-coupling effects in hover for a helicopter are collective - yaw, collective - lateral cyclic, and longitudinal - lateral cyclic. A change in collective on the blades will require a change in applied torque by the motor controllers. This torque exerts a reaction torque on the aircraft. To mitigate this issue, the two rotors must be counter rotating. With the pilot only inputting the same collective setting simultaneously the torque change on both shall counter each other, resulting in no yaw. Secondly, after a lateral control input, the aircraft rotates, and the thrust has a component in the lateral direction. To counter this, the aircraft must have an automatic control system that turns the aircraft in the opposite lateral direction after the sufficient rotation has been achieved. Finally, the longitudinal and lateral cyclic coupling is mitigated by mixing the controls in the swashplate [103].

To measure the state of the aircraft, a multitude of sensors are required. To measure the velocity of the aircraft, two pitot tubes are installed on either side of the aircraft near the nose. An angle of attack sensor is required as well. An Altitude and Heading Reference System is needed to measure the roll, pitch, and yaw during flight. GPS and radar data is needed as well to understand the heading and global position of the aircraft. To control the outputs, sensors for the actuators of the forward flight control surfaces, swashplates and nacelle hinge, as well as the motor controllers, must transmit data to the computer. This can be seen in section 9.4.

Navigation Control

Navigation control is essential to flight planning. The navigational control serves as additional inputs to the dynamic control system, apart from the pilot inputs, to reach the correct heading. Route planning is set before the flight begins based on allowed airspace, optimal distance covered, and velocity during flight [105]. The pilot can change waypoints during the cruise in flight. Error in position for control system guidance is reliant on accurately measuring the state. To do this, an extended Kalman Filter is employed to aggregate different data and predictions to more accurately estimate the state [105]. The combination of the dynamic control and navigation control can be seen in Figure 7.8.

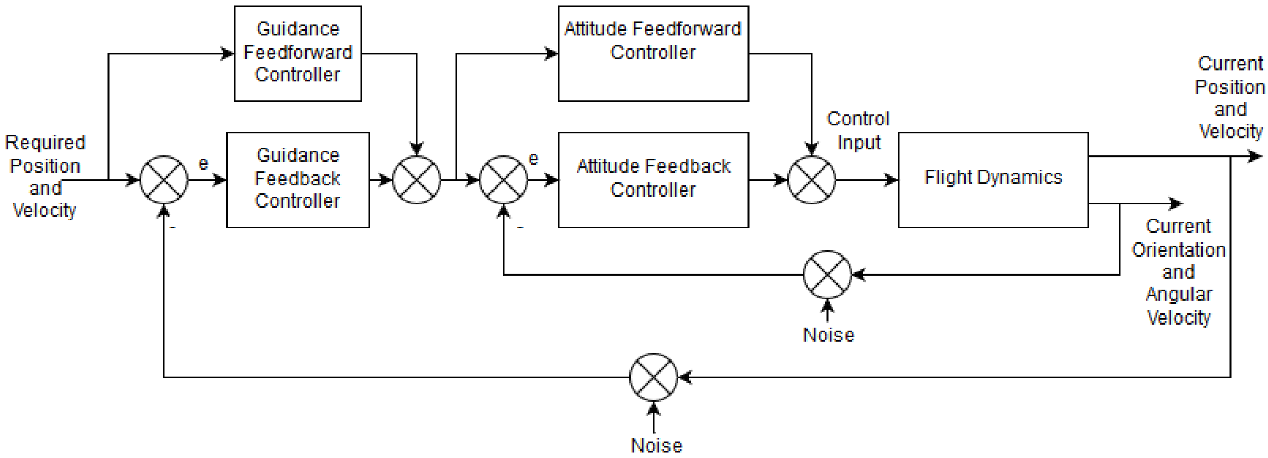

Figure 7.8: Block diagram of flight control system [105].

7.6 Mass

The mass of the control mechanics hardware must be estimated. The mass of the hydraulic, control surfaces and required electronics are estimated statistically based on the previous aircraft in the same weight category [40]. With a safety factor of 1.5 for the mass of the hydraulic system is approximately 175 kg. The weight of the nacelle swivels are in total approximately 40 kg [104]. The mass of the avionics are estimated in section 5.3. The rudder and elevator weights are included in the empennage structural sizing in section 8.3.

7.7 Validation

The horizontal and vertical empennages are smaller than aircraft of the same class [30]. Although the surface areas obtained are roughly twice as small than the average reference areas, the area ratio of the horizontal stabiliser over the vertical fin is comparable, resulting in a value of 0.62 against a value of 0.64 from the references. For the vertical control methods, the systems are comparable to that of the V-22 and the AW609. However, as the control system is a critical point of failure in the system, it must be rigorously tested in development, especially in consideration of having a single pilot [106].

Conclusion

The nose gear is placed 3.4 m in front of the centre of gravity and the main landing 0.28 m behind to provide ground stability and manoeuvrability. For in flight, the control methods of the aircraft are determined as swashplate and nacelle rotation for vertical control and a T-tail for horizontal flight control. The empennage is sized for stability and controllability, resulting in the centre of gravity range from the rotor to 5% of the MAC in front of the centre of gravity. The wing must be positioned at 34% of the fuselage, from the nose, for optimum stability. The empennage planform is design as well as the planform control surfaces. The required mechanisms on the swashplate are described as well as the necessary torque on the nacelle for vertical stability. Finally, the pilot inputs, of a stick and lever collective, are defined as well as the combination of the dynamic and navigational control system.

8. Aerodynamic Surfaces Structures

The main goal of the aerodynamic surfaces is to provide lift, stability and control to the aircraft. To perform this task, they have to be connected to the aircraft fuselage and be able to carry the aerodynamic and static loads encountered during operations. This chapter focuses on the structural sizing of both the wing and the empennage. First, the operating loads and the structural layout of the component is described. Furthermore, the structural calculations involved in the sizing process are discussed as well as verified and validated. Finally, structural weight results will be presented. In section 8.1 the methodology for analysis is presented, followed by the structural analysis of the main wing structure in section 8.2 and finally an analysis of the empennage structures is carried out in section 8.3.

8.1 Methodology

8.1.1 Calculations

To analyse the structure of the wing, a few critical structural features were selected. The first feature is the yield stress in the skin. The stress is skin is calculated using Von Mises stress as a combination of the bending stress and the shear stress on the skin. The stress taken account for in Von Mises stress can be seen in the equation

$$\sigma_v = \sqrt{\frac{\sigma_y^2 + 6\tau_{xz}^2}{2}} \tag{8.1}$$

Where σ_y is the direct stress due to bending and τ_{xz} is the shear in xz-plane due to torsion and shear loading. The shear is calculated assuming a symmetrical wing box with shear centre at the middle of the box and boom idealisation on the stringers in the box. The second critical structural feature is the buckling stress of the panels due to the stiffener pitch on the skin. The buckling strength considers the effect of the stiffener width on the effective panel strength. Buckling stress is calculated using equation

$$\sigma_{cc\,\text{panel}} = \frac{(A_{\text{stiffener}} + 2w_e t_{\text{skin}})(\sigma_{cc})_{\text{stiffener}} + (b - 2w_e)t_{\text{skin}}\,\sigma_{cr}}{A_{\text{stiffener}} + bt_{\text{skin}}} \tag{8.2}$$

where $A_{\text{stiffener}}$ is the area of a stiffener, w_e is the effective sheet width due to stiffener width, $(\sigma_{cc})_{\text{stiffener}}$ is the crippling stress of the stiffener, b is the stiffener pitch, t_{skin} is the thickness of the skin and σ_{cr} is the buckling stress of the plate without stiffeners. With an aspect ratio the pitch of the ribs can also be determined.

8.1.2 Verification

Verification of the calculations was done by comparing results with hand calculated values for each function in the code, such as the moment of inertia, boom idealisation and stresses. As well, the code is fed example structural sizing problems, and the results come out as the example solutions [41].

8.2 Wing Structure

The main wing is the most critical structural member of the aircraft as it provides the load path from the rotors to the fuselage in hover, as well as from the lift to the fuselage. In the particular case of Futura, the wing also has to house radiators. The combination of different load cases for different phases of operation together with the integration with the radiator assembly makes the design of the wing particularly challenging.

8.2.1 Design Conditions and Layout

The primary purpose of the wing, as mentioned, is to provide a load path for aerodynamic as well as static loads to the fuselage. Futura uses a cantilever wing that is clamped at the fuselage. The main statics load carried are the weight of the wing itself, the weight of the nacelle including its sub-components and the weight of the radiators together with the coolant in the radiators. The main aerodynamic load in hover is the thrust generated by the rotor while in cruise it is the lift generated by the wing. For the preliminary structural sizing, the weights in the y-direction (concerning the reference frame of Figure 8.1 and Figure 8.2), as well as torques along x, are taken into account to converge to a preliminary structural weight. This weight will then be compared to statistics to judge how the sizing approach compares to previously build wings.

Loads

The loads encountered during hover and supported by the wing are depicted in Figure 8.1 and they include the radiator, wing and nacelle as well as the thrust generated by the rotors. This loading case reaches its maximum under gusts loads according to CS-29 with a load factor of up to 3.5 as specified in section 5.2 [35]. The internal moment at the root can be calculated with Equation 8.3 while the internal shear is just the sum of forces without arms.

$$M_{root} = T \cdot (b/2) + W_{nacelle} \cdot (b/2) + W_{radiator} \cdot (b/4) + W_{wing} \cdot (b/4) \tag{8.3}$$

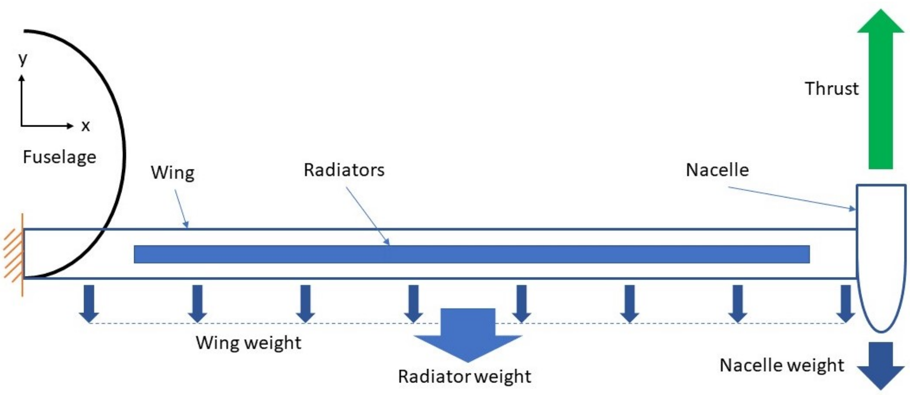

Figure 8.1: Wing loads in hover.

The second load case, encountered in cruise, is depicted in Figure 8.2. Here the thrust from the rotor is replaced by the lift generated by the wing. The lift distribution over the span has been simplified to a linear lift distribution up to 75% of the span while a triangular lift distribution was assumed up to the tip [107]. Under gust loads, according to CS-23 regulation, the load factor in cruise reaches 3.8, as shown in section 5.2.

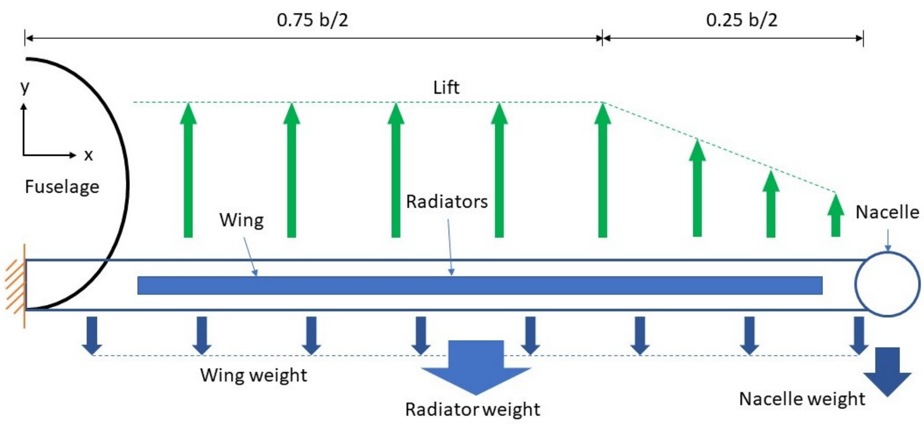

Figure 8.2: Wing loads in cruise.

are carried

$$M_{root} = q_L \cdot 0.75 \cdot \frac{b}{2} \cdot \left(0.75 \cdot \frac{b}{2}\right) + q_L \cdot 0.25 \cdot \frac{b}{2}/2\left(0.75 \cdot \frac{b}{2} + 0.25 \cdot \frac{b}{2}/3\right) \cdot W_{nacelle} \cdot \left(\frac{b}{2}\right) + W_{radiator} \cdot \left(\frac{b}{4}\right) + W_{wing} \cdot \left(\frac{b}{4}\right) \tag{8.4}$$

Layout

The main structure of the wing consists of two boxes that carry all the main loads. The two box configuration was chosen as the radiators are placed in the middle of the wing and the skin in this point has to open to allow air-flow through the wing. Stringers are placed along the span to provide additional rigidity and resistance to buckling. Finally, spars are placed along the span to transfer torque loads between the two boxes and keep the aerodynamic shape of the wing.

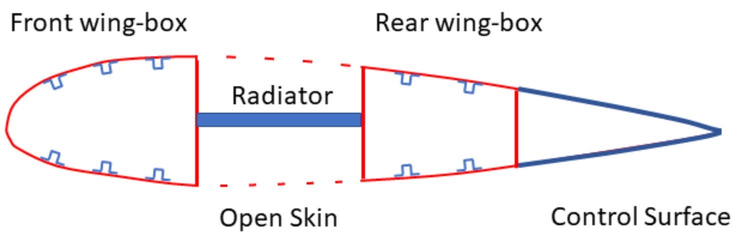

Figure 8.3: Wing structural cross-section.

The hat stringers were chosen to be the most efficient possible in terms of the added moment of inertia and resistance to buckling. Therefore, a hat stringer was chosen [41]. To simplify and reduce manufacturing costs, the same stringer cross-section as used in the tail surfaces was chosen (Figure 8.6). Finally, as the wing has the same cross-section along the span, it was decided to design a constant-thickness structure to simplify the manufacturing and the assembly further.

The material selected for the wing is aluminium 2024 T6 (Table 8.1). This decision was taken after a preliminary analysis showed that composites would lead to a decrease in weight that was not needed as the aircraft was well below the MTOW. Therefore, the cheapest and easier to recycle aluminium alloy was selected that was still able to sustain all the loads and remain within the bounds of the MTOW requirement. It has to be underlined that to use such material, protective coatings against corrosion have to be applied [41].

8.2.2 Structural Optimisation and Results

As the geometrical layout is given by aerodynamics and systems integration, the three main variables that influence the structure are the thickness of the spars, the thickness of the skin and stringer pitch. To calculate the weight of the structural stresses have been analysed according to the methodology explained in section 8.1 for a combination of these three variables yielding to an optimised final design. First of all, the critical case has been identified as being the hover phase as this phase induces the highest internal moments at the root. This is because the aircraft is lifted from the tip of the wing having a moment arm of $b/2$ while at cruise, the effective lift acts closer to the root. If the distributed lift is q_L and the distribution is rectangular up to $0.75b/2$ and triangular until $b/2$ then the acting arm can be calculated with a weighted average of the rectangular and triangular distributions to be at $0.44b/2$. The 11% increase in load factor in cruise is lower than the 56% reduction in arm confirming the hover as the critical phase.

Furthermore, some boundary conditions are imposed for the optimisation.

- The overall von Mises stress in the structure shall not be higher than the yield stress to comply with the regulation

- The skin buckling stress should be as close as possible or higher than the bending stress to avoid buckling and to avoid over-designing the structure for buckling
- The mass should be minimised in the final available design space

Another boundary was set for the spar thickness. This is done because from a theoretical point of view having only skin and no spar would generate a higher moment of inertia but would not be able to give structural support to the radiators, control surfaces and the hinge mechanism of the nacelle. Thus the spar thickness was limited to the skin thickness to reduce further the manufacturing costs as aluminium panels of the same thickness can be used for most of the wing structure.

The optimisation solution space is represented in Figure 8.4 and clearly shows how the bending stress at the root increases with decreasing thickness and increasing stringer pitch due to the lower moment of inertia. The opposite is true for the buckling stress of the skin panel as thicker skin, and more stringers improve the bearable load before buckling. Finally, the optimum weight of the wing-box structure is found at around 161.38 kg with the structure bearing 213 MPa of von Mises stresses due to internal moment and shear at the root. Furthermore, with a skin and spar thickness of 2.7 mm and a stringer pitch of 16.78cm bending stress of 242 MPa and buckling strength of 243 MPa are reached. From these values, we understand that the critical failure mode of the wing is buckling near the root as both von Mises and bending stresses are lower than the yield stress. On top of this, the weight of the ribs has been estimated by taking the cross-sectional area of the wing and a span-wise pitch of 0.5 meters from similar aircraft representation to be 41.7 kg for a total of 10 ribs per half wing [108]. Finally, the weight of the opening skin with a thickness of 1.5 mm was calculated to be 38.97 kg yielding a total wing structural weight of 241.85 kg.

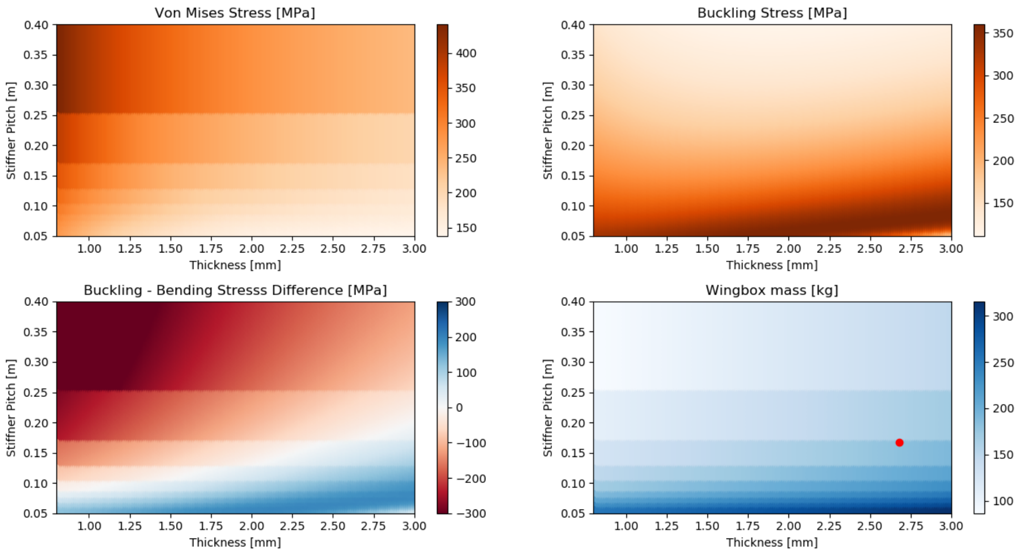

Figure 8.4: Wing structure optimisation design space with final result.

8.2.3 Validation

To validate the results, the final weight was compared to empirical class II weight estimation methods based on statistics as found in Roskam [40]. As can be seen in Figure 8.5, the weight of Futura's wing is 41% higher than the average of comparable wings of traditional aircraft. The main reason is because of the higher stresses in the structure under maximum load in hover as well as the double wing box structure that has a lower structural efficiency than a continuous one.

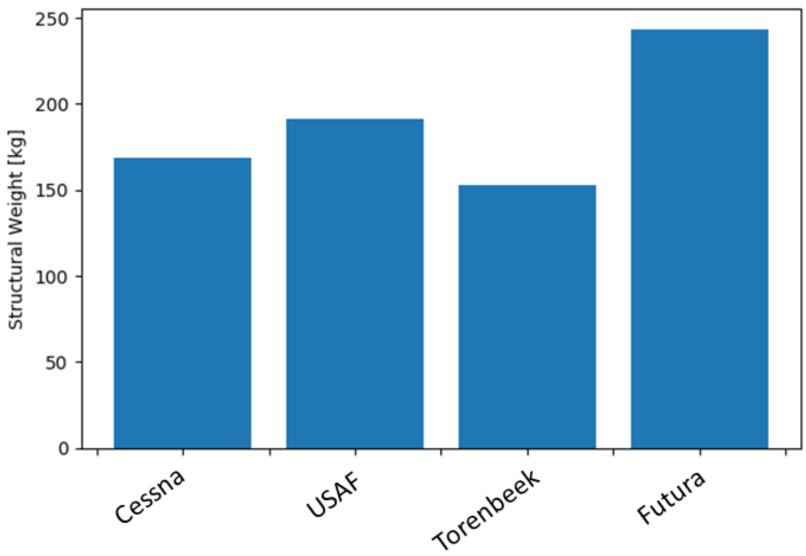

Figure 8.5: Wing weight comparison with empirical design methods.

8.3 Empennage Structure

To sustain the stabilising aerodynamic loads during flight while achieving an adequate mass, a structural analysis of the empennage structures is completed for both the vertical and horizontal stabilisers. Hence the cross-section of the wing box is designed for skin thickness and stiffener pitch.

8.3.1 Stiffeners

The stiffeners chosen for both the vertical and horizontal stabilisers are the same. Hat stringers were chosen for their ability to resist torsion and their large effective width in reducing buckling stress. The dimension of the stiffener can be seen in Figure 8.6. The dimensions were chosen to be minimal to reduce the mass of the wing box, yet maintain structural integrity.

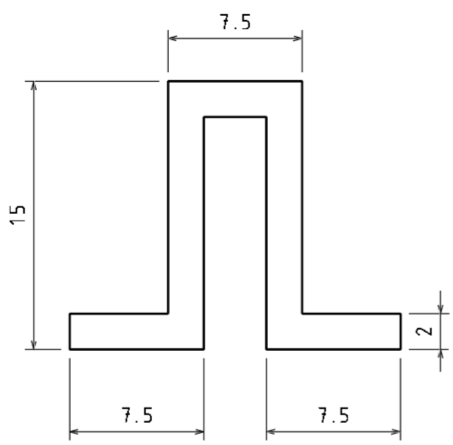

Figure 8.6: Stiffener Cross-section in mm.

8.3.2 Horizontal Empennage

The platform design of the horizontal empennage is described in subsection 7.4.1. With this, the loads acting on the surface can be approximated, and the structural analysis carried out.

Loads

Two types of load act on the horizontal stabiliser during flight, namely a torsional load and the lift. The torque acting on the wing cross section is computed assuming that all the loads are carried by a rectangular shaped torsional box, having a height and width of 0.057 m and 0.389 m respectively. Such box extends from the front spar located at 25% of the cord until the rear spar which is placed at the elevator location, namely at 73% of the cord chapter 8. The shear centre of the section is therefore approximated at the centre of the rectangular box, the point about which the torque is calculated. For symmetric airfoils, a good approximation of the aerodynamic centre through which the lift acts is at 25% of the cord. Hence, an arm of 0.1945 m is obtained. Having defined a lift of 4485 N based on a maximum load factor of 3.8 as established in section 5.2, a torque of 585 Nm is consequently found. Furthermore, given the rectangular planform geometry defined in subsection 7.4.1 the lift is homogeneously distributed along the span and the cord of the horizontal stabiliser.

Materials

Different materials were considered for the structure of the empennage based on previous aircraft. The main materials considered are Aluminium 2024 T6, Aluminium 7075 T6 and Carbon Fibre Reinforced Polymer. For structural calculations, Young's modulus is needed for bending stress, and the Shear Modulus is needed for shear. For analysis of the best materials, yield strength was not considered because the maximum Von Mises stresses in the skin were far below the yield strength for any material. Therefore, the material was chosen based on its density and price. Of the three Aluminium 2024 T6 is the least expensive for a volume of the material. Although Carbon Fibre Reinforced Polymer is much lighter, it performs worse in terms of price and sustainability; end-of-life processes for carbon fibre are less effective. As our design is not too constrained by mass considerations, Aluminium 2024 was selected as the material. Aluminium 2024 boasts good end-of-life solutions as well as good fatigue properties, making it ideal to satisfy the availability requirement by reducing the chance for unplanned maintenance. The material properties can be seen in Table 8.1. It has to be underlined that to use such material, protective coatings against corrosion have to be applied [41].

Table 8.1: Aluminium 2024 T-3 Properties [9].

Young's Modulus [GPa]	73.1	Yield Strength [MPa]	360
Shear Modulus [GPa]	28.5	Density [$\mathrm{kg m^{-3}}$]	2780
Poisson's Ratio [-]	0.33	Price [$\$\backslash\mathrm{kg}$]	2.16

Design Point

The design point of the horizontal stabiliser was chosen to reduce the mass of the cross-section yet maintain sufficient structural integrity. However, because the stress generated at limit loads caused stresses in the skin that did not constrain, the design point was chosen based on validation with other aircraft empennage. In Figure 8.7, the different design criteria for varying skin thickness and stiffener pitch are shown.

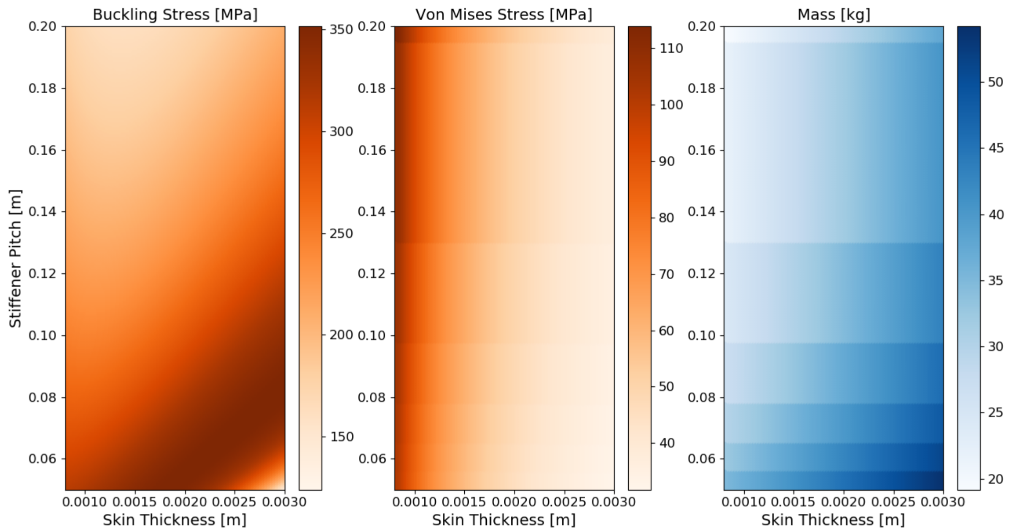

Figure 8.7: Structural properties of the horizontal stabiliser for varying skin thickness and stiffener pitch.

The final design point was chosen as a skin thickness of 1.5 mm, a stiffener pitch of 130 mm and a rib pitch of 330 mm. The rib pitch was found by assuming an aspect ratio of 3 for the skin panels given the supported nature of the panel [41]. This gives a cross-sectional area of the wing box of 0.0025 mm resulting in a mass for the wing box of 34 kg with a 1.5 safety factor. Accounting for the skin, ribs and actuator hinges in the rest of the wing section the total mass is 75 kg. The cross-section can be seen in Figure 8.8.

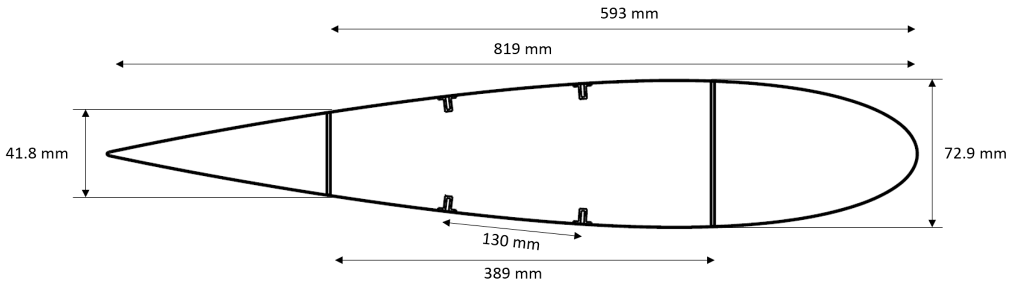

Figure 8.8: Cross-section of horizontal stabiliser.

8.3.3 Vertical Stabiliser

The platform design of the vertical empennage is described in subsection 7.4.1. With this, the loads acting on the surface can be approximated, and the structural analysis carried out. The material analysis for the vertical stabiliser is the same as the horizontal stabiliser.

Loads

The torsional load and lift acting on the vertical stabiliser are determined with the same approach as described in section 8.3.2. However, the torsional loads on the vertical fin are indeed calculated assuming a rectangular wing box extending from 25% to 58.5% of the cord, therefore resulting in a torsional wing box length and height of 0.395 m and 0.094 m respectively. The load case taken into account for the structural sizing of the horizontal stabiliser follows from the vertical fin sizing process as described in subsection 7.3.4 and is therefore based on the aircraft stalling conditions. Approximating the point of application of the resultant lift vector to 25% of the vertical fin cord and 50% of the span a torsional load of 515 Nm and a lift of 1763 N can be determined.

Design Point

The design point of the vertical stabiliser was chosen to reduce the mass of the cross-section yet maintain sufficient structural integrity. However, because the stress generated at limit loads caused stresses in the skin that did not constrain, the design point was chosen based on validation with other aircraft empennage. In Figure 8.9, we see the different design criteria for varying skin thickness and stiffener pitch.

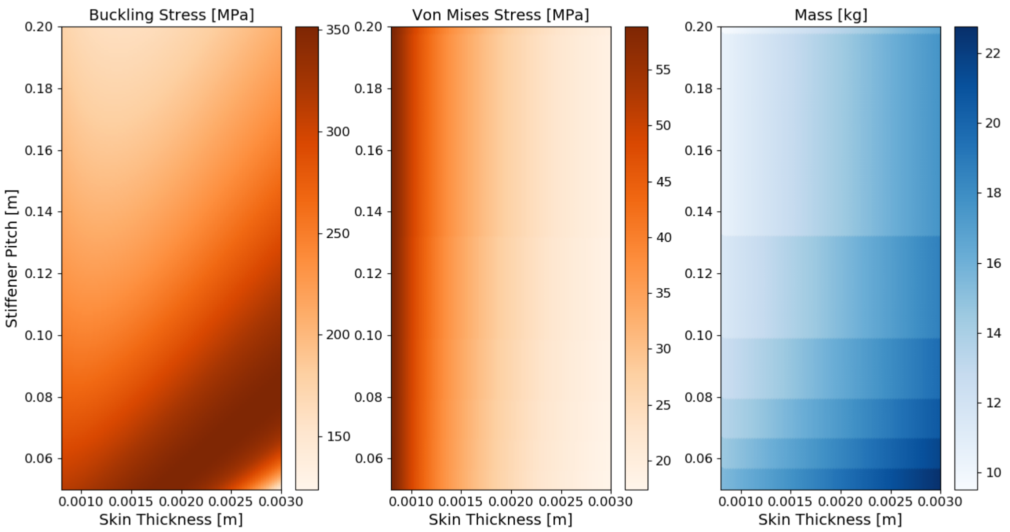

Figure 8.9: Structural properties of the horizontal stabiliser for varying skin thickness and stiffener pitch.

The final design point was chosen as a thickness of 1.5 mm, a stiffener pitch of 131 mm and a rib pitch of 344 mm resulting in 3 ribs. This gives a cross-sectional area of 0.0031 m^2 over the length of the span resulting in a mass for the wing box of 18 kg. Accounting for the skin and actuator hinges in the rest of the wing section the total mass is 43 kg. The cross-section can be seen in Figure 8.10.

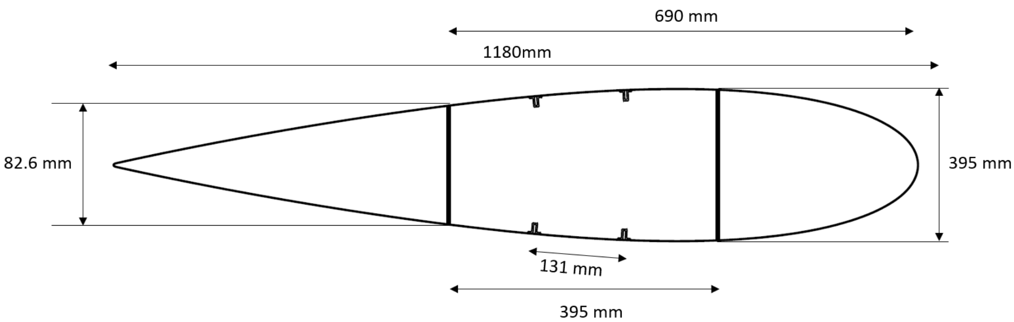

Figure 8.10: Cross-section of vertical stabiliser.

8.3.4 Validation

Statistical estimation puts the total mass of the vertical and horizontal stabilisers at 72 kg. The value for this design is larger by 46 kg [40]. The reason for this larger value is mainly due to the configuration. No taper was used for either the vertical tail or the horizontal tail meaning the mass must be larger than the average twin-propeller engine without a T-tail. Also, the presence of a T-tail required the safety factor of 1.5 to avoid flutter in flight. The structural analysis of the empennage must be further validated in testing both structurally with load tests, and aerodynamically with flutter tests in a wind-tunnel.

For what concerns the surface area values obtained in section 7.3 and subsection 7.4.1 for the horizontal and vertical stabiliser, validation is possible by mean of comparison with reference aircraft data as reported in [30]. It is concluded that, although the surface areas obtained are roughly twice as small than the average reference areas, the area ratio of the horizontal stabiliser over the vertical fin is comparable, resulting in a value of 0.62 against a value of 0.64 from the references. Similar conclusions can be drawn when comparing the elevator over horizontal tail area ratio and the rudder over vertical fin area ratio, resulting in values of 0.27 and 0.41 respectively against values of 0.32 and 0.415 derived from [30].

Conclusion

The wing will have a double wing box structure to allow the integration with other systems. It has four spars, stringers and ribs that support the radiators as well as torque transfer between the wing boxes. The critical load case is reached at a load factor of 3.4 in hover. Using aluminium 2024 T3, the structural weight of the wing reaches an optimum at 241.85 kg. The wing is comparably heavier than traditional aircraft because of the wing box layout and load case encountered. The empennage members are not constrained by the structural loads imposed on them. Therefore, their weight can be minimised, which results in 75 kg for the horizontal stabiliser and 43 kg for the vertical stabiliser.

9. Interface Integration

In this chapter the interface integration of all the systems designed in the previous chapter is presented. First, after all the systems have been designed, the final external layout is presented in section 9.1. Then the results of the iteration tool is outlined presenting the value of the MTOW it converges to. After that the communication flow diagram and hardware and data diagram are presented to show how the systems will communicate and data will be exchanged in section 9.3 and section 9.4. Eventually the mass and power budgets are presented in section 9.6 and section 9.7.

9.1 Futura's Layout

Firstly an overall view of Futura is shown in Figure 9.1.

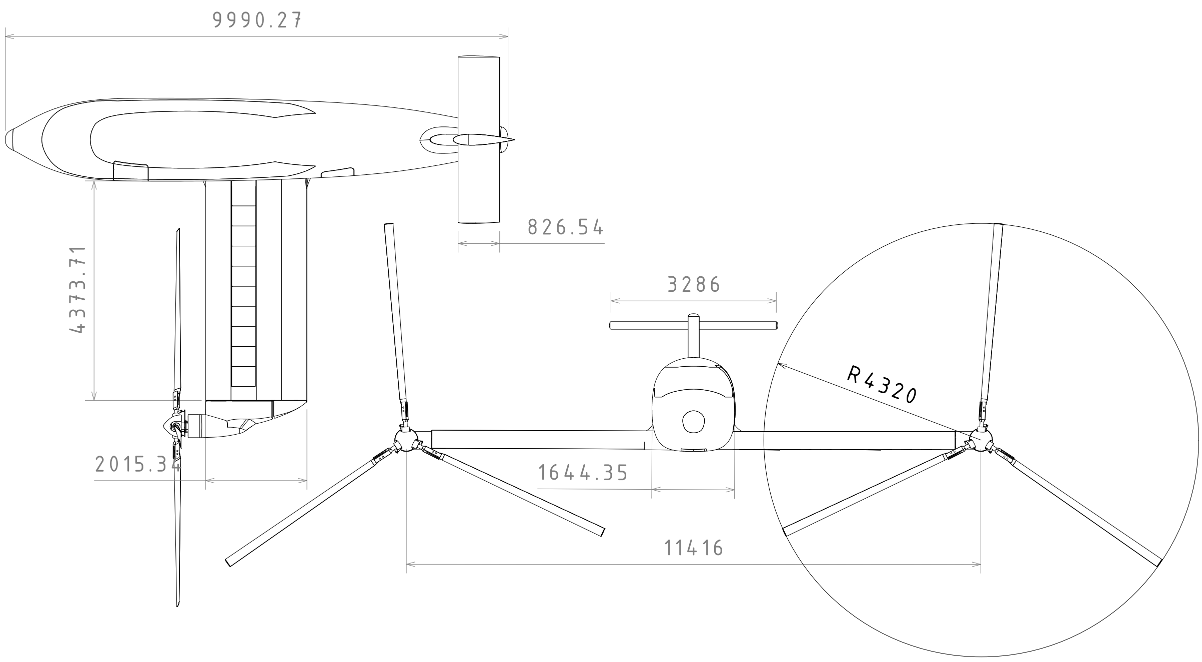

Figure 9.1: Overall Futura's configuration.

An exploded view of the fuselage is also shown in Figure 9.2 in order to show how the subsystems are placed within the aircraft.

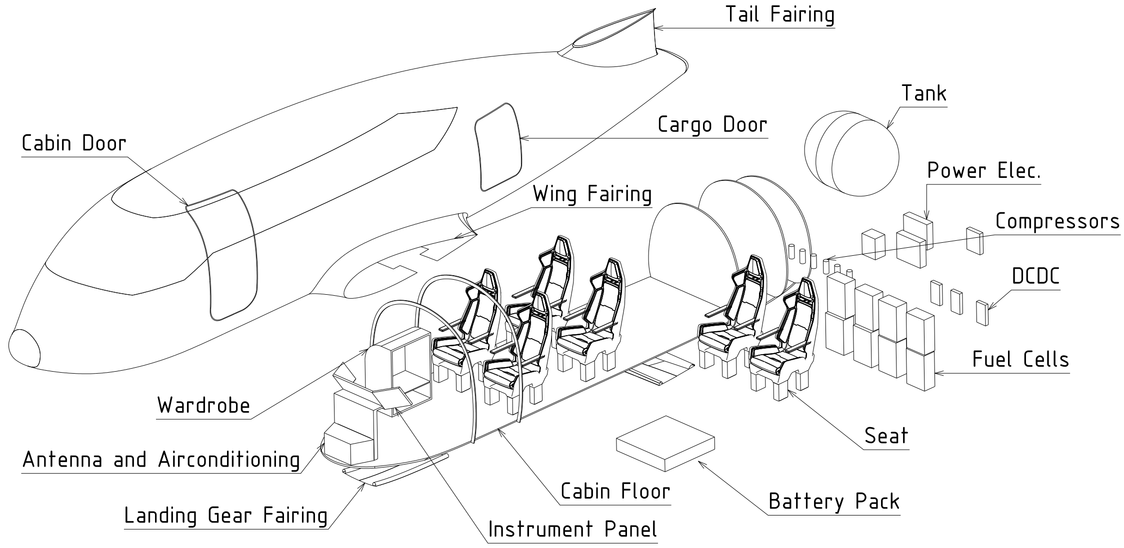

Figure 9.2: Fuselage exploded view.

Figure 9.2, however, is not enough to give all the details on how subsystems interfaces are placed. Hence, an exploded view of the nacelle assembly is presented in Figure 9.3.

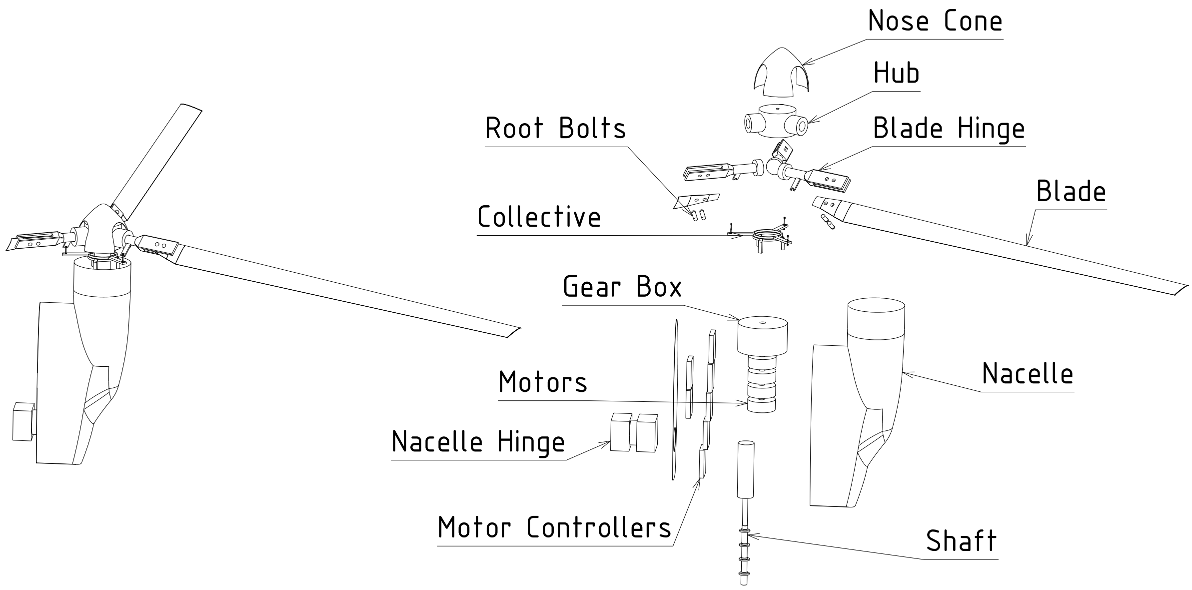

Figure 9.3: Nacelle assembly exploded view.

In particular, Figure 9.3 shows the rotor assembly components.

9.2 Mass Convergence

The design of the system, as described in section 3.4, requires an iteration through the different subsystems to find a mass that the aircraft settles at. The main aspect of the iteration is the change of the wing area due to a change in MTOW, this, in turn, reduces the wingspan, constraining the rotor size, changing the power required throughout the flight. The largest weight change due to this is in the power plant system, which must supply a different amount of power and energy over the flight. This finally changes the weight of the wing as the loading case changes. The iteration begins assuming a MTOW of 4000 kg and changes from there summing up component weights of the different subsystems. The convergence in the mass can be seen over 11 iterations to a final value of 3925 kg.

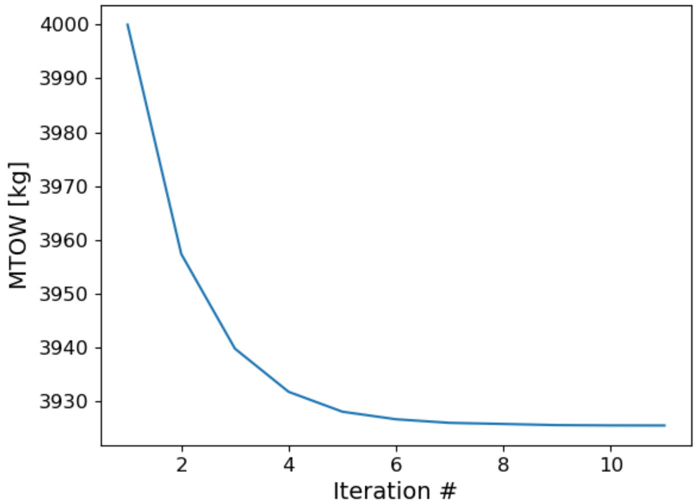

Figure 9.4: System mass convergence over convergence.

9.3 Communication Flow Diagram

The communication flow diagram presented in Figure 9.5 shows the flow of data through the system components and to/from its external environment, it contains all the elements that are part of the communication chain and represents data or command flows between them as arrows. It is possible to see in the figure that the communication flow diagram includes two main elements, the airport infrastructure (the yellow box) and the Futura aircraft (everything else). The airport includes air traffic control (ATC) as fundamental components, while the Futura aircraft includes the pilot and the flight computer. The sensors, flight controls, power plant, cabin equipment, and avionics are included in Futura. Each of this component/ subsystem of the aircraft is connected and communicate through the flight computer, which elaborates the data coming to and from them. For example, when the pilot moves the flight control commands, these are not directly connected to the control surfaces with mechanical cables. Indeed, the movement of the flight controls from the cockpit are converted into electronic signals by the flight computer and then transmitted by wires to the actuators that perform the movement of each control surfaces. This system is called fly-by-wire that in Futura is replacing the mechanical flight control system that uses cables and pulleys to transmit the pilot inputs to the control surfaces. From this diagram, it is possible to notice that the communication between all the components of the subsystems inside Futura but also with the elements in the external environment are fundamental for the correct and safe performance of the designed mission.

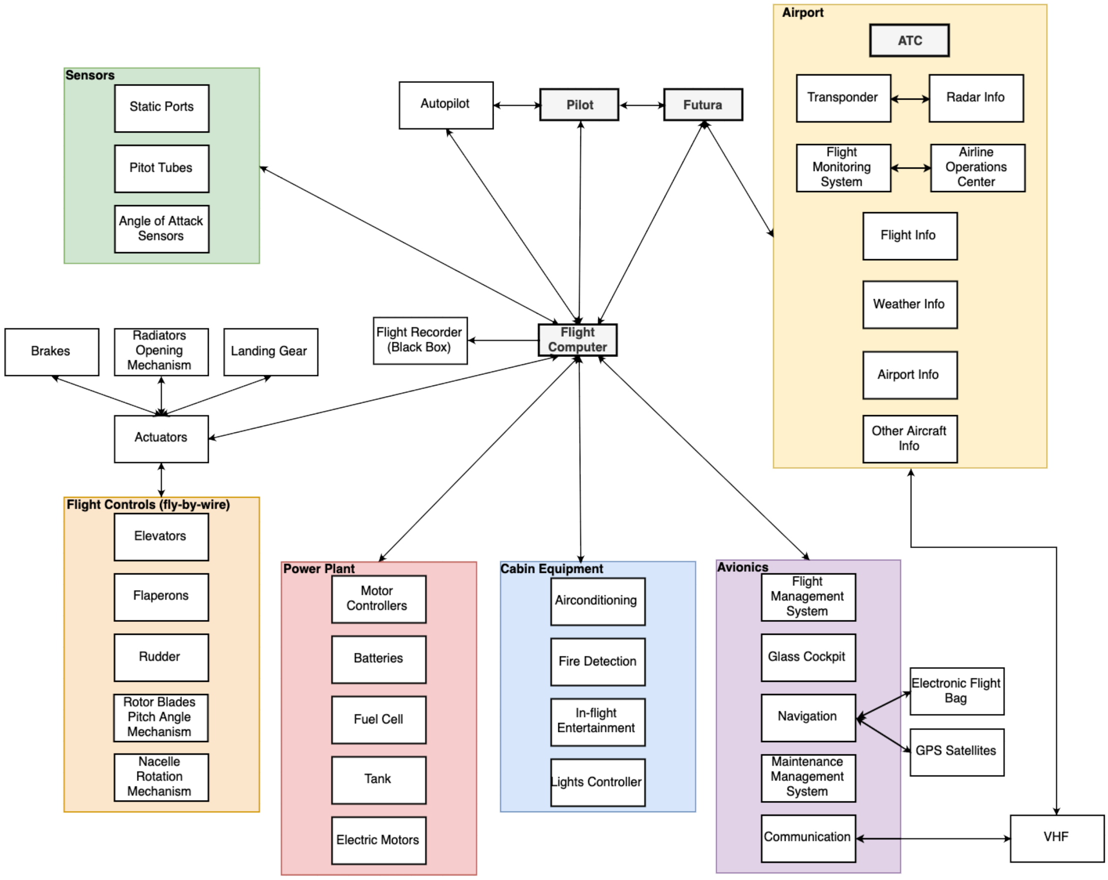

Figure 9.5: Communication flow diagram.

9.4 Hardware and Data Diagram

The aircraft has a multitude of data to handle in order to complete a mission successfully. Data is sent from hardware to the flight computer, and relevant data is sent back. The system can be seen in Figure 9.6. The main sections of the hardware of the aircraft are State Measurement, Aircraft Dynamic Control, Power plant Environment, Communications, and Cabin Busbar. State measurement contains the hardware used to measure the current environmental and dynamic state the aircraft is experiencing, including orientation, location, and atmospheric conditions. It also includes the display of this data to the pilot. Aircraft Dynamic Control contains all the actuated parts of the aircraft by either the pilot control input or control system automatic output. Included in this section are the pilot inputs on both the stick and the collective lever, the state and hydraulic actuation of different control surfaces and mechanisms, and the control of the motors for torque. The motor controller is in the loop with a quadrature encoder to measure the state of the propeller rotation accurately. The power plant environment controls and measures the state of the different power is supplying and managing units, including the fuel cell, compressors, radiators, and batteries. It is controlled by the charge load controller to ensure that voltage loads are safe for different electric components. For communications, two radio systems are used, a transponder and ADS-B data receiver and transmitter. The cabin busbar is connected by a solenoid to ensure the system can be restarted and manages the power usage in the cabin. Finally, the black box stores all relevant flight data.

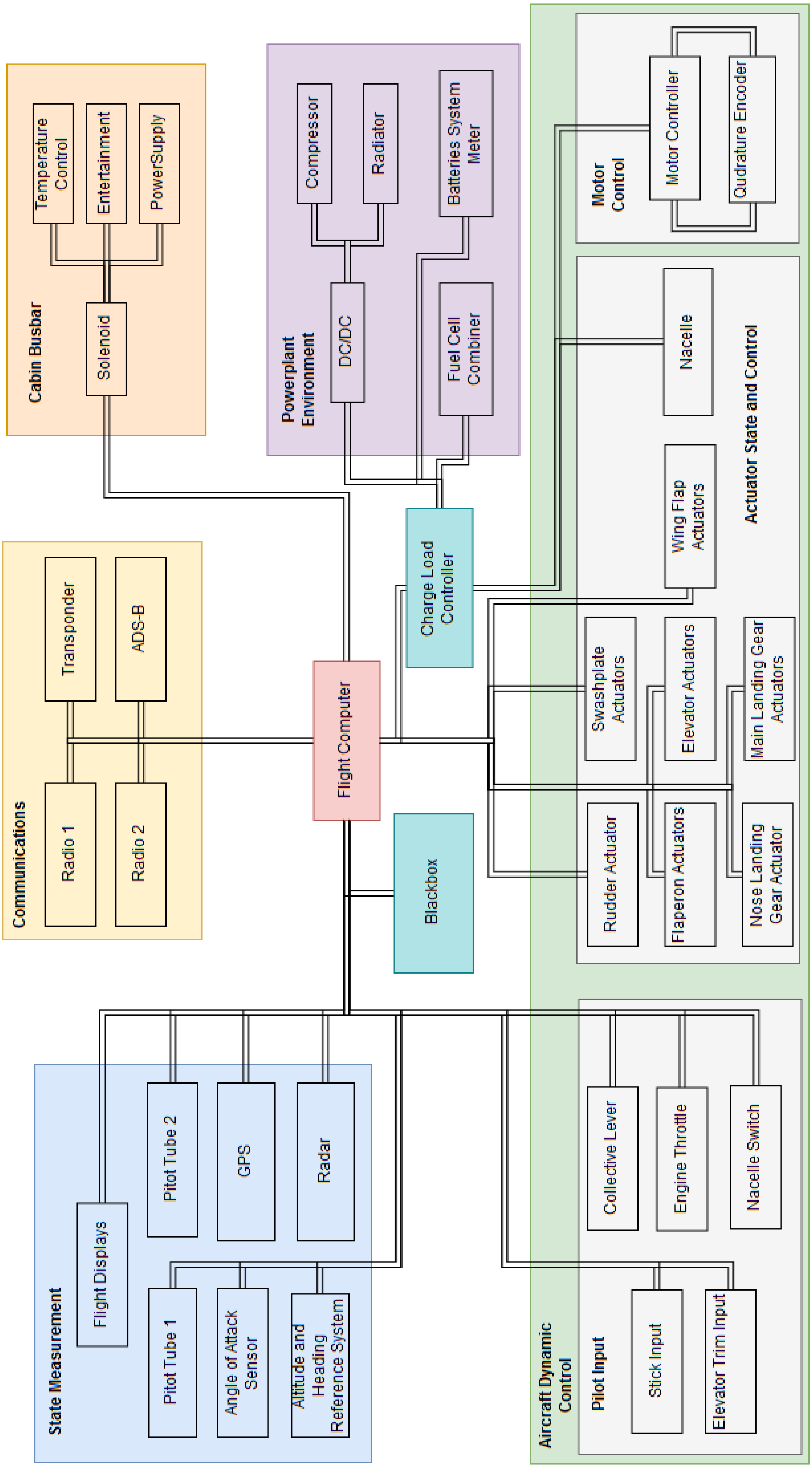

Figure 9.6: Hardware and data handling diagram.

9.5 Sensitivity Analysis

To ensure the actual feasibility of the design, the assumptions made while estimating different values or parameters need to be examined. If this analysis is not performed, some mayor setbacks that may be encountered when further developing the project may bring the design to an unacceptable position, where the top level requirements are not met anymore. For example, if the mass of a given component was underestimated, and the added weight results in a MTOW over 4000 kg, the design would not be feasible anymore. With a rigorous analysis of the assumptions made, and the validity of the methods and theories used, one is able to predict the different setbacks that will be encountered in the further development of the report, and assess their severity.

As the MTOW at which the aircraft converged is so close to the 4000 kg, changes in the mass can easily drive the aircraft over the requirement. Therefore, the assumptions for weight saving due to new materials and manufacturing techniques will be studied and tested for robustness. This will be performed on two subsystems: the fuselage mass and the propeller mass.

9.5.1 Fuselage Mass

At this stage of the design, the mass of the fuselage had to be estimated based on reference aircraft. Due to the similar dimensions, it was assessed that its weight should also resemble that of the reference aircraft. Furthermore, an initial estimate of 15% weight reduction was applied, derived from the use of new materials such as composites and new manufacturing techniques like additive manufacturing, was deemed reasonable. At the same time, all of the reference aircraft presented a pressurised cabin. Since Futura does not use a pressurised cabin, the weight of the fuselage is expected to be lower than the reference value of 327 kg. The lifting body nature of the fuselage, however, may compromise this weight save and counterbalance the non-pressurised cabin. Different possible scenarios are contemplated were the weight save reduction is decreased from 15% to 0%. The MTOW associated with each of these different weight saving estimated is reflected in Figure 9.7.

As it can be seen in the figure, the MTOW only goes beyond the 4000 kg when the weight reduction factor is less than 2%. With the inclusion of the new technology and not having to pressurise the cabin, a worst-case scenario of only 10% weight reduction compared to reference aircraft is contemplated, ensuring an increase in the weight of the fuselage will not drive the design beyond the top level requirement of maximum MTOW.

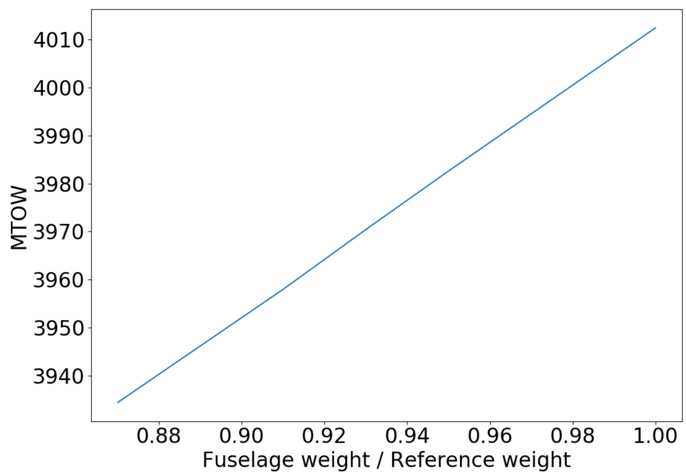

Figure 9.7: MTOW for different fuselage weight saving factors.

9.5.2 Blade Mass

The second element worth considering is the rotor. Contrary to the fuselage, the rotors are sized based on empirical relations. Due to the optimisation performed in the rotor design, a small value of solidity was obtained, what translates to a small blade surface area. Since the rotor solidity value obtained in the optimisation is rarely used in rotorcraft, the empirical formulas employed may not fully apply, and a heavier structure may be necessary. Once more, the empirical formulas used were developed before the commercial introduction of composites into the rotorcraft design. To these formulas a weight reduction factor was applied of 15% due to the use of composites. New materials and new manufacturing techniques have contributed in the past to decrease the weight of rotor blades, and therefore will be used in this design as well. To assess the importance of a possible weight increase due to the novel shape of the blades, the MTOW is shown, in Figure 9.8, as a function of the weight decrease from the parametric estimate to the actual blade used in the design. The change in MTOW due to a change in the weight of the blades is so small, that the blades would need to be 15% heavier than the estimated value for the MTOW to exceed the 4000 kg limit. An weight save of up to 1.1% of the MTOW can be derived from the implementation of composite materials [109]. Since the estimation does not account for new materials, such a big increase is deemed not realistic.

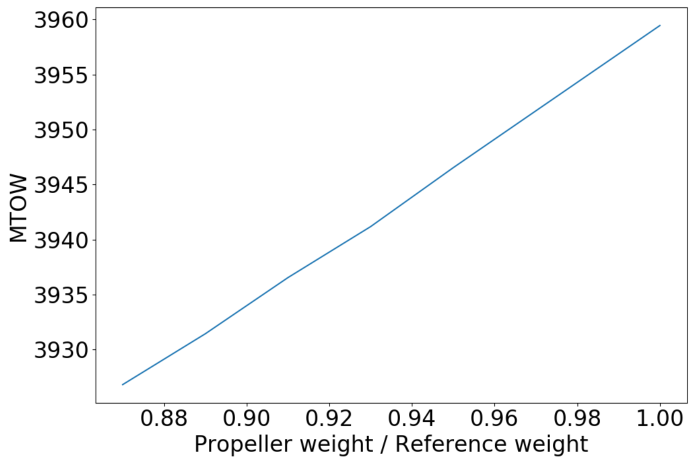

Figure 9.8: MTOW for different rotor weight saving factors.

The potential change in MTOW due to a change in component weight was assessed. The two main components analysed were the fuselage and the blade. For all of the design, the weights of the different components have been calculated based on sizing. For these two components, their weights were estimated based on empirical relationships (blades) and reference aircraft (fuselage), and no actual sizing was performed. These two elements were deemed as most critical and its change in weight was studied. It was found that even if significant component weight change occurs, the design still meets the 4000 kg MTOW requirement.

9.6 Mass Budget

Once all the subsystems were designed, it is essential to ensure that the sum of all the components does not jeopardise the ability to respect the requirement regarding MTOW. For this reason, a mass breakdown of the aircraft systems' and subsystems' masses is presented below.

Table 9.1: Futura mass budget.

System	Subsystem	Mass [kg]
Fuselage		278.0
Fixed Equipment	Radar Antenna	3.6
	Air Conditioning	69.5
	Avionics	72.0
	Flight Control	80.6
	Furnishing	225.0
	Hydraulics	175.0
Propeller	Rotors	110.6
	Hub and Shaft	205.9
Nacelle	Electric motor	128.0
	Motor controller	49.0
	Gearbox	266.0
	Tilt Mechanism	40.0
Wing		241.9
Main Landing Gear		122.6
Nose Landing Gear		50.5
Power Plant	Battery Pack	228
	Tank Inner Wall	7.5
	Tank Outer Wall	13.8
	Tank MLI Shield	2.6
	Tank MLI Spacer	1.7
	Fuel Cell	168.0
	Radiators	201.0
	DC/DC converter	9.6
	DC/DC Bus	32.0
	Compressor	6.3
Vertical Tail		43.0
Horizontal Tail		75.0
Pilot		100.0
Fuel		18.7
MTOW-Payload		3025.4

The estimation of each component's mass is derived and explained in their respective chapters. The MTOW of Futura excluding the payload shall not exceed 3100 kg as Futura-TECH-VCM-5 and Futura-TECH-VCM-6 establish. As it can be seen in Table 9.1 the OEW of the aircraft plus the mass of the fuel is 3025.4 kg. The current mass estimation could go change as the design progresses. In order to take account of this possible variation in mass, a contingency value of 15% can be applied to the systems which are most sensible to future engineering analysis and design choices [5]. This is the case of the fuselage and the rotors whose detailed structural analysis was not addressed in this report. By applying a conservative 15% increase in mass for this two systems, the MTOW excluding the payload can increase up to a value of 3155.2 kg. In this case Futura-TECH-VCM-5 will not be achieved. The risk of not achieving such requirement in the future, however, can be mitigated: a compromise between materials like aluminium that are more attractive from a sustainable point of view and composites, currently used marginally in the aircraft, with excellent specific properties will allow the team to respect the requirements in the next phases of the design too.

9.7 Power Budget

In this section the power budget of the aircraft is defined. Table 9.2 shows that the combination of the fuel cell and batteries can provide the power needed to drive the propellers at all times, but also the necessary power to power the electrical systems and the hydraulics systems systems.

Table 9.2: Futura's power budget.

System	Power [kW]
Max power	1096.60
Electrical System	4.90
Hydraulics	5.92
Radiator Pump	0.50
Compressor	8.00
Total	1115.92

As it can be seen by adding the power to drive the hydraulics and the electrical systems in the aircraft to the maximum power that has to be achieved during flight a total power required on 1115.92 kW is found. All the components of the power can be retrieved in chapter 6; the compressor and radiators power ratings were found respectively from the components characteristics [53, 88]. This value is lower than 1394 kW, being the total power which the power plant can provide in a fully reliable manner as outlined in chapter 6. It is important to state that if the mass of the aircraft would increase in future designs, the power required by the aircraft is going to increase as well. In this sense the most sensitive component of the power is the power required for flight, while those ones for the electrical and hydraulic systems are not likely to increase contributing to a very small proportion of the total power.

9.8 Compliance Matrix

The requirements compliance matrix presented below in Table 9.3 contains all the Futura main requirements analyzed during the entire design phases and already presented in section 3.1. It was decided not to put all the requirements that we establish during the first phase of the design since the majority of them do not apply to the final design. In fact, they are based on different and configurations (wing-embedded and compound coaxial helicopter) and different types of subsystem, for example regarding power plant (turbines). Instead, all the customer requirements and the primary requirements based on these are listed. It indicates whether or not the requirements are met. The table includes five columns, in the first two columns, the requirement identifier, and the actual requirements are stated. In the third column, the compliance of the requirements are checked, and the status is indicated. Indeed, the tick symbol (V) with the green cell suggests that the aircraft complies with the requirement, while the cross mark (X) with the red cell means that it does not comply with the requirements. Finally, in the fourth column, all the relevant sections, where the requirement is treated, are presented. As it is possible to see in the table all the requirements are met, the only requirement that is not met is Futura-CONS-RES-1, the reasons behind this missed compliance are presented in subsection 12.1.3.

Table 9.3: Driving requirements compliance matrix.

Identifier	Requirement	Compliance	Section
Futura-TECH-VCM-1	The range shall be at least 200 km.	V	section 4.2
Futura-TECH-VCM-2	The maximum speed shall be 400 $\mathrm{km h^{-1}}$.	V	section 4.2
Futura-TECH-VCM-3	The cruise speed shall be at least 350 $\mathrm{km h^{-1}}$.	V	section 4.2
Futura-TECH-VCM-4	Futura shall achieve vertical take-off and landing (VTOL) capabilities.	V	section 4.5
Futura-TECH-VCM-5	The payload shall be at least 900 kg.	V	section 9.6
Futura-TECH-VCM-6	The maximum take-off weight (MTOW) shall not exceed 4000 kg.	V	section 9.6
Futura-TECH-VCM-7	The service ceiling shall be of at least 1500 m.	V	section 4.2
Futura-TECH-VCM-8	Futura shall have, at maximum, a 1 h turnaround time.	V	section 4.6
Futura-TECH-VCM-9	Futura shall have 90% availability, by considering the time required for other scheduled and unscheduled maintenance.	V	subsection 13.1.2
Futura-TECH-VCS-3	Futura shall use hydrogen as source of energy.	V	chapter 6
Futura-CONS-RES-1	The design and manufacturing cost of the first prototype shall not exceed 2 million €.	X	subsection 12.1.3
Futura-CONS-RES-3	The cost of refuelling a full tank shall not exceed 345 €.	V	section 4.4/subsection 4.3.4
Futura-CONS-SUS-5	Futura shall not produce any emissions other than water.	V	chapter 6
Futura-CONS-SUS-12	All parts shall be assigned a sustainable end-of-life (EOL) solution among reuse, re-manufacturing, recycling or downcycling.	V	section 11.4

Conclusion

The design iterations led the team to obtain the conceptual design of an aircraft with a total mass of 3025.4 kg. This value is within the required one as established by the customer. However, in further design iteration, the structural design of the fuselage could lead to an increase of the total mass up to 3155.2 kg. The result of the conceptual design shows that the power plant, the propulsion and the fuselage and cabin design can be integrated. Futura's power plant, in particular, can deliver enough power for all critical flight conditions. The communication flow diagram and hardware and data diagram have shown that a fly-by-wire system would be able to connect and communicate with all the aircraft systems. Eventually, the compliance matrix has highlighted that all requirements have been met except for the prototype cost which exceeds the required one by the customer.

10. Manufacturing Plan

In chapter 9 it is shown how the different systems came together in one aircraft without specifying how the different elements of the design are produced. In this chapter, the characteristics of the production plan of Futura are discussed. In section 10.1 the characteristics of the production plant are discussed, specifying which subsystems are produced internally and which ones are manufactured. The risks associated with such a manufacturing organisation are evaluated too. In section 10.2 the material decomposition of the aircraft is presented and section 10.3 the related manufacturing techniques needed to produce the different systems are presented as well. Eventually, the assembly techniques and assembly plan are presented in section 10.4.

10.1 Production Organisation and Risks

In chapter 9, the integration of the systems and subsystems in the aircraft are presented. Some of the systems are produced and manufactured in-house while others are going to be purchased and installed only in the assembly line.

The production of Futura has been developed according to the lean manufacturing philosophy. As a consequence, the manufacturing of the aircraft will be as integral and centralised as possible. The central systems' components that will be manufactured in the factory's workshops are structural. The airframe, the wing, and the empennage structural parts will be produced in the factories' workshops. Spars, stringers, ribs, or skin panels will be manufactured ad hoc for Futura. In these processes, half - products are going to be transformed into essential structural components using one or multiple of the manufacturing techniques presented in section 10.3. While most of the production of half-products such bulk aluminum parts or sheets for the skin are not going to occur in workshops close to the assembly line, subparts such as ribs and spars will be. The optimized aerodynamic design of the fuselage requires the adoption of non-traditional jigs which will be produced specially for such a purpose. The manufacturing of such elements close to the assembly line will eliminate any transport cost and waste during the production, according to the lean manufacturing philosophy [110]. Not only the airframe structure but also some of the interiors will be manufactured in specialised workshops. Futura is a particularly sustainable vehicle: its interior materials will have to follow customised manufacturing processes. The landing gear retraction mechanism and strut will be manufactured in the factories workshops as well as the composite rotor blades. Eventually, the core of the power plant system, namely the hydrogen fuel tank, will also be produced in the factory's workshops, close to the assembly line. This will allow to build a tank with a high safety standard without relying on other-party manufacturing processes. Such a process will require many different manufacturing techniques and specialised training for workers.

For what concerns the components which are purchased, it is essential to specify that raw materials and half products are going to be bought by other firms. This includes aluminium, steel alloys, titanium, composites resin and fibre, and many others as outlined in section 10.2. Then, many of the joining parts needed in the assembly such as bolts, rivets, nuts or bonding adhesives will be purchased from specialised producers unless peculiar pieces have to be produced ad hoc. Eventually, most components of the power plant system must be purchased from external parties: batteries, electric motors, gearbox, DC-DC converters, motor controllers, and radiators. It is essential to highlight that the batteries that Futura will mount are not developed yet. Eventually, most of the instrumentation, avionics, and electrical systems will also be purchased by external parties.

This manufacturing plan includes certain risks. If following the lean manufacturing process will ensure an efficient production process, the starting cost to obtain such an integrated manufacturing plant with workshops close the assembly line could be very high. This could discourage investors and decrease the chances for the aircraft to be successful. Additionally, the staff training needed to assemble new systems such as the lifting body fuselage or the power plant could potentially increase the delivery time and slow down the production rate with repercussions on the profits. Eventually, even though the technology to produce batteries has already been proven, as mentioned in chapter 6, production facilities that manufacture such batteries are not present yet. Hence on this matter, a strategy will have to be thought in the post-DSE activities as explained in chapter 14. It can be concluded that the risks mentioned above can be mitigated in the later stages of the design; in fact, they will be dependent on the outcome of the development phase of the aircraft as explained in chapter 14.

10.2 Materials Break-down

Before analysing the manufacturing techniques needed to produce the most important parts of the aircraft, it is necessary to present its materials, since the manufacturing techniques depend directly from them.

The choice of the different materials has been treated throughout the design of the different subsystems. It has to be specified, however, that to select the different materials for the fuselage, its body has been divided into five different subsystems: the frame, the floor, the skin panels, the interiors, and the glass window. The proportions are based on typical Roskam estimations [40]; hence, variations in the actual mass of material that will be used for each subsystem will happen in the next design iterations. Figure 10.1 presents the proportion of each material used in the aircraft in terms of mass. Software CES did not only allow to obtain the required mass of materials before the manufacturing process, but also to produce the necessary manufacturing techniques and sustainability of the process as outlined in section 10.3 and chapter 11 [9]. According to Jos Sinke (personal communication, June 12, 2019), 33% of the original material is scrapped on average by secondary processes. Hence a 33% scrap material has been used to come up with a total material mass of 3473 kg. This value is likely to be underestimated since some components have not yet been considered as this material break-down is still at a conceptual level.

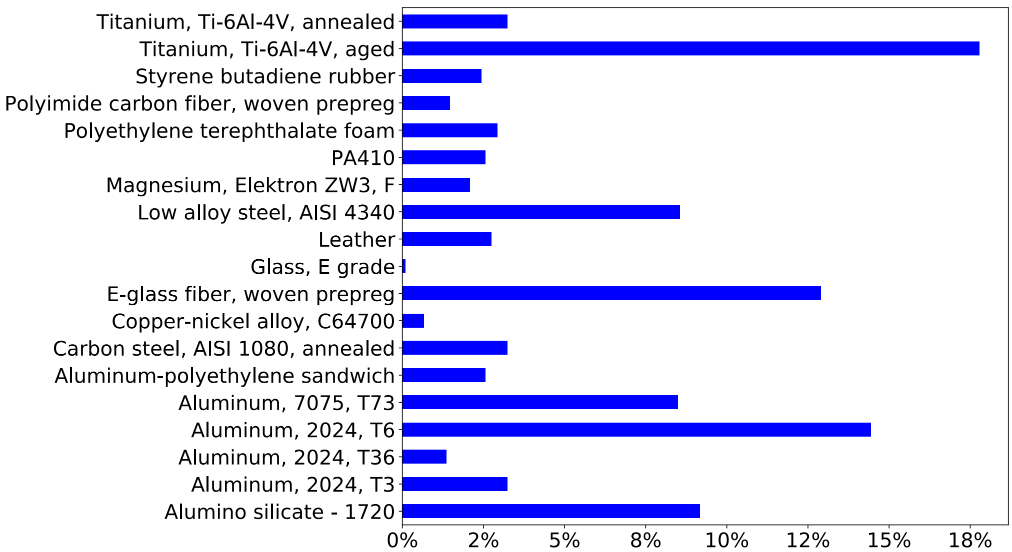

Figure 10.1: Futura's material break-down.

Figure 10.1 shows that Aluminium 2024 T6 is the most used material in Futura. The advantages that the use of this material brings, come at the expense of using coatings to avoid corrosion as explained in section 8.2 and section 8.3. Additionally, in order to apply such coatings, particular mechanical polishing have to be performed in order to ensure the coating effectiveness [111]. It can also be seen that composites have a crucial role in the aircraft blades and fuselage floor even though their percentage on the total is low. Another material which stands out in the break-down is leather: for the cabin interiors, recycled leather will be used. It is important to notice that the use of Ecopaxx (PA410) for the interiors means that 3% of the total weight is made by a completely renewable material and not a thermoset plastic which is typically used for the fuselage interiors. There is a presence of Copper Nickel alloy too as this is the material used for the electrical cabling used in Futura, but its proportion is rather small as it can be seen in Figure 10.1. Additionally, the relatively extensive use of Aluminosilicate 1720 for the fuselage window could greatly reduce the mass in the next design iterations. Eventually, the contribution of titanium can be seen in the aircraft joints whose percentage of the total mass of the aircraft is 2-4%, according to Jos Sinke (personal communication, June 17, 2019), but also from the propeller hub whose contribution to the weight of the aircraft is of about 18 % as can be seen in Figure 10.1. Different materials have been considered for joints on top of Titanium: Carbon Steel AISI 1080 annealed and aluminum 2024 T3 have also been taken into consideration in the analysis. It is important to specify that the material break-down currently, does not include all the materials that are contained in purchased products, but it only includes the material of the components that are manufactured in the factory's workshops. However, this material break-down summary provides the base to outline the environmental impact that the manufacturing process will produce as shown in section 11.1.

10.3 Manufacturing Techniques

The dominant material for the airframe structure is aluminium. To make ribs, spars and the fuselage shell extrusion is going to be essential. Also, roll forming is going to be needed to manufacture the fuselage panels which are going to be placed on top of the fuselage ribs and longerons. Fine machining and cutting and trimming will be complementary to the manufacturing process of aluminum. Additive manufacturing techniques such as metal powder forming will be used for the aluminum sandwich panels placed in the fuselage. Also, the same techniques applied to polymer molding will be applied to Ecopaxx, the recyclable plastic used for the fuselage's interiors. For what concerns the manufacturing of the propeller blades skin and core, Polymide Carbon Fiber woven prepreg bi-axial layup is going to be shaped using vacuum assisted resin infusion while Epoxy glass fiber is woven prepreg bi-axial layup used for the core is going to be molded in the autoclave. Then manufacturing the hydrogen tank is going to be performed with simple roll forming for what concerns the outer and inner wall. Eventually forging and casting are going to be necessary respectively to manufacture the landing gear and the propeller hub.

10.4 Assembly Techniques and Assembly Plan

The assembly line of Futura is pivotal to have an efficient production while keeping the costs low. The manufacturing line is going to be divided into mounting and manufacturing divisions.

Mounting divisions include all the parts necessary for the use of the aircraft which can be removed such as propeller blades, doors, flaperons. Manufacturing divisions include all the structural components and systems which are an integral part of Futura and cannot be substituted. The Figure 10.2 shows the order in which major subsystems are assembled as well the time it takes to assemble the subsystems in different stations. Some of the activities are performed in series; for example, the fuselage has to be placed in the jig to mount the empennage and the main wing box. Other activities are performed in parallel; Figure 10.2 shows that the propulsion units are assembled while the empennage and the main wing box are installed in the fuselage. The assembly of Futura is based on the combination of rigid and flexible parts. For example, the flexible double curved parts dominating the lifting body fuselage will be mounted to the airframe fuselage structure. Complex jigs will be used in the assembly of Futura due to the innovative lifting body fuselage. This means that the cost of the jigs will be higher, but in terms of maintenance, less calibration will be needed. Using a series of simpler jigs would increase the maintenance cost of such tools [112]. The assembly of Futura allows to deliver one aircraft every 28 days. Such delivery time was established based on the return on investment needed to make the profitable program chapter 12.

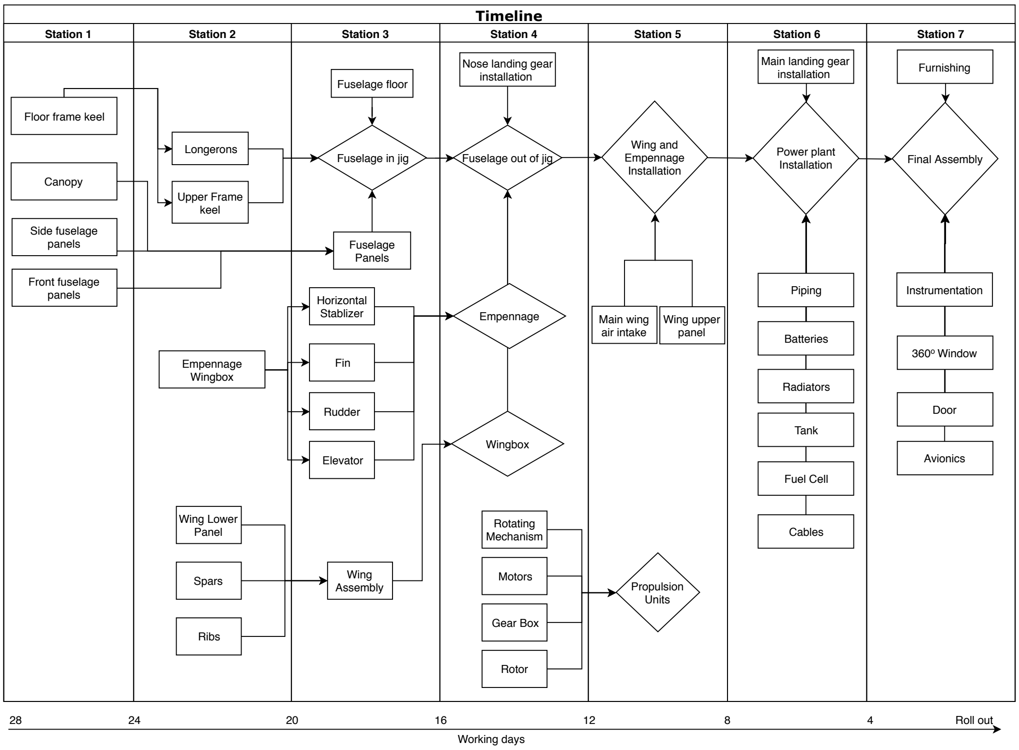

Figure 10.2: Assembly plan.

Conclusion

Futura's production plan is fundamental to ensure the sustainability of the aircraft also from a profitability point of view. For this reason, the production manufacturing plan has been envisioned to be a centralised factory in which workshops are extremely close to the assembly line following the lean manufacturing philosophy. The material break-down of the manufactured components showed a dominance of the certain metal alloys: aluminum 2024 and Titanium TI-6Al. Composites do not play a major role in Futura, except in the rotors and on the fuselage floor. The manufacturing plan has been thought to have a delivery time that would lead to the return of investment. Eventually, it is important to mention that, because the design is particularly innovative new production jigs and several manufacturing techniques are going to be needed: this will increase the initial training cost for the workers and the initial investment to obtain the production plant.

11. Sustainable Development Implementation

The implementation of the sustainable development strategy is detailed in this chapter. Environmental and societal impacts at all stages of Futura's life are evaluated. Environmental impacts are assessed in terms of equivalent CO_2 emissions, representing all greenhouse gas emissions into one variable (hereinafter referred to as CO_2 emissions). Societal impact is assessed in terms of energy consumption, as finite amounts of produced energy are shared among all individuals.

These impacts are evaluated for the production of the aircraft in section 11.1, both looking at raw material extraction and manufacturing. The impacts of fuel refuelling and delivery are investigated in section 11.2 for a single tank refill and battery recharge. Noise emissions are discussed in section 11.3, and especially further steps to be taken to ensure compliance with regulations. For each material, an End-of-Life solution is assigned in section 11.4. The potential savings in CO_2 emissions and energy from material recycling are calculated to underscore the high recyclability of Futura. Lastly, the sustainability of Futura is evaluated over its entire lifetime by way of a Life Cycle Assessment in section 11.5. To highlight the high sustainability of Futura, it is compared to its main competitor, the H145.

11.1 Production

Production, encompassing material extraction and manufacturing, generates large amounts of greenhouse gases and consume a substantial amount of energy. This section discusses the efforts to reduce this environmental and societal impact and explains the method to quantify them.
Raw material extraction is reduced by using recycled materials for various components. This is especially the case for metals, for which an industry-wide "typical" recycled content is used. A specific value for each metal is obtained from the material selection software CES Edupack [9]. Other raw material usage reductions come from using recycled leather for seats, as recent innovations have shown high-end applications of such material.[1] Lastly, a bio-based polymer is used for cabin interiors to reduce fossil fuel consumption for polymer synthesis.[2]
For manufacturing, a philosophy focused on minimising waste is adopted as laid-out in section 10.1. By having manufacturing workshops close to the assembly line, transportation is reduced. It should be noted, however, that there exists little freedom in choosing a manufacturing process for a given material and design. Sustainability is therefore ensured in the manufacturing organisation rather than in the processes themselves.
The CO_2 emissions and energy consumption associated with production are directly estimated with the material-selection software CES Edupack, used for the material breakdown [9]. These calculations take into account, on the one hand, the environmental impact savings from using recycled materials. On the other hand, material waste during manufacturing (e.g. trimming and cutting) increases resource use by approximately 33% according to section 10.2.
The total impact is, however, difficult to estimate as the material of bought parts cannot be tracked accurately. As only about 50% of the OEW has been assigned a specific material, the rest of the mass is divided by typical aircraft material use fractions. This translates to aluminium, composites and steel & titanium representing 79%, 2.9% and 18.1% of the rest of the OEW respectively [113]. The impact

[1] URL `www.recycleather.com` [cited 20 June 2019]
[2] URL `/www.dsm.com/markets/engineering-plastics/en/products/ecopaxx/markets/automotive.html` [cited 20 June 2019]

of this additional material mass is calculated in CES Edupack. The total CO_2 emissions and energy consumption for production are presented in section 11.5.

11.2 Fuel Production and Delivery

While flying, Futura generates no-climate warming gases due to its clean propulsion technology. Indeed, while water vapour is a greenhouse gas, it has a negligible climate impact when emitted at low altitudes [1]. Therefore, all operational impacts originate from fuel production and transportation. The sustainability of the processes proposed in section 4.3 are analysed below.
Firstly, fuel production is investigated. Electrolysis was selected for Gaseous Hydrogen (GH_2) production, which energy consumption per kilogram of hydrogen produced equals $\bar{E}_{\mathrm{H_2}} = 124\,\mathrm{MJkg}$ according to a study conducted by Shell [10]. Then, GH_2 is converted to LH_2 through a liquefaction process which requires $\bar{E}_{\mathrm{H_2}} = 39.6\,\mathrm{MJkg}$ [21]. From the mission fuel mass of $m_{\mathrm{fuel}} = 14.3\,\mathrm{kg}$, the required amount amount of energy to refuel one tank amounts to $E_{\mathrm{H_2}} = 2.34 \cdot 10^3\,\mathrm{MJ}$.

11.2.1 Production

The CO_2 emissions of LH_2 production vary heavily depending on the electricity source. If using the average European electricity mix, electrolysis leads to more CO_2 emissions than fossil-fuel based gas reforming [10]. It was therefore decided to use renewable electricity which produces no direct emissions. As the European electricity market has been liberalised, this easily allows the hydrogen producer to source its electricity from renewable energies provided the operator pays a higher fee[3]. It is foreseen that the aircraft operator will not oppose paying the fee, since the refuelling cost remains 20% cheaper to that of a kerosene aircraft for the same mission, according to section 4.4.

The indirect impacts of renewable electricity (R.E.) are assessed using Linde's Leuna (Germany) plant as production site example. These correspond to the impacts of the rare earth metal extraction for solar panels and wind turbine manufacturing for instance. According to Germany's current electricity mix[4] and the specific CO_2 emissions of each renewable energy evaluated by the Intergovernmental Panel on Climate Change, an average CO_2 footprint of $\bar{m}_{\mathrm{CO_2,R.E.}} = 17.6\,\mathrm{gMJ^{-1}}$ is found [114]. This translates to emissions of $m_{\mathrm{CO_2,R.E.}} = 47.7\,\mathrm{kg}$ per tank refill when adding battery recharging.

11.2.2 Delivery

Fuel transportation, however, will generate direct emissions as long as the production is fully off-site and LH_2 pipelines are not built. Truck transportation from the production plant to the airport is minimised by using large capacity trucks and airport storage of $4\,\mathrm{t}$ [21, 70]. An estimated 11 roundtrips are needed each year, according to the fuel weight and an average of 8 flights per day ($t_{\mathrm{1flight}} = 119\,\mathrm{min}$ including turnaround, operating from 6:00 until 22:00). For the example distance from Linde Leuna's plant to Schiphol Airport, $1.37 \cdot 10^4\,\mathrm{km}$ are travelled each year. According to CES Software's Eco-audit tool, truck transportation requires a distance and payload-specific energy of $\bar{E}_{\mathrm{km,pay}} = 1.50\,\mathrm{MJkm^{-1}t^{-1}}$, and generate energy-specific CO_2 emissions of $\bar{m}_{\mathrm{CO_2truck}} = 72.0\,\mathrm{gMJ^{-1}}$ [9]. This translates to an average energy consumption of $E_{\mathrm{truck}} = 28.2\,\mathrm{MJ}$ and CO_2 emissions of $m_{\mathrm{CO_2,truck}} = 2.03\,\mathrm{kg}$ per tank refill. It will be assessed with fuelling station manufacturer whether active cooling of the airport storage tank (from renewable electricity) is needed or if passive insulation is more cost efficient.

[3]URL `https://ec.europa.eu/energy/en/content/electricity-market-liberalisation` [cited 20 June 2019]

[4]URL `www.cleanenergywire.org/factsheets/germanys-energy-consumption-and-power-mix-charts` [cited 15 June 2019]

The total CO_2 emissions and energy consumption per tank refill and battery recharging amount to $m_{CO_2} = 49.8\text{kg}$ and $E = 2.40 \cdot 10^3\,\text{MJ}$ respectively. These impacts are shown for the entire operational lifetime of Futura in section 11.5.

11.3 Noise Emissions

Futura's noise emissions will comply with ICAO regulations on tilt-rotor aircraft, as defined in Attachment A of ICAO Regulations Annex 16 Chapter 1 [25]. The most strict noise limits applicable to Futura correspond to 96EPNdB at take-off and 97EPNdB at landing. EPNdB refer to the Effective Perceived Noise (EPN) in decibels [25].

Noise emissions are, however, extremely complex to predict, and no numerical simulation has been used at this point to estimate them. Later in the design, wind tunnel tests are to be performed on a scale model to obtain a first estimate. A possible redesign of the blades or a change in their rotational speed is envisioned to reduced noise if needed. It is foreseen, however, that noise emissions will remain acceptable as the XV-15, a tilt-rotor aircraft of similar size, has demonstrated satisfactory noise levels [24].

11.4 End-of-Life Processes

This section discusses the End-of-Life (EOL) of the aircraft. While it is currently the operator's responsibility to dispose or recycle the aircraft, regulations may soon put the responsibility on the manufacturer [12]. This is why, since the early design of Futura, ensuring sustainable EOL solutions has had a significant influence on material selection. EOL solutions are proposed below to ensure environmental and societal impacts are minimised.

11.4.1 Organisation

Depending on its condition, the aircraft will be sold or donated to an aircraft recycling plant. It will be disassembled at an Aircraft Fleet Recycling Association certified plant, present in all major European countries.[5][6][7][8] Disassembled components may be reused or re-manufactured, typically engine parts or avionics [115]. "As users will typically operate Futura as a fleet, parts can be used for servicing operational vehicles" [116]. Other parts are segregated per material and assigned a specific process depending on the material as shown in Table 11.1.

11.4.2 Process Identification

The choice of EOL has a significant impact on the sustainability of the aircraft. This can be seen from a low-waste generation point of view, but also from potential CO_2 emissions and energy savings. If some material is recycled for the manufacturing of a new product, credits can be attributed to avoiding the extraction of raw material. These savings calculated in CES Edupack are shown for all Futura's materials in Table 11.1.
The EOL processes are shown per material type below. The recycling of parts which are not easily separated in a first sorting are also assigned an EOL solution.

- **1 - Metal Alloys:** Recycling for this type of material is common practice in the industry and energy efficient. "A pre-treatment and cleaning are applied to the old part. The scrap undergoes melting

[5]URL `http://moreaero.de` [cited 20 June 2019]
[6]URL `http://www.tarmacaerosave.aero/aircraft-recycling` [cited 20 June 2019]
[7]URL `http://jetaircraftservices.com/wordpress/en/products` [cited 20 June 2019]
[8]URL `https://www.aels.nl/aels-for-you/what-can-aels-do-for-airlines` [cited 20 June 2019]

Table 11.1: EOL process # and associated potential CO_2 emissions and energy savings for Futura's materials.

#	Material	Saved CO_2 emissions [kg]	Saved Energy Consumption [MJ]
1	Aluminium alloys	$2.65 \cdot 10^3$	$4.08 \cdot 10^4$
1	Steel alloys	187	$2.61 \cdot 10^3$
1	Titanium alloys	$8.71 \cdot 10^3$	$1.56 \cdot 10^5$
1	Magnesium alloy	848	$5.64 \cdot 10^3$
2	PA410 (bio-based)	150	$5.81 \cdot 10^3$
2	Polyethylene foam	26.1	525
3	Aluminum-polyethylene	129	$2.28 \cdot 10^3$
4	Synthetic rubber	$2.71 \cdot 10^{-1}$	3.90
5	Polyimide CFRP lay-up	$1.65 \cdot 10^{-1}$	2.35
6	Epoxy GFRP lay-up	1.45	20.7
7	E-Glass fibres	$1.02 \cdot 10^{-2}$	$1.60 \cdot 10^{-1}$
8	Alumino silicate (glass)	41.5	367
9	Leather	0	0
10	Cables	29.0	510

and refining. Then the cycle is finished by alloying and casting the metal. If the scrap is contaminated, it can be used for lower grade metals, such as ferro-titanium for old titanium parts. This process has the advantage of not deteriorating mechanical properties, and to be economically viable and mature enough" [6, 117, 118].

- **2 - Thermoplastics:** Recycling of the polymer is possible by heating the part above its melting temperature as its chemical properties will not change. With little energy, a new part can be remoulded [119].
- **3 - Metal-Polymer Sandwich:** The sandwich component will be separated per material by heating. This is possible as the melting temperature of polyethene (thermoplastic) is lower than that of aluminium [9]. The metal and the thermoplastic will then be recycled according to process **1** and **2** respectively.
- **4 - Synthetic Rubber:** A downcycling process is proposed, which entails transforming the material for a different, lower-value, application. After shredding, waste rubber aggregates have shown useful applications in concrete and pavement reinforcement [120, 121]. The environmental savings from this process are low due to the lower-value application, yet provide an effective way to avoid waste accumulation.
- **5 - Thermoplastic-based CFRP:** Recycling of fibres and matrix is possible by heating the part above the polymer's melting temperature. Fibres can be reclaimed and reused as they typically do not age while the resin can be remelted for the making new parts [119].
- **6 - Thermoset-based GFRP:** Recycling of fibres and down cycle for the matrix is proposed. "Pyrolysis or chemical dissolution are suitable processes for fibre extraction that will continue to mature until Futura retires. The high retention of mechanical properties and economic value of used fibres will make this process viable economically. The matrix can be used as a chemical feedstock or for heat production. Alternatively, comminution is a downcycle process that allows for low-value applications such as concrete reinforcement" [6, 122, 123].
- **7 - Fibreglass Paper:** Fibreglass paper can be directly reused for other insulation applications, depending on condition. If it has degraded (e.g. due to moisture), the downcycling process of **6** is preferred.
- **8 - Alumino Silicate:** This type of strong glass, also sold as Gorilla glass, is difficulty recycled alone. It can, however, be shredded and mixed with other types of glass to be recycled.[9]
- **9 - Leather:** Leather from the seats can be recycled into other leather products. Typically, these are smaller than the original item due to shape restrictions.[10,11]
- **10 - Cables:** Copper cables can be recycled after material separation. Innovative processes allow for more than 99% of metal recovery while the PVC coating is remelted, ensuring the economic viability of the process. This process is applicable irrespective of cable size.[12]

[9]URL `www.designlife-cycle.com/corning-gorilla-glass` [cited 20 June 2019]
[10]URL `www.looptworks.com/collections/in-flight-collection` [cited 20 June 2019]
[11]URL `www.recycleather.com` [cited 20 June 2019]
[12]URL `www.mtb-recycling.fr/en/cables-recycling.html` [cited 20 June 2019]

- **11 - Fuel Cells:** ”A combination of recycling and downcycling is possible. A hydro-metallurgy process can separate the membrane and catalyst layers [124]. The catalyst, typically containing Platinum Group Metals, can be recycled with a rate up 95% [125]. Flow plates and membranes (containing the thermoset Nafion) can be used for other applications such as desalination or heavy metal removal [126]. Currently, such processes are not mature and available commercially only on a small scale at a high price [127]. It is expected, however, that the maturity will grow rapidly as fuel cells in the automotive industry spread further.” [116, 128]

- **12 - Lithium-ion Batteries:** ”A recycling process is recommended for this device. ”It will be done by way of a hydro-metallurgical process, a medium scale and already available close to zero waste solution provided by Umicore [129]. Some of the energy needed for such a process is directly extracted from the battery components, decreasing the energy demand. While this process creates almost zero waste, it comes with a high cost. It is expected that by the time Futura retires, this maturity and economic viability of the process will have increased.” [116, 129]

- **13 - Electric Motors:** Electric motors retain a high value due to their precious materials. Small motors are shredded while specialised companies separate bigger ones. This process applies to any motor size.[13]

It can be seen from the material breakdown in Figure 10.1, that only about 15% of the mass is assigned to a thermoset-based material (from the total mass with assigned material). This low value compared to current modern aircraft (about 50%) was achieved by preferring metals over thermoset-based composites where the design space allowed [113]. Even so, these less sustainable materials were assigned downcycling solutions to low-value applications to reduce waste.

11.5 Life Cycle Assessment

As major design decisions have been taken to make Futura as sustainable as possible, this section is about quantifying their impact. A Life Cycle Assessment, during which the CO_2 emissions and energy consumption of all stages of Futura's life from material extraction until the End-of-Life are evaluated and seen in Table 11.2.

The impacts are calculated according to section 11.1, section 11.2 and section 11.5. Operational impacts are assessed over the operational lifetime of Futura, estimated at 30 years, according according to the aircraft average [130].
For the End-of-Life calculations, the additional material mentioned in section 11.1 are used to have a global picture of the EOL sustainability. The reprocessing of materials, however, consumes energy and releases CO_2 emissions, depending on the choice of EOL. This includes material collection and sorting. These impacts are shown as 'Process' in Table 11.2.
To judge the sustainability performance of Futura, a comparison with the closest currently operating competitor, the Airbus Helicopter H145 is carried out.

11.5.1 H145 Environmental and Societal Impacts

Production and End-of-Life

To estimate the production and End-of-Life CO_2 emissions and energy consumption of the H145, the aforementioned typical aircraft material use fractions are used. As these fractions have not been found for helicopters specifically, this provides the best estimate. The calculations are based on the H145's OEW, equal to 1895kg [131]. Recycled material use and manufacturing waste are also taken into account using CES Edupack.

[13] URL http://interbaro.nl/en/products-metals/electric-motors-recycling/ [cited 20 June 2019]

Operations

For comparison purposes, the operational impacts of the H145 are calculated for the same mission as Futura's. The Swiss Federal Office of Civil Aviation has estimated that the H145 consumes on average $\dot{m}_{\text{fuel}} = 283\text{kgh}^{-1}$ and releases $\dot{m}_{\text{NOx}} = 1.99\text{kgh}^{-1}$, translating to equivalent CO_2 emissions of $\dot{m}_{CO_2} = 1.49 \cdot 10^3\text{kgh}^{-1}$.[14] The distance and payload-specific energy for helicopters is estimated by CES' Eco audit tool at $\bar{E}_{\text{km,pay}} = 55.0\text{MJkm}^{-1}\text{kg}^{-1}$. From the mission flight time of 59min and an average of 8 daily flights, the impacts of fuel combustion can be estimated over the operational lifetime.

The production of kerosene also generates CO_2 emissions and consumes energy. Production includes extraction, refinery and long-distance transportation as these processes typically take place outside Europe. These have been estimated to represent 3.97% of fuel combustion's impact [132]. This fraction is added to the operational impacts of the H145.

11.5.2 Comparison

A comparison of the life-cycle CO_2 emissions and energy consumption of Futura with its competitor, the H145, is shown in Table 11.2. It is observed that Production has higher impacts for Futura, mostly because Futura's $\left(\frac{\text{OEW}}{\text{MTOW}}\right)$ ratio is 54% higher meaning more structure has to be carried [131]. The EOL, on the other hand, shows higher impact reduction potentials due to the high recyclability of Futura. Lastly, Futura's operational impacts being drastically lower than the H145's, a life-cycle reduction of 97% and 87% in terms of CO_2 emissions and energy consumption, respectively, is reached. This reduction is deemed excellent and highlights the potential of liquid hydrogen for reducing the climate footprint of aviation.

Table 11.2: Life cycle assessment of Futura and H145.

		CO2 Emissions [ton]		Energy Consumption [MJ]	
Stage	**Aircraft**	Futura	H145	Futura	H145
Production	Material extraction	39.4	20.3	$6.06 \cdot 10^5$	$2.93 \cdot 10^5$
	Manufacturing	4.24	1.88	$5.55 \cdot 10^4$	$2.5 \cdot 10^4$
Operations	Fuel production, transportation	$4.36 \cdot 10^3$	$5.05 \cdot 10^3$	$2.10 \cdot 10^8$	$5.16 \cdot 10^7$
	Combustion	0	$1.27 \cdot 10^5$	0	$1.3 \cdot 10^9$
End-of-Life	Process	$9.72 \cdot 10^{-1}$	$8.96 \cdot 10^{-2}$	$6.81 \cdot 10^1$	$1.28 \cdot 10^3$
	Potential	-124	-9.87	$-7.14 \cdot 10^3$	$-1.54 \cdot 10^5$
Total		$4.28 \cdot 10^3$	$1.32 \cdot 10^5$	$2.11 \cdot 10^8$	$1.35 \cdot 10^9$
Difference		-96.8%		-84.4%	

Conclusion

The sustainability of Futura has been evaluated in terms of equivalent CO_2 emissions and energy consumption. Production's footprint was reduced by selecting recycled materials and bio-based materials as well as following a lean manufacturing philosophy. While Futura is emission-free in flight, indirect impacts from fuel production and delivery were accounted for. A sustainable EOL solution was assigned for all materials and main components of the aircraft. Eventually, this allowed the generation of a Life Cycle Assessment of Futura's sustainability. CO_2 emissions of Futura are 97% lower than a comparable aircraft over its entire lifetime. This significant reduction highlights the exceptionally high sustainability of Futura.

[14] URL `www.climatechangeconnection.org/emissions/co2-equivalents/` [cited 15 June 2019]

12. Return On Investment

As project clients and investors want to make sure that the project will be profitable in the long run, the Return On Investment (ROI) needs to be predicted: this ROI can be defined as the ratio between net profit and investment costs. Therefore, high ROI is necessary for the sustainability of the project. First, the total costs related to the project will be estimated in section 12.1. After that, Futura's competitors will be analyzed in section 12.2. Finally, with this information, the ROI will be determined in section 12.3.

12.1 Cost Break-down

The total design costs of the Futura project can be subdivided into three main groups: development, testing, and manufacturing. These are graphically presented in Figure 12.1 and will be discussed in subsection 12.1.1, 12.1.2 and 12.1.3 respectively. After that, an overview of the total investment for design and manufacturing of Futura will be given in subsection 12.1.4. To conclude, the operational costs of Futura will be analysed in subsection 12.1.5.

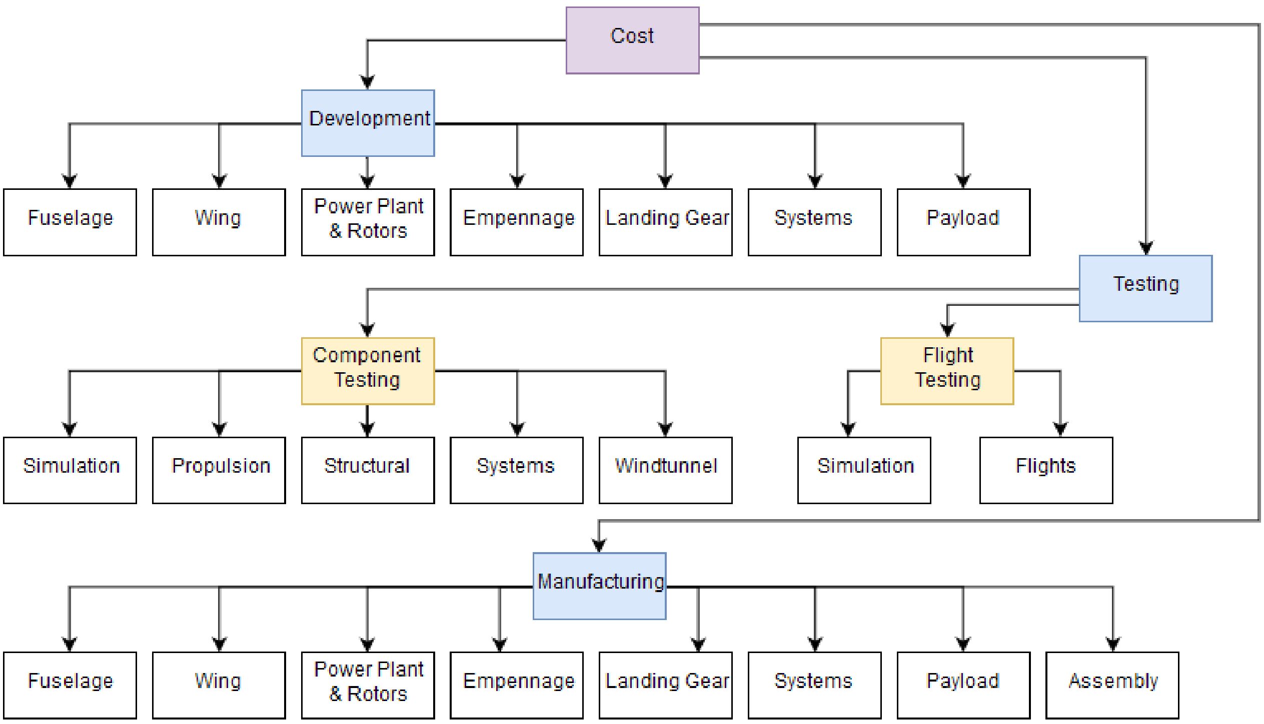

Figure 12.1: Cost break-down of Futura.

12.1.1 Development

To approximate the total development cost of Futura, a project valuation tool from MIT was used. First, the mass of the different subsystems of Futura needed to be determined, which was done in chapter 9. After that, the development cost per unit mass of that subsystem was multiplied with the actual mass of that subsystem to obtain the development cost of the subsystem. As the development costs per subsystem in the MIT report are given in $\$\mathrm{lb}^{-1}$ in FY2002, these values had to be converted to €/kg in FY2019 as the development of Futura started in the year 2019. With an average inflation rate in the US of 2% and a conversion rate of 0.453592 $\mathrm{kg\,lb^{-1}}$, the subsystem development costs in SI units could be found.[1,2]

The development cost of the complete Futura system is then the sum of the development costs of its subsystems, which was found to be 182.32 M€ in FY2019. Table 12.1 gives a clear overview of the subsystems and their corresponding development costs [133].

Table 12.1: Futura's development costs in FY2019.

	Cost per Unit mass [$ (FY2002)/lb]	Cost per Unit mass [€ (FY2019)/kg]	Mass [kg]	Cost [M€ (FY2019)]
Fuselage	32,093	87,678.10	278	24.375
Wing	17,731	48,441.10	244	11.820
Power Plant & Rotors	8,691	23,743.82	1,609	38.204
Empennage	52,156	142,490.23	118	16.814
Landing Gear	2,499	6,827.27	174	1.188
Systems	34,307	93,726.75	677	63.453
Payload	10,763	29,404.52	900	26.464
TOTAL			**4,000**	**182.32**

12.1.2 Testing

As testing is not included in the MIT development cost estimation tool, these testing costs were estimated with Roskam [134]. They can be divided into two main processes: system component testing and actual flight testing.

Component Testing

To find the total cost related to component testing, the following formula was used: [134]

$$C_{component} = 0.008325 \cdot W_{ampr}^{0.873} \cdot V_{max}^{1.890} \cdot N_{rdte}^{0.346} \cdot CEF \cdot F_{diff} \tag{12.1}$$

$$= 0.008325 \cdot \left[10^{0.1936+0.8645 \cdot log(W_{TO})}\right]^{0.873} \cdot V_{max}^{1.890} \cdot N_{rdte}^{0.346} \cdot CEF \cdot F_{diff} \tag{12.2}$$

$$= 0.008325 \cdot \left[10^{0.1936+0.8645 \cdot log(8819)}\right]^{0.873} \cdot V_{max}^{1.890} \cdot N_{rdte}^{0.346} \cdot CEF \cdot F_{diff} \tag{12.3}$$

In this equation, W_{ampr} represents the aeronautical manufacturers planning report weight in pounds which can be estimated with the take-off weight of the Futura, V_{max} the maximum design speed in knots, N_{rdte} the number of aircraft built during the RDTE (Research, Development, Testing, Evaluation) phase, CEF the Cost Escalation Factor, and F_{diff} the relative program difficulty. N_{rdte} was assumed to be 6 based on the number of V-22 prototype aircraft built [135], and CEF and F_{diff} were considered to be 1.1 and 2 respectively based on Roskam [134].

This results in a total component testing cost of 1.69 M€. Considering that component testing will start in the year 2024, as predicted in chapter 14, this value is given in FY2024.

Flight Testing

To estimate the costs related to flight testing, the following calculations were performed: [134]

[1]URL `https://www.thebalance.com/u-s-inflation-rate-history-by-year-and-forecast-3306093` [cited 18 June 2019]
[2]URL `https://www.metric-conversions.org/weight/kilograms-to-pounds.htm` [cited 18 June 2019]

$$
\begin{aligned}
C_{component} &= 0.001244 \cdot W_{ampr}^{1.160} \cdot V_{max}^{1.371} \cdot (N_{rdte} - N_{st})^{1.281} \cdot CEF \cdot F_{diff} \cdot F_{obs} \\
&= 0.001244 \cdot \left[10^{0.1936+0.8645 \cdot log(W_{TO})}\right]^{1.160} \cdot V_{max}^{1.371} \cdot (N_{rdte} - N_{st})^{1.281} \cdot CEF \cdot F_{diff} \cdot F_{obs} \\
&= 0.001244 \cdot \left[10^{0.1936+0.8645 \cdot log(8819)}\right]^{1.160} \cdot V_{max}^{1.371} \cdot (N_{rdte} - N_{st})^{1.281} \cdot CEF \cdot F_{diff} \cdot F_{obs}
\end{aligned}
$$

Compared to the component testing cost equation, the only new parameters are N_{st} and F_{obs}: they represent the number of static test airframes built and the observables characteristics. These were assumed to be 0 and 1 respectively based on Roskam [134].

Plugging in these values results in a total flight testing cost of 931.08 k€. This value is given in FY2026 as it was assumed in chapter 14 that flight testing will start in the year 2026.

Total

Summing the values of component and flight testing results in a total testing cost of 2.62 M€.

12.1.3 Manufacturing

Calculation of the manufacturing cost per Futura aircraft is done in the same way as subsection 12.1.1: by multiplying the mass of a subsystem with the manufacturing costs per unit mass of the subsystem, the total manufacturing cost was found [133]. This is shown in Table 12.2.

Table 12.2: Futura's manufacturing costs in FY2027.

	Cost per Unit Mass [$ (FY2002)/lb]	Cost per Unit Mass [€ (FY2027)/kg]	Mass [kg]	Cost [k€ (FY2027)]
Fuselage	967	3,095.34	278	860.51
Wing	900	2,880.88	244	702.93
Power Plant & Rotors	374	1,197.16	1,609	1,926.24
Empennage	2,331	7,461.47	118	880.45
Landing Gear	221	707.42	174	123.09
Systems	452	1,446.84	677	979.51
Payload	564	1,805.35	900	1,624.81
Assembly	65	208.06	4,000	832.25
TOTAL			**4,000**	**7,929.80**

When summing the manufacturing costs for the different subsystems, a total manufacturing cost of 7.93 M€ was found for the first produced vehicle. However, a learning curve of 95% can be applied to this manufacturing cost per vehicle, meaning that each vehicle will be produced with 5% fewer resources than the one before it [133]. Quantitatively, this results in a manufacturing cost of 5.64 M€ for the 100th vehicle, or a reduction of 29%.

For the production of the prototype, the costs related to payload were removed as no seats and cargo equipment will be installed for the test flight. Also, assembly costs were halved as the costs to install the payload can be ignored in this case. This was done to try to comply with the prototype cost requirement of 2 M€. However, it can be concluded that the cost to produce the prototype, which is predicted to take place in the year 2023, is still 5.44 M€, or 3.44 M€ over budget. The main reasons for this are the high manufacturing cost of the power plant & rotors subsystem, which take up 25% of the total manufacturing cost of Futura, and the yearly inflation rate of 2%.[1] Solutions to decrease this deficiency can be to start manufacturing the prototype sooner, as the influence of inflation will decrease, and to look for government or alternative investor funding such as the promising Clean Sky initiative.[3]

[3]URL `https://www.cleansky.eu/` [cited 19 June 2019]

12.1.4 Design Cost Overview

As Futura uses innovative technology and a hydrogen-electric power plant instead of jet engines, a safety factor of 2 was applied to the development and testing costs to make sure that the estimated costs will not be exceeded throughout the project. Combined, their costs are approximated to be 369.87 M€. Verification of the results was done by calculating arbitrary intermediate results by hand. Unfortunately, validation of this estimation was not possible as no reliable development cost data was found for modern aircraft.

12.1.5 Operations

To give an idea of the operational costs to the future operators of Futura, an overview of the major costs is given in Figure 12.2 [136].

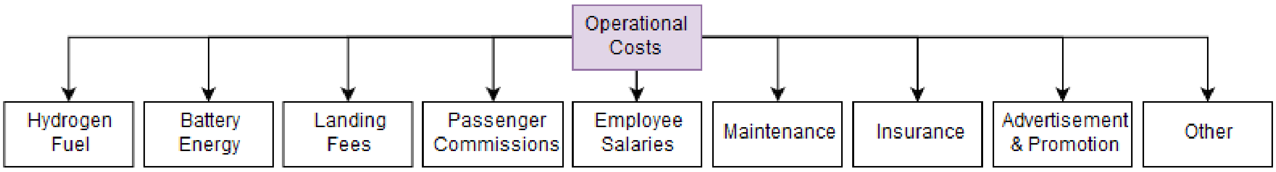

Figure 12.2: Operational cost break-down of Futura.

The largest contributors to the operational costs are the hydrogen refuelling and battery recharging: their exact costs were assessed in chapter 4, which were found to be 182.1€ per flight. The costs of the other elements in the break-down are only a fraction of refuelling and recharging [136]. As the exact annual operational costs for Futura are challenging to estimate in advance, it will be assumed for now that they are similar to the operational costs of current existing helicopters. This was determined to be approximately 880 k€ per year as will be treated in section 12.2.

12.2 Competitor Analysis

To determine the selling price for Futura, the aircraft and helicopters of different competitors were analysed and compared to Futura based on multiple parameters. Prices of existing competitors were converted to Euro in FY2027[4] and the number of passengers to payload [137]. The competitor comparison can be seen in Table 12.3.[5,6,7,8,9]

From this table, it can be deduced that Futura will be most competitive with helicopters as it performs better in terms of the selling price, payload, and cruise speed. Compared to aircraft, it can be seen that Futura only performs better than current aircraft on a payload-to-MTOW ratio. However, the VTOL capabilities of Futura are an added value which has to be taken into account in the price determination.

Based on this data, it was decided to set the selling price of Futura at 8 M€ (FY2027): this is 800 k€, or 10%, less than the average competing helicopter, which should make it possible for Futura to reach the intended 10% market share, as discussed in chapter 2.

[4] URL `https://www.ofx.com/en-au/forex-news/historical-exchange-rates/yearly-average-rates/` [cited 19 June 2019]
[5] URL `https://www.bjtonline.com/` [cited 19 June 2019]
[6] URL `https://www.airbus.com/helicopters/key-figures.html` [cited 19 June 2019]
[7] URL `https://www.leonardocompany.com/press-release-detail/-/detail/2million-flight-hours-aw139` [cited 19 June 2019]
[8] URL `https://www.sherpareport.com/aircraft/sales-business-jets-2017.html` [cited 19 June 2019]
[9] URL `https://www.textron.com/assets/FB/2016/aviation.html` [cited 19 June 2019]

Table 12.3: Futura's competitor analysis and comparison.

	Selling Price [M€]	Payload [kg]	MTOW [kg]	Range [km]	V_{cruise} [km/h]	Annual Sales	Annual Operational Cost [k€]
H125	3.01	420	2,370	483	254	162	575.14
H135	5.91	525	2,950	447	254	27	780.71
H145	10.06	840	3,700	418	248	121	999.23
H160	22.81	1,260	5,670	796	255	15	-
AW109	5.70	525	3,175	575	293	-	887.32
AW139	11.41	840	6,400	740	306	60	1,269.25
AW169	8.3	840	4,600	820	268	50	1.076.36
Bell 407	3.21	525	2,381	624	246	-	567.03
Average Helicopters	**8.80**	**722**	**3,906**	**613**	**266**	**84**	**879.29**
Citation M2	4.87	630	4,853	1,117	748	39	972.87
King Air	3.94	525	4,756	1,453	507	106	804.22
Piper M600	3.01	420	2,722	1,019	507	-	485.36
Average Aircraft	**3.94**	**525**	**4,110**	**1,196**	**587**	**72.5**	**754.15**
FUTURA	**8.00**	**900**	**4,000**	**300**	**350**	**30**	**880**

12.3 Return On Investment

The ROI can be defined as the amount of profit of a project compared to the total investment in the project. The following formula can, therefore, be used to calculate the ROI:

$$\mathrm{ROI} = \frac{\text{Revenues} - \text{Manufacturing Costs} - \text{Testing Costs} - \text{Development Costs}}{\text{Manufacturing Costs} + \text{Testing Costs} + \text{Development Costs}} = \frac{\text{Profits}}{\text{Costs}} \tag{12.4}$$

As explained in chapter 2 and section 12.2, Futura will have a selling price of 8 M€ and an average annual sales of 30 units. A slow start in unit sales is considered for the first five selling years as it is expected that customers will be hesitant to adopt Futura's new technology. Once the innovative technology has been proven to work, and potential customers are convinced of its benefits, it is predicted that unit sales will increase to approximately 30 per year, reaching a market share of 10%.

As calculated in section 12.1, it will cost approximately 369.87 M€ to develop and 7.93 M€ to manufacture the first Futura vehicle. Based on a total sales of 809 Futura vehicles over 30 years, it is estimated that the total investment in the project will be 4.59 B€. It is important to note that these investment costs are including development, testing (both component and in-flight) and manufacturing of all these 809 vehicles. Taking into account the learning curve of 95%, the ROI per selling year could then be found, which is shown in Figure 12.3. From this graph, it can be deduced that the total ROI after 30 years will be 41.04%, which corresponds to a total profit of 1.88 B€ over the whole project. Besides, the break-even point will be achieved at 172 sold Futura units, which will take approximately 8.77 years.

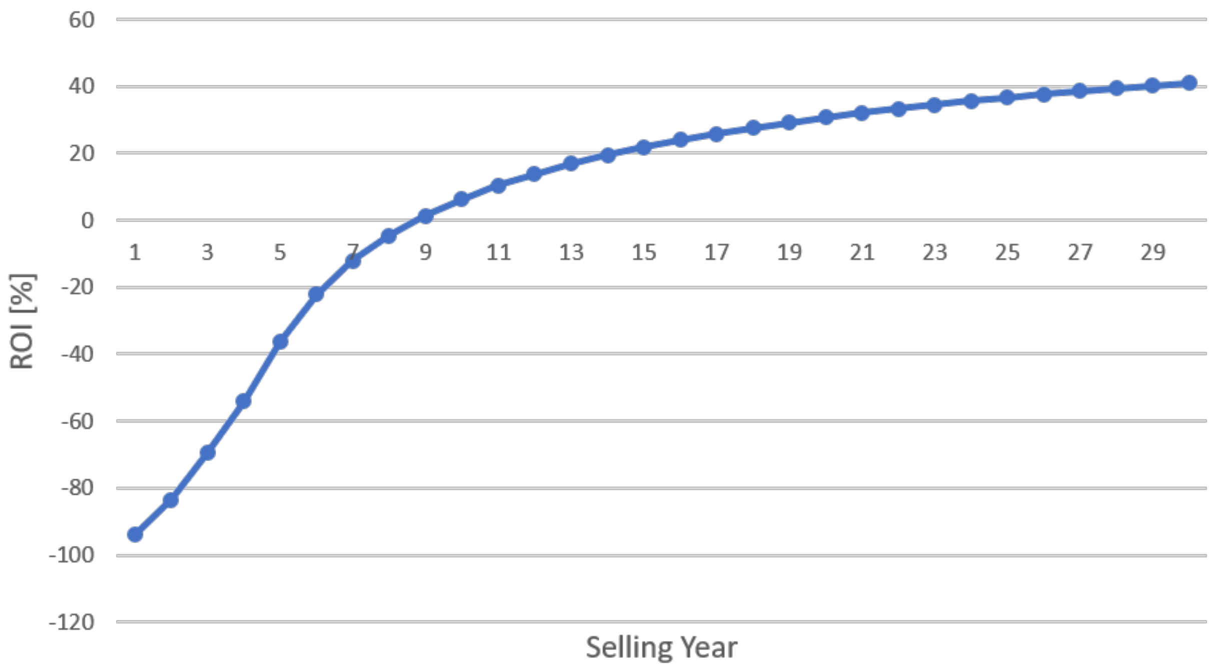

Figure 12.3: ROI of Futura for each selling year.

Conclusion

Based on a development cost of 182.32 M€ and a testing cost of 2.62 M€, and by applying a safety factor of 2 due to Futura's innovative technology, a total development cost of 369.87 M€ was found for the project. Also, a manufacturing cost of 7.93 M€ was computed for the first Futura aircraft, which decreases by 5% per vehicle that is produced. By subtracting the costs related to payload from this manufacturing cost, a prototype cost of 5.44 M€ was computed, which is 3.44 M€ more than the critical requirement of 2 M€. However, it is expected that this requirement can be achieved with the help of government and alternative investor funding. The operational costs of Futura were estimated to be 880 k€ per year based on current competing helicopters. With a selling price of 8 M€ and a market share of 10%, which is realistic as Futura performs better in multiple parameters and costs on average 10% less than existing helicopters, the break-even point is achieved at 172 units taking approximately 8.77 years to attain. Over a time of 30 years, a ROI of 41.04% is predicted, resulting in a total project profit of 1.88 B€.

13. Risk Analysis and RAMS

After having presented the different aspects which characterise the design of Futura and all the issues related to it, this chapter focuses on two other major essential topics. section 13.1 aims at investigating the reliability, availability maintainability, and safety of the aircraft. Furthermore, section 13.2 discusses the significant technical, commercial, and operational risks Futura could be subjected to and proposes adequate mitigation strategies.

13.1 RAMS

High reliability and safety are key aspects of the design. Futura has to be reliable and safe to be successful on the market. Besides being dependent on each other, these two aspects are also related to the availability and maintainability for which requirements and regulations must comply with.

13.1.1 Reliability

The reliability of the aircraft can be defined as a result of the reliability of the different system the aircraft is composed of. Estimates related to the airframe, the electrical, the power plant, the ground control, and the cockpit instrumentation system can be derived from [138], which provides reliability values for a sample of general aviation aircraft. Reliability estimates for the flight control system and the power plant are also provided; however, since these systems differ significantly from the one of a conventional aircraft, new estimates have to be determined. For what concerns the power plant system, a failure rate per component has been defined in section 6.5, resulting in an overall failure rate of $3.48e^{-9}\ \frac{failures}{time[h]}$ for the complete system. To determine the related reliability, a negative exponential distribution can be used such that:

$$R = e^{-\lambda t} \tag{13.1}$$

Due to its simplicity, this function is often used in reliability analysis to model random failures and is therefore, suitable for this estimate [5]. The time at which the reliability is calculated depends on the time interval between the maintenance sessions. As prescribed by regulations, after 400 hours of flight an A type inspection is mandatory to assess the integrity, the functionality and the correct placement of the different components of the control system and the power plant system. Having defined the failure rate and a suitable time interval, reliability of 0.999 can, therefore, be derived for the power plant system.

A similar approach has been used to unsuccessfully determine a reliability estimate for the flight control system. Very little information could be retrieved concerning the failure rate of the flight control system components. According to what is reported by the V-22, the flight control system of the V-22 tilt-rotor aircraft was subjected 69 failures out of 804 hours of flight testing, leading therefore to a failure rate of $0.085\ \frac{failures}{time[h]}$[106]. Calculating the reliability using this failure rate and a time of 400 h leads to a reliability estimate close to zero. The obtained result does not provide a useful indication for this analysis. The mentioned failure rate is indeed extremely high and cannot, therefore, be considered as a reliable value. From [106], it is indeed not clear how failures are defined; furthermore, such failures have been assessed under testing conditions instead of normal operating conditions, resulting therefore in a failure rate higher than the average. On the other hand, the same report states that the flight control system and in particular the swash plate is responsible for the majority of the failures, and it is, therefore, the system which affects the reliability the most. In conclusion, no reliable value could have been defined for the reliability of the flight control system.

The reliabilities for the different systems are summarised in Table 13.1. By multiplying these values, it is possible to define a reliability estimate of 0.9714 for the whole aircraft, excluding the flight control system.

Table 13.1: Reliability of aircraft systems.

System	Reliability Estimate
Airframe	0.99940
Electrical	0.99997
Power Plant	0.99999
Ground Control	0.99598
Cockpit Instrumentation	0.976

13.1.2 Availability

An availability of 90% has to be reached to satisfy the customer requirement. For this goal to be achieved, it is important to minimize the time the aircraft spends on the ground due to maintenance operations. When taking a time of one year as a reference, this requirement translates into availability of 328.5 days. Consequently 36.5 days or 401.5 hours a year can be dedicated to maintenance, considering the aircraft is operative for a maximum of 11 hours per day. According to what prescribed by regulations, the aircraft is yearly subjected to the so-called A inspections at least every 400 hours of flight, requiring 10 hours each to be completed. Since it is expected from the aircraft to be operative 11 hours per day, an inspection of this type has to be performed every 36 days. This leads to 100 hours of required maintenance per year. In addition to this estimate, B checks are also performed every 6 months, requiring 72 hours of maintenance.[1] It is therefore concluded that, by regulations, the aircraft has to be grounded for at least 244 hours per year. This estimate leaves room for 157.5 hours to be possibly dedicated to further unscheduled maintenance. Furthermore, the time outside the aircraft daily shift hours could also be used for the same purpose, leading to an extra of 4270.5 hours per year. Given that the flight control system is more subjected to failure than other control systems, it is expected from this system to require more maintenance hours than the ones planned from the regulations [106]. However, considering that on the average a commercial aircraft requires the same amount of hours for unscheduled maintenance as for scheduled maintenance (Wim Verhagen, personal communication, 23 June 2019), it is concluded that given the spare amount of hours, the 90% availability requirement can still be met.

13.1.3 Maintainability

The maintenance of Futura is based primarily on periodic inspections (A, B, C, and D checks) as already described in [116]. However, each aircraft will have to spend more hours under maintenance than the minimum prescribed by the regulations. According to [106], the V-22 Osprey takes on the average 18.6 maintenance working hours per flight hour. One of the main issues because of which the V-22 requires such a consistent maintenance effort is due to hydraulic and nacelle related problems: hydraulic lines, flight control system actuators and all the nacelle components are claimed to be crucial maintenance items [106]. Since Futura has a comparable configuration as the V-22, such items are of equal fundamental importance for its maintenance. However, unlike the V-22, Futura will not operate in harsh environments (e.g., desert or similar) which rapidly deteriorate the components of its systems. It is, therefore, possible to drastically reduce the maintenance of working hours per flight hour to less than 10.

To guarantee easy accessibility of the nacelles without the need of removing them completely, multiple panels are placed on the side, on the bottom and on the top of the nacelle itself along its length. Furthermore, the lower wing configuration also contributes to making the inspection of the wing itself and the

[1]URL `https://www.qantasnewsroom.com.au/roo-tales/the-a-c-and-d-of-aircraft-maintenance` [cited 21 May 2019]

nacelles easier.

When looking at the components of the power plant system, the tank, in particular, requires special considerations. As explained in detail in section 13.2, leaks from the tank are possible. Hence the tank compartment shall be cleaned after each flight. Furthermore, to avoid the risk of hydrogen ignition within the tank itself, all the related minor maintenance operations shall be performed with the tank being always at least 15% filled. The performance of other power plants components such as the fuel cells and batteries can be continuously monitored on the ground and during the flight and consequently, they do not require visual inspections as frequently as for the tank.

13.1.4 Safety

Safety of the passenger and crew members of an aircraft is of fundamental importance: their lives at any point in time during operation shall never be in danger. To ensure this goal is achieved, the first step from the design point of view is to meet all the CS-29 requirements. An extensive requirement analysis has been performed already at an early stage of the project, and the design of the aircraft design has therefore been developed to achieve the minimum safety performance imposed by the regulations. What is more, since safety plays a central role in the design itself, the effort has been spent to enhance the safety level above the bare acceptable minimum. As an example to start with, in case of crash or emergency, an extra emergency door has been included in addition to the single one the regulations prescribe. On a more general level, a fail-safe philosophy has been adopted as explained in [116]. Such redundancy philosophy is of particular importance for the power plant system: being the hydrogen technology yet subject of research in the aerospace engineering field, the implemented power plant is one of the key innovations of the current design. It is, therefore, important to guarantee a high level of reliability and safety. The estimated reliability of 0.99999 for the power plant system as reported in [139] results indeed from the application of a sufficient number of redundant units per component. Table 6.7 in subsection 6.5.2 summarises the degree of redundancy applied per component.

Another safety consideration that has to be done concerns the corrosion resistance of Aluminum 2024T6, which is the material used the most in the design of Futura. The application of aluminum alloys, in general, is indeed restricted by poor corrosion resistance, which is due to the easily erodible protective oxide layer [140]. Although corrosion inhibitors such as chromates are widely used in aerospace applications to enhance the corrosion resistance, these are also environmentally unfriendly since they could contain metals such as chromium and zinc. Equally effective ceramic coatings are therefore implemented.
Finally, a major risk for safety is related to the use of hydrogen: due to its low flammability, ignition or even explosion can generate as a consequence of hydrogen leaks from the fuel tank. This risk is elaborated in detail in subsection 13.2.2, where effective mitigation measures are proposed to minimize the likelihood and impact of this event.

13.2 Risk Analysis

This section focuses on the major risks deriving from the design of Futura. Based on the preliminary analysis performed in the previous phases of the design, the current risk analysis aims at reassessing and further elaborating on some of the major risks already addressed [116]. Furthermore, with the detailed design being developed, new uncertainties arise which are also tackled here. The structure of this section is, therefore, as follows: firstly, the risks in consideration are introduced, and the causes and consequences for each are reported. The risks are then assessed, and a risk mitigation strategy is consequently planned. Finally, the post-mitigation matrix shown in Table 13.6 summarises the expected effects of the mitigation implemented.

13.2.1 Risk Identification

The first step to take in the risk analysis process is to identify the major risks to take care of. To be consistent with the method previously adopted in [116], also, in this case, a division of the risks into a technical, commercial, and operational category is considered. Table 13.2 shows the main risks that are analyzed with their related causes and consequences.

Table 13.2: Risk identification table.

Risk ID	Risk	Cause	Effect
Technical Risks			
T4	Catastrophic rupture of the fuel tank	Over pressure, internal tank combustion	Hydrogen ignition, tank explosion
T6	Small leaks from hydrogen tank	stress cracks in tanks due to pressure cycling, faulty pressure relief device, faulty coupling from tank to feed line	Hydrogen losses, hydrogen ignition
T9 *	Battery failure during operation	Electrolyte leakage, over charging, over discharging, thermal runaway	Loss of aircraft power, battery ignition damage of nearby located electrical components
Commercial Risks			
C4*	Short flight routes get cancelled	Political decisions based on environmental considerations	Futura becomes more competitive on the market
C5*	Futura is not profitable	More competitors on the market, loss in competitivity	Failure of the project
Operational Risks			
O6*	Entering the dead man zone during operation	Operational constraints (e.g. departing from a roof top)	Autorotation not achievable
O7*	Failure of nacelle rotation during operation	failure of the tilt rotor mechanism	Loss of aircraft controllability

All the risks listed in Table 13.2 are defined by the mean of an identifier; furthermore, the new risks which are considered in this analysis are additionally marked by a star sign. Among these, risk C4 differs significantly from the risks found so far, since it represents an opportunity rather than a threat. By definition, a risk can indeed be both, and for complete risk identification, it is, therefore, essential to include also relevant opportunities [141]. Risk T4 and T6 have already been considered in [116]. However, a reassessment is here necessary, considering the critical consequences they could lead to as explained in subsection 13.2.2.

13.2.2 Risk Assessment and Mitigation

The main risks which have been identified in subsection 13.2.1 are consequently assessed and mitigated. The risk assessment is done following the same approach as defined in [116]: the likelihood of occurrence and the severity of the impact are evaluated on a scale from 1 to 4 where value 1 refers to a remote probability of occurrence and negligible impact while value 4 represents high likelihood and catastrophic impact. With respect to the scale used in this assessment, a remote likelihood refers to an event which is extremely unlikely to occur, while an event is likely when it will occur several times. Similarly, a catastrophic impact results in serious damages to the system or to the environment around it or even in human losses. By contrast a negligible impact does not imply any major damage to the system. In case an opportunity is considered, such as for risk C4*, the risk impact is intended to affect positively the system or the operational environment the aircraft operates in: in the specific case of risk C4* less flight routes used by the competitors will have a positive impact on the profit of Futura. A total score given by the product of the likelihood and the impact can be defined per risk: such score gives a measure of how important the risk itself is and it consequently allows for risk prioritisation.
A total score of 16 resulting from maximum likelihood and impact represents therefore the highest level of risk.

The results are summarised in Table 13.3 and Table 13.4. It can be seen that the risk scores range between 6 and 8, meaning that although they are not close to the highest risk level, they are still important risks for which a mitigation measure is required.

Table 13.3: Risk Assessment Matrix (RAM).

Likelihood & Impact	Remote (1)	Unlikely (2)	Possible (3)	Likely (4)
Catastrophic (4)		T4		
Critical (3)		T6,T9*, C5*,O7*	C4,O6	
Marginal (2)				
Negligible (1)				

Table 13.4: Total score per risk.

Technical		Commercial		Operational	
T4	8	C4*	9	O6*	6
T6	6	C5*	6	O7*	6
T9*	6				

Legend
Risk
Risk ID
Total Score

For each of the assessed risk in Table 13.3, a detailed explanation is provided. Furthermore, the mitigation measures implemented per risk are discussed right after.

- **T4) Catastrophic Rupture of the Fuel Tank**: given that detailed design of the tank has been developed, a reassessment of this risk has become necessary. In [116], it was claimed that one of the causes of this risk is the over-pressurisation of the tank itself. At standard conditions, the tank operates at 2.5 bars, which corresponds to 3% of the total hydrogen being gas and 97% being liquid. Whenever this pressure value is exceeded over pressurisation occurs, which could ultimately lead to an explosion if the pressure level, including the safety factor, is reached. An additional cause which could lead to a fatal rupture of the tank is combustion within the tank itself, which could occur in the case air is let into the tank. Therefore, as reported in the [116], while the likelihood of this risk to happen is still remote, the severity of the impact is catastrophic.

  MITIGATION: To avoid over pressurisation of the fuel tank, two pressure relief valves are implemented, one for redundancy purposes. At normal operating conditions (i.e. a temperature of 50°C and pressure of 2.5 bars) these valves allow the internal pressure decrease when a 3% gas content is reached as explained in section 6.3.3. A cryogenic safety valve of type 06810 is suitable for the performance the tank has to sustain, since it has been certified by the manufacturer to correctly operate between temperature ranges of -270°C and +400°C. On the drawback side this valve type works with a spring load system which requires regular maintenance [142]. Concerning this mitigation measure, an additional remark has to be made: it has indeed been estimated that if a power higher than 26.6 kW is applied to the tank, the rate at which liquid hydrogen turns into a gas is higher than the discharge rate the safety valve can generate. It is therefore of fundamental importance that the tank is as much isolated as possible from any heat source: for this reason, the tank has been located in a sealed compartment. To prevent the risk of catastrophic rupture due to internal fire, the mitigation measure recommended to the operators of the aircraft is to leave at least 15% of hydrogen always in the tank: on one side this allows to maintain always the tank at the sufficient operating temperature, and, on the other hand, the pressure is enough to prevent air from flowing into the tank. Furthermore, ground operations shall be meticulous to guarantee an airtight refuelling.

- **T6) Small Hydrogen Leaks from the Fuel Tank**: as for risk T4), also this risk has already been discussed in [116]; however, with a detailed tank design being developed, a reassessment of this risk is necessary. In particular, there is the concern that, although the tank is characterised by three different alternating layers of metal and composite material, the tank walls can still allow for a negligible amount of hydrogen molecules to pass through. This is because hydrogen has a minimal molecular size and can easily permeate into most metals [142]. A faulty connection of the tank with the pipeline can also be the cause of small leaks from the tank itself. The mentioned leaks which occur during the time of a single flight do not represent a relevant danger for the safety of the aircraft. However, the hydrogen released during multiple flights and accumulating in the tank compartment could reach a critical level for which a minimum amount of energy is sufficient for ignition. In the worst case hydrogen to air ratio of 0.04 and 0.02 mJ of energy would be enough for the mixture to ignite [143].

MITIGATION: although it is challenging to give an estimate of how much hydrogen is released through the walls in a defined time interval and most likely also experimental measures would lead to negligible hydrogen concentrations, it is still essential to plan a mitigation measure for this risk. This is in contrast to what reported in the [116], where it was stated that no mitigation measure was required. However, by reassessing the severity of this risk and consequently defining a suitable mitigation strategy, the safety of the aircraft will be enhanced. Coping with this risk is therefore done in two steps: firstly it is necessary to monitor the concentration of hydrogen in the tank compartment at any point in time, and, secondly, such concentration has to be decreased whenever the critical hydrogen to air ratio of 0.04 is reached. The first step can be achieved by implementing hydrogen detecting sensors: these shall be able to warn the pilot if the mentioned maximum allowable hydrogen level is met. Following this warning, the pilot shall land as soon as possible. Furthermore, since only 0.02 mJ of energy are required to ignite the Hydrogen-air mixture, it is of fundamental importance to limit the electrical components in the compartment. Therefore, it is required that the hydrogen detector wiring within the tank compartment is made of optical fibres rather than standard electric cables. Hydrogen sensors implementing optic fibres have already been subjected to research for their potential of not generating sparks or short circuits [144]. To lower the concentration of Hydrogen, two pneumatic control valves are installed on the pressure side and of the suction side of the fuselage. Pneumatic actuators operate these valves instead of electric ones, and when opened, they allow for a flow of air to the external environment. After every flight, these control valve shall be completely open, and the tank compartment has to be cleaned from the hydrogen that could have been released during the flight.

- **T9*) Battery Failure during Operation**: 36 batteries connected in parallel are installed on board of the aircraft. Each of them is composed of 126 cells connected in series. Given that these batteries provide 73% of the peak power required for normal take-off and landing operations, it is important to be aware of the causes which can lead to their failure as well as to investigate effective mitigation strategies. The modes which can lead to a cell failure can be divided into not-energetic and energetic failure modes [145]. An important failure mode belonging to the first category consists in the electrolyte leakage caused by mechanical damage: such leakage could result in the short-circuiting of the adjacent systems, and most importantly its contact is hazardous for humans. Furthermore, an ideal not-energetic failure mode follows from the natural cell ageing, which consists into a slow decrease in battery capacity and an increase in impedance over time, until the point where the power demanding from the battery is no longer satisfied. However, factors such as overcharge and over discharge, can greatly affect the battery life: these are also related to one of the primary energetic failure modes, namely the thermal runaway of the cell itself. In runaway reactions, the energy stored in the battery is rapidly released, leading to a rise in temperature up to 600°C [145]. This failure mode could result therefore in a fire or even explosion, as it has already occurred on board of two 787 airliners in 2013.[2] It is therefore clear how seriously this risk can affect the safety of the aircraft and how critical its consequences are.

  MITIGATION: As already discussed in [116] in case of failure of one of the batteries, the other ones can take over and still satisfy the power demand, meaning that a fail-safe approach is adopted as a first measure to mitigate the risk of battery failure. Several other simple measures could, how-

[2]URL `https://www.faa.gov/news/press_releases/news_story.cfm?newsId=14233` [cited 16 June 2019]

ever, be implemented to limit the impact of this risk. To prevent overcharge and over discharge, a common solution is to set specific voltage limits which allow the electrical load of the battery pack to be disconnected when such a limit is reached. Battery pack design usually contains also mechanisms to disconnect the battery if its performance deteriorates remarkably [145]. A protection safety module (PCM) is implemented to serve both the function of overcharging/over-discharging prevention and overcurrent prevention [146]. Furthermore, to protect the nearby components from the risk of battery failure due to leakage or thermal runaway batteries are isolated from the nearby components by mean of sealed casings capable of both contain the leakage and to resist the 600°C temperatures resulting from the thermal runaway.

- **C4*) Short Flight Routes get Cancelled**: in contrast with many risks that have been so far reported, the current one is an opportunity rather than a threat. Due to environmental reasons short-range routes such as the one connecting Amsterdam to Brussels will be most likely be banned soon. If this risk is triggered, Futura will become more competitive on the market.[3]

  MITIGATION: the mentioned opportunity is dependent only on political decisions external to the development of Futura. It follows consequently that no mitigation measures can be taken to enhance the likelihood of this risk to occur.

- **C5*) Futura is not Profitable**: A Return Of Investment of 10% is expected in 9 years, assuming Futura manages to take 10% of the current helicopter market share. However, the risk of not achieving this goal due to the growth in the number of competitors would make Futura not profitable. Another cause which would reduce the margin of profit is related to the customers being sceptical about the technologies implemented: although hydrogen as a fuel source for commercial aircraft is currently an object of research, no commercial hydrogen aircraft are now available on the market. Therefore it is possible that customers prefer investing in proved kerosene powered solutions. The impact of this risk would be critical since the realisation of this event would translate into a failure of the project.

  MITIGATION: The Return of Investment is closely related to the development and testing cost, which has been estimated to be 335 million euros. Such estimate already includes a safety factor of two as explained in chapter 12, and it represents, therefore, an implicit mitigation measure by itself. Furthermore, to push more investors to invest in this project, European governments shall take the first step, such that the investors themselves will have to share a lower risk.

- **O6*) Entering the Dead Man Zone during Operation**:— For each helicopter combinations of heights and velocities exist defining the so-called dead man curve such that autorotation can be performed in case of engine failure. The critical consequence of this risk is, therefore that, being the conditions for autorotation not met in this area, a safe autorotational landing cannot be achieved. This will consequently result in a crash with potential injuries on board or and/or the surface. During standard operations from airport to airport, sufficient space shall be guaranteed so that the pilot in command always has the room to safely perform a take-off or landing without entering this dangerous zone. Therefore the likelihood of this risk is low.

  MITIGATION: In regular operations, the helicopter is always expected to have enough manoeuvring space during take-off and landing such that a safe combination of height and speed is guaranteed. On the other hand, departing from a heliport at the top of a building is also an operating condition that the aircraft will encounter. It is, therefore, possible that the dead man triangle is entered. In such a case, sufficient speed or height shall be gained as soon as possible. However, no specific mitigation measure can be defined for this risk besides ensuring proper flight training: the pilot in command is indeed expected to know what the boundaries of the dead man zone

[3]URL `https://www.brusselstimes.com/all-news/brussels-all-news/54246/dutch-parliament-wants-brussels-amsterdam-flights-axed/` [cited 16 June 2019]

are and he/she is at any time of the flight responsible for safely operating the aircraft. This risk also highlights the importance of spending sufficient effort on training the pilots: the safety of the aircraft depends not only on the aircraft itself but also on the way pilots can manage the aircraft. This is especially remarkable for Futura for which only one pilot is in charge of all flying related tasks.

- **O7*) Failure of Nacelle Rotation during Operation**: Being able to tilt the rotors during take-off and landing is crucial for the successful accomplishment of these phases of the flight. A failure in the mechanism which allows the nacelle rotation would, therefore, result in the possibility of losing control of the aircraft with the consequent possible crash. It has been assessed that for the V-22 Osprey, the majority of the failures during the testing period is related to the flight control systems. This risk ranks therefore high both in terms of likelihood and impact.

  MITIGATION: Two different scenarios have to be analyzed to define an appropriate mitigation strategy. In the first case, the failure of the tilt-rotor mechanism occurs with the engine being vertical or at a tilt angle smaller than the maximum value for which propeller ground clearance is guaranteed. Since such scenario is most likely met during the take-off phase, the safest solution would be to lock the nacelle in place and to perform a landing with the functioning rotor being brought back to its initial vertical position. In case the failure occurred during the cruise, with the rotor axis being parallel to the fuselage axis, the situation would be more critical since an emergency landing would have to be performed without propeller clearance. Additional titanium swivels allowing the nacelle rotation such as the ones used by the V22 are therefore implemented for redundancy [104].

13.2.3 Post Mitigation Risk Assessment

The mitigation measures discussed in subsection 13.2.2 are summarised in Table 13.5. Their effect are furthermore reported in Table 13.6.

Table 13.5: Summary mitigation measures.

Risk ID	Risk	Mitigation
Technical Risks		
T4	Catastrophic rupture of the fuel tank	Implement cryogenic safety valve, leave always the tank at least 15% full
T6	Small leaks from hydrogen tank	Implement hydrogen detecting sensors, Implement pneumatic actuators to allow flow through the tank compartment
T9*	Battery failure during operation	implement back up batteries, implement protection safety module, place batteries within casings
Commercial Risks		
C4*	Short flight routes get cancelled	No mitigation measure is required
C5*	Futura is not profitable	Involve governments as stakeholders
Operational Risks		
O6*	Entering the dead man zone during operation	Ensure proper pilot training
O7*	Failure of nacelle rotation during operation	Implement redundant swivels

Table 13.6: Post mitigation risk assessment matrix (RAM).

Likelihood & Impact	Remote (1)	Unlikely (2)	Possible (3)	Likely (4)
Catastrophic (4)	T4			
Critical (3)	T6,T9*,O7*		C4,O6*	
Marginal (2)		C5*		
Negligible (1)				

Conclusion

In this chapter the RAMS and Risk analysis have been addressed. It was concluded that a high level of reliability characterise the power plant system and the overall design of Futura, although a feasible value for the reliability of the flight control system could have not been defined. This result is also related to the fail safe approach implemented which has a drastic impact on the safety of the aircraft. It has furthermore been assessed that the 90% availability requirement can be met on the basis of the estimated time required for scheduled and unscheduled maintenance.Concerning maintenance itself, the critical items that shall be regularly inspected are the nacelle components and the fuel tank. Due to possible hydrogen leaks which could lead to ignition or even explosion, the tank itself is object of an extensive risk analysis, as a result of which several mitigation measures are adopted. Among them, optic fibre sensors are implemented to detect hydrogen leaks and a safety valves are installed to to release gaseous hydrogen from the tank or from the tank compartment when needed. Furthermore other major commercial and operational risks are investigated including the opportunity that short flight routes get cancelled.

14. Future Development

This chapter addresses the post DSE activities needed to bring forward the design of Futura. The conceptual design phase completed in this project is going to be followed by other development phases: section 14.1 outlines the logical steps in development that are needed to bring the development of the aircraft forward. A particular focus is placed on the initial phase of the development (Early configuration and Market Analysis phase) for which the logical sequence of actions has been outlined in Figure 14.1. In section 14.2, eventually, the timeline that has to be followed to complete the different development stages of the aircraft is shown.

14.1 Project Development Logic

Throughout this report, the conceptual design of Futura has been presented. The design presented in this report, however, is only the beginning of a development project which, to lead to the prototype, has to follow several other phases. The development cycle of a civil aircraft can be divided into three main phases: development, component testing, and flight testing. The development phase, however, can be decomposed in the other three sub-phases: Early Configuration and Market Analysis, Product Definition and Detail structural, systems, and process design [147]. The timeline of Futura's airframe encompasses eight years: after the eighth year, the first aircraft will be delivered. The post-DSE activities are those concerning the 12 months of the Early Configuration and Market Analysis phase.

The logic of the activities included in this part of the aircraft development have been explored and presented in Figure 14.1. The activities have been grouped into inputs, outputs, and outcomes: the inputs are the set of objectives that have to be completed; the outputs are the sequence of activities which allow to reach such objectives; the outcomes deriving from reaching the objectives are presented in the short, medium and long term. On top of reaching a higher level of detail in designing the configuration, two fundamental objectives of this phases are the development of a business plan and the complete identification of a timeline related to the development of the battery pack. The first one is essential to make sure that the product is going to be profitable in the future, while the second one is crucial to go through an active product definition phase. In the short run, the final concept configuration should be obtained to obtain the government funds needed to go through the product definition phase.

The following phases are also fundamental since they will define the aircraft characteristics much higher level of detail. One key phase of the cycle is the product definition: in this phase, three equal design cycles are included thanks to which final aerodynamic and control and stability characteristics will be obtained thanks to repeated wind tunnel tests. These cycles will allow to converge to final results concerning the aerodynamic and stability properties of the aircraft. The product definition phase is going to be followed by the detailed structural, systems and process design in which the complete CAD models of the aircraft will be produced as well as the simulations needed to predict the aircraft performances. Eventually, the manufacturing and logistics process is also going to be precisely defined, and the basis for the aircraft certification will be established to obtain it before the first delivery. The development phase of Futura will be followed by the components testing phase in which systems will be installed, and static and fatigue tests will be completed. Eventually, the last phase of the development is made by the flight tests which are necessary to validate the performance characteristics of the aircraft. The time order of the activities of the complete development cycle is presented in section 14.2 based on typical development times [147].

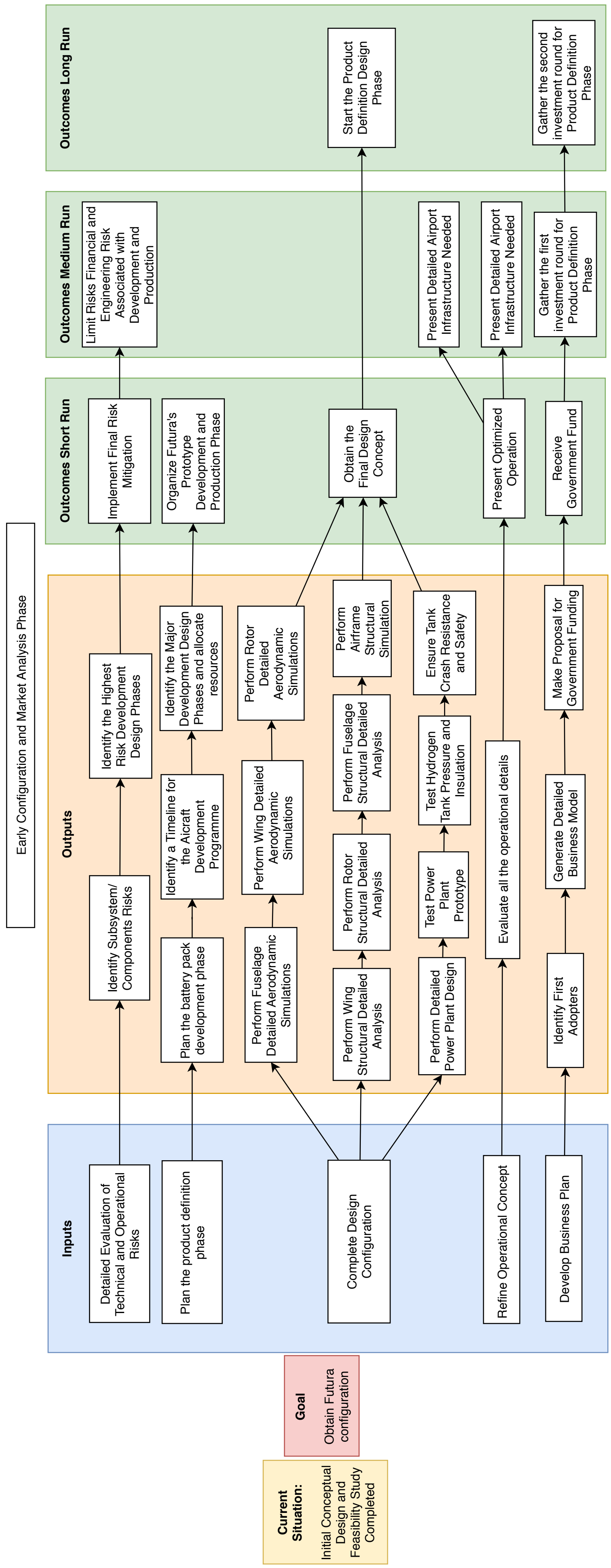

Figure 14.1: Development logic of early configuration and market analysis.

14.2 Project Gantt Chart

ID	Task Name	Duration	Start	Finish
1	**Development**	**58,8 mons**	**Sat 22-6-19**	**Fri 22-12-23**
2	**Early Configuration & Market Analysis**	**12 mons**	**Sat 22-6-19**	**Thu 21-5-20**
32	**Product Definition**	**24 mons**	**Wed 22-4-20**	**Tue 22-2-22**
33	**Cycle 1**	**8 mons**	**Wed 22-4-20**	**Tue 1-12-20**
34	Finalize Aerodynamic Design	4 mons	Wed 22-4-20	Tue 11-8-20
35	**Wind Tunnel Tests**	**4 mons**	**Sat 1-8-20**	**Thu 19-11-20**
36	Cruise Aerodynamics	1 mon	Mon 3-8-20	Fri 28-8-20
37	VTOL Aerodynamics	1 mon	Tue 1-9-20	Mon 28-9-20
38	Loads	1 mon	Thu 1-10-20	Wed 28-10-20
39	Stability & Control	1 mon	Thu 1-10-20	Wed 28-10-20
40	**Cycle 2**	**8 mons**	**Sun 1-11-20**	**Thu 10-6-21**
47	**Cycle 3**	**8 mons**	**Tue 1-6-21**	**Mon 10-1-22**
54	**Detail Structural, Systems & Process Design**	**18 mons**	**Fri 22-4-22**	**Thu 7-9-23**
55	Freeze the Design	3 mons	Fri 22-4-22	Thu 14-7-22
56	Final Load Calculation	4 mons	Mon 1-8-22	Fri 18-11-22
57	CAD/CAE Completed	4 mons	Thu 1-12-22	Wed 22-3-23
58	Certification Basis	12 mons	Fri 1-7-22	Thu 1-6-23
59	Simulation Basis	12 mons	Mon 3-10-22	Fri 1-9-23
60	Define final manufacturing process and logistics	4 mons	Mon 1-5-23	Fri 18-8-23
61	**Components Testing**	**30 mons**	**Wed 22-11-23**	**Tue 10-3-26**
62	Component Fabrication	12 mons	Fri 1-12-23	Thu 31-10-24
63	Component Testing	7 mons	Mon 1-7-24	Fri 10-1-25
64	Major Assembly	3 mons	Wed 1-1-25	Tue 25-3-25
65	Static Test	3 mons	Mon 3-3-25	Fri 23-5-25
66	Fatigue Test	3 mons	Mon 2-6-25	Fri 22-8-25
67	System Installation	6 mons	Tue 1-7-25	Mon 15-12-25
68	**Development of training & support services**	**5 mons**	**Wed 1-10-25**	**Tue 17-2-26**
69	Install Necessary faciltities for refuelling in airports	2 mons	Wed 1-10-25	Tue 25-11-25
70	Install Necessary falcitities for recharging in airports	2 mons	Mon 1-12-25	Fri 23-1-26
71	**Flight Testing**	**12 mons**	**Wed 22-4-26**	**Tue 23-3-27**
72	Final Certification Tests and Proof of Compliance	7 mons	Wed 22-4-26	Tue 3-11-26

Figure 14.2: Project Gantt chart for post-DSE activities.

15. Conclusion and Recommendations

15.1 Conclusion

This paper has presented the design for Futura, a hydrogen electric aircraft with VTOL capabilities. In chapter 2 it was found that the market opportunity of Futurais intra-city and inter-regional hub connections. The ever-increasing number of passengers in the air transport network has encouraged the use of small airports that need to be better connected to the main hubs. A mission profile based on a flight from Amsterdam to Brussels, approximately 300 km is developed. In chapter 4 it is determined that liquid hydrogen is optimal for Futura, with a refuelling time of 26 minutes for 14.30 kg of liquid hydrogen, estimated in the future to be price at about 10.72 €/kg for a total cost of 153.3€ for a full refuel. The current cost for 300 km helicopter mission is at about 227€. Combined with battery recharging this result in a total refuelling cost of 182€. The total procedure, including engine shutdown, disembarkment, mechanical checks, refuelling, cleaning, boarding the passengers and starting up the aircraft takes 50 minutes.

In chapter 5 the wing is sized according to its loading. It is found that the design space is constrained by the stall speed and the manoeuvring performance resulting in an optimal wing area of 21.035 m^2. Subsequently, the NACA 23018 air-foil is chosen to shape the wing due to its large enough thickness to chord ratio. Finally, the aspect ratio is found to be 5.258. As a result of the restrictions of the radiators on the wing, only flaps can be used as high lift devices, whilst simultaneously acting as ailerons. An operational envelope is created for the flight of Futura. This takes into account loads in both vertical and horizontal flight by CS-23 and CS-29 requirements. The largest load factor possible on the aircraft is 3.8 while the most negative cannot be 0.4 times the maximum load factor. To provide a safe and comfortable flight experience, a cabin design is carried out. The cabin is designed by minimising accessories while not sacrificing comfort. The aircraft will boast continuous glass windows, which is made possible by the lack of a need to pressurise the cabin. The cabin width is 1.48 m and the height is 1.4 m. The aircraft has the main door and an emergency door. With a cabin configuration set, a fuselage design is carried out. In addition to the wing, the fuselage is also a lifting member. The fuselage is designed in the shape of an airfoil to provide lifting capabilities. The airfoil for the fuselage design was selected to conform to the interior cabin design and resulted in the NACA 25121. The final major aerodynamic member of the aircraft are the rotors on the end of both wings. A study of the rotor geometry was carried out to optimise for the lowest power required for the propulsion system throughout the flight. The final rotor conceptual design consists of each hub having 3 blades with a radius of 4.415 m and a linear twist of 18°C.

In chapter 6 from the mission power and energy required a detailed system is designed to minimise weight. The general designing philosophy adopted is to select readily available components to minimise the delivery time of the product. Some components as the radiators, fuel tank and battery pack were designed in-house to meet the particular requirements of Futura. The system consists of three main components: fuel cell, battery and electric motors. Temperature control of fuel cells, batteries and motors is essential for the correct functioning of these. This is done using radiators, with 50/50 ethylene glycol solution. The total mass of the radiator and cooling liquid, with a pump, is 215.7 kg separated over three radiators in each wing.

With the radiators and the tanks decided the different components of the power plant system are decided. In the system, batteries supply the peak power requirements, while the fuel cell supplies more energy. The division of the batteries and fuel cell is optimised for ratings, stack design and redundancy measures. The minimum mass is achieved when the fuel stack delivers 343 kW and the batteries deliver the rest with a capacity of 103 kWh. The reliability of the system is analysed to ensure the avoidance of catastrophic events. Using a failure rate model and adjusting the component choices a failure rate of $3.66 \cdot 10^{-8} h^{-1}$, which allows for safe operation. With all the components selected an electric block diagram is developed, combining the different components of the system through a charge/load controller to manage loads.

In chapter 7 the landing gear is sized and positioned to avoid tipping and ensure manoeuvrability. This resulted in placing the nose landing gear 3.4 meters in front of the centre of gravity and the main landing gear 0.28 metres behind. Subsequently, the control surfaces are selected and designed. For vertical control, a swashplate with cyclic and collective is used and in horizontal flight, a T-tail, as well as ailerons, elevators and a rudder, are used. The T-tail is chosen instead of a canard because the canard cannot satisfy stability requirements for this design. The empennage size and wing position are chosen as a function of horizontal stability and controllability and are 13% of the main wing area and 34% of the fuselage length, respectively. For the empennage, both vertical and horizontal, the NACA0018 airfoil is used. Considering the vertical control, the swashplate is sized to accommodate the different control modes as well as the relevant degrees of freedom by being flapped and feathered. The nacelle hinges are sized for appropriate yaw control, requiring a torque of 43 Nm.

In the Aerodynamics Surface Structures, it is found that the load case on vertical hover constrains the main wings. The wing is optimised to not reach yield strength, and have similar maximum bending stress and buckling stress. With this design method, a wing weight of 241.6 kg is found. A similar procedure is carried out for the empennage wing structure resulting in a total empennage mass of 108 kg. Aluminium 2024 is used for its lower density and price and its excellent recycling capabilities.

Concluding the designing of the aircraft, chapter 9 presents how the design has been iterated to arrive at the overall minimum MTOW of 3925 kg. Concluding the chapter a sensitivity analysis is performed. This shows that even if a more conservative mass values for propellers and fuselage are assumed, the maximum take off requirement is still met.

In chapter 10 sustainability is considered in the manufacturing of all different subsystems. An important manufacturing process is a roll forming for the complex curvature of the fuselage. The main materials used in manufacturing will be Aluminium 7075 and Aluminium 2024. An assembly plan is developed for efficiency to allow for the production of a single product in 28 days. Sustainability is then further developed, and it is estimated that Futuracan reduce up to 97% CO_2 emissions and up to 84% in energy consumption when compared to conventional helicopters over their entire lifetime.

In chapter 12, it is found that the cost to produce the first aircraft is 7.93 M€, and the development cost is 370 M€. This leads to a break-even point of about nine years and returns on investment of 41% after 30 years.

The risk analysis is estimated that the overall reliability of the aircraft is 0.9714 and the 90% availability requirement is met.
With a full description of the system, market and processes, Futura is ready to move to the next stage. Futura aims to satisfy a glaring need in the aviation sector while setting a benchmark for the future of sustainable and accessible air transportation.

15.2 Recommendations

Market Analysis and Return On Investment

To ensure that Futura can achieve a strong position in the future aviation market, the market analysis needs to be performed more in-depth. This includes looking at flight routes in which Futura will be implemented first and carrying out surveys with business customers. These surveys might give valuable information for the design of Futura: its strengths can be touted, and its weaknesses can be improved upon. Furthermore, airports need to be contacted to assess their view on their expansion possibilities with the VTOL vehicles and their willingness to invest in VTOL infrastructure.

Based on this information, together with additional research on the design and manufacturing costs of Future, the ROI can be updated and made more precise. Also, to meet the requirement of 2 M€ for the prototype manufacturing, government investment options such as the Clean Sky initiative need to be applied for. Finally, the analysis of the current helicopter and aircraft competitors needs to be elaborated upon.

Aerodynamics

Regarding the Aerodynamics, in the future, an extensive Computational Fluid Dynamics (CFD) analysis of the lifting-body fuselage should be performed to have a more precise and detailed study of the aerodynamic properties like lift and drag, because the DATCOM method used until now uses formulas based on statistics from the previously designed aircraft and is not very accurate. At the same way, to have a clear overview of what the aerodynamics interaction between the rotor and the integration of the fuselage-wing is, the same study should be conducted. Similarly, a CFD analysis of the rotor should be performed to validate the results obtained with BEMT, as well as to provide accurate noise estimations. These could then be further analysed with wind tunnel experiments.
Further design iterations may include additional rotor optimisation by including sweep in the wing tips. This reduces the wing tip Mach number and could have two possible benefits: noise reduction or power reduction. This analysis could further improve the aerodynamic performance of the aircraft.

Power Plant

The fuel connection between the fuel tank and the fuel cell should be performed. In particular, it should include a heat exchanger to evaporate the fuel before it reaches the fuel cell. This will be done by using the warming power of the fuel cell cooling system concerning the cryogenic fuel.

To allow for this new heat exchange action and to connect the radiators to the analysis of the components of where to run the coolant lines in the aircraft should be performed. This, combined with the mechanical connection of the radiators to the wing, will finalise the design of the cooling system.

Weight of electric cables depends on the current set to flow through them. High currents require wider and so heavier cables. To minimise the weight of these, a trade-off between at which voltage and at which current power shall be delivered has to be performed. Furthermore, the weight of cables is also dependent on their length. It shall be analysed what is the effect of positioning the components on the length and weight of the cables. This two measures applied simultaneously will help to contain cables weight and bring the power plant design as a whole to a new optimum.

Stability and Control

The Stability and Control system of Futura sees margins of improvement on two fronts, namely the development of an automatic system to land the aircraft without the assistance of the pilot and the implementation of a mitigation strategy in case the landing gear fails to open.

Concerns could indeed arise about the fly-ability of the aircraft; in the event, the pilot feels sick and is unable to fulfil his duty. With sufficient time and resources, an automatic control system will, therefore, have to be developed, allowing the aircraft to land at the nearest airport safely. The possibility to remotely control the aircraft from an operator on the ground has also to be investigated as an additional mitigation measure for this risk.

Concerning the landing gear design, a belly landing both in the case of emergency gliding and vertical landing could have fatal consequences on the structure of the aircraft if the landing gear itself fails. Due to the possibility of battery ignition, the placement of the batteries under the cabin floor represents an important source of concern. As a consequence, on the one hand, an emergency landing gear deploying mechanism could be designed. On the other hand, the lower part of the fuselage structure shall be designed to sustain a load in case of belly landing to protect the batteries.

Sustainability

Because Futura's power plant is new for the industry, the disassembly plants will have to adapt to it. It has to be made sure that they establish a streamlined recycling process for fuel cells and batteries with the already-identified partners, such as Umicore. The developments of the chemical-based fibre extraction process for thermoset composites will be monitored. As they become more mature, they should be preferred over downcycling to lower-value applications.
Noise emissions will be calculated and tested to ensure compliance with ICAO regulations. At the first stage, CFD will be used to optimise the blade design in terms of noise emissions. At the second stage, wind tunnel experiments will validate the results.

A. Appendix

Functional Flow Diagram

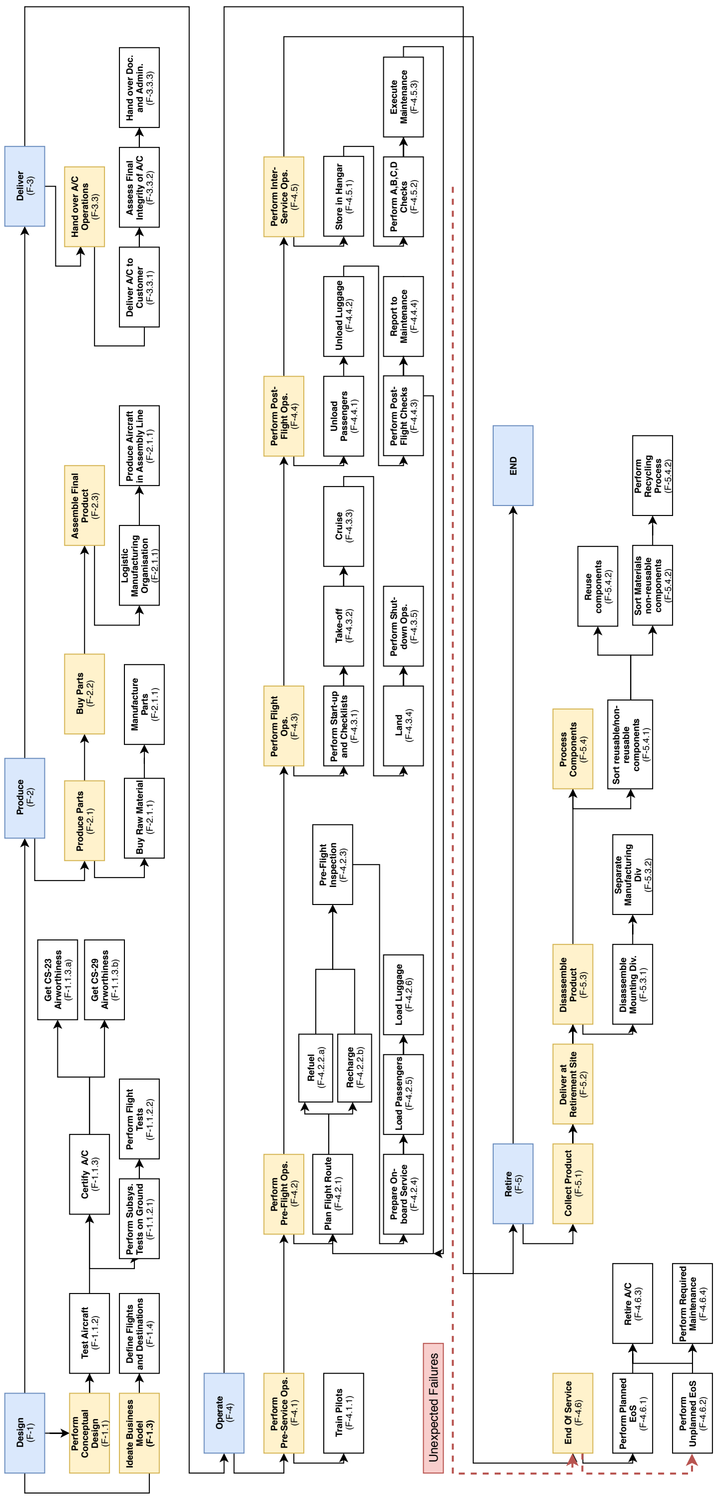

Figure A.1: Functional flow diagram.

Functional Break-Down

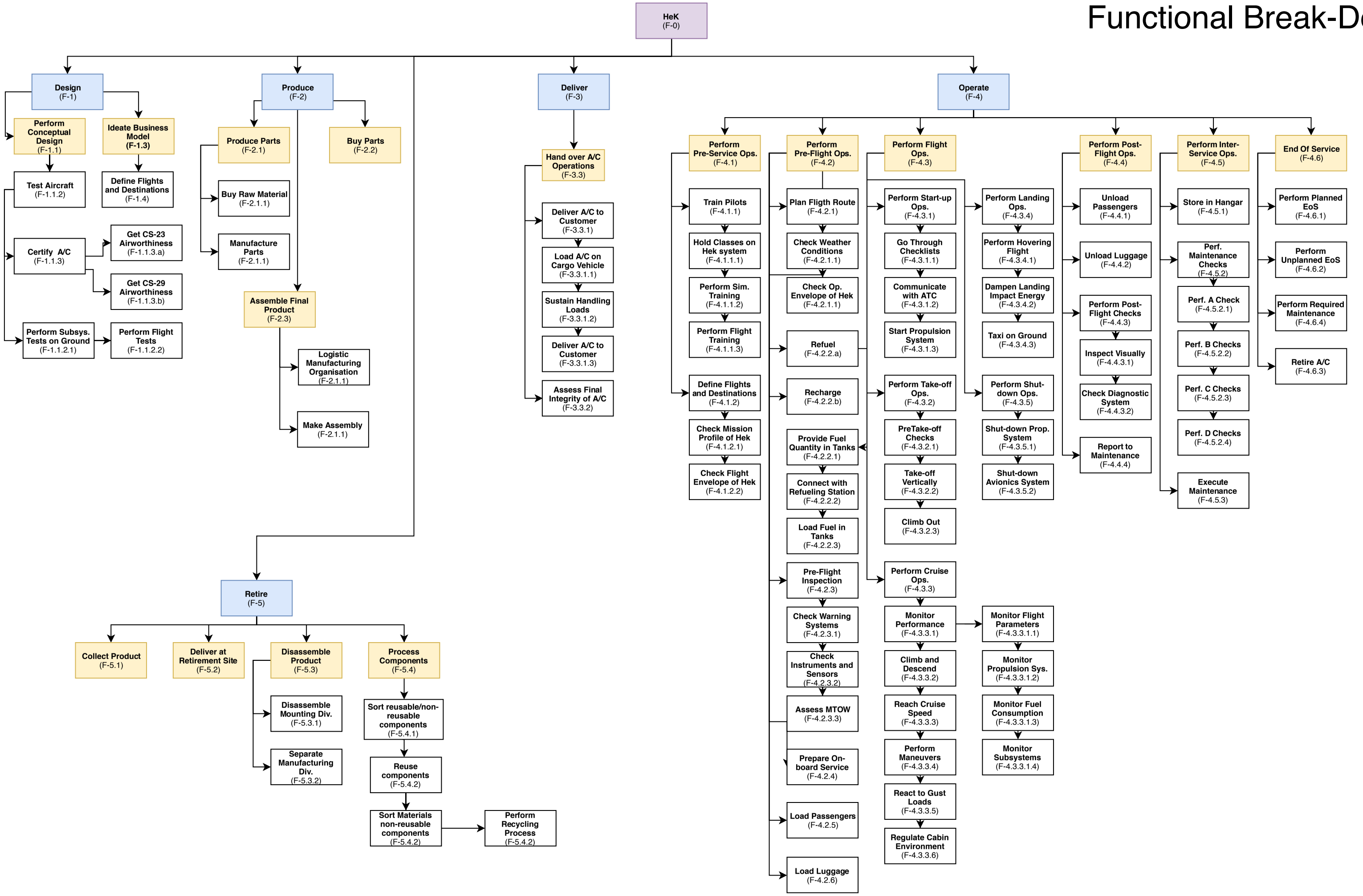

Figure A.2: Functional break down structure.

References

[1]D. S. Lee, D. W. Fahey, P. M. Forster, P. J. Newton, R. C. Wit, L. L. Lim, B. Owen, and R. Sausen, "Aviation and Global Climate Change in the 21st Century," *Atmospheric Environment*, vol. 43, no. 22, pp. 3520 – 3537, 2009.

[2]BP plc, "BP Statistical Review of World Energy," 2019.

[3]Eurostat, "Record number of air passengers carried at more than 1 billion in 2017," 2018. [Online; accessed 29-April-2019].

[4]Google, "Google Earth."

[5]R. Curran and W. Verhagen, "AE3221-I: Systems Engineering and Aerospace Design," 2019. [Online; accessed 22-May-2019].

[6]A. Barberia, K. Dally, T. D. Ponti, T. D. Smedt, B. Keltjens, G. Mancini, M. Piras, A. Scoccimarro, and F. Taccaliti, "Baseline Review - Design Synthesis Exercise," 2019.

[7]European Helicopter Association, "The Social and Economic Value of European Helicopter Operations," November 2016. [Online; accessed 19-June-2019].

[8]M. Kutz, *Handbook of Environmental Degradation of Materials*. Elsevier, third ed., 2018.

[9]Granta Design Limited, "CES Edupack 2018."

[10]Shell, "Shell Hydrogen Study Energy of the Future? Sustainable Mobility through Fuel Cells and H2," 2017.

[11]G. De Clercq and D. Psaledakis, "Reuters - EU nations aim high with plan to tax air travel," June 2019.

[12]J. S. Ribeiro and J. de Oliveira Gomes, "Proposed framework for end-of-life aircraft recycling," *Procedia CIRP*, vol. 26, pp. 311 – 316, 2015. 12th Global Conference on Sustainable Manufacturing – Emerging Potentials.

[13]R. Bontempo and M. Manna, "Analysis and evaluation of the momentum theory errors as applied to propellers," *AIAA Journal*, vol. 54, pp. 3840–3848, 08 2016.

[14]M. D. Corporation, "The United States Air Force Stability and Control Digital DATCOM Volume I, Users Manual," 1976. [Online; accessed 19-June-2019].

[15]A. S. of Mechanical Engineers, "Boiler and pressure vessel code," 2015.

[16]M. Jackson, Paul, *Jane's all the World's Aircraft 2004-05*. London: Jane's Publishing Group, (2005) edition ed., 2002.

[17]G. van Es, "Landing Long: Why does it happen?," 2011. [Online; accessed 19-June-2019].

[18]M. Voskuijl, "Flight and orbital mechanics," March 2019.

[19]B. Z. R. Vos, J.A. Melkert, "Aerospace Design and Systems Engineering Elements I – AE1222-II, A/C Preliminary Sizing (T/W-W/S diagram)," 2019. [Online; accessed 19-June-2019].

[20]Shell, "Energy Of The Future?," 2017. [Online; accessed 18-June-2019].

[21]Praxair, "Advanced Hydrogen Liquefaction Process," 2011.

[22]Irena, "Renewable Power Generation Cost in 2017," 2018.

[23]Neha Rustagi and Amgad Elgowainy and James Vickers, "Current Status of Hydrogen Delivery and Dispensing Costs and Pathways to Future Cost Reductions," 2018. [Online; accessed 18-June-2019].

[24]NASA, "Modeling High-Speed Civil Tiltrotor Transports in the Next Generation Airspace," October 2011. [Online; accessed 15-May-2019].

[25]ICAO, "Environmental Protection - Annex 16 - Volume I Aircraft Noise," July 2008. [Online; accessed 15-May-2019].

[26]Amsterdam Airport Schiphol, "Schiphol Regulations," November 2017. [Online; accessed 20-June-2019].

[27]M. Jackson, Paul, *Jane's all the World's Aircraft, Bell Boeing V-22 Osprey*. London: Jane's Publishing Group, 2019.

[28]F. Oliviero, "Aerospace Design and Systems Engineering Elements II AE2111-II aircraft part, Aircraft aerodynamic analysis – Lift and Drag ," 2019. [Online; accessed 19-June-2019].

[29]E. Obert, "Helicopter Performance, Stability, and Control," 2009. [Online; accessed 19-June-2019].

[30]J. Roskam, "Airplane Design, Part II: Preliminary Configuration Design and Integration of the Propulsion System," 1997.

[31]EASA, "Easy access rules for large rotorcraft (cs-29)," 2018.

[32]F. Oliviero, "Aerospace Design and Systems Engineering Elements II AE2111-II aircraft part, Aircraft aerodynamic analysis - fundamentals," 2019. [Online; accessed 19-June-2019].

[33]D. P. Raymer, "Aircraft Design: A Conceptual Approach," 1992. [Online; accessed 19-June-2019].

[34]F. Oliviero, "Aerospace Design and Systems Engineering Elements II AE2111-II aircraft part, A Aircraft aerodynamic analysis – Mobile surfaces of the wing ," 2019. [Online; accessed 19-June-2019].

[35]EASA, "Certification specifications and acceptable means of compliance for large rotor-craft," 2016.

[36]EASA, "Certification specifications for normal, utility, aerobatic, and commuter category aeroplanes," 2018.

[37]Faculty of Aerospace Engineering Delft University of Technology, *AE2100 second year project Work Package 4*, 2010.

[38]J. Roskam, "Airplane Design, Part III: Layout Design of Cockpit, Fuselage, Wing and Empennage: Cutways and Inboard Profiles," 1997.

[39]B. Z. R. Vos, J.A. Melkert, "Aerospace Design and Systems Engineering Elements I – AE1222-II, The Design of the Fuselage ," 2019. [Online; accessed 19-June-2019].

[40]J. Roskam, "Airplane Design, Part V: Component Weight Estimation," 2003.

[41]T. H. G. Megson, *Aircraft Structures*. Elsevier, 2007.

[42]S. J.G.Leishman, "An optimum coaxial rotor system for axial flight."

[43]G. A.Gessow, *Aerodynamics of the Helicopter*. Macmillan Co., 1952.

[44]J.C.Leishman, *Principles of Helicopter Aerodynamics*. Cambridge University Press, 2006.

[45]R. X.Chen, *Inclusion of a Simple Dynamic Model in the Blade Element Momentum Theory for Wind Turbine Application*. Proceedings of the ASME 2014 Power Conference, 2014.

[46]H. S. F.Mahmuddin, S.Klara, "Airfoil lift and drag extrapolation with viterna and montgomerie methods."

[47]R. W. Prouty, "Helicopter Performance, Stability, and Control," 2002.

[48]R. C.C.Critzos, H.H.Heyson, "Aerodynamic characteristics of naca 0012 airfoil section at angles of attack from 0° to 180°," 1955.

[49]F. S. Cunha, "Conceptual Helicopter Design."

[50]Powercell, "Powercell fuel cell stack and systems." [Online; accessed 20-June-2019].

[51]Yasa Limited, "P400 R Series Datasheet." [Online; accessed 16-May-2019].

[52]Q. Zhao, Y. Zhang, Y. Meng, Y. Wang, J. Ou, Y. Guo, and D. Xiao, "Phytic acid derived lifepo 4 beyond theoretical capacity as high-energy density cathode for lithium ion battery," 2017.

[53]M. Motor, "Coolant pump catalogue," 2019.

[54]D. Verstraete, "The potential of liquid hydrogen for long range aircraft propulsion," 2009.

[55]G. D. Brewer, "Chapter 15 - material profiles," 1991.

[56]R. Barron and N. G., "Cryogenic heat transfer," 05 1999.

[57]T. Flynn, "Cryogenic engineering: Second edition, revised and expanded," 01 2004.

[58]C. Winnefeld, T. Kadyk, B. Bensmann, U. Krewer, and R. Hanke-Rauschenbach, "Modelling and Designing Cryogenic Hydrogen Tanks for Future Aircraft Applications," *Energies*, vol. 11, no. 1, p. 105, 2018.

[59]. Kaufman, J. G. (John Gilbert), *Properties of aluminum alloys : tensile, creep, and fatigue data at high and low temperatures*. Materials Park, Ohio : ASM International ; Washington, D.C. : Aluminum Association, 1999. Includes bibliographical references.

[60]I. Burhan and H. Kim, "S-n curve models for composite materials characterisation: An evaluative review," *Journal of Composites Science*, vol. 2, no. 3, p. 38, 2018.

[61]H. Barthelemy, M. Weber, and F. Barbier, "Hydrogen storage: Recent improvements and industrial perspectives," *International Journal of Hydrogen Energy*, vol. 42, no. 11, p. 7254–7262, 2017.

[62]D. Gleich, "Development of a filament-overwrapped cryoformed metal pressure vessel," 01 1971.

[63]S. Mital, J. Gyekenyesi, S. Arnold, R. Sullivan, J. Manderscheid, and P. Murthy, "Review of current state of the art and key design issues with potential solutions for liquid hydrogen cryogenic storage tank structures for aircraft applications," 01 2006.

[64]U. O. of Energy Efficiency and R. Energy, "Hydrogen Storage," 2019. [Online; accessed 30-April-2019].

[65]L. Das, "7 - hydrogen-fueled internal combustion engines," in *Compendium of Hydrogen Energy* (F. Barbir, A. Basile, and T. N. Veziroğlu, eds.), Woodhead Publishing Series in Energy, pp. 177 – 217, Oxford: Woodhead Publishing, 2016.

[66]J. Villatoro, D. Luna-Moreno, and D. Monzón-Hernández, "Optical fiber hydrogen sensor for concentrations below the lower explosive limit," *Sensors and Actuators B: Chemical*, vol. 110, no. 1, pp. 23 – 27, 2005.

[67]Herose GMBH, "Cryogenic Safety Valve, angle type, stainless steel, Type 06810 - Data Sheet." [Online; accessed 5-June-2019].

[68]"15 - emission and dispersion," 2005.

[69]Valcor Engineering Application, "V44700 - Cryogenic 2-Way Normally Open or Normally Closed Shut-Off Solenoid Valve - Data Sheet." [Online; accessed 5-June-2019].

[70]Linde Group, "Hydrogen fuelling station with cryo pump technology - Data Sheet." [Online; accessed 5-June-2019].

[71]Powercell, "Powercell s3 fuel cell stack." [Online; accessed 15-May-2019].

[72]Walther Prazision, "Hydrogen refuelling system." [Online; accessed 20-June-2019].

[73]Staubli, "Inline safety break-away BRH for electric vehicles powered by hydrogen." [Online; accessed 10-June-2019].

[74]International Organization for Standardization, "Iso 13984:1999 - liquid hydrogen — land vehicle fuelling system interface." [Online; accessed 20-June-2019].

[75]B. T. Skoczeń, *Properties of Austenitic Stainless Steels at Cryogenic Temperatures*, pp. 65–75. Berlin, Heidelberg: Springer Berlin Heidelberg, 2004.

[76]H. Bednar and H. Saunders, "Pressure Vessel Design Handbook, 2nd Edition," 1987.

[77]S. Aceves, J. Martinez-Frias, and O. Garcia-Villazana, "Analytical and experimental evaluation of insulated pressure vessels for cryogenic hydrogen storage," *International Journal of Hydrogen Energy*, vol. 25, no. 11, pp. 1075 – 1085, 2000.

[78]Laminated Plastics, "Technical Data Sheet G-10." [Online; accessed 10-June-2019].

[79]R. K. Praharaj, "Design and development of liquid nitrogen storage vessel using asme boiler and pressure vessel code," May 2015.

[80]R. G Ross, "Quantifying mli thermal conduction in cryogenic applications from experimental data," *IOP Conference Series: Materials Science and Engineering*, vol. 101, p. 012017, 12 2015.

[81]G. Bennett and F. Kerry, "Industrial gas handbook: Gas separation and purification," *J. Hazard. Mater.*, vol. 161, 01 2009.

[82]J. G. Kaufman, "Properties of aluminum alloys: Tensile, creep, and fatigue data at high and low temperatures," *Materials Park*, 2006.

[83]A. Adibekyan, E. Kononogova, C. Monte, and J. Hollandt, "Review of ptb measurements on emissivity, reflectivity and transmissivity of semitransparent fiber-reinforced plastic composites," *International Journal of Thermophysics*, vol. 40, p. 36, Mar 2019.

[84]D. F. Windenburg and C. Trilling, "Pressure vessel and piping design: Collected papers," 1960.

[85]S. P. Timosenko and J. M. Gere, *Theory of elastic stability*. Dover publ., 2009.

[86]G. L. Mills, B. Buchholtz, and A. Olsen, "Design, Fabrication and Testing of a Liquid Hydrogen Fuel Tank for a Long Duration Aircraft," *AIP Conference Proceedings*, vol. 1434, no. 1, pp. 773–780, 2012.

[87]R. Shah, "Design and optimization of cryogenic storage vessel," *International Journal of Engineering Development and Research*, vol. 3, 2014.

[88]Celereton, "Ct-14-1000," June 2019.

[89]PowerCell, "Powercell s3," June 2019.

[90]Fraunhofer, "Bidirectional full sic 200kw dc-dc converter," June 2019.

[91]G. Aviation, "20kw dc-dc converter," June 2019.

[92]Fraunhofer, "100 kw sic-inverter for automotive application," June 2019.

[93]P. L. Daan Moreels, "High efficiency axial flux machines," Nov. 2018.

[94]Stober, "Servofit."

[95]Neugart, "Precision on the highest level."

[96]A. T. Duane Pettit, "General aviation aircraft reliability study," 2001.

[97]M. Kimble and M. Hoberecht, "Performance evaluation of electrochem's pem fuel cell power plant for nasa's 2nd generation reusable launch vehicle," 2003.

[98]J. Roskam, "Airplane Design, Part IV: Layout of Landing Gear and Systems," 1997.

[99]J. Roskam, "Airplane Design, Part I: Preliminary Sizing of Airplanes," 1997.

[100]E. Torenbeek., "Synthesis of subsonic airplane design: an introduction to the preliminary design, of subsonic general aviation and transport aircraft, with emphasis on layout, aerodynamic design, propulsion, and performance.," 1982.

[101]D. Velupillai, "T-tail and top technology."

[102]E. Tulapurkara, "Chapter 6 fuselage and tail sizing - 4 lecture 26," 2014.

[103]T. van Holten and J. Melkert, "Helicopter performance, stability and control," 2002.

[104]Eaton, "Bell boeing v-22 osprey," 2014.

[105]A. Tewari, *Advanced Control of Aircraft, Spacecraft and Rockets*. John Wiley and Sons, 2011.

[106]Department of Defense , "Report of the Panel to review the V-22 program," April 2001. [Online; accessed 5-June-2019].

[107]S. Gudmundsson, *General Aviation Aircraft Design*. Elsevier, 2014.

[108]M. C. Y. Niu, *Airframe Structural Design*. Hong Kong Conmilit Press LTD., 1988.

[109]G. Beziac, "Application of composite materials in helicopter construction," 1983.

[110]J. Sinke, "Lecture notes in production of aerospace systems," March 2019.

[111]X. S. L. C. W. A. R. M. T. Foster, "Surface effects in

chromate conversion coatings on 2024-t3 aluminum alloy," *Journal of Materials Science*, vol. 36, p. 3215–3220, 07 2001.
[112] J. Sinke, "Lecture notes in production of aerospace systems," March 2019.
[113] C. Drew and J. Mouawad, "The jump to a composite plane," *New York Times*, 2013.
[114] Intergovernmental Panel on Climate Change, "Emissions of selected electricity supply technologies," 2014.
[115] A. Eylem, O. Michael, and T. Janet, "Recycling of aircraft: State of the art in 2011," *Journal of Industrial Engineering*, December 2012.
[116] DSE Group 19 , "Futura, Hydrogen electric helicopter," May 2019. [Online; accessed 5-June-2019].
[117] Y. Yang, "Lecture Notes in Recycling of Engineering Materials (MS43315)," 2019.
[118] B. Björkman and C. Samuelsson, "Recycling of steel," in *In Handbook of Recycling: State-of-the-art for Practitioners, Analysts, and Scientists* (M. F. Ashby, ed.), p. 65–83, Waltham, Mass: Butterworth-Heinemann, second edition ed., 2014.
[119] L. Shen and E. Worrell, "Plastic recycling," 12 2014.
[120] B. S. Thomas and R. C. Gupta, "A comprehensive review on the applications of waste tire rubber in cement concrete," 2016.
[121] S. Swarna, "Stabilization of subgrade soil of highway pavement using waste tyre pieces," *International Journal of Innovative Research in Science, Engineering and Technology*, vol. 4, pp. 3265–3273, 05 2015.
[122] Y. Yang, R. Boom, B. Irion, D.-J. van Heerden, P. Kuiper, and H. de Wit, "Recycling of composite materials," *Chemical Engineering and Processing: Process Intensification*, vol. 51, p. 53–68, 01 2012.
[123] S. Pimenta and S. Pinho, "Recycling of carbon fibers," 12 2014.
[124] J. Koehler, R. Zuber, M. Binder, V. Baenisch, and M. Lopez, "Process for Recycling Fuel Cell Components Containing Precious Metals. WIPO Patent No. WO/2006/024507," 3 2006.
[125] C. Hagelüken, B. Kayser, J. Romero-Ojeda, and I. Kleinwächter, "Process for the Concentration of Noble Metals from Fluorine-Containing Fuel Cell Components. WIPO Patent No. WO/2004/102711," 11 2004.
[126] M. Pehnt, "Life-cycle analysis of fuel cell system components," 2010.
[127] R. Zuber, C. Hagelüken, K. Seitz, R. Privette, and K. Fehl, "Recycling of precious metals from fuel cell components," 11 2004.
[128] R. Wittstock, A. Pehlken, and M. Wark, "Challenges in automotive fuel cells recycling," *Recycling*, vol. 1, p. 343–364, Dec 2016.
[129] Umicore, "Battery Recycling - Our Recycling Process." [Online; accessed 7-May-2019].
[130] Aircraft End-Of-Life Solutions BV, "What can aels do for airlines?." [Online; accessed 16-May-2019].
[131] Airbus SE, "H145," 2019. [Online; accessed 1-May-2019].
[132] C. Koroneos, A. Dompros, G. Roumbas, and N. Moussiopoulos, "Life cycle assessment of kerosene used in aviation (8 pp)," *The International Journal of Life Cycle Assessment*, vol. 10, pp. 417–424, Nov 2005.
[133] Jacob Markish, "Valuation Techniques for Commercial Aircraft Program Design," June 2002. [Online; accessed 18-June-2019].
[134] J. Roskam, "Airplane Design, Part VIII: Airplane Cost Estimation: Design, Development, Manufacturing and Operating," 2002.
[135] Jeremiah Gertler, "V-22 Osprey Tilt-Rotor Aircraft: Background and Issues for Congress," March 2011. [Online; accessed 18-June-2019].
[136] Peter P. Belobaba, "Operating Costs and Productivity Measures," February 2006. [Online; accessed 1-July-2019].
[137] Z. Berdowski, F. van den Broek-Serie, J. Jetten, Y. Kawabata, J. Schoemaker, and R. Versteegh, *Survey on standard weights of passengers and baggage*. EASA, may 2009. [Online; accessed 1-May-2019].
[138] Duane Pettit,Andrew Turnbull , "General Aviation Aircraft Reliability Study," February 2001. [Online; accessed 18-June-2019].
[139] Defense Technical Information Center, "Structural integrity and aging-related issues of helicopters," October 2000. [Online; accessed 14-May-2019].
[140] Jingyi Yue, Yan Cao* , "Corrosion Prevention by Applied Coatings on Aluminum Alloys in Corrosive Environments ," February 2015. [Online; accessed 18-June-2019].
[141] J. d. K. Hans Bakker, *Management of engineering projects: people are key*. NAP - The Process Industry Competence Network, 2014.
[142] A. Kostival, C. Rivkin, W. Buttner,R. Burgess , "Pressure Relief Devices for High-Pressure Gaseous Storage Systems: Applicability to Hydrogen Technology ," November 2013. [Online; accessed 5-June-2019].
[143] Russel Rhodes, "Explosive lessons in hydrogen safety ." [Online; accessed 5-June-2019].
[144] Joel Villatoro, Donato Luna Moreno, David Monzon Hernandez, "Optical fiber hydrogen sensor below the lower explosive limit." [Online; accessed 5-June-2019].
[145] Celina Mikolajczak,Michael Kahn, Kevin White, Richard Thomas Long, "Lithium-Ion Batteries Hazard and Use Assessment ," July 2011. [Online; accessed 5-June-2019].
[146] VARTA, "Handling precautions and prohibitions for VARTA Microbattery GmbH LiIon batteries and General SUPPLY Notices," March 2011. [Online; accessed 5-June-2019].
[147] William Spitz, Richard Golaszewski, and Frank Berardino, "Development Cycle Time Simulation for Civil Aircraft," January 2001. [Online; accessed 17-June-2019].